Theoretical studies of novel graphene based nanostructures

Van Binh Vu

université PARIS-SACLAY

Theoretical studies of novel graphene based nanostructures

Étude théorique de nouvelles nanostructures à base de graphène

Thèse de doctorat de l'université Paris-Saclay

École doctorale n° 572 Ondes et Matière (EDOM)

Spécialité de doctorat: Physique

Graduate School : Physique. Référent : Faculté des sciences d'Orsay

Thèse préparée au **Service de Physique de l'État Condensé** (Université Paris-Saclay, CEA, CNRS), sous la direction de **Yannick DAPPE**, Chargé de Recherches CNRS, la co-encadrement de **Sylvain LATIL**, Chercheur CEA

Thèse soutenue à Paris-Saclay, le 21 juin 2024, par

Van Binh VU

Composition du jury

Membres du jury avec voix délibérative

Vincent HUC Directeur de recherche, ICMMO, CNRS, Université Paris-Saclay	Président
Eleonora LUPPI Maître de conférences HDR, Laboratoire de Chimie Théorique, Sorbonne Université	Rapporteuse & Examinatrice
Sylvain CLAIR Directeur de Recherche CNRS, IM2NP, CNRS, Université Aix-Marseille	Rapporteur & Examinateur
Linda Angela ZOTTI Assistant Professor, Facultad de Ciencias, Universidad Autónoma de Madrid	Examinatrice

THESE DE DOCTORAT

NNT : 2024UPASP039

université PARIS-SACLAY

ÉCOLE DOCTORALE
Ondes et Matière (EDOM)

Titre: Étude théorique de nouvelles nanostructures à base de graphène.

Mots clés: Matériaux de faible dimension, graphène, hBN, simulations STM, simulations optiques

Résumé: Depuis sa découverte, le graphène est devenu un centre de recherche et d'intérêt important en raison de ses caractéristiques mécaniques, thermiques et électriques exceptionnelles. Néanmoins, l'absence de bande interdite dans le graphène constitue un obstacle aux applications dans les domaines de l'optique, de la nanoélectronique et de la spintronique. L'ingénierie de la bande interdite impliquant la nanostructuration du graphène a été développée au fil des ans, par exemple par confinement quantique, pour surmonter cette limitation.

Ce travail théorique est consacré à la modification des réponses électroniques, optiques et de microscopie/spectroscopie à effet tunnel (STM/STS) en fonction de la taille du système de nouveaux matériaux de carbone tels que les nanomeshs de graphène (GNM), les boîte quantiques de graphène de forme/taille contrôlée (GQD) et les nanorubans de graphène (GNR), afin de comparer et d'analyser les données expérimentales.

Ces nouveaux matériaux carbonés sont théoriquement déposés sur des surfaces d'or Au(111) dans une simulation STM réalisée à l'aide du formalisme des fonctions de Green hors équilibre (NEGF) basé sur la méthode DFT Fireball afin d'étayer les données expérimentales.

En ce qui concerne les GQD, nous simulons leur spectre d'absorption en utilisant la correction GW et les équations de Bethe-Salpeter (BSE), si possible, pour les comparer directement aux données expérimentales. Dans le cas contraire, leurs propriétés optiques sont obtenues par une approche inférieure, l'approche Tight-Binding (TB). Les impacts des agrégations et des impuretés sur leurs réponses optiques sont également explorés en étudiant la bicouche torsadée des GQDs via la méthode TB.

En outre, les changements dans les propriétés électroniques de ces nouveaux matériaux de carbone en fonction de la taille de leur système sont extraits à l'aide de la méthode TB. La performance de la méthode TB est vérifiée par des simulations DFT et GW.

Enfin, d'autres matériaux de faible dimension, les nouvelles structures bicouches de nitrure de bore hexagonal torsadées à près de 30° (hBN-TBLs), sont également étudiées dans cette thèse. Les méthodes DFT et TB réalisent les structures électroniques et optiques de nouveaux hBN-TBLs plus loins de 30° afin d'obtenir les paramètres d'ajustement pour le modèle TB. Ces paramètres sont ensuite utilisés pour prédire des hBN-TBL plus proches de 30°, ce qui est difficilement réalisable par DFT.

Title: Theoretical studies of novel graphene based nanostructures.

Keywords: Low-dimensional materials, graphene, hBN, STM simulations, optical simulations

Abstract: Since its discovery, graphene has become a focal point of extensive research and interest because of its exceptional mechanical, thermal, and electrical characteristics. Nevertheless, the absence of a bandgap in graphene constitutes a barrier to applications in optics, nanoelectronics, and spintronics. Bandgap engineering involving the nanostructuration of graphene has been developed over the years, such as by quantum confinement, to overcome this limitation.

This theoretical work is dedicated to the change of electronic, optical, and scanning tunneling microscopy/spectroscopy (STM/STS) responses as a function of system size of new carbon materials like graphene nanomeshes (GNMs), shape/size controlled graphene quantum dots (GQDs) and graphene nanoribbons (GNRs), in order to compare and analyze experimental data.

These new carbon materials are theoretically deposited on gold Au(111) surfaces in STM simulation performed using the Non-equilibrium Green's function (NEGF) formalism based on the Fireball DFT method to support the experimental data.

Concerning GQDs, we simulate their absorption spectrum using the GW approximation and the Bethe–Salpeter equations (BSE), if possible, to compare directly with the experiment data. Otherwise, their optical properties are achieved by a lower approach, the Tight-Binding (TB) approach. Also, the impacts of aggregations and impurities on their optical responses are explored by studying the twisted bilayer of the GQDs via the TB method.

Moreover, the changes in these new carbon materials' electronic properties as a function of their system size are extracted using the TB method. The performance of the TB method is verified by DFT and GW simulations.

Finally, other low-dimensional materials, new close-to 30° twisted hexagonal boron nitride bilayer structures (hBN-TBLs), are also studied in this thesis. DFT and TB methods perform the electronic and optical structures of further 30° hBN-TBLs to obtain the fit parameters for the TB model. These parameters are then used to predict closer to 30° hBN-TBLs, which are hardly to be obtained by DFT.

Université Paris-Saclay
Espace Technologique / Immeuble Discovery
Route de l'Orme aux Merisiers RD 128 / 91190 Saint-Aubin, France


université
PARIS-SACLAY
ÉCOLE DOCTORALE
Ondes et Matière
(EDOM)


cea
spec
IPhT

Luận án tiến sĩ này xin được đặc biệt dành tặng cho ông bà nội và em, Hà !

Acknowledgements

Je suis tout d'abord reconnaissant envers mes directeurs de thèse, Yannick et Sylvain, qui sont d'excellents chercheurs et qui m'ont donné l'opportunité de travailler avec eux et de réaliser cette thèse.

Merci à Yannick d'être toujours positif, bienveillant, et surtout très généreux. Tu m'as toujours donné les meilleures choses que tu avais sans condition. J'ai commencé cette thèse avec beaucoup de difficultés dans ma vie personnelle, j'étais malheureux et un peu perdu en France, plein de doutes sur ma vie : ma vie en France, mes études, mes compétences... Et boum ! Tu es apparu de nulle part avec ce sujet de thèse, comme une lumière au bout d'un long tunnel, ce qui m'a relevé et m'a sorti des pensées négatives que je vivais. Pendant ces trois ans, tu m'as offert les meilleures opportunités que je n'aurais jamais imaginées. J'ai vraiment eu la chance de travailler à tes côtés. Tu m'as appris bien plus que la science et la physique : tu m'as donné des leçons de vie que personne ne m'avait enseignées. Cela a changé l'homme que je suis, cela m'a permis de trouver mon identité et de mieux me comprendre. Désormais, je peux réussir ma vie où que je sois, en faisant ce que j'aime.

Je tiens également à te remercier, Sylvain, pour tout. Tu as toujours été franc et honnête avec moi, ce que j'ai énormément apprécié. Tu m'as véritablement transmis la passion de la physique, et j'ai redécouvert à quel point cette discipline peut être intéressante, retrouvant ainsi le plaisir de travailler. Merci de m'avoir écouté et aidé, peu importe l'heure ou le lieu. Tu m'as toujours donné des idées, et ton exigence m'a permis de progresser rapidement en peu de temps. Merci de m'avoir introduit dans ton univers de la physique ; je suis profondément reconnaissant pour tout ce que tu as fait pour moi. Je suis fier d'être ton premier doctorant. Du fond du cœur, merci infiniment.

Ensuite, je tiens à remercier tous mes collaborateurs dans les projets BOGART et GANESH. Un merci particulier à Stéphane : tu as toujours été très humble et bienveillant. Merci de m'avoir inclus dans ces beaux projets, d'avoir été patient et compréhensif face à mes erreurs. Je voudrais remercier tes doctorants, Julien et Daniel, pour leurs mesures ; j'ai également beaucoup été inspiré par leurs manuscrits. Je remercie aussi mes autres collaborateurs, Sylvain, Jean-Sébastien et son doctorant Thanh Trung, Hamid et son doctorant Hamza, pour avoir réalisé les mesures précises et les belles images présentées dans cette thèse.

Je voudrais aussi remercier mes collaborateurs à l'ONERA, dans le cadre du projet sur les bicouches torsadées de nitrure de bore hexagonal. Merci à Lorenzo et Hakim de m'avoir inclus dans ce magnifique projet. Merci de m'avoir accueilli à l'ONERA, et un merci spécial à Lorenzo et à sa doctorante Elisa, qui m'ont énormément aidé à utiliser les simulations d'*ab initio*, ce qui m'a permis de trouver les beaux résultats présentés dans cette thèse.

Ensuite, je voudrais remercier ma deuxième maison, l'équipe GMT au SPEC. Merci aux membres permanents, Alex, Cyrill et Cosimo, de m'avoir si bien accueilli et traité au sein de l'équipe. Vous avez créé une ambiance très familiale, sans pression. Je tiens surtout à remercier les autres doctorants et post-docs de l'équipe, comme Omar, Mahé, Poonam, Ian-Evan, Mohamed et Lilian, qui m'ont énormément soutenu, tant sur le plan scientifique que personnel. Grâce à vous, chaque jour a été amusant et rempli de rires. C'est le meilleur environnement de travail que j'ai connu jusqu'à présent.

Je remercie l'ensemble du Service de Physique de l'État Condensé (SPEC), ainsi que le chef, Patrice Roche, pour m'avoir accueilli dans son laboratoire. Je remercie tout particulièrement François, Corinne, Claude, Nadine, et Julie, qui ont toujours été minutieux. Votre travail a grandement facilité ma vie au laboratoire. Un merci tout spécial à François : tu as vraiment été la clé pour résoudre mes problèmes de titre de séjour et pour me donner les meilleurs conseils sur la vie au laboratoire. Je pense aussi aux autres doctorants du SPEC : Artem, Zixin, Aifei, Charles, Benjamin, Céline, Raphaël, Rémi et Nghia, avec qui j'ai partagé de nombreux repas. J'ai eu la chance d'être entouré de vous au labo.

Pendant ma thèse, j'ai eu la chance de rencontrer de nombreux amis avec qui j'ai partagé des moments formidables. Nous nous apprécions, aimons voyager et jouer ensemble. Merci aux amis du groupe de Saint-Malo : Paul, Maïkane, Anyssa, Grégoire, et Anas. Merci aux amis du groupe de Bruxelles et Bologne : Sanjay, Agathe, Noujoud, Jérôme, et Lamya.

Je pense très fort à vous, mes amis et amies de P7, avec qui j'ai partagé cinq magnifiques années d'études à l'université Paris-Diderot : Issam, Robin, Ayoub, Daianah, Yasser, Omaid, Fatimat, Reda et Estelle. Merci de m'avoir encouragé, poussé vers le haut, et de m'avoir toujours soutenu discrètement

Để mở đầu phần cảm ơn dành cho bạn bè Việt Nam, em xin trân trọng cảm ơn: gia đình anh Ti và chị Duyên, anh Lâm và chị Béo, gia đình anh Nghĩa và chị Kim Anh, gia đình anh Tâm và chị Tâm, gia đình anh Long và chị Xuân. Cảm ơn các anh chị đã xuất hiện đúng vào thời điểm em khó khăn nhất, hy sinh thời gian và công sức để nâng đỡ và giúp đỡ em.

Tiếp theo, tôi xin cảm ơn những người bạn mà chúng ta có duyên gặp gỡ và trở nên thân thiết trong quá trình sinh sống ở Pháp. Xin cảm ơn những người bạn đã cùng học tiếng Pháp, đặc biệt là chị Phương và Minh Châu, hai người là những người bạn đầu tiên, luôn bên cạnh và động viên em rất nhiều. Em xin chân thành cảm ơn đặc biệt đến anh Đức, cô Đào và em Xé. Nếu không có sự định hướng và giúp đỡ của anh và gia đình, em sẽ không bao giờ có được thành quả học tập như hôm nay.

Phần tiếp theo, tôi xin cảm ơn những người em và những người bạn đã cùng nhau chia sẻ hàng tuần ăn uống, hát hò, du lịch khắp nơi: Vân và Tùng, Quỳnh Anh, Chíp, Linh, Nga, Hiếu. Xin cảm ơn Việt Anh và anh Hưng bên Bỉ đã dành thời gian trò chuyện và những chuyến công tác đáng nhớ cùng nhau.

Em xin cảm ơn người thầy đã để lại ấn tượng sâu sắc nhất trong cuộc đời học sinh của em, cô Chiến. Em cảm ơn cô vì đã dành thời gian dạy riêng miễn phí cho em trong suốt thời gian cô làm chủ nhiệm. Sau 20 năm, em chưa ngày nào quên được sự tận tụy và nhiệt tình của cô. Em xin chân thành cảm ơn các thầy cô giáo cấp 2 và cấp 3: thầy Trường, thầy Cương, thầy Nam, thầy Hoàn (cấp 2), cô Châu Liên, cô Huế, cô Mến, cô Hảo, cô Trang (cấp 3). Các thầy cô đã đóng góp không nhỏ vào sự hình thành con người em ngày hôm nay.

Tôi xin cảm ơn các bạn bè từ cấp 1, cấp 2 đến cấp 3. Cảm ơn vì những cuộc trò chuyện, những lời động viên. Cảm ơn vì đã luôn ở đó, luôn là bạn của tớ. Đặc biệt xin gửi lời cảm ơn đến: Trang, Hiếu, Ngọc Anh, Hường, Thu, Phạm Thu, Phương, Ụt, Xuân, Đạt, Đương, Phan Tuấn, Tuấn 4, Bôn, Ngọc, Nguyên, Minh Dương, Minh, Khánh, Nguyên Minh, Thơm. Cảm ơn Trang một lần nữa vì đã đồng hành với tớ từ cấp 2 đến bây giờ ở Pháp, cảm ơn vì đã luôn bên tớ.

Cuối cùng, tôi xin gửi lời cảm ơn đặc biệt nhất đến gia đình của tôi. Anh xin cảm ơn em, Hà, vì đã dành cả tuổi trẻ bên cạnh anh và không bao giờ quay lưng với anh. Tiếp theo, con xin cảm ơn bố mẹ vì đã sinh ra con và tạo điều kiện cho con sang Pháp. Cảm ơn Minh và Hà đã giúp đỡ anh, và luôn là những người em tuyệt vời của anh. Chú xin cảm ơn gia đình Trang và Minh Khế vì đã luôn đồng hành và hỗ trợ chú vô điều kiện. Cháu xin chân thành cảm ơn gia đình chú Bộ và cô Lan cùng các em Thương, Phượng và Biển. Cảm ơn vì đã luôn thấu hiểu và giúp đỡ cháu bằng mọi cách. Em xin cảm ơn gia đình chị Thủy, bác Duyên và anh Trung đã giúp đỡ cháu trong thời gian học cấp 3. Cháu xin cảm ơn bác Men và chị Hiền vì đã luôn hỏi thăm sức khỏe và quan tâm đến cháu. Cuối cùng, em xin chân thành cảm ơn gia đình anh Đoàn, chị Hương và cháu Mít đã luôn động viên tinh thần trong suốt thời gian qua và giúp đỡ em trong quá trình chuẩn bị sang Pháp.

VU Van Binh

Résumé en français

Le graphène est un réseau en nid d'abeilles constitué d'une seule couche d'atomes de carbone. C'est un semi-métal transparent sans bande interdite, avec une structure de bande linéaire. Grâce à sa structure unique, le graphène possède plusieurs propriétés impressionnantes telles qu'une haute conductivité, une grande résistance mécanique et une transparence optique. Depuis sa découverte, le graphène est devenu un sujet de recherche majeur en raison de ses caractéristiques mécaniques, thermiques et électriques exceptionnelles. Cependant, l'absence de bande interdite dans le graphène constitue un obstacle à son utilisation dans des applications comme l'optique, la nanoélectronique et la spintronique. Pour remédier à cela, l'ingénierie de la bande interdite, notamment par la nanostructuration du graphène, a été développée au fil des années. Il existe plusieurs méthodes pour ouvrir sa bande interdite, et dans cette thèse, nous nous intéressons au confinement quantique. En réduisant une ou deux dimensions du graphène à l'échelle nanométrique, on obtient des boîtes quantiques de graphène (GQDs) ou des nanorubans de graphène (GNRs). Alternativement, on peut créer un réseau régulier de trous à l'échelle nanométrique dans une feuille de graphène pour obtenir des nanomailles de graphène (GNMs).

Participant à divers projets ayant des objectifs communs, en collaboration avec des chimistes, expérimentateurs et théoriciens, nous visons à produire de nouveaux GQDs, GNRs et GNMs. Nos objectifs principaux sont de : (i) produire ces nanomatériaux en utilisant une méthode « bottom-up » en les contrôlant précisément à l'échelle atomique ; (ii) caractériser leurs propriétés électroniques, optiques et leurs réponses en microscopie/spectroscopie à effet tunnel (STM/STS).

Au cœur de ces projets, dans un premier temps, j'ai réalisé des simulations et des calculs pour prédire leurs propriétés électroniques, optiques, ainsi que leurs réponses en STM/STS, afin de comparer et analyser les données expérimentales. Ensuite, mon travail théorique se concentre sur la modification des réponses électroniques, optiques et en microscopie/spectroscopie en fonction de la taille et de la symétrie de ces nouveaux matériaux carbonés.

Dans cette thèse, les méthodes utilisées se divisent en trois catégories : semi-empiriques, *ab initio* et une combinaison des deux. La première utilise des approches adaptées à ces systèmes à base de graphène, appelée méthode de liaison forte (Tight-Binding (TB)), ce qui permet de simuler ces systèmes

avec un simple ordinateur de bureau. Toutefois, ces résultats doivent être validés par des calculs *ab initio*. Les méthodes *ab initio* reposent sur des principes premiers tels que la théorie de la fonctionnelle de la densité (DFT), GW, et les équations de Bethe-Salpeter (BSE). Ces méthodes, adaptées aux mesures électroniques et optiques expérimentales, nécessitent des supercalculateurs en raison de leur lourdeur, ce qui les rend impraticables pour de grands systèmes. La troisième approche combine les avantages des deux premières, ce qui la rend adaptée à des systèmes plus grands, comme ceux déposés sur une surface métallique, bien que sa précision soit moindre comparée à la méthode *ab initio*.

Dans ce manuscrit, mes études portent sur cinq familles de structures de GQDs, classées selon leur forme : GQD C42 en forme hexagonale (S1), GQD C30 en forme de trapèze (S2), GQD T C96 en forme triangulaire (S3), et GQDs R de C78 à C96 en forme rectangulaire (S4-S7).

Ces nouveaux matériaux carbonés sont théoriquement déposés sur des surfaces d'or Au(111) dans une simulation STM, réalisée à l'aide du formalisme des fonctions de Green hors équilibre (NEGF) basé sur la méthode Tight-Binding *ab initio* Fireball-DFT, afin de valider les données expérimentales. Mes simulations ont réussi à prédire les images STM attendues pour le GNR C42 ($p2mg$), GNR C30 ($p2mg$), et GNM C42 ($cmmm$) sur la surface d'or. Bien que ces deux GNRs aient des largeurs différentes (deux anneaux de carbone d'écart), ils appartiennent au même groupe de symétrie et partagent des signatures similaires, avec des électrons fortement confinés le long de l'ossature du GNR. Dans le GNM C42, les électrons sont confinés autour des trous. Malheureusement, ces structures n'ont pas encore été obtenue expérimentalement, malgré les nombreux efforts de nos chimistes pour créer plusieurs précurseurs. Les surfaces obtenues avec les GQD T C96 (S3) ainsi que les GQDs S3 fonctionnalisés avec des groupes tert-butyle (S3-T) et des chaînes alkyles (S3-A) sont complexes et n'ont pas donné de résultats convaincants lors de mes simulations.

Pour les GQDs, j'ai simulé leur spectre d'absorption en utilisant les corrections GW et les équations de Bethe-Salpeter (BSE) lorsque cela est possible, afin de les comparer directement aux données expérimentales. Sinon, leurs propriétés optiques sont obtenues à l'aide de la méthode Tight-Binding (TB). Mes simulations BSE sont en parfait accord avec les mesures expérimentales pour les GQDs C42 (S1) et C78 (S4). Les simulations TB sur les GQDs de forme rectangulaire (S4-S7) ont montré que la bande interdite diminue à mesure que la taille du GQD augmente, et qu'il est possible de déplacer la réponse optique de plus de 283 nm en passant de S4 à S7. Cependant, ces réponses optiques n'ont pas été complètement révélées expérimentalement en raison de l'agrégation due à la mauvaise solubilité des GQDs. Nos collaborateurs ont ajouté des groupes fonctionnels tels que des groupes tert-butyle et des chaînes alkyles. La présence de ces groupes a considérablement amélioré la solubilité des GQDs, en particulier avec les groupes tert-butyle, mais cela reste insuffisant, surtout pour les petits GQDs comme le S4. Les impacts de l'agrégation et des impuretés sur leurs réponses optiques ont également

été explorés en étudiant les bicouches torsadées de GQDs via la méthode TB. Ces facteurs peuvent provoquer un changement de symétrie des GQDs, entraînant une division des niveaux d'énergie, une réduction de la bande interdite et l'apparition de pics supplémentaires.

Enfin, d'autres matériaux bidimensionnels, comme les bicouches torsadées de nitrure de bore hexagonal (hBN-TBLs) à un angle proche de 30°, sont également étudiés dans cette thèse. Les méthodes DFT et TB ont permis de déterminer les propriétés électroniques et optiques de nouveaux hBN-TBLs éloignés de 30°, afin d'obtenir des paramètres d'ajustement pour le modèle TB. Ces paramètres ont ensuite été utilisés pour prédire les propriétés des hBN-TBLs plus proches de 30°, un angle difficile à modéliser avec la DFT. Ce travail purement théorique a mis en évidence un nouvel "angle magique" à 30°, ce qui est un résultat intéressant pour les expérimentateurs, car depuis la découverte de l'angle magique dans les bicouches de graphène torsadées, la recherche s'est principalement concentrée sur les petits angles de torsion.

Contents

List of abbreviations

Ψ N-interacting-electrons wavefunction.

ε Microscopic dielectric function.

ε^M Macroscopic dielectric function.

ϵ_i One-particle eigenvalues.

φ_i One-particle wavefunctions.

ϕ_j Atomic orbitals.

ABS Absorption spectroscopy.

BSE Bethe–Salpeter equation.

CVD Chemical vapor deposition.

DFT Density functional theory.

EELS Electron energy loss spectroscopy.

GNM Graphene nanomesh.

GNR Graphene nanoribbon.

GQD Graphene quantum dot.

GWA GW approximation.

HBC Hexa-peri-benzocoronene.

hBN Hexagonal boron nitride.

IP Independent particle.

IPES Inverse photoemission spectroscopy.

KS Kohn-Sham.

LSD Liquid solution deposition.

MBPT Many-body perturbation theory.

NEGF Non-equilibrium Green's function formalism.

PAH Polycyclic aromatic hydrocarbon.

PES Photoemission spectroscopy.

PL Photoluminescence.

PLE Photoluminescence excitation.

PVD Physical vapor deposition.

QE Quantum Espresso.

QP Quasi-particle.

RPA Random phase approximation.

STM/STS Scanning Tunneling Microscopy/Spectroscopy.

TB Tight-Binding.

TBL Twisted bilayer.

Introduction

P. R. Wallace's 1947 study [1] laid the foundation for understanding graphene's properties by describing graphite's conductivity and outlining a single layer of carbon atoms. Despite theoretical insights, graphene synthesis remained challenging until 2004, when Andre Geim and Konstantin Novoselov isolated and characterized graphene using mechanical exfoliation. Their groundbreaking work, including measurment of the quantum Hall effect [2, 3], awarded them the Nobel Prize in Physics in 2010, highlighting the significance of their contributions.

In graphene, carbon atoms are arranged in a hexagonal lattice, where the $2s$, $2p_x$, and $2p_y$ orbitals of each carbon atom are hybridized to form three sp^2 orbitals while the $2p_z$ orbital remains unchanged. The three hybridized orbitals in the same plane form σ bonds with neighboring carbon atoms. These bonds are responsible for the exceptional mechanical properties of graphene. For instance, graphene exhibits a tensile strength of around 130 GPa and Young's modulus of approximately 1 TPa [4]. These values correspond to a hundred times those of structural steel [5], which make graphene one of the strongest known materials and one of the most potential materials for applications [6–8] in automobile, aerospace, sports industries, ... The remaining $2p_z$ orbitals, perpendicular to the sigma plane, overlap with adjacent orbitals, forming a π-bond where electrons can be delocalized. These delocalized orbitals are responsible for the splendid electronic properties of graphene. The bonding, antibonding π and π^* degenerate, and form a linear structure at $\mathbf{K}$ and $\mathbf{K}'$ points, called Dirac cones (see latter in 7). This linear relationship results in electrons propagating through graphene as being of zero mass and traveling at relativistic speeds [9]. Graphene has the high-end values of electron mobilities [2, 10], such as, 200 000 $cm^2V^{-1}s^{-1}$ on suspended graphene, 15 000 $cm^2V^{-1}s^{-1}$ in contact with a silicon dioxide interface. Moreover, graphene is a quasi-transparent material, absorbing only 2.3$\%$ of visible and infrared light [11], and it shows high thermal conductivity, such as 3 100 $Wm^{-1}K^{-1}$ in suspended graphene [12]. These exceptional properties make graphene an exciting candidate for transparent conducting electrodes [13, 14], and for thermal sensors and heat management [15–18], in order to meet the increasing demand on the smaller, more efficient, and powerful electronic components. However, according to J. Kedzierski *et al.* [19], epitaxial graphene transistors on SiC substrates exhibited mobilities up to 5 000 $cm^2V^{-1}s^{-1}$ and I_{on}/I_{off} ratios up to seven. Although the observed electron mobility is greatly higher than one in silicon devices, the I_{on}/I_{off} ratios are still not big enough and hinder its applications in digital electronics, which is an intrinsic consequence of the absence of bandgap resulting in an inability to turn off the conduction. Hence, one of the greatest interests is controlling and opening a band gap in graphene. Opening a bandgap in graphene can be divided into two groups of methods.

In the first group, the intrinsic structure of graphene is not modified, and the change in band structure stems from graphene's interaction with its environment. For instance, a 320 meV band gap was observed in bilayer graphene when charge inequality between layers was induced by changing the carrier

concentrations with the deposition of potassium atoms on the top layer [20]. Moreover, a 160 meV gap was observed in an epitaxially synthesized graphene on hexagonal boron nitride (h-BN) heterostructure because of the lattice mismatch between the two structures that generate a Moiré superlattice potential [21]. The heterostructures of two-dimensional materials allow for a synergy of properties between two different two-dimensional materials and the emergence of new properties not present in the isolated materials. Until now, it has been a hot topic. S. Y. Zhou *et al.* [22] reported that when graphene is grown epitaxially on specific substrates like silicon carbide (SiC), the interaction between graphene and the substrate can induce changes in its electronic structure, resulting in the formation of a band gap.

In the second group, the main strategies are to change the configuration of graphene by introducing new chemical elements or limiting the size of graphene to nanometric dimensions. In the former strategy, the simplest way is to substitute one carbon atom in the graphene lattice with another element. For instance, nitrogen-doped graphene exhibited a bandgap of 0.2 eV, obtained by Angle-resolved photoemission spectroscopy (ARPES) [23]. The synthesis of graphene doped with boron and nitrogen domains exhibited bandgaps up to 0.6 eV for low B-N concentrations, reported by Chan *et al.* [24]. Moreover, numerous other examples of substitutional doping were also observed with phosphorous [25], silicon [26, 27], iron [28], manganese [29], and other transition elements [30]. Another way is to introduce new chemical elements in the structure of graphene, such as fluorographene [31–33], graphene oxide (GO) [34], and reduced graphene oxide (rGO) [35–38]... In this case, the sp^2 character of graphene will be broken to create new bonds with carbon in graphene. The π-bands of the material are disturbed, and the band gap is opened. Nevertheless, overall, modifying the chemical structure of graphene can harm the unique electrical properties of pristine graphene [39], such as in rGO, the electron mobility drops to the order of tens of $cm^2.V^{-1}.s^{-1}$ [40].

Finally, it is possible to open a band gap in graphene by quantum confinement, which limits the distribution of charge carriers in space. The gap width increases in energy as size diminishes. The reduction of one dimension of graphene down to the nanoscale leads to graphene nanoribbons (GNRs) [41] while the reduction of the two dimensions leads to graphene quantum dots (GQDs) [42]. On the other hand, size reduction is not the only way to open a gap in graphene. Another appealing alternative is forming an ordered array of pores in a graphene sheet. This two-dimensional material theoretically proposed by Thomas G. Pedersen *et al.* [43] in 2008 was called a Graphene Nanomesh (GNM) or a Graphene Anti-dot Lattice (GAL). For the size reduction of graphene, the synthesis of material can be divided into two large groups: top-down and bottom-up. A top-down strategy is to take a bulk material, which is then shaped via physical or chemical methods (lithography and etching, thermal treatments, and oxidation of bulk materials) until the desired structure is obtained. On the contrary, the bottom-up strategy consists of assembling sub-units to achieve the target structure. Over the past decade, significant effort has

been directed towards reducing the size of graphene using conventional top-down methods to create graphene quantum dots [44–52], nanoribbons [53–57], and nanomeshes [58–61]. However, top-down approaches do not provide the ability to manipulate the material's structure at the atomic scale. Specifically, they lack sufficient control over the edges' morphology and oxidation state, which significantly impacts the material's properties. For instance, top-down methods are rather known to show that the resulting optical properties were mainly governed by defects states [62–65]. The challenge relied on the distinction between the intrinsic emission and the emission originated by defects in the GQD. sp^2 carbon causes the intrinsic emission. In contrast, the defect emission can be caused by undesired functional groups at the edges and missing or unhybridized sp^2 carbon atoms in the core of the GQD. Moreover, numerous theoretical studies showed how the properties could degrade or be quenched in the presence of variability and defects [66–69]. On the other hand, it is worth noting that most of the top-down GQDs have been investigated mainly for biological applications because of their large photoluminescence in the visible and the near-infrared, and they are not suitable for quantum applications [70–72]. While top-down GNRs and GNMs have been investigated for their electronic properties and mostly field-effect transistors exhibiting modest I_{on}/I_{off} ratios have been realized so far [41, 53, 58, 73, 74]. Therefore, it is necessary to produce graphene materials with a level of control way beyond the capabilities of top-down methods. For this reason, the bottom-up approach must be considered because it allows to achieve atomically precise graphene materials.

From a bottom-up perspective, since graphene is considered as an infinite array of benzene subunits, between these two extrema, benzene and graphene, there is a plethora of finite structures called polycyclic aromatic hydrocarbons (PAHs). Small PAHs (benzene, naphthalene, pyrene...) occur naturally in coal, petroleum, and as side products of the combustion of organic materials [75]. At the end of the '90s and beginning of the 2000s, the group of K. Müllen at the Max Planck Institute for Polymer Research in Mainz developed the chemical synthesis of large PAHs through cyclotrimerization, cross-coupling, and Diels-Alder reaction [76, 77]. These materials are similar to small pieces of graphene, GQDs or graphene nanoparticles, exhibiting atomically controlled sizes (from C42 (hexa-peri-benzocoronene (HBC)) up to C222[1]), shapes (hexagonal, triangular, rectangular...), edges (zigzag and armchair), and functionalities (alkyl chains, tert-butyl chains, arylamine...) [78–84]. All these parameters define the structure of the GQD and have significant impacts on its properties. For instance, zigzag-edged GQDs exhibit increased chemical reactivity, smaller optical gaps, and open-shell characters than their armchair ones [85, 86]. It is worth noting that since the structures become bigger, the π-stacking effect is more significant, raising the difficulty of their synthesis and characterization. Therefore, the different functional groups were

[1] C222 is the biggest GQD reported to this date, synthesized by Simpson *et al.* [77], it has a hexagonal form containing 222 sp^2 carbon atoms.

designed into the surface of the PAH to try to counteract this problem.

Until today, most optical, electronic studies were based on HBC and its derivatives because of its small size and relatively easy synthesis [78]. For HBC and its derivatives, the use of different functional groups has improved its solubility in various organic solvents and even in aqueous media with surfactants [87, 88]. Haines *et al.* [89] recently showed that the substituent groups significantly affect HBC's optical and electronic properties. For instance, while tert-butyl chains were neutral and had no significant impact on HBC's optical and electronic properties, the symmetry of HBC was broken with the presence of the electron-withdrawing group (-NO_2, -COOH, -COH). The authors observed attenuation of the main band and red-shifted absorption and emission spectra and the appearance of phosphorescence at low temperatures when the electron-withdrawing effect increased. Significantly, the strong electron withdrawing group, NO_2, triggered a redistribution of charge density with a high influence of the solvent and consequently significantly impacted the electronic properties of HBC. The optical and electronic of "bottom-up" larger GQDs were not fancy because of low solubility, aggregation, and impurity. Michael G. Debije *et al.* [90] observed that the experimental absorption spectra become broader as the size of GQDs increases, and their solubility reduces, even in the presence of solubilizing functional groups. Later, Tan *et al.* [91] observed that the absorption bands of chloro-functionalized GQDs from C42 (HBC) up to C222 were shaper and better resolved than those GQDs functionalized with alkyl chains as the chlorinated GQDs displayed less aggregation in solution. Moreover, they also observed a bathochromic shift in the absorption spectra, compared to their hydrogenated GQDs, due to the electron-withdrawing effects of the chlorine atoms. Hans Riesen *et al.* [92] reported on a C132 GQD with side alkyl chains that impurities presented in the sample have a strong interaction with light, which results in fluorescence emission—meanwhile, phosphorescence emission results rather than fluorescence emission of the GQD. Recently, Zhao *et al.* [93] reported that the C96 GQDs functionalized with alkyl chains and chlorinated C96 GQDs can emit a single photon at room temperature with high purity; high brightness (at least as bright as the brightest single-photon source reported in other 2D materials) and a good photostability. This study showed the high potential of C96 GQDs as quantum emitters in comparison with other alternatives, such as defects in 2D materials [94, 95]. However, the aggregation did not ultimately reveal the intrinsic optical properties of C96 GQDs, and there is still much work to do.

Concerning GNRs, "bottom-up" GNRs can be synthesized through liquid-phase or on-surface chemistry. Using the former approach (similar to the synthesis of GQDs), the group of K. Müllen at the Max Planck Institute reported the formation of short nanoribbons of graphene by polymerization of monomers in solution followed by the aromatization of the structures [96–99]. For instance, the obtained cove-type nanoribbon GNRs had lateral and longitudinal extensions $\sim$ 2 nm and over 100 nm, synthesized through Diels-Alder polymerization. In 2010, the groups of Fasel and Müllen reported on the on-surface chem-

istry approach for synthesizing GNRs. It was based on the polymerization of monomers on crystalline metal surfaces via Ullman coupling followed by thermal annealing to aromatize the structures [100]. They deposited a 10-10'-dibromo9,9'-bianthracene and a 6,11-dibromo-1,2,3,4-tetraphenyltriphenylene on an Au(111) and Ag(111) surface to achieve straight N = 7 armchair GNRs and a chevron-type armchair graphene nanoribbon, respectively. The lengths of the obtained GNRs were approximately 20 nm. After this work, several structures have been synthesized over the years, varying in widths, shape, edges, and dopants [99–106]. For instance, Ruffieux *et al.* [106] reported the synthesis of a straight zigzag GNRs on an Au(111) surface, in this report, the lengths of GNRs were also observed to be longer, approximately 50 nm. Notably, on-surface reactions are commonly characterized by scanning probe microscopy techniques such as scanning tunneling microscope (STM) and noncontact atomic force microscopy (nc AFM) with functionalized probes.

Further, similarly to the case of GQDs, all these parameters, widths, shapes, edges, and dopants significantly impact the optical and electronic properties of GNRs. For instance, Yang *et al.* [107] reported that the band gap of GNRs decreased as the width of the GNRs increased. Compared to armchair GNRs, the energy states near the band gap in zigzag GNRs are observed to be sensitive to wavevector, and this gives rise to a larger bandwidth and smaller effective mass for carriers in zigzag GNRs. Recently, numerous studies dealt with the fabrication of two terminal or three terminal field effect transistor devices based on GNRs [108–113]. According to these studies, graphene nanoribbon field-effect transistors (GNR-FETs) showed relatively large current but limited I_{on}/I_{off} ratio. Moreover, several research groups have investigated the optical properties of "on-surface" synthesized GNRs. First, R. Denk *et al.* [114, 115] performed reflectance difference spectroscopy experiments (RDS) on a film of oriented GNR on gold (substrate used for the synthesis of the GNR), and they showed that excitonic effects dominated the optical transitions of armchair and chevron-type GNRs. Investigating the emission properties requires transferring the GNRs onto an insulating substrate. Senkovskiy *et al.* [116] investigated the photophysics of armchair GNR transferred on quartz. They reported that the intrinsic photoluminescence of the GNR was low and that the creation of sp^3 defects could enhance it. Moreover, Schull's group reported another approach to studying the luminescence of GNRs. They employed an STM tip to lift a single armchair GNR from the Au substrate, and they recorded the electroluminescence spectrum [117]. The study of the optical properties of GNRs synthesized in solution is almost exclusively limited to the absorption spectra realized on ensembles, the GNRs exhibited broad absorption bands in the visible spreading in the near-infrared region (NIR) [96, 97]. Finally, Zhao *al.* [118] reported the time-resolved photoluminescence experiments (TR-PL) exhibits non-mono-exponential behavior, and the emission arises from excimer states in small aggregates of GNRs that blur the intrinsic properties of GNR. This work highlights the need for further research to obtain well-individualized GNRs, which are

prerequisites to taking advantage of the great possibilities of those nano-objects.

Concerning GNMs, the formation of ordered 2D covalent molecular networks on surfaces is a field of intense development [119–125]. First, GNMs can be obtained via chemical vapor deposition growth (CVD) as reported in [126, 127]. The obtained GNM has huge pores of an average size of 14 nm and neck width of 24 nm [126]. It offers scalability and the ability to produce graphene films over large areas. However, it is more suitable for industrial applications. Although CVD can produce graphene with defects and controlled doping, achieving precise control over the size, shape, and density of pores to form GNMs remains challenging. As discussed previously, physical vapor deposition (PVD) can offer high precision on the quality of pores and be able to solve these problems. Despite the interest shown, real graphene nanomeshes have yet to be realized. Only a limited number of nanomesh-like structures have been reported [128–137]. For instance, Bieri *et al.* [129] deposited hexaiodo-cyclohexa-m-phenylene (CHP) on an Ag(111) surface, and after annealing at 532ºC, obtained ideally expected two-dimensional polyphenylene networks which exhibit an interpore distance of 7.4 Å and continuous domains of up to 10 x 10 nm. Moreover, Moreno *et al.* [138] reported one of the most impressive examples of GNM synthesis via GNR. In this work, the authors deposited diphenyl–10,10dibromo-9,9-bianthracene (DP-DBBA) on Au(111) and heated the surface to 200ºC coupling the monomers into a GNR. Further annealing at 400 ºC triggered the intramolecular cyclodehydrogenation, and cross-coupling was achieved at 450ºC. Finally, a highly ordered GNM was achieved with continuous domains up to 50 x 70 nm. Using a similar approach, Multu *et al.* [139] obtained GNM with rubicene necks by depositing methylated 6,11-dibromo-1,2,3,4-tetraphenyltriphenylene on an Au(111) surface. In this work, the graphene hexagonal network is broken in the presence of rubicenes, and the GNM exhibits exciting properties. On the other hand, 2D covalent organic frameworks (2D-COFs) containing heteroatoms are also of interest. Steiner *et al.* [133] reported the formation of 2D-COF from carbonyl-bridged triphenylamines (CTPA) substituted with iodine and bromine atoms, a doped nanoporous network was achieved through hierarchical reactivity. It is important to note that, to this day, all these “graphene bottlenecks” are constituted by a single C-C bond between 2 phenyl rings. In such structures, because of the free rotation along the single bond and the steric hindrance between the hydrogen atoms in ortho of the C-C bond, the phenyl rings are not coplanar, significantly reducing the delocalization of electrons and decreasing the conductivity. The optical and electronic properties of these GNM-like materials have not been investigated experimentally.

Although GNMs are more recent than GNRs, more studies have been performed on them recently. One of the reasons is that GNM-based transistors can support currents nearly 100 times greater than individual GNR devices, and the I_{on}/I_{off} ratio is comparable with the values achieved in these devices [140, 141]. Concerning optical and electronic properties, there are very few experimental works [142, 143, 143]. In contrast, several theoretical works were published [43, 144–150]. These reports

showed that all these parameters, bottleneck width, pore size, pore shape, and pore edges have very great impacts to the optical and electronic properties of GNMs. Pedersen *al.* [43] reported a linear scaling of the band gaps, $E_g \propto N_{removed}^{1/2}/N_{total}$, for circular GNM where $N_{removed}$ is the number of carbon atoms removed, N_{total} is the total number of carbon atoms in the unit cell [144, 148, 149]. Later, Liu *et al.* [147] demonstrated that this relation is validated for both armchair- and zigzag-edged GNM; additionally, a spin-splitting gap only opens up in the zigzag-edged triangular GNM with a ferromagnetic ground state, which is not observed in in the zigzag-edged rectangular GNM. Also, the band gap is approximately inversely proportional to bottleneck width, which is in good agreement with the experimental results [143, 143]. Thus, the energy band gap can be adjusted to the desired value by creating holes and managing their distributions. In 2020, Sakkaki *et al.* [145] reported that by increasing the pore diameter of GNMs, its absorption peaks shift from the absorption spectrum of graphene towards the infrared region where the GNMs with small pore diameter has very close absorption spectrum graphene. Moreover, the authors reported a similar way to move absorption peaks to the infrared region by decreasing the GNR's width and approaching the GNR's spectrum from GNM by increasing the pore diameter. Later, in 2021, they showed another possibility to tailor the absorption peaks into the infrared region by changing the structure of the hole edges through passivation of these materials with nitrogen atoms [144]. By the way, the GNM can transform from a semiconductor to a semi-metal or inverse due to the hybridization of p_z orbitals of the nitrogen atom.

*During my thesis, I am participating in two very close projects: **Gra**phene **n**anom**esh** (GANESH) and **Bo**ttom-up synthesis and properties of **gra**phene **r**elated ma**t**erials (BOGART). The project BOGART aims to achieve a breakthrough in synthesizing and exploiting the optical and electronic properties of graphene-related materials: GQDs, GNRs, and GNMs. While the project GANESH has the same aims but specifically "bottom-up" GNMs. These projects have been done in consortium between chemists, theoretical physicists, and experimentalists mainly located in the Paris-Saclay area. These projects aim to progress significantly beyond the state of the art on these materials. First, the GQDs and precursors are synthesized via bottom-up approaches by chemists at Nanosciences et Innovation pour les Matériaux, la Biomédecine et l'Energie (CEA-NIMBE) laboratory. Secondly, the precursors are deposited and polymerized on a metal surface to achieve the expected materials (GNRs or GNMs) via a heating process by experimentalists at Institut des Sciences Moléculaires d'Orsay (ISMO) laboratory and Institut Matériaux Microélectronique Nanosciences de Provence (IM2NP) laboratory. A second alternative strategy is also used by the experimentalists, which is to obtain GNRs and then GNMs through the GNRs by heating at a higher temperature. We aim to obtain GNMs with graphene bottlenecks that exhibit more than a single C-C bond. Collaborators then characterize the optical and electronic properties of these obtained materials (GQDs, GNRs, and GNMs) in situ analyses such as absorption spectroscopy, photo-*

luminescence (PL) spectroscopy, and Scanning Tunneling Microscopy/Spectroscopy (STM/STS). These characterizations are alternatively evaluated by our theoretical group at Service de Physique de l'Etat Condensé (CEA-SPEC) laboratory via ex situ analysis with ab initio and semi-empirical calculations in order to compare to experimental measurements. The objectives of this PhD thesis are first to calculate the optical and electronic properties of these target materials to eliminate the effects due to bad solubility and aggregation in absorption spectra in order to achieve their intrinsic properties. Also, the STM/STS are evaluated to predict the structures obtained on the metallic surface and explain the experimental substrate. The end goal of this thesis is to reveal the change in their properties as a function of system size and system symmetry. In this manuscript, we will first show the theoretical background of used ab initio and semi-empirical methods to characterize the target materials in part . Then, results and applications will be explored in part .

Background

Chapter 1

Spectroscopy methods.

Three methods exist to determine properties of a material: empirical, semi-empirical, and ab initio. The former is based on observation and experience, like spectroscopy methods. The second is a theoretical approach combining elements of pure theoretical modeling and empirical data, such as the Hückel approach, the Tight-Binding (TB) approach,... The latter is an entirely theoretical approach based on first principles, such as density functional theory (DFT) and many-body perturbation theory (MBPT). In this chapter, we will first briefly introduce several empirical spectroscopy methods frequently used to characterize materials in experiments to determine the desired electronic, optical, and transport properties of novel 2D materials. In the second part, we will discuss in detail the theoretical approaches used in this Ph.D. thesis to obtain results that are directly comparable to experimental measures. This thesis mainly focuses on absorption spectroscopy (ABS), scanning tunneling spectroscopy, and microscopy (STS and STM) experiments. Since our studied objects have huge dimensions, standard ab initio methods like DFT or post-DFT can hardly be used. Hence, we need to consider lower approaches, such as the Tight-Binding method and the Tight-Binding ab initio method (TB-DFT), to speed up the calculations and obtain the results. However, we must also use standard ab initio methods to obtain reference results to verify our lower approaches' efficiency. For optical response, since both TB and DFT methods cannot provide a correct band gap, it is necessary to go beyond these methods to get the correct absorption spectra. We will correct the band gap using Green's function formalism (GF) and then get the correct absorption spectrum using the Bethe–Salpeter equation (BSE). For transport response, to better describe the STM images, we need to include the tip-sample interaction in STM simulation, which is taken into account by using Keldysh-Green's function approach based on the Fireball DFT method (Fireball-DFT). All these theoretical methods will be discussed later in detail in this chapter.

1.1 Spectroscopies.

Spectroscopy is one of the most powerful and widely used techniques for obtaining information about solid-state materials' electronic, optical, and transport properties. For the former properties, a spectroscopy experiment comprises a source, a scatterer, and an analyzer, reported in Fig. (1.1a). Hence, the source beams an incoming particle (electron or photon, see Tab. 1.1) impinged on the sample of the scatterer (the solid that we want to study, *i.e.* our N-electron system). This particle plays the role of an external field and comes to perturb the sample's electrons. As a result of this interaction, the system exchanges energy with the perturbing field, leading to various excitations. Subsequently, due to these excitations, the system ejects an outgoing particle (electron or photon as mentioned in Tab. 1.1) that is detected by an analyzer. This outgoing field carries much vital information about the nature of the sample, such as the quantities exchanged during the interaction, energy levels, bandgaps, electronic structures, etc.

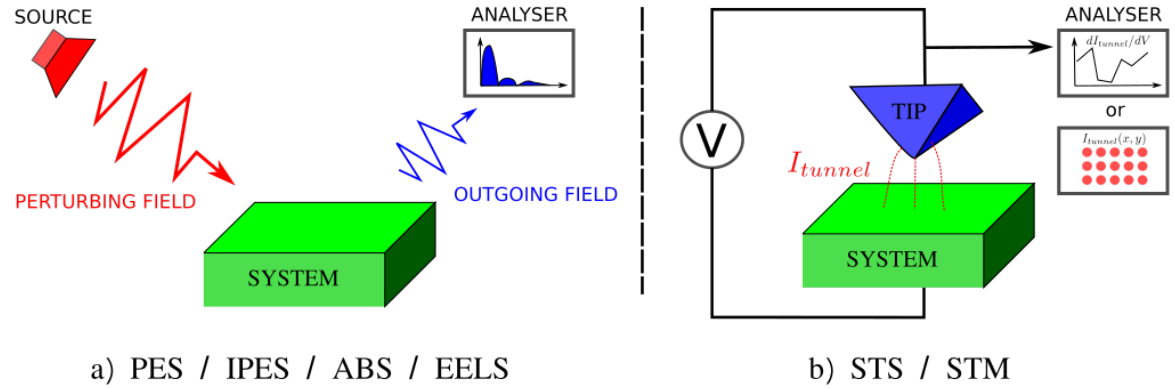

Figure 1.1 – Schema of spectroscopies. a, For PES/IPES/ABS/EELS experiment. **b,** For STS/STM experiment.

According to the charge state of the sample, we can classify the different kinds of spectroscopies into two categories of excitations: charged and neutral excitations. Under the influence of an external field, the system transits from the fundamental state to the excited state; when the number of electrons in the system is conserved, these excitations are called neutral excitations. Otherwise, these are charged excitations. The Tab. 1.1 illustrates the features of the five most common spectroscopy techniques such as direct and inverse photoemission spectroscopy (PES and IPES), scanning tunneling spectroscopy (STS), absorption spectroscopy (ABS), and electron energy loss spectroscopy (EELS) according to their excitation nature.

In a direct photoemission PES experiment, the scatterer absorbs one photon to emit an electron; this electron is called **photoelectron**. This photoelectron propagates into the solid, interacts with the

Spectroscopy techniques	In	Out	No. é of sample	Types of Excitations
Direct photoemission (PES)	photon	electron	N $\rightarrow$ N-1	Charged
Inverse photoemission (IPES)	electron	photon	N $\rightarrow$ N+1	Charged
Scanning tunneling (STS)	electron/hole	$\varnothing$	N $\rightarrow$ N+1/N-1	Charged
Absorption (ABS)	photon	photon	N $\rightarrow$ N	Neutral
Electron energy loss (EELS)	electron	electron	N $\rightarrow$ N	Neutral

Table 1.1 – Categorization of various spectroscopic techniques based on the probing particle (incoming beam or 'In') and the detected particle resulting from the interaction with the target (outgoing beam or 'Out'). In addition, the third column shows the changing number of electrons within the sample. Finally, the last column indicates the types of excitations for each spectroscopy experiment. The spectroscopies we mainly used on my thesis are reported in gray.

system during its travel, and finally, leaves the vacuum. The missing electron creates a hole in the system, leaving consequently the system in an excited state. In this way, the spectroscopic experiment can capture all the occupied states, including core levels. Nevertheless, to measure an empty state, it is necessary to reverse the photoemission experiment using inverse photoemission (IPES). Besides, a combination of an additional electron or hole in the system that interacts with its surrounding polarization cloud due to the absence of other system's electrons around this additional one is called **quasi-particle**. In this case, the incoming particle is an electron absorbed by the sample, emitting a photon detected by the analyzer. Alternatively, another technique that can capture both occupied and unoccupied states can be used in the same experimental set-up as PES, called two-photon photoemission spectroscopy (2PPES) [151]. These methods are specifically designed to measure the density of states, electronic band structures, band gaps, or constant-energy maps... In Fig. (1.2), we report ARPES experimental results on graphene on SiC(0001) obtained by Bostwick *et al.* [152] as valence band structure and constant-energy maps.

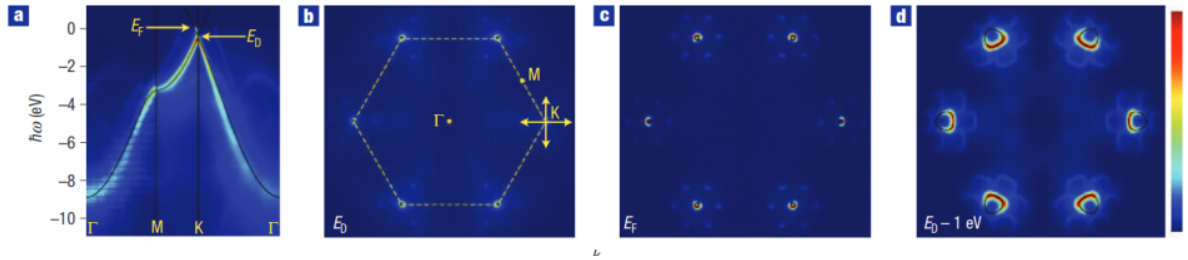

Figure 1.2 – ARPES experimental results of Graphene on SiC(0001) [152]: **a,** The band structure of graphene $\epsilon_{n\mathbf{k}_{||}}$. **b-d,** Constant-energy maps at $E_D = 0$ eV, $E_D + 0.45$ eV, and $E_D - 1$ eV where E_D is binding energy.

In an absorption spectroscopy (ABS) experiment, the light source beams photons to the sample, which the sample absorbs. Their energy excites an electron from the valence to the conduction band, revealing the energetic map of the system. In this experiment, the number of electrons in the sample is conserved, as we create a hole in an occupied state and an electron in an unoccupied state simul-

taneously, which creates an electron-hole pair in the system, called **exciton**. On the other hand, the analyzer detects transmitted or reflected light after interacting with the sample. We stress that the process in which incident radiation interacts with the system's electrons with energy transfer is called an inelastic scattering process. Instead of a photon beam, an electron energy loss spectroscopy (EELS) experiment uses an incident electron beam. In this case, an electron undergoes an inelastic scattering with the sample to induce excitations such as **plasmon** excitations. The spectroscopic result here is the energy loss and the electron direction change.

Unlike all these previous spectroscopy methods that involve the emission or detection of particles, scanning tunneling spectroscopy (STS) shares the same experimental set-up and common principles as scanning tunneling microscopy (STM) as depicted in Fig. (1.1b). It uses a metallic tip brought very close to the sample's surface, creating a small tunneling gap between the tip and the sample. When a bias voltage is applied between the tip and the sample, electrons can tunnel through this gap from the tip to the unoccupied states of the sample or vice versa, depending on the bias voltage. In other words, the incident source is the metallic tip; these electrons probing stay in the sample and will relax back to their ground states. Therefore, no particles were emitted from the sample. The tunneling current measured at different applied voltages provides information about the local electronic density of states (LDOS) and the material's electronic properties at the atomic scale.

At the theoretical level, the TB and DFT methods discussed in Sections 1.3 and 1.4 are insufficient to model those spectroscopies. However, these methods are considered a good starting point for reaching the final results using additional formalisms. For instance, Green's function formalism (GF) discussed in Section 1.4.7 enables the simulation of PES's and IPES's experiences. In contrast, the BSE approach discussed in Section 1.4.8 enables the simulation of ABS's and EELS's. Also, non-equilibrium Green's function formalism (NEGF) discussed in Section 1.4.9 allows the simulation of STS's and STM's experiences. This Ph.D thesis will mainly focus on the simulation of ABS, STS, and STM experiments.

1.2 The many-body problem.

Predicting the physical properties of solids is equivalent to solving the Schrödinger equation $\hat{\mathbf{H}}\mathbf{\Psi} = \mathbf{E}\mathbf{\Psi}$ where the Hamiltonian of a non-spin-polarized and non-relativistic N-electron system is written as below:

$$\hat{\mathbf{H}}(\mathbf{r},\mathbf{R}) = \sum_i -\frac{\hbar\boldsymbol{\nabla}_i^2}{2m_e} + \sum_I -\frac{\hbar\boldsymbol{\nabla}_I^2}{2M_I} + \frac{1}{2}\sum_{i\neq j}\frac{e^2}{|\mathbf{r}_i-\mathbf{r}_j|} + \sum_{i,I}\frac{-Z_I e^2}{|\mathbf{r}_i-\mathbf{R}_I|} + \frac{1}{2}\sum_{I\neq J}\frac{Z_I Z_J e^2}{|\mathbf{R}_I-\mathbf{R}_J|} \tag{1.1}$$

that describes the energetic state of any solid system constituted by atomic nuclei or ion (represented by coordinates R_I with corresponding mass M_I and atomic number Z_I in capital letters) and electrons

(represented by coordinates r_i with mass m_i in lower-case letters). In this expression, these two first terms illustrate the kinetic energy of electrons and ions, respectively, whereas the other terms stand for electron-electron, electron-ion, and ion-ion Coulomb interactions, respectively.

Therefore, we "only" need to diagonalize the Hamiltonian (1.1) to solve this problem in order to obtain energies (*i.e.* eigenvalues) $\mathbf{E}$ and wave-functions (*i.e.* eigenvectors) Ψ. However, this diagonalization has become very complicated rapidly, and in particular, it is impossible to achieve directly for solids, even with our present-day computers. Indeed, the number of particles is 6.022x10^{23}, and even the problem of two interacting particles in an arbitrary external potential can not be solved analytically. Consequently, we understand that there is no way to directly solve equation (1.1), so it is necessary to simplify the problem by making approximations at different levels. We will detail the main approximations in the following sections.

Since now, in this manuscript, we will use common simplifications, such as $\hbar = e = m_e = 4\pi/\epsilon_0 = 1$. In other words, atomic units will be used. Thus, energies are expressed in Hartree, masses in electron mass, lengths in Bohr radius, etc.

1.2.1 The Born-Oppenheimer approximation.

The first important approximation is called the Born-Oppenheimer (or adiabatic) approximation, which is based on the observation that the nuclear mass is much more important than that of electrons. Moreover, the electrons move too fast with respect to the slow motion of the ions. So, we can focus only on the electron dynamics. The ions can be considered fixed during the evolution of electronic degrees of freedom. As a first consequence, we can neglect the ion's kinetic energy and ion-ion Coulomb interactions. In addition, Coulomb interactions between electrons and ions are now considered as the external potential operator $\hat{\mathbf{V}}_{ext}(\mathbf{r})$. Hence, the Eq. (1.1) becomes:

$$\hat{\mathbf{H}}(\mathbf{r},\mathbf{R}) = \hat{\mathbf{T}}_e + \hat{\mathbf{W}}_{ee} + \hat{\mathbf{V}}_{ext} = \sum_i -\frac{\boldsymbol{\nabla}_i^2}{2} + \frac{1}{2}\sum_{i\neq j}\frac{1}{|\mathbf{r_i}-\mathbf{r_j}|} + \sum_{i,I}\frac{-Z_I}{|\mathbf{r}_i-\mathbf{R}_I|} \tag{1.2}$$

Again, $\hat{\mathbf{T}}_e$ is the electrons kinetic energy, $\hat{\mathbf{W}}_{ee}$ is the electron-electron interaction operator, and $\hat{\mathbf{V}}_{ext}$ is the interaction with an external field represented by the nuclear potential. We can rewrite $\hat{\mathbf{V}}_{ext}$ as a sum of single-electron potential $v_{ext}(\mathbf{r}_i) = \sum_I \frac{-Z_I}{|\mathbf{r}_i-\mathbf{R}_I|}$ over the number of electron of the system: $\hat{\mathbf{V}}_{ext} = \sum_i^N v_{ext}(\mathbf{r}_i)$. Similarly, we can have $\hat{W}_{ee} = \frac{1}{2}\sum_{i\neq j} v(\mathbf{r}_i,\mathbf{r}_j)$ where $v(\mathbf{r}_i,\mathbf{r}_j)$ is the Coulomb potential. Compared to the Eq. (1.1), the Hamiltonian is much simpler, and the issue is reduced to solve the time-independent Schrödinger equation of N-interacting electron system in Dirac notation:

$$\hat{\mathbf{H}}\,|\Psi\rangle = E\,|\Psi\rangle \tag{1.3}$$

where $|\Psi\rangle = |\Psi(\mathbf{x}_1, \mathbf{x}_2, ..., \mathbf{x}_N)\rangle$ is a N-interacting-electrons wave function depending on space-spin coordinates $\mathbf{x}_i = (\mathbf{r_i}, \sigma_\mathbf{i})$ with the space coordinate $\mathbf{r}_i \in \mathbb{R}^3$ and the spin one $\sigma_i \in \{\uparrow, \downarrow\}$. The wave function is asymmetric once we exchange the two coordinates according to the Pauli principle. It is a superposition of many single Stater determinants[1], noted $\Psi \in \mathcal{W}$[2]. Moreover, E is the eigenvalue corresponding to the eigenvector $|\Psi\rangle$. Nevertheless, a system containing more than three electrons is analytically insolvable even in a non-interacting picture. Thus, further approximations need to be done.

Since spin-polarization effects are neglected, the electron spins are considered equally distributed between spin-up and spin-down states. Consequently, spin variables will not be explicitly considered in the following sections of this thesis.

1.3 *Semi-empirical* Tight-Binding Method.

Semi-empirical methods are the simplest theoretical methods to solve the Eq. (1.3). They aim to balance accuracy and computational efficiency by incorporating empirical parameters into a theoretical framework. This section will present the main principles of the most usual semi-empirical method, the Tight-Binding method (TB). Characterization schemes based on the TB method, like total, projected density of states, velocity, and microscopic dielectric function, will also be discussed in this section.

1.3.1 Description of the *semi-empirical* Tight-Binding Method.

As proposed by Bloch in 1920, the Tight-Binding (TB) method represents the electronic states of a crystal by expressing them as a linear combination of atomic orbitals (LCAO) from the constituent atoms. First, in crystal, we need to introduce the Bloch functions[3] [153]:

$$\left|\tilde{\phi}^a_{j\mathbf{k}}(\mathbf{r})\right\rangle = \frac{1}{\sqrt{N_{cell}}} \sum_m e^{i\mathbf{k}.\mathbf{R}_m} \left|\phi^a_{jm}\right\rangle \tag{1.4}$$

where $\mathbf{R}_m$ is the coordinate of the m-th unit cell, N_{cell} is the number of unit cells in the crystal, and ϕ^a_{jm} is the localized orbital j of atom a centered at r_a of the cell $\mathbf{R}_m$, i.e $\left\langle r\middle|\phi^a_{jm}\right\rangle = \phi_j(\mathbf{r} - \mathbf{R}_m - \mathbf{r}_a)$. Then,

[1] A single Slater determinant wave function is built from a set of N orthogonal occupied spin-orbital $\{\psi_i(\mathbf{x})\}_{i=1...N}$ with $\psi_i(\mathbf{x}) = \varphi_i(\mathbf{r})\chi_{\sigma_i}(\sigma)$ where $\varphi_i(\mathbf{r})$ is a spatial orbital, and $\chi_{\sigma_i}(\sigma)$ is the spin function (σ_i is the spin-orbital i, and σ is the spin of the electron of coordinate $\mathbf{x}$). In non-relativistic cases, without an external magnetic field, spin can be either up or down, so $\chi_{\sigma_i}(\sigma) = \delta_{\sigma_i,\sigma}$. Now, the spin function ensures that the determinant state is equal to zero if two electrons with the same spin cannot be in the same spatial position.

[2] In general, each single electron Hilbert space is $L^2(\mathbb{R}^3 \times \{\uparrow, \downarrow\}, \mathbb{C})$, means $||\Psi||_\infty < \infty$ with $\mathbf{r}_i \in \mathbb{R}^3$ and $\sigma_i \in \{\uparrow, \downarrow\}$. Therefore, the N-interacting electron wave function is an antisymmetric product of the N single electron wave function; the N electron Hilbert space is then: $\mathcal{H} = \wedge^N L^2(\mathbb{R}^3 \times \{\uparrow, \downarrow\}, \mathbb{C})$.

[3] The presence of the term $\exp\{i\mathbf{k}.\mathbf{R}_m\}$ permits the transfer of the basis from the direct space to reciprocal space.

the single-electron wave-functions $|\varphi_{n\mathbf{k}}\rangle$[4] can be expressed as the LCAO of Bloch functions $\left|\tilde{\phi}^{a}_{j\mathbf{k}}(\mathbf{r})\right\rangle$ as:

$$|\varphi_{n\mathbf{k}}\rangle = \sum_{a}^{N_{atom}} \sum_{j} c^{a}_{nj}(\mathbf{k}) \left|\tilde{\phi}^{a}_{j\mathbf{k}}(\mathbf{r})\right\rangle \tag{1.5}$$

where $\varphi_{n\mathbf{k}}$ stands for n-th wave-function at the point $\mathbf{k}$, and N_{atom} is the number of atoms inside the primitive cell. According to the Hamiltonian, the Tight-Binding approach completely disregards electron-electron interactions $\hat{W}_{ee}$, so the total Hamiltonian can be divided into numerous single-independent-electron Hamiltonian to be solved as [154]:

$$h_{TB}(\mathbf{r}) = -\frac{\boldsymbol{\nabla}^2}{2} + v_{ext}(\mathbf{r}) \tag{1.6}$$

Now, the single-electron Schrödinger equation to be solved under matrix form is:

$$\mathbb{h}_{TB}.\mathbf{c}_n = \mathbb{E}^{TB}_{n}.\mathbb{S}.\mathbf{c}_n \tag{1.7}$$

where $\mathbf{c}_n$ is a column vector containing the coefficients c^{a}_{nj} of n-th eigenstate. The Hamiltonian and overlap matrices, $\mathbb{h}_{TB}$ and $\mathbb{S}$, are constituted by the following integrals (in reciprocal space)[5] [154, 155]:

$$h^{aj,bl}_{TB}(\mathbf{k}) = \sum_{m} e^{i\mathbf{k}.\mathbf{R}_m} \int \phi^{*}_{j}(\mathbf{r}-\mathbf{r}_a) h_{TB}(\mathbf{r}) \phi_l(\mathbf{r}-\mathbf{R}_m-\mathbf{r}_b) d^3\mathbf{r} \tag{1.8}$$

$$S^{aj,bl}(\mathbf{k}) = \sum_{m} e^{i\mathbf{k}.\mathbf{R}_m} \int \phi^{*}_{j}(\mathbf{r}-\mathbf{r}_a) \phi_l(\mathbf{r}-\mathbf{R}_m-\mathbf{r}_b) d^3\mathbf{r} \tag{1.9}$$

Furthermore, the *semi-empirical* evaluations are usually applied by considering only each single-electron crystal potential $v_{ext}(\mathbf{r})$[6] as a sum of spherically symmetric atomic-like potentials $v_{am}(\mathbf{r}-\mathbf{R}_m-\mathbf{r}_a)$ centered at $\mathbf{r}_a$ of the cell $\mathbf{R}_m$ [153]. The overlap matrix elements (1.9) involve only one center if the two orbitals are on the same site and two centers otherwise. According to the Hamiltonian matrix elements (1.8), the kinetic part always involves one or two centers. In contrast, the potential terms may involve one-, two-, and three-center integrals, depending on the positions of the other atoms.

Moreover, because of the localized nature of the atomic orbitals, we can limit the Hamiltonian matrix elements (1.8) to a small number of neighbors, for instance, first or second neighbor contributions. In 1954, J. C. Slater and G. F. Koster [156] suggested employing only two-center integrals, considered adjustable constants determined from experimental results. More recently, these constants can be ob-

[4] In the case of the molecule, since $\mathbf{k} = 0$, thus the phase is turned to 0.
[5] Since h_{TB} is translational invariance, therefore we can choose $\mathbf{R}_{m'} = 0$ [153].
[6] This means that we disregard the other symmetric atomic potentials of v_{ext}.

tained by more efficient methods, such as *ab initio*. These constants are:

$$h_{TB}^{aj,aj} = \xi_{aj} \qquad \text{and} \qquad h_{TB}^{bl,aj} = t_{bl,aj} \tag{1.10}$$

where ξ_{aj} are the diagonal terms corresponding to the energy within the orbital j of atom a. ξ_{aj} depending on the environment, for instance, the nature and position of surrounding atoms. The off-diagonal terms $t_{bl,aj}$ are the hopping energies from the atomic orbitals l of an atom b to the atomic orbitals j of the neighboring atom a. The hopping energy depends on the angular momentum of the orbitals $|\phi_{ajm}\rangle$ and $|\phi_{blm'}\rangle$ via the simple trigonometric relations called Slater-Koster formulas. In the case of atomic orbitals only of type s and p like for graphene or hexagonal Boron Nitride (hBN), four different integrals $V(ss\sigma)$, $V(sp\sigma)$, $V(pp\sigma)$, and $V(pp\pi)$ are involved (see Fig. (1.3)), and $t_{bl,aj}$ have five different values as shown Tab. 1.2 below:

Two-center integrals	$t_{bl,aj}$
$\int \phi_s^*(\mathbf{r}-\mathbf{r}_a)v_{bm}(\mathbf{r}-\mathbf{R}_m-\mathbf{r}_b)\phi_s(\mathbf{r}-\mathbf{R}_m-\mathbf{r}_b)$	$V(ss\sigma)$
$\int \phi_s^*(\mathbf{r}-\mathbf{r}_a)v_{bm}(\mathbf{r}-\mathbf{R}_m-\mathbf{r}_b)\phi_{p_x}(\mathbf{r}-\mathbf{R}_m-\mathbf{r}_b)$	$l_x V(sp\sigma)$
$\int \phi_{p_x}^*(\mathbf{r}-\mathbf{r}_a)v_{bm}(\mathbf{r}-\mathbf{R}_m-\mathbf{r}_b)\phi_{p_x}(\mathbf{r}-\mathbf{R}_m-\mathbf{r}_b)$	$l_x^2 V(pp\sigma)+(1-l_x^2)V(pp\pi)$
$\int \phi_{p_x}^*(\mathbf{r}-\mathbf{r}_a)v_{bm}(\mathbf{r}-\mathbf{R}_m-\mathbf{r}_b)\phi_{p_y}(\mathbf{r}-\mathbf{R}_m-\mathbf{r}_b)$	$l_x l_y[V(pp\sigma)-V(pp\pi)]$
$\int \phi_{p_x}^*(\mathbf{r}-\mathbf{r}_a)v_{bm}(\mathbf{r}-\mathbf{R}_m-\mathbf{r}_b)\phi_{p_z}(\mathbf{r}-\mathbf{R}_m-\mathbf{r}_b))$	$l_x l_z[V(pp\sigma)-V(pp\pi)]$

Table 1.2 – Representation of two-center integrals involving atomic orbitals of the type s, p_x, p_y, p_z [153, 156]. The director cosines of the two-center distance vector $\mathbf{D}_{ab} = \mathbf{R}_m + \mathbf{r}_b - \mathbf{r}_a$ are defined as $\mathbf{D}_{ab} = (l_x, l_y, l_z)|\mathbf{D}_{ab}|$, where $l_x = X_{ab}/D_{ab}$, $l_y = Y_{ab}/D_{ab}$, and $l_z = Z_{ab}/D_{ab}$ with $D_{ab} = |\mathbf{D}_{ab}|$.

Moreover, the atomic orbitals are usually considered to be orthogonal. Thus, the overlap matrix becomes the identity matrix: $S^{aj,bl} = \delta_{ab}\delta_{jl}$. Finally, most of the semi empirical Tight-Binding models usually depend on only these two parameters: ξ_{aj} and $t_{bl,aj}$.

Whenever necessary, the spin-orbit interaction can be included in the Hamiltonian matrix in the tight-binding model with manageable on-site spin-orbit terms of the constituting atoms. It can also embody effects beyond the independent electron picture, such as using the Hubbard model of one-site correlation effects [153]. The Tight-Binding method not only allows the description of the electronic properties of various periodic systems, but one of its most significant advantages is the possibility of describing those properties of non-periodic, incommensurate, or disordered systems. Furthermore, because of its low computational cost, this method can also be employed in Density Functional Theory (DFT) to solve self-consistently the Schrödinger equation, which will be discussed later in 1.4.5.

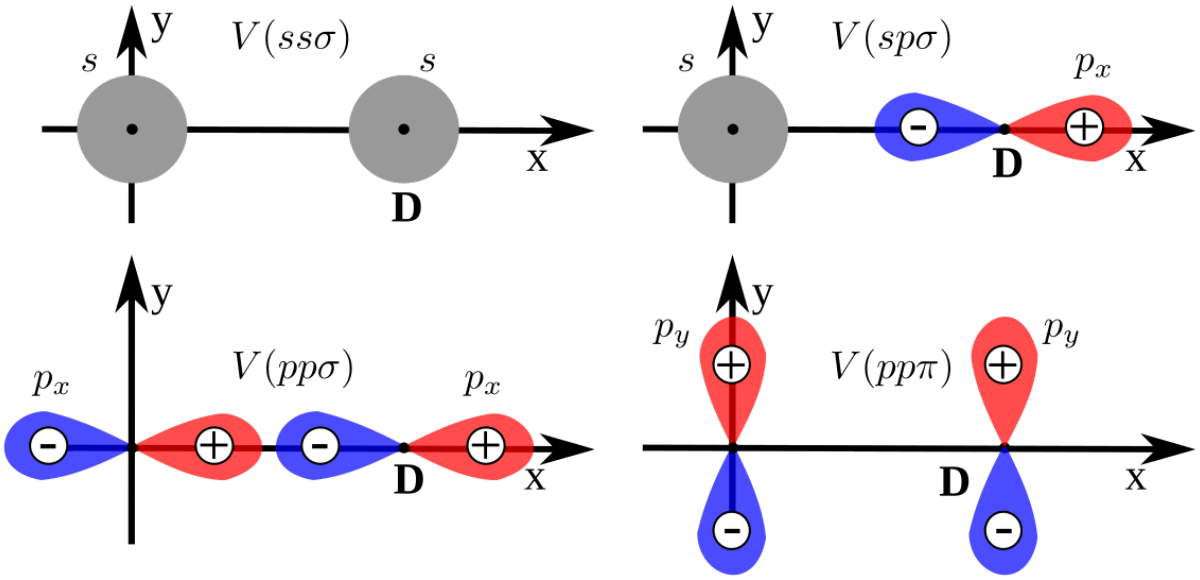

Figure 1.3 – Schema depicting the independent two-center integrals concerning s and p orbitals mentioned in Tab. 1.2. One center is taken at the origin and the other center $\mathbf{D}$ is set in the x-axis. While $\sigma(m=0), \pi(m=\pm 1)$ denote that the angular part with respect to the axis of quantization (along the two centers) is characterized by $\exp\{im\theta\}$.

Since now, in order to simplify, we have assumed that the Tight-Binding method is a shorthand for the *semi-empirical* Tight-Binding method; thus, if later we mention Tight-Binding method, that means the *semi-empirical* Tight-Binding method.

The Tight-Binding model for graphene and hexagonal Boron Nitride (hBN).

In graphene, Carbon atoms are periodically arranged in an infinite two-dimensional honeycomb lattice. The hexagonal Boron Nitride (hBN), sometimes nicknamed $white$ graphene, is almost isomorphic to graphene, the two atoms of the primitive cell being replaced by one atom of boron and one of nitrogen. Graphene presents many symmetry operations, including one rotation of order 6, two of order 3, and three of order 2, adding three planes of mirror and six sliding symmetries. It belongs to the 2D group of symmetry $p6m$. Since hBN has a less rich planar symmetry group than graphene, it belongs to the wallpaper group $p3m1$.

These hexagonal networks can be seen as a triangular Bravais lattice with two atoms per unit cell, A and B (in graphene, A and B are all Carbon atoms, whereas, in hBN, A (B, respectively) stands for Boron atom (Nitrogen atom, respectively)), and lattice vectors $(\mathbf{a}_1, \mathbf{a}_2)$ as shown in Fig. (1.4a):

$$\mathbf{a}_1 = a\left(\frac{\sqrt{3}}{2}, \frac{1}{2}\right), \qquad \mathbf{a}_2 = a\left(\frac{\sqrt{3}}{2}, -\frac{1}{2}\right) \tag{1.11}$$

Here, we just introduced $a = \sqrt{3}a_{AB}$, where a_{AB} is the inter-atomic distance, so that $a_{AB} = a_{CC} = 1.42$

Å in graphene, $a_{AB} = a_{BN} = 1.45$ Å in hBN. Then, the reciprocal lattice vectors $(\mathbf{b}_1, \mathbf{b}_2)$ can be obtained by using the relation $\mathbf{a}_i.\mathbf{b}_j = \delta_{ij}$:

$$\mathbf{b}_1 = b\left(\frac{1}{2}, \frac{\sqrt{3}}{2}\right), \qquad \mathbf{b}_2 = b\left(\frac{1}{2}, -\frac{\sqrt{3}}{2}\right) \tag{1.12}$$

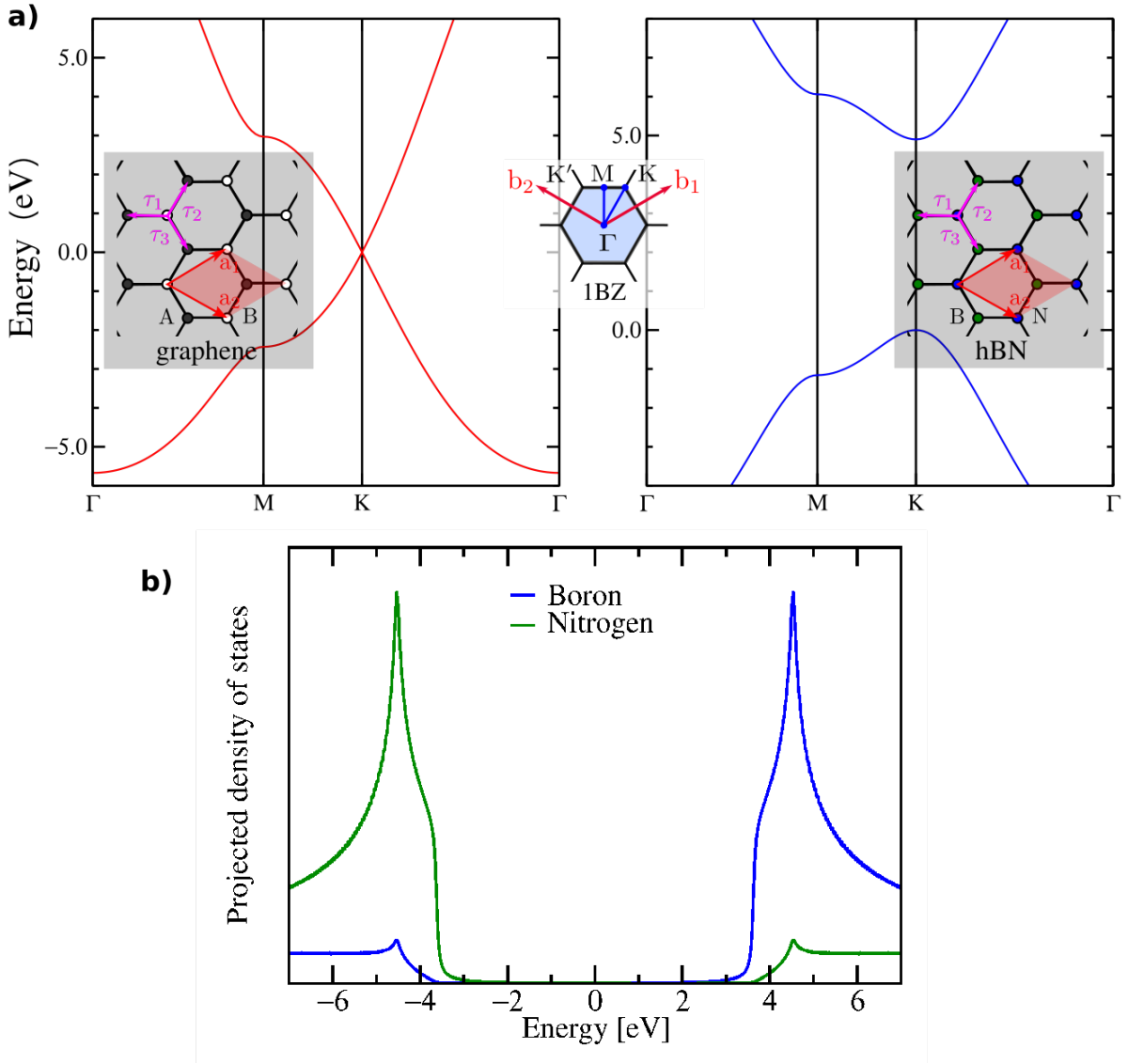

Figure 1.4 – π and π^* electronic bands of the hexagonal networks of graphene and hBN obtained by Tight-Binding method. a, Electronic band-structures of graphene (left part) and hBN (right part) obtained by using the set of parameters in Tab. 1.3. Their hexagonal networks are shown in light-gray rectangle, in which we define the vectors τ_i joining first neighbors between the two sublattices, and the lattice vector $\mathbf{a}_i$, with $i \in [1, 2, 3]$. In red, we present an unit cell $\mathbf{R}_m = m_1\mathbf{a}_1 + m_3\mathbf{a}_2 + m_3\mathbf{a}_3$ where $\mathbf{a}_3 = 30$Å$.\mathbf{e}_z$. In center part, their first Brillouin zone (1BZ) are shown. The top valence band has been aligned to 0 eV. **b,** Projected density of states on Boron atom (in green) and Nitrogen (in blue) calculated by T. Galvani *et al.* [157].

where $b = 4\pi/(a\sqrt{3})$. These vectors are depicted in the middle part of Fig. (1.4a) with the first

Brillouin zone (blue turquoise). Two of the 1BZ's six corners are inequivalent, denoted with $\mathbf{K}$ and $\mathbf{K}'$. Another high symmetry point is at the mid $\mathbf{K}\mathbf{K}'$ path, denoted $\mathbf{M}$. They can be chosen as:

$$\mathbf{K}' = \frac{4\pi}{3a}\left(\frac{\sqrt{3}}{2}, -\frac{1}{2}\right), \qquad \mathbf{K} = \frac{4\pi}{3a}\left(\frac{\sqrt{3}}{2}, \frac{1}{2}\right), \qquad \mathbf{M} = \frac{2\pi}{\sqrt{3}a}(1, 0) \tag{1.13}$$

Graphene and hBN present $sp^2 + p_z$ hybridization. As such, the valence $2s, 2p_x, 2p_y$, orbitals combine to form the xy inplane σ (bonding or occupied) and σ^* (antibonding or unoccupied) orbitals. The $2p_z$ orbitals causing the $V_{pp\pi}$ interaction combine to form localized π (bonding) and π^* (antibonding) orbitals, which are perpendicular to the m_z planar symmetry and decoupled from the σ states [1]. Therefore, the $2p_z$ electrons can be treated separately from the other valence electrons. Moreover, the bonding and antibonding σ states are very far from the Fermi level. For instance, their separation in graphene is greater than 12 eV at Γ [153]. Therefore, their contribution to electronic properties is commonly disregarded. Oppositely, the bonding and antibonding π orbitals produce valence and conduction bands at vertices of the hexagonal Brillouin zone, as shown in Fig. (1.4a). Proposed by Wallace [1] in 1947, until now, the two-band model on graphene has been very exploited in the Tight-Binding method by taking into account only $2p_z$ orbitals. In this approach, the A atom (or B atom) has uniquely one orbital per atom site $p_z(\mathbf{r} - \mathbf{r}_A)$ (or $p_z(\mathbf{r} - \mathbf{r}_B)$). Applying into the Eq. (1.5), the wave-function $|\varphi_{n\mathbf{k}}\rangle$ become:

$$|\varphi_{n\mathbf{k}}(\mathbf{r})\rangle = c^A_{np_z}(\mathbf{k})\left|\tilde{p_z}_{\mathbf{k}}{}^A(\mathbf{r})\right\rangle + c^B_{np_z}(\mathbf{k})\left|\tilde{p_z}_{\mathbf{k}}{}^B(\mathbf{r})\right\rangle \tag{1.14}$$

where $\tilde{p_z}_{\mathbf{k}}{}^{A/B}(\mathbf{r}) = \frac{1}{\sqrt{N_{cell}}}\sum_m e^{i\mathbf{k}.\mathbf{R}_m} p_z(\mathbf{r} - \mathbf{R}_m - \mathbf{r}_{A/B})$. Then, if we neglect the overlap S^{Ap_z,Bp_z} (the Eq. (1.9)) between neighboring p_z orbitals, the Hamiltonian becomes a 2 x 2 matrix as below:

$$\mathbb{h}_{TB} = \begin{bmatrix} \xi^{(1)}_{AA} + \xi^{(2)}_{AA} g_2(\mathbf{k}) & t_{BA} g_1(\mathbf{k}) \\ t_{AB} g_1^*(\mathbf{k}) & \xi^{(1)}_{BB} + \xi^{(2)}_{BB} g_2(\mathbf{k}), \end{bmatrix} \tag{1.15}$$

with

$$\begin{aligned} g_1(\mathbf{k}) &= 1 + e^{-i\mathbf{k}.\mathbf{a}_1} + e^{-i\mathbf{k}.\mathbf{a}_2} \\ g_2(\mathbf{k}) &= \sum_{i=1}^{6} e^{i\mathbf{k}\mu_i} = |g_1(\mathbf{k})|^2 - 3 \end{aligned} \tag{1.16}$$

where τ_i are the in-plane first-nearest-neighbor A to B (or B to A) vectors τ_i[7], and $\mu_i = \tau_i - \tau_j$ $(i \neq j)$ are the in-plane second-nearest-neighbors A to A (or B to B) vectors. $\xi^{(1)}$ is the on-site energy within the atoms (A or B) in the same site, $\xi^{(1)}$ is usually set to 0 for graphene [153]. t is the hopping

[7] We have chosen $\tau_1 = -a_{AB}\mathbf{e}_x$, $\tau_2 = \tau_1 + \mathbf{a}_1$, and $\tau_3 = \tau_1 + \mathbf{a}_2$.

energy between the first nearest neighbors within the atoms A and B in the same site, and since $\mathbb{h}_{TB}$ is Hermitian, thus $t_{AB} = t_{BA}$. $\xi^{(2)}$ is the hopping energy between the second nearest neighbors within the atoms (A or B) in the different sites. We note that t and $\xi^{(2)}$ are kind of $V_{pp\pi}$ integral. In graphene, $t = -2.70$ eV, and $\xi^{(2)} = 0.10t$ usually provide the good fit with *ab initio* results, according to H. Castro Neto *et al.* [158]. All the set of parameters used in this part for graphene and hBN is presented in Tab. 1.3.

	Hamiltonian set of parameters				Eigenvalues
	On-site energies (eV)		Hopping energies (eV)		
	$\xi^{(1)}_{AA}$	$\xi^{(1)}_{BB}$	t_{AB} (1st NN)	$\xi^{(2)}_{AA/BB}$ (2nd NN)	$E_{\pm}(\mathbf{k})$
graphene (**p6m**)	0.00	0.00	-2.70	0.27	$\xi^{(2)}_{AA} g_2(\mathbf{k}) \pm \lvert t_{BA} g_1(\mathbf{k}) \rvert$
hBN (**p3m1**)	4.90	0.00	-2.65	0.00	$\frac{1}{2}\xi^{(1)}_{AA} \pm \frac{1}{2}\sqrt{(\xi^{(1)}_{AA})^2 + 4(t_{BA} g_1(\mathbf{k}))^2}$

Table 1.3 – Set of parameters used for Fig. (1.4a), and the band energies obtained by diagonalization, for graphene and hBN. Note that, in both cases, we set $\xi^{(2)}_{AA} = \xi^{(2)}_{BB}$. In hBN, A corresponds to the Boron atom, whereas A corresponds to a Nitrogen atom.

Figure (1.4a) illustrates the electronic band-structures of graphene (left part) and hBN (right part) obtained using a set of parameters shown in Tab. 1.3. In the left part, we recover the Dirac cone at $\mathbf{K}$ and $\mathbf{K}'$. The presence of $\xi^{(2)}$ shifts in energy the position of the Dirac point and leads to the symmetry breaking of electron-hole bands [158]. In the right part, we obtain the direct gap of 4.89 eV at $\mathbf{K}$ and $\mathbf{K}'$; the gap is observed to be very close to DFT result, nevertheless much smaller than GW one (7.25 eV, approximately) [157]. Furthermore, Figure (1.4b) illustrates the projected density of states (PDOS) on Boron and Nitrogen atoms obtained by T. Galvalni *et al.* [157]. This figure proves that Nitrogen atoms participate in the valence band while Boron atoms participate in the conduction band. This latter is significant to understanding the electronic properties of twisted bilayer hBN presented later in chapter 2.

1.3.2 Total density of states (TDOS), Projected density of states (PDOS), and Local density of states (LDOS).

In this part, we will define important quantities used in this thesis. Firstly, the total density of states (TDOS) can be defined as:

$$\text{TDOS}(\omega) = \rho(\omega) = \sum_{n,\mathbf{k}} \langle \varphi_{n\mathbf{k}} | \varphi_{n\mathbf{k}} \rangle \, \delta(\omega - \epsilon_{n\mathbf{k}}) = \sum_{n,k} \delta(\omega - \epsilon_{n\mathbf{k}}) \tag{1.17}$$

The TDOS refers to the density of available electronic states per unit energy interval in a material. In this non-interacting particle picture, the TDOS can be considered as the lowest approximation of the photocurrents of PES and IPES. This approach reproduces the experimental spectra for atomic and molecular gases very well, where the interactions between those are feeble. The TDOS can also be obtained by the retarded Green's function (see later in 1.4.9).

By using the closure relation of orbital basis $\{\left|\tilde{\phi}^a_{j\mathbf{k}}\right\rangle\}$[8], the Eq. (1.17) can be rewritten as $\rho(\omega) = \sum_{a,j}\rho^a_j$ where the projected density of states (PDOS) on the orbital j of the atom a is defined as:

$$\text{PDOS}^a_j(\omega) = \rho^a_j(\omega) = \sum_{n,\mathbf{k}}\left|\left\langle\varphi_{n\mathbf{k}}\middle|\tilde{\phi}^a_{j\mathbf{k}}\right\rangle\right|^2\delta(\omega-\epsilon_{n\mathbf{k}}) = \sum_{n,\mathbf{k}}\left|c^a_{nj}(\mathbf{k})\right|^2\delta(\omega-\epsilon_{n\mathbf{k}}) \tag{1.18}$$

Moreover, we can obtain the PDOS on a specific atom a as $\text{PDOS}^a(\omega) = \sum_j \text{PDOS}^a_j$. In the relation (1.18), we can also introduce the projected band structure (PBND) on the orbital j of the atom a at the band n and the $\mathbf{k}$:

$$\text{PBND}^a_{nj}(\mathbf{k}) = \left|c^a_{nj}(\mathbf{k})\right|^2 \tag{1.19}$$

Similarly, if we do the same work with position basis $\{|\mathbf{r}\rangle\}$[9], the Eq. (1.17) can be also rewritten as $\rho(\omega) = \int d\mathbf{r}\rho(\mathbf{r},\omega)$ where the local density of states (LDOS) at energy ω is defined as:

$$\text{LDOS}(\mathbf{r},\omega) = \rho(\mathbf{r},\omega) = \sum_{n,\mathbf{k}}\left|\varphi_{n\mathbf{k}}(\mathbf{r})\right|^2\delta(\omega-\epsilon_{n\mathbf{k}}) \tag{1.20}$$

The LDOS refers to the density of electronic states resolved locally in space. In the case where the tip can be assimilated to an s orbital or when the tip effect is very weak, it is possible to obtain STM images from the sum of $\text{LDOS}(\mathbf{r},\omega)$ over the energy range $\omega \in [0, V_{bias}]$ where V_{bias} is the bias voltage. This approximation is known as Tersoff-Hamman approximation [159]:

$$\text{LDOS}(\mathbf{r}) = \sum_{\omega=0}^{V_{bias}}\text{LDOS}(\mathbf{r},\omega) \tag{1.21}$$

In this thesis, the Tight-Binding method is used to study novel low-dimensional material based on graphene and hBN. Similarly to pristine graphene and hBN, only p_z orbital are taken into account, thus, $\left|\tilde{\phi}^a_{j\mathbf{k}}\right\rangle = |\tilde{p}^a_{z\mathbf{k}}\rangle$. The sum over j-th orbital in the Eq. (1.5) vanishes, the wave-function (1.5) becomes $\left|\varphi^{TB}_{n\mathbf{k}}(\mathbf{r})\right\rangle = \sum_a^{N_{atom}} c^a_{np_z}(\mathbf{k})\,|\tilde{p}^a_{z\mathbf{k}}(\mathbf{r})\rangle$. Hence, after diagonalization, the wave-function $\varphi^{TB}_{n\mathbf{k}}$, and the eigenvalues $\epsilon^{TB}_{n\mathbf{k}}$ are obtained. Finally, the wave-function $\varphi^{TB}_{n\mathbf{k}}(\mathbf{r})$ can be also displayed in three-

[8] The closure relation in orbital basis $\{\left|\phi^a_{jm}\right\rangle\}$ is: $\mathbb{1} = \sum_{a,j,\mathbf{k}}\left|\phi^a_{j\mathbf{k}}\right\rangle\left\langle\phi^a_{j\mathbf{k}}\right|$.
[9] The closure relation in position basis $\{|\mathbf{r}\rangle\}$ is: $\mathbb{1} = \int d\mathbf{r}\,|\mathbf{r}\rangle\langle\mathbf{r}|$.

dimension space with $\kappa = 1.625$ atomic units as below [160]:

$$\varphi^{TB}_{n\mathbf{k}}(\mathbf{r}) = \sum_{a}^{N_{atom}} c^{a}_{np_z}(\mathbf{k}) \frac{z - z_i}{|\mathbf{r} - \mathbf{r}_i|} \exp\{-\kappa|\mathbf{r} - \mathbf{r}_i|\} \tag{1.22}$$

It is worth noting that in this thesis, the wave-function $\varphi^{TB}_{n\mathbf{k}}(\mathbf{r})$, the local density of states LDOS$(\mathbf{r})$, and the projected band structure PBND$^{a}_{nj}(\mathbf{k})$ are sometimes interpolated to present as two-dimension maps using a similar way with a Lorentzian function (see Eq. (1.23)). For instance, the interpolated local density of states, LDOS$(\mathbf{X}, \mathbf{Y}; \mathbf{x}, \mathbf{y}; \sigma_{Lorentz})$, is implemented as follows:

$$\text{LDOS}(\mathbf{X}, \mathbf{Y}; \mathbf{x}, \mathbf{y}; \sigma_{Lorentz}) = \frac{\text{LDOS}(\mathbf{x}, \mathbf{y}) * \sigma^2_{Lorentz}}{(\mathbf{X} - \mathbf{x})^2 + (\mathbf{Y} - \mathbf{y})^2 + \sigma^2_{Lorentz}} \tag{1.23}$$

where $\mathbf{x}, \mathbf{y}$ are atomic coordinates, and $\mathbf{X}, \mathbf{Y}$ are interpolated coordinates. $\sigma_{Lorentz}$ represents half of the full width at half maximum of the peak, chosen to be around 0.5.

1.3.3 Tight-Binding approach for single particle optical properties.

Once the eigenvalues and eigenvectors are obtained, we can use them to characterize our target materials, which are hardly calculated by *ab initio* methods. One of our most desired characterization is the optical response of the material. It is well known that the optical response is described by the imaginary part of macroscopic transverse dielectric function[10] ε^M, called ε^M_2. In the entire report, we will work in the frame of the linear response regime at $T = 0$ K to simplify the problem.

Absorption scheme in Tight-Binding.

The system is subjected to a transverse electromagnetic plane wave of frequency ω, wavevector $\mathbf{q}$ and polarization vector $\hat{\mathbf{e}}$, which is described by its vector potential:

$$\mathbf{A}(\mathbf{r}, t) = A_0 \mathbf{u} \exp\{i(\mathbf{q}.\mathbf{r} - \omega t)\} + c.c. \qquad \mathbf{u} \perp \mathbf{q} \tag{1.24}$$

Initially, the system is described by an unperturbed Hamiltonian of independent electrons h_{TB}, labeled h_0 whose states and eigenvalues, $\varphi^{TB}_{n\mathbf{k}}$, and $\epsilon^{TB}_{n\mathbf{k}}$ are known. Under the influence of the electromagnetic field, its kinetic term changes according to $\frac{1}{2}\boldsymbol{\nabla}^2 \rightarrow \frac{1}{2}\left(\boldsymbol{\nabla} - \mathbf{A}(\mathbf{r}, t)/c\right)^2$. The total Hamiltonian becomes $h_{tot} = h_0 + h_{e-l}(t)$, where if neglecting the non-linear term in $1/c$, the coupling between the electron of

[10] The macroscopic transverse dielectric function is constituted the real part ε^M_1, and the imaginary part ε^M_2 so that $\varepsilon^M = \varepsilon^M_1 + i\varepsilon^M_2$. They are connected via the Kramers-Kronig relations.

the system and the light is [153]:

$$h_{e-l}(\mathbf{r},t) = -\frac{1}{c}\mathbf{A}(\mathbf{r},t).\boldsymbol{\nabla} = -\frac{A_0}{c}e^{i\mathbf{q}.\mathbf{r}}\mathbf{u}.\boldsymbol{\nabla}e^{-i\omega t} + c.c. \tag{1.25}$$

Since the time dependence of the coupling operator follows $e^{-i\omega t}$, Eq. (1.25) can be treated within the time-dependent perturbation theory. The probability per unit of time of transition between an initial state $\left|\varphi^{TB}_{m\mathbf{k}}\right\rangle$ (an occupied state) and a final state $\left|\varphi^{TB}_{\mu\mathbf{k}+\mathbf{q}}\right\rangle$ (an unoccupied state) by the absorption of a photon is given at the first order by the Fermi golden rule [153]:

$$P_{m\mathbf{k}\to\mu\mathbf{k}+\mathbf{q}} = 2\pi\left(\frac{A_0}{c}\right)^2\left|\left\langle\varphi^{TB}_{\mu\mathbf{k}+\mathbf{q}}\right|e^{i\mathbf{q}.\mathbf{r}}\mathbf{u}.\boldsymbol{\nabla}\left|\varphi^{TB}_{m\mathbf{k}}\right\rangle\right|^2\delta(\epsilon^{TB}_{\mu\mathbf{k}+\mathbf{q}} - \epsilon^{TB}_{m\mathbf{k}} - \omega) \tag{1.26}$$

At thermal equilibrium, the occupation of the electronic states is described by Fermi-Dirac distribution function $f(\epsilon)$; the net number of transitions per unit time involving energy ω is given by the expression [153]:

$$W(\mathbf{q},\omega) = 2\pi\left(\frac{A_0}{c}\right)^2 2\sum_{m}^{(\text{occ})}\sum_{\mu}^{(\text{unocc})}\sum_{\mathbf{k}}^{1\text{BZ}}\left|\left\langle\varphi^{TB}_{\mu\mathbf{k}+\mathbf{q}}\right|e^{i\mathbf{q}.\mathbf{r}}\mathbf{u}.\boldsymbol{\nabla}\left|\varphi^{TB}_{m\mathbf{k}}\right\rangle\right|^2\delta(\epsilon^{TB}_{\mu\mathbf{k}+\mathbf{q}} - \epsilon^{TB}_{m\mathbf{k}} - \omega)\left[f(\epsilon_{m\mathbf{k}}) - f(\epsilon_{\mu\mathbf{k}})\right] \tag{1.27}$$

where the factor 2 in front of the summation takes into account the spin degeneracy. The imaginary part of the dielectric function can be related to the microscopic transition rate as $\varepsilon_2(\mathbf{q},\omega) = 2\pi\left(\frac{c}{\omega}\right)^2\frac{1}{V}\frac{W(\mathbf{q},\omega)}{A_0^2}$ [153]. At $T = 0$ K, the electronic states are either fully occupied or unoccupied, and the expression of the imaginary part of the dielectric function is [153]:

$$\varepsilon_2(\mathbf{q},\omega) = \left(\frac{8\pi^2}{\omega^2}\right)\frac{1}{V}\sum_{m}^{(\text{occ})}\sum_{\mu}^{(\text{unocc})}\sum_{\mathbf{k}}^{1\text{BZ}}\left|\left\langle\varphi^{TB}_{\mu\mathbf{k}+\mathbf{q}}\right|e^{i\mathbf{q}.\mathbf{r}}\mathbf{u}.\boldsymbol{\nabla}\left|\varphi^{TB}_{m\mathbf{k}}\right\rangle\right|^2\delta(\epsilon^{TB}_{\mu\mathbf{k}+\mathbf{q}} - \epsilon^{TB}_{m\mathbf{k}} - \omega) \tag{1.28}$$

Moreover, if we consider the usual experimental situations (infrared region, visible, up to near and far ultraviolet region), where the wavelength of the incident radiation is much larger than the lattice parameter, the photon wavevector $\mathbf{q}$ of the incident radiation is very small compared to the range of values of $\mathbf{k} \in$ 1BZ. Therefore, we can neglect $\mathbf{q}$, called dipole approximation [11]; it means that we consider only vertical transitions, *i.e.* from an occupied state $\left|\varphi^{TB}_{m\mathbf{k}}\right\rangle$ to an empty state $\left|\varphi^{TB}_{\mu\mathbf{k}}\right\rangle$ (see Fig. (1.5)). Finally, the Eq. (1.28) becomes:

$$\varepsilon_2(\omega) = \left(\frac{8\pi^2}{\omega^2}\right)\frac{1}{V}\sum_{m}^{(\text{occ})}\sum_{\mu}^{(\text{unocc})}\sum_{\mathbf{k}}^{1\text{BZ}}\left|v_{m\mu\mathbf{k}}\right|^2\delta(\epsilon^{TB}_{c\mathbf{k}} - \epsilon^{TB}_{v\mathbf{k}} - \omega) \tag{1.29}$$

[11] It means that the longitudinal and transverse part of ε is undistinguished.

where we have just defined the velocity matrix elements $v_{m\mu\mathbf{k}} = \left\langle \varphi^{TB}_{\mu\mathbf{k}} \middle| \mathbf{u}.\boldsymbol{\nabla} \middle| \varphi^{TB}_{m\mathbf{k}} \right\rangle$. In the relation (1.29), the last term $\delta(\epsilon^{TB}_{\mu\mathbf{k}} - \epsilon^{TB}_{m\mathbf{k}} - \omega)$ describes the energy conservation, so that a transition is only excited, if and only if the photon energy ω matches the direct electronic transition energy $\epsilon^{TB}_{c\mathbf{k}} - \epsilon^{TB}_{v\mathbf{k}}$. Consequently, the absorption results never occurs at energies inferior to the band gap. Additionally, Eq. (1.29) allows the building of a connection between the macroscopic constants relying on Maxwell's equations like absorption index, refractivity, etc., and the microscopic structure of the material like band structure, energy levels, etc. Finally, even using *ab initio* (DFT or GW) eigenvalues and eigenvectors instead of Tight-Binding ones, the correct macroscopic dielectric function ε^M can not be obtained via Eq. (1.29). This is because the macroscopic dielectric function (1.29) is obtained by neglecting the local effects[12]. The average integral of the microscopic dielectric function will be properly calculated further in the Bether-Salpether equation in 1.4.8.

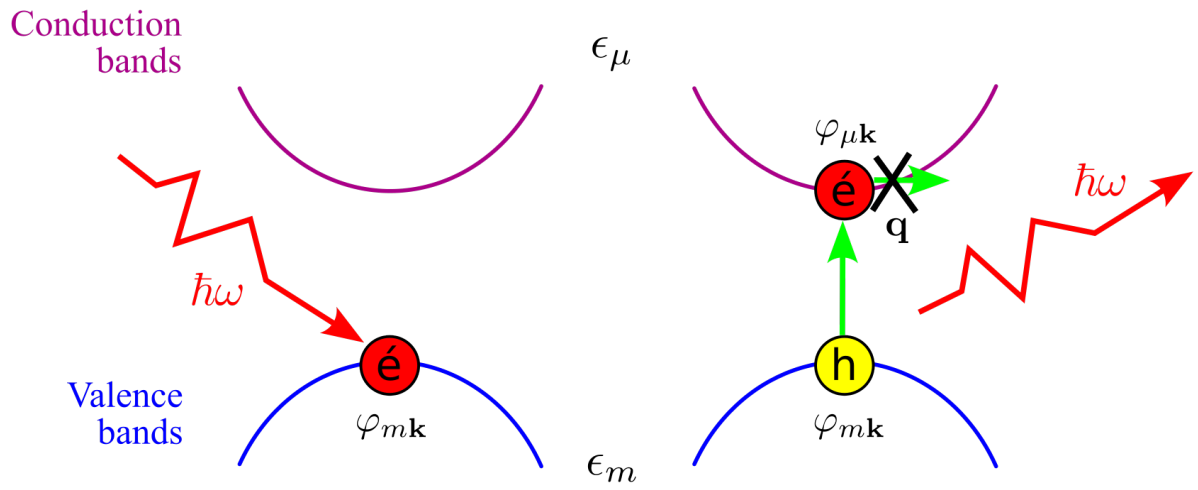

Figure 1.5 – Schema representation of an optical vertical transition in the energy band diagram. a, Before the absorbing the incoming photon. **b,** After absorbing the incoming photon. The photon wavevector $\mathbf{q}$ is defined as $\mathbf{q} = \mathbf{k}_c - \mathbf{k}_v$. The transitions are considered vertical at $\mathbf{q} \to 0$.

Velocity matrix elements in Tight-Binding.

In this part, we will present the last ingredient to determine ε_2 via Eq. (1.29), the velocity matrix elements $v_{m\mu\mathbf{k}}$. In the atomic units, the velocity operator can be expressed in terms of the commutator between

[12] The macroscopic dielectric function can be obtained from the microscopic one via an average integral $\varepsilon^M(\omega) = \lim_{\mathbf{q}\to 0}\left[\int d\mathbf{r}d\mathbf{r}' e^{i\mathbf{q}.(\mathbf{r}-\mathbf{r}')}\varepsilon^{-1}(\mathbf{r},\mathbf{r}',\omega)\right]^{-1}$ or $\varepsilon^M(\omega) = \lim_{\mathbf{q}\to 0}\frac{1}{\varepsilon^{-1}_{\mathbf{G}_m=0,\mathbf{G}_{m'}=0}(\mathbf{q},\omega)}$ where $\varepsilon_{\mathbf{G}_m=0,\mathbf{G}_{m'}=0}(\mathbf{q},\omega)$ is the microscopic dielectric function expressed in $\mathbf{G}_m$ space [161, 162]. However, the Eq. (1.29) has implicitly taken into account as $\varepsilon^M(\omega) = \lim_{\mathbf{q}\to 0}\int d\mathbf{r}d\mathbf{r}' e^{i\mathbf{q}.(\mathbf{r}-\mathbf{r}')}\varepsilon(\mathbf{r},\mathbf{r}',\omega)$ or $\varepsilon^M(\omega) = \lim_{\mathbf{q}\to 0}\varepsilon_{\mathbf{G}_m=0,\mathbf{G}_{m'}=0}(\mathbf{q},\omega)$. The latter is only correct in the case of homogeneous electron gas in which ε is diagonal in $\mathbf{G}_m, \mathbf{G}_{m'}$. However, normally, ε is not diagonal in $\mathbf{G}_m$ space because it is not only distance dependent but only position dependent (inhomogeneities in space, called the crystal local effects). Thus the correct expression has to be the former one.

the system's Hamiltonian $\hat{\mathbf{h}}_{TB}$ and the position operator $\hat{\mathbf{r}}$:

$$\hat{\mathbf{v}} = \hat{\mathbf{p}} = -i\left[\hat{\mathbf{r}}, \hat{\mathbf{h}}_{TB}\right] = -i\left[\hat{\mathbf{r}}\hat{\mathbf{h}}_{TB} - \hat{\mathbf{h}}_{TB}\hat{\mathbf{r}}\right] \tag{1.30}$$

Then, first we know that $\hat{\mathbf{r}}\left|p^a_{zm}\right\rangle = (\mathbf{R}_m - \mathbf{r}_a)\left|p^a_{zm}\right\rangle$. Second, thanks to the relation (1.10), we multiply Eq. (1.30) by $\left|p^a_{zm}\right\rangle$, we obtain: $\hat{\mathbf{h}}_{TB}\left|p^a_{zm}\right\rangle = \xi^{(1)}_{aa}\left|p^a_{zm}\right\rangle + \sum_{a'}^{1n.n} t_{aa'}\left|p^{a'}_{zm'}\right\rangle + \sum_{a''}^{2n.n}\xi^{(2)}_{aa''}\left|p^{a''}_{zm''}\right\rangle$. Using those relations above, we do the similar work by multiplying the Eq. (1.30) by $\left|p^a_{zm}\right\rangle$, we have:

$$\hat{\mathbf{v}}\left|\tilde{p}^a_{zm'}\right\rangle = -i\left(\sum_{a'}^{1nn} t_{aa'}\Delta^{aa'}_{mm'}\left|p^{a'}_{zm'}\right\rangle + \sum_{a''}^{2nn}\xi^{(2)}_{aa''}\Delta^{aa''}_{mm''}\left|p^{a''}_{zm''}\right\rangle\right) \tag{1.31}$$

where the distance vectors Δ^{ij}_{kl} is defined as: $\Delta^{ij}_{kl} = \mathbf{R}_l + \mathbf{r}_j - \mathbf{R}_k - \mathbf{r}_i$. Afterwards, we multiply the Eq. (1.31) by $\left\langle p^b_{zl}\right|$, and we have:

$$\left\langle p^b_{zl}\right|\hat{\mathbf{v}}\left|p^a_{zm}\right\rangle = \begin{cases} 0 & \text{if a=b} \\ -it_{ab}\Delta^{ab}_{ml} & \text{if a and b are first nearest neighbors (1nn)} \\ -i\xi^{(2)}_{ab}\Delta^{ab}_{ml} & \text{if a and b are second nearest neighbors (2nn)} \end{cases} \tag{1.32}$$

In reciprocal space, the Eq. (1.32) becomes:

$$\left\langle \tilde{p}^b_{z\mathbf{k}}\right|\hat{\mathbf{v}}\left|\tilde{p}^a_{z\mathbf{k}}\right\rangle = \frac{1}{N_{cell}}\sum_{lm} e^{i\mathbf{k}.(\mathbf{R}_m - \mathbf{R}_l)}\left\langle p^b_{zl}\right|\hat{\mathbf{v}}\left|p^a_{zm}\right\rangle \tag{1.33}$$

Finally, the velocity matrix elements $v_{m\mu\mathbf{k}}$ are expressed in the form below:

$$v_{m\mu\mathbf{k}} = \sum_{a,b}^{N_{atom}} c^{b*}_{\mu p_z} c^a_{mp_z}\left\langle \tilde{p}^b_{z\mathbf{k}}\right|\hat{\mathbf{v}}\left|\tilde{p}^a_{z\mathbf{k}}\right\rangle \tag{1.34}$$

1.4 Density functional theory (DFT)

This section will show more accurate approaches than Tight-Binding ones, called *ab initio* approaches. We will start with density functional theory (DFT), where the system is still considered a non-interacting electron. Then, we will show how to go toward the interacting electron system from DFT to characterize the material better.

1.4.1 The Hohenberg and Kohn theorem.

As shown in the previous parts, more approximations are truly needed, and the wave-function variation principle proposes an excellent way to treat the electronic density instead of the wave-function from which the density functional theory (DFT) stems. In a spin-unpolarized system, the electronic density is[13]:

$$n(\mathbf{r}) = 2N \int d\mathbf{r}_2 \ldots \int d\mathbf{r}_N |\Psi(\mathbf{r}, \mathbf{r}_2, \ldots, \mathbf{r}_N)|^2 \tag{1.35}$$

where $n(\mathbf{r})$ is normalized to the total electron number of the system: $N = \int_{\mathbb{R}^3} n(\mathbf{r}) d\mathbf{r}$. The factor of 2 accounts for the equal contributions from spin-up and spin-down electrons. Now, we consider an electronic system by replacing the external potential $v_{ext}(\mathbf{r})$ with an arbitrary local potential $v(\mathbf{r})$. The corresponding ground state Ψ is then obtained by solving the Schrödinger equation with the new Hamiltonian. After that, the associated electronic ground state density can be calculated. However, in 1964, Hohenberg and Kohn [163] showed that the inverse is also true, starting with a ground state density $n(\mathbf{r})$ to determine the potential $v(\mathbf{r})$ up to an additive real-valued constant:

$$n(\mathbf{r}) \xrightarrow[\text{theorem}]{\text{Hohenberg-Kohn}} v(\mathbf{r}) + cte \quad \rightarrow \quad \mathbf{H} \quad \rightarrow \quad (E \quad \& \quad \Psi) \quad \rightarrow \quad \text{Properties} \tag{1.36}$$

Understandably, a constant shift in local potential does affect neither the ground-state wave-function Ψ nor the ground-state density $n(\mathbf{r})$. Also, two local potentials differing by more than an additive constant having the same ground state wave function and ground density cannot exist. Therefore, the local potential $v(\mathbf{r})$ (with an additive constant, which can be chosen to 0) and all other quantities, including the ground state wave function, are the unique functionals of the ground state density $n(\mathbf{r})$. Moreover, Hohenberg and Kohn revealed the universal density functional, which is independent of the external potential $v_{ext}(\mathbf{r})$:

$$F[n] = \langle \Psi[n] | \hat{\mathbf{T}}_e + \hat{\mathbf{W}}_{ee} | \Psi[n] \rangle = T_e[n] + W_{ee}[n] \tag{1.37}$$

and only defined for the N-electron ground state densities $n(\mathbf{r})$ associated with some local potential $v(r)$, these are called set of v-representable densities, denoted by $\mathcal{A}$. By applying the variational theorem, the exact ground state energy E_0 of the system is reached by minimizing the total electronic energy functional $E[n]$ with respect to v-representable densities:

$$E_0 = \min_{n \in \mathcal{A}} E[n] = \min_{n \in \mathcal{A}} \left(F[n] + \int v_{ext}(\mathbf{r}) n(\mathbf{r}) d\mathbf{r} \right) \tag{1.38}$$

[13] In general case, the electronic density is defined as: $n(\mathbf{r}) = N \sum_{\sigma_1} \ldots \sum_{\sigma_N} \int d\mathbf{r}_2 \ldots \int d\mathbf{r}_N |\Psi(\mathbf{r}, \sigma_1; \mathbf{r}_2, \sigma_2; \ldots; \mathbf{r}_N, \sigma_N)|^2$. The former is the integration over space variables, whereas the latter is the integration over spin variables. In a spin-unpolarized system, the probability density for finding an electron at $\mathbf{r}$ with spin-up is the same as for spin-down, thus we can separate the spin part from the spatial part: $\sum_{\sigma_1} \ldots \sum_{\sigma_N} |\Psi(\mathbf{r}, \sigma_1; \mathbf{r}_2, \sigma_2; ...; \mathbf{r}_N, \sigma_N)|^2 = 2|\Psi(\mathbf{r}, \mathbf{r}_2, ..., \mathbf{r}_N)|^2$ where the factor of 2 accounts for the contributions from both spin-up and spin-down electrons.

From the exact ground state energy E_0, we can deduce the exact ground state density $n_0(\mathbf{r})$ corresponding to the external potential $v_{ext}(\mathbf{r})$. In other words, Eq. (1.38) allows us to find the ground state density n among all the possible ground state densities (among v-representable densities) associated with some local potential that minimizes the total electronic energy. This minimum energy is the exact ground state energy, and the corresponding density n is the exact ground state n_0. Nevertheless, $F[n]$ is very hard to approximate, or the approximations exist but are not entirely accurate because its explicit expression in terms of electronic density is unknown.

1.4.2 Kohn-Sham method.

In 1965, to determine an expression of $F[n]$, Kohn and Sham [164] linked the unknown interacting system to the well-known non-interacting system. The universal functional $F[n]$ was re-defined as below:

$$F[n] = \min_{\substack{\Phi\in\mathcal{S}\\ \Phi\to n}} \left(\langle\Phi|\hat{\mathbf{T}}_e|\Phi\rangle \right) + E_{Hxc}[n] = T_s[n] + E_{Hxc}[n] \tag{1.39}$$

where $T_s[n]$ is the non-interacting kinetic energy function defined in a constrained-search formulation [165–167]. The non-interacting wave function, called Kohn-Sham wave-function, is now a single Slater determinant $\Phi \in \mathcal{S}$ yielding the fixed density n. Understandably, $T_s[n]$ is well-defined over the entire set of N-representable densities denoted $\mathcal{D}$[14] because any single Slater determinant validates the mathematical condition of $\mathcal{D}$. So the expression of $T_s[n]$ is exact and can be treated explicitly, unlike $T_e[n]$ in Eq. (1.38). All the differences between $F[n]$ and $T[s]$ are defined by the Hartree-exchange-correlation functional $E_{Hxc} = T_e[n] + W_{ee}[n] - T_s[n]$, which is still unknown and needs to be approximated as a density functional. In practice, E_{Hxc} can be decomposed in two parts :

$$E_{Hxc}[n] = E_H[n] + E_{xc}[n] \tag{1.40}$$

where the exact Hartree energy functional $E_H[n]$ is known and can be calculated explicitly:

$$E_H[n] = \frac{1}{2}\int\int \frac{n(\mathbf{r}_1)n(\mathbf{r}_2)}{|\mathbf{r}_1 - \mathbf{r}_2|} d\mathbf{r}_1 d\mathbf{r}_2 \tag{1.41}$$

[14] In 1979, Levy[166, 167], and later Lieb [165], proposed to redefine $F[n]$ using a constrained-search formulation, called an extension of Hohenberg Kohn functional. In this case, the ground state energy of the system is minimized over the densities $n(\mathbf{r})$ in $\mathcal{D}$, which is a huge simplification compared to the minimization over a many-body wave function Ψ used in the beginning by Hohenberg and Kohn as shown in Eq. (1.38). It is worth noting that $\mathcal{D}$ is a larger set of N-representable densities and includes the set of v-representable densities.

and all the rest unknown functionals are pushed into an unique term, namely the exchange-correlation E_{xc}:

$$E_{xc}[n] = T[n] + W_{ee}[n] - T_s[n] - E_H[n] \tag{1.42}$$

Similarly, the exact ground state is also rewritten by replacing the fixed density n by n_Φ. Eq. (1.38) becomes:

$$E_0 = \min_{\Phi \in \mathcal{S}} \left(\langle \Phi | \hat{\mathbf{T}} + \hat{\mathbf{V}}_{ext} | \Phi \rangle + E_{Hxc}[n_\Phi] \right). \tag{1.43}$$

Kohn and Sham minimized the single Slater determinant wave function Φ instead of the multiple-determinant wave function Ψ or the density n in this attempt. Additionally, using only the single determinant is also an overwhelming simplification. According to (1.43), the exact ground state energy E_0 and density n_0 are also determined by Kohn Sham method but not the exact ground state wave function Ψ_0 (the ground state Kohn-Sham wave function Φ_0 instead), unlike Hohenberg-Kohn and Levy-Lieb methods.

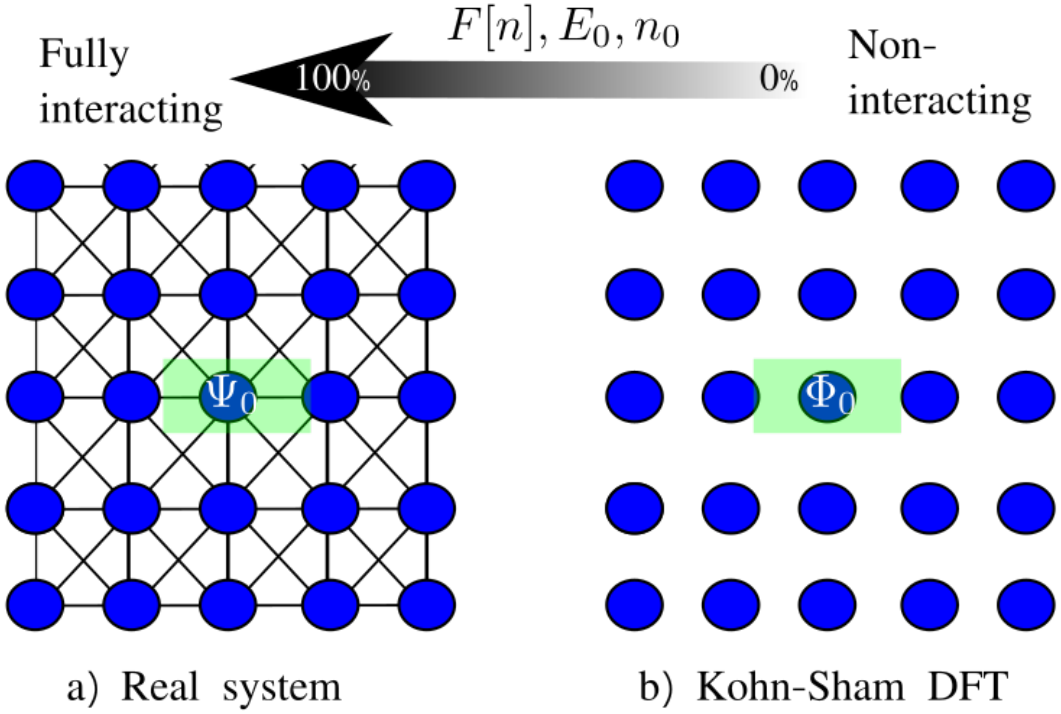

Figure 1.6 – Schema depicting the connection between a, the real system that the electrons are fully interacting and **b,** the Kohn-Sham's world that electrons are independent. These different worlds connect together via $F[n]$, E_0, and n_0.

1.4.3 Kohn-Sham equations.

The total electronic energy in Eq. (1.43) can be expressed as:

$$E[\{\varphi_i\}] = \sum_{i=1}^{N} \int \varphi_i^*(\mathbf{r}) \left(-\frac{1}{2}\boldsymbol{\nabla}^2 + v_{ext}(\mathbf{r}) \right) \varphi_i(\mathbf{r}) d\mathbf{r} + E_{Hxc}[n], \tag{1.44}$$

and the density is :

$$n(\mathbf{r}) = 2 \sum_{i=1}^{N} |\varphi_i(\mathbf{r})|^2 \tag{1.45}$$

where the factor 2 stems from the spin-degeneracy. The ground state energy is achieved once the minimum of Lagrangian is reached, corresponding to the stationary condition. Then, the Kohn-Sham equations are obtained [164]:

$$\left(-\frac{1}{2}\boldsymbol{\nabla}^2 + v_{ext}(\mathbf{r}) + v_{Hxc}(\mathbf{r}) \right) \varphi_i^{KS}(\mathbf{r}) = \epsilon_i^{KS} \varphi_i^{KS}(\mathbf{r}) \tag{1.46}$$

where the Kohn-Sham potential (or the effective potential) is:

$$v_{KS}(\mathbf{r}) = v_{ext}(\mathbf{r}) + v_{Hxc}(\mathbf{r}) \tag{1.47}$$

where the Hartree-exchange-correlation potential is just defined as $v_{Hxc}(\mathbf{r}) = \frac{\delta E_{Hxc}[n]}{\delta n(\mathbf{r})}$, and can be decomposed as $v_{Hxc}(\mathbf{r}) = \frac{\delta E_{Hxc}[n]}{\delta n(\mathbf{r})} = \frac{\delta E_H[n]}{\delta n(\mathbf{r})} + \frac{\delta E_{xc}[n]}{\delta n(\mathbf{r})} = v_H + v_{xc}$. We emphasize that the Eq. (1.46) can be self-consistently solved since $v_{KS}(\mathbf{r})$ depends on all the occupied orbitals through the density $n(\mathbf{r})$, according to the Eq. (1.45). The convergence is reached once the density $n_{out}(\mathbf{r})$ obtained by solving the Eq. (1.46) is the same as the density $n_{in}(\mathbf{r})$ used to construct the effective potential $v_{KS}(n_{in})$ in the Eq. (1.47) (see Fig. (1.6)). On the other hand, the N-interacting electrons system connects to the N-non-interacting electrons one via the Kohn-Sham potential $v_{KS}(\mathbf{r})$. In other words, $v_{KS}(\mathbf{r})$ ensures that the ground state energy E_0 and density $n_0(\mathbf{r})$ of N-non-interacting electrons system are exactly the ones of N-interacting electrons system. Nevertheless, all the Kohn-Sham orbital energies ϵ_i^{KS} and also Kohn-Sham orbitals $\varphi_i^{KS}(\mathbf{r})$ are the ones of N-non-interacting electrons system.

Once the self-consistent solutions have been found, the ground-state energy is given by

$$E[n_0(\mathbf{r})] = 2 \sum_{i=1}^{N} \epsilon_i^{KS} - E_H[n_0(\mathbf{r})] + E_{xc}[n_0(\mathbf{r})] - \int v_{xc}[n_0(\mathbf{r})] n_0(\mathbf{r}) d\mathbf{r}^3, \tag{1.48}$$

We note that before the convergence is reached, for each iteration, if the input density n_{in} is employed to solve the KS equations (1.46), the non-interacting kinetic energy from the output density T_s can be

determined by:

$$T_s[n_{out}] = 2\sum_{i=1}^{N}\epsilon_i^{KS} - \int v_{KS}[n_{in}]n_{out}d\mathbf{r}^3$$

The output total energy is then:

$$E[n_{out}] = 2\sum_{i=1}^{N}\epsilon_i^{KS} - \int v_{KS}[n_{in}]n_{out}d\mathbf{r}^3 + V_{ext}[n_{out}] + E_{Hxc}[n_{out}] \tag{1.49}$$

which means that the total energy depends not only on the output density n_{out} but also on the input one n_{in}.

1.4.4 Kohn-Sham Density Functional Theory in Quantum Espresso.

This part details the Kohn-Sham DFT developed in a standard Open-Source computer code such as Quantum-Expresso, Abinit... such as the basis wave-function set-up, the pseudo-potentials, and the periodic boundary conditions.

Usual exchange-correlation approximations

Since the exact expression of E_{xc} is unknown, the accuracy of Kohn-Sham DFT depends entirely on the approximations for the exchange-correlation functional. First, it is worth to define the exchange-correlation density e_{xc} from E_{xc}:

$$E_{xc} = \int e_{xc}(\mathbf{r}).d\mathbf{r} \tag{1.50}$$

According to Jacob's Ladder, the non-local exchange-correlation density approximations such as hybrid functional RPA-like functional are the nearest approximations to the exact exchange-correlation functional; it is when the exchange-correlation density e_{xc}^{nl} at the position $\mathbf{r}$ depends on density everywhere in space. The higher the approximation is, the higher the computational cost is. The local and semi-local exchange-correlation densities are more adapted to our systems, and we will prove why these work remarkably well.

(a) Local-Density approximations (LDA): Introduced by Kohn and Sham [164] in 1965, it consists of assuming that the local exchange-correlation energy density only depends on the local density and that it is the same as that of a homogeneous electron gas with the same density:

$$e_{xc}(\mathbf{r}) = e_{xc}^{LDA}(n(\mathbf{r}), \mathbf{r}) = n(\mathbf{r})e_{xc}^{hom}\left(n(\mathbf{r})\right) \tag{1.51}$$

where the exchange density is analytically known while the correlation one is unknown; however,

the latter is numerically obtained from accurate Quantum Monte Carlo simulations and fitted to a parametrized function of n satisfying the known high- and low-density expansions. As expected, LDA works very well for infinite systems where the density varies spatially very smoothly or where the electron-electron interaction is well-screened. However, LDA has unexpectedly provided accurate results for inhomogeneous systems such as molecules and atoms. The reason is that the LDA exchange-correlation hole correctly fulfills sum-rule conditions[15] [168]. However, because of the local form of the electronic density, LDA presents some defaults, such as self-interaction and self-correlation errors. The LDA exchange-correlation functional does not entirely eliminate the Hartree functional's self-interaction and self-correlation contributions; thus, an electron interacts with itself and correlates with its own charge density, which is not physically correct.

(b) Generalized-gradient approximations (GGA): Considered as one of the next steps beyond LDA started in the 1980s, e_{xc} is now expressed under the form:

$$e_{xc}(\mathbf{r}) = e_{xc}^{GGA}\left(n(\mathbf{r}), \boldsymbol{\nabla} n(\mathbf{r})\right) \tag{1.52}$$

For this reason, GGA functionals are also called semi-local approximations because they require the information of the electronic density at any position $\mathbf{r}$ and the *semi information* of its local surrounding neighbors via its gradients. There are many different functionals proposed in GGA, such as Becke 88 (B88) exchange functional [169], Lee-Yang-Parr (LYP) correlation functional [170], Perdew-Wang 91 (PW91) exchange-correlation functional [171, 172]... They have been created to deal with specific problems in DFT. Overall, they provide a significant improvement over LDA for 0D systems. Nevertheless, self-interaction and static-correlation errors have not been solved, so their accuracy is limited. In this thesis, we used Perdew-Burke-Ernzerhof (PBE) functional [173], which consists of fewer exact conditions than others and with no fitted parameters. However, its accuracy for molecular systems makes it the most widely used functional with more than 130 000 article citations. In PBE, the logarithm divergence of LDA at high-density limit has been removed, the correlation energy per particle vanishes at large-reduced-density gradient limit, the second-order small-gradient expansions have been enforced at weak-gradient limit for both exchange and correlation, and the Lieb-Oxford bound has been used at the large-gradient limit.

[15] Where the exchange-correlation hole describes how electrons repel each other in three ways : (classical effects) through Coulomb interaction, (quantum effects) through the exchange (by Pauli principle) and correlation.

Plane wave basis set

A crystal is invariant under translations; it can be described by one unit cell with periodic boundary conditions to figure out the properties of the whole crystal. According to Bloch's theorem, the Kohn-Sham single particle orbital wave function φ_i can be expanded in a plane wave basis like:

$$\varphi^{KS}_{n\mathbf{k}}(\mathbf{r}) = \frac{1}{\Omega_{cell}} e^{\mathbf{ik.r}} \sum_{\mathbf{m}} c_{n\mathbf{k}} e^{\mathbf{iG_m.r}} = e^{\mathbf{ik.r}} u_{n\mathbf{k}}(\mathbf{r}) \tag{1.53}$$

where $u_{n\mathbf{k}}(\mathbf{r})$ is a periodic function with the same periodicity as the crystal; the wave vector $\mathbf{k}$ lying in the 1BZ is the crystal momentum vector, and $\mathbf{G}_m$ is a reciprocal lattice vector. In practice, we need to increase more and more plane waves to reach the convergence of total energy, and the Eq. (1.53) needs to be truncated by using the cutoff energy E_{cut}:

$$\frac{1}{2}|\mathbf{k} + \mathbf{G}_m| \leq E_{cut} \tag{1.54}$$

where the bigger E_{cut} is, the higher is the number of plane waves used to describe the system ($N_w = \Omega_{cell}(E_{cut})^{3/2}$), but also the higher is the obtained accuracy.

Pseudopotential

The idea of the pseudopotential method is that the core electrons do not participate in the chemical bonds since they are localized very closely to the nuclei, and it is very challenging to expand their wave function on a plane wave basis. Therefore, the core electrons can be treated as an effective pseudopotential influence on the valence electrons. This latter ensures that the valence electrons' behavior is reproduced as closely as possible to the original atom.

Because of the high accuracy and excellent precision of KS-DFT with using LDA and GGAs for low dimensional materials, in this thesis, we employ the KS-DFT developed in Quantum Espresso. As shown previously, using a plane wave basis plays a crucial role in getting results with high precision; it is highly needed, especially in achieving electronic and optical responses. For this reason, many post-DFT tools are developed to employ KS-DFT databases, such as GW approximation and Bethe-Salpeter equation (BSE) coded in Yambo [174, 175]. This will be discussed in the following sections. Nevertheless, because of the numerous required plane waves, we can only use KS-DFT, besides GW and BSE, for limited-size systems in a vacuum. When the considered systems are big or deposited on large metallic surfaces like in STM/STS experiments for transport properties, it becomes impossible to use KS-DFT on a plane wave basis set.

1.4.5 Density Functional Theory in Fireball

Since *ab initio* methods with plane wave basis, like Quantum Espresso, are very heavy, the range of applications of these simulation techniques is limited to situations with small numbers of atoms, approximately 100–200 atoms in the unit cell, and short simulation times. On the other hand, Tight-Binding methods (TB) can work with much more extensive systems beyond 5000 atoms in a unit cell; however, it must be validated by experiments or *ab initio* results. For these reasons, a so-called "*ab initio* Tight-Binding" can meet the demands, aiming at improving the range of applications on more significant size systems with high accuracy.

On the other hand, O. F. Sankey, one of the first researchers, reported that molecular dynamics (MD), a method used to simulate the physical movements of atoms and molecules, could be effectively integrated with electronic structure calculations [176]. Later, he and co-authors developed an *ab initio* tight-binding MD formalism called Sankey–Niklewskiy (SN) method [177]. This method approximates complex LDA exchange-correlation matrix elements using a multicenter approach with the minimal sp^3 basis set and faster evaluation of materials over other approaches. Over the years, several improvements to the method have been proposed and employed. One of the most reported improved methods is Fireball, which includes include a self-consistent extension, can work with various exchange-correlation functionals (LDA, GGA), and goes beyond for double numerical (DN) basis sets by adding polarization orbitals and d-orbitals to the basis set. These improvements enhance computational efficiency, expand the range of applicable systems, and make Fireball a powerful and versatile tool for large-scale simulations of complex materials. For this reason, in this thesis, we used the Fireball code to study electronic and further STM/STS simulations (see later in 1.4.9) of complex interfaces such as 0D-2D structures on a metallic surface.

In the following part, we will outline the key differences between Fireball and the conventional *ab initio* methods based on the Kohn-Sham framework, as previously described.

The Harris–Foulkes functional

Firstly, at the core of the theory is the replacement of the Kohn–Sham functional by Harris–Foulkes functional [178–181]:

$$E[n(\mathbf{r})] = 2\sum_{i=1}^{N} \epsilon_i^{FB} + \Big[E_{ion-ion} - E_H[n_{in}(\mathbf{r})]\Big] + \Big[E_{xc}[n_{in}(\mathbf{r})] - \int V_{xc}[n_0(\mathbf{r})]n_{in}(\mathbf{r})d\mathbf{r}^3\Big], \tag{1.55}$$

where ϵ_i^{FB} are eigenvalues of the one-electron Schrodinger given by Eq. (1.46), obtained by Fireball. Addionally, the short-range ion-ion repulsion is taken into account at this time (in atomic units):

$$E_{ion-ion} = \frac{1}{2}\sum_{I\neq J}\frac{Z_I Z_J}{|\mathbf{R}_I - \mathbf{R}_J|}$$

This energy provides a measure of the repulsion between the positively charged nuclei. It contributes to the balance between the attractive electron-nucleus interactions and the repulsive ion-ion interactions, along with electron-electron interactions. Therefore, this term allows to better determine the system's stability and equilibrium geometry.

Further, we note that the difference between the Harris-Foulkes and the Kohn-Sham functional (1.49) is that the Harris-Foulkes is an approximation of the Kohn-Sham, depending only on n_{in}, whereas Kohn-Sham depends on both n_{in} and n_{out}. It is shown [177] that errors of the Harris-Foulkes functional are of the second order in the error on the input density $\Delta n = n_{out} - n_{in}$. It means that the total energy can, therefore, be evaluated without needing to know the one-electron eigenfunctions or the output density. The principle advantage of the Harris–Foulkes functional is that it is possible to choose an appropriate form for the input charge density, which is a sum of densities localized at various sites, together with the use of localized orbitals to solve the one-particle Schrodinger equation (see later), which simplifies the electron-electron Coulomb integrals at most three centers. However, for many years, the Harris-Foulkes functional was primarily used in non-self-consistent methods [177, 178, 182]. In the following parts, we will demonstrate how this functional can be employed in a self-consistent manner.

Fireball orbitals and basis sets

In solving the one-electron Schrodinger equation of Eq. (1.46), a set of slightly excited pseudoatomic *fireballs* orbitals (or Sankey-Niklewski orbitals) $\phi^{FB} = f(\mathbf{r})Y_{lm}(\theta,\phi)$ are used, where $f(\mathbf{r})$ is a radial component and $Y_{lm}(\theta,\phi)$ is the angular component which is a spherical harmonic function. The *fireballs* orbitals, introduced by Sankey-Niklewski [177] are obtained with the boundary condition that $\phi^{FB}(\mathbf{r})\big|_{r\geq r_c} = 0$, instead of $\phi^{FB}(\mathbf{r})\big|_{r\to\infty} = 0$ as the true pseudo-atomic orbitals. This boundary condition is a purely semi-empirical approximation; it is made to reduce the number of nearest neighbors, so the overlap matrix elements of the Hamiltonian are quite sparse for large systems. Moreover, similarly to the problem of "a particle in a box," it also has some effects of raising the electronic levels. Nevertheless, this slight excitation comprises Fermi compression in solids, better representing the solid-state charge densities. Further, r_c is chosen to preserve the chemical trends of the atoms, such as relative ionization energies and relative atomic sizes (it varies between 5-8 Å, depending on the type of orbitals). Contrary to the plane-wave basis set, these *fireballs* localized orbitals are a real-space technique. Finding a

universally robust optimized minimal basis set is needed to speed up performed simulations while maintaining the desired accuracy. The use of this basic set is the greatest innovation of Sankey-Niklewski [177]. Addionally, an alternative method implemented in Fireball is employed to establish a single numerical basis set by creating a linear combination of two primitive numerical atomic orbitals. These orbitals correspond to the ground states of the neutral atom and the 2+ ion, respectively [181, 183]. This development refines greatly the accuracy of the Fireball. Finally, all the electronic interactions involving the system's atoms are calculated beforehand and placed in data tables for use during the DFT calculations.

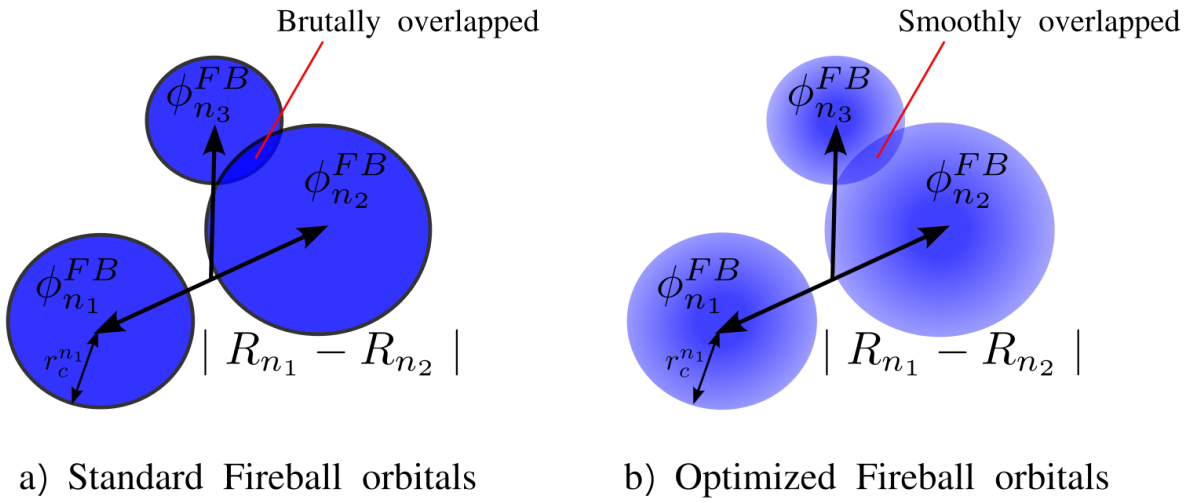

Figure 1.7 – Schema depiciting the difference between a, standard Fireball orbitals and **b,** optimized minimal Fireball orbitals.

Exchange–correlation interactions

In Fireball, the McWEDA method [184] is used for evaluating exchange-correlation interactions, in which the nonlinear-in-$n(\mathbf{r})$ exchange-correlation matrix elements can be approximated in terms of matrix elements of $n(\mathbf{r})$. In this way, each on-site exchange-correlation matrix element corresponds to a one-center contribution plus a correction, thanks to the Horsfield approximation [185]. Also, each off-site exchange-correlation matrix element corresponds to a two-center main contribution, with a correction using the generalized Sankey-Niklewski (GSN) approximation [177]. In the end, only one-, two-, and three-center integrals are calculated and tabulated beforehand. Finally, in this thesis, the approximation used for the exchange-correlation functional in the Fireball code is very similar to Local-Density approximations (LDA).

Self-consistency scheme

One of the most critical improvements in Fireball compared to Sankey and Niklewski [177] is the possibility of solving self-consistently. First, in Fireball, the input density to be evaluated is a sum of confined spherical atomic-like densities [179, 181]:

$$n_{in} = \sum_o f_o^{in} \sum_{i,I} \left|\phi_i^{FB}(\mathbf{r} - \mathbf{R_I})\right|^2. \tag{1.56}$$

The main point is that the occupation number is considered a self-consistent parameter in Fireball instead of the charge density as in the standard Kohn-Sham method: $E[n_{in}] = E[f_o^{in}]$. The convergence is reached once $f_o^{out} = f_o^{in}$, and f_o^{out} is calculated by projecting the output electron density (1.45) obtained by the Kohn-Sham equations (1.46) into a density of the form given by the Eq. (1.56):

$$f_o^{out} = 2\sum_j \left|\langle \varphi_j^{FB} | \phi_o^{LD} \rangle\right|^2 \tag{1.57}$$

where ϕ_i^{LD} are the atomic-like orthogonal orbitals of Lowdin: $\phi_i^{LD} = \sum_k (S_{ik}^{-\frac{1}{2}})\phi_k^{FB}$. Since the optimized minimal basis set is not orthogonal, it is better to work in the Löwdin orthogonal basis set, in which the Hamiltonian is significantly more simplified. For each iteration, the total energy is recalculated by using Harris-Foulkes functional (1.55) with the updated electron density (1.56). Diagonalization requires looking up the necessary information from the already prepared data tables; only a few integrals need to be recalculated for each iteration because of the change in electronic density, which speeds up the calculations. Once the convergence is reached, the eigenvalues ϵ_i^{FB} and eigenvectors φ_i^{FB} are achieved.

1.4.6 Band gap problem

According to the principle of PES experiment discussed in 1.1, the definition of the experimental photoemission fundamental band gap is:

$$E_g^{fund} = I^N - A^N \tag{1.58}$$

where the ionization energy is the lowest energy for removing an electron: $I^N = E_{N-1,0} - E_{N,0}$; whereas the electron affinity is the lowest energy possible for adding an electron: $A^N = E_{N,0} - E_{N+1,0}$. In these relations, $E_{N,0}$ stands for the ground state energy of the neutral system with N electrons; the other terms can be defined similarly. We emphasize that all the involved states above are ground states of its system, *i.e.* the system should be relaxed after losing or adding the electron, even including interactions. Since KS-DFT does not respect the Koopmans' theorem, the KS eigenvalues do not have physical meaning,

except to the highest occupied energy ϵ_N, which is equal to the ionization energy I^N in KS-DFT [186]. This latter stems from the fact that I^N governs the asymptotic form of density in vacuum, which is well respected in KS-DFT. On the other hand, the electron affinity A^N is equal to the ionization energy of N+1 electron system, I^{N+1}. Thanks to the Eq. (1.58), the fundamental gap is now [187]:

$$E_g^{fund} = \epsilon_{N+1}^{N+1} - \epsilon_N^N = \epsilon_{N+1}^{N+1} - \epsilon_{N+1}^N + \epsilon_{N+1}^N - \epsilon_N^N = \Delta_{xc} + E_g^{KS} \tag{1.59}$$

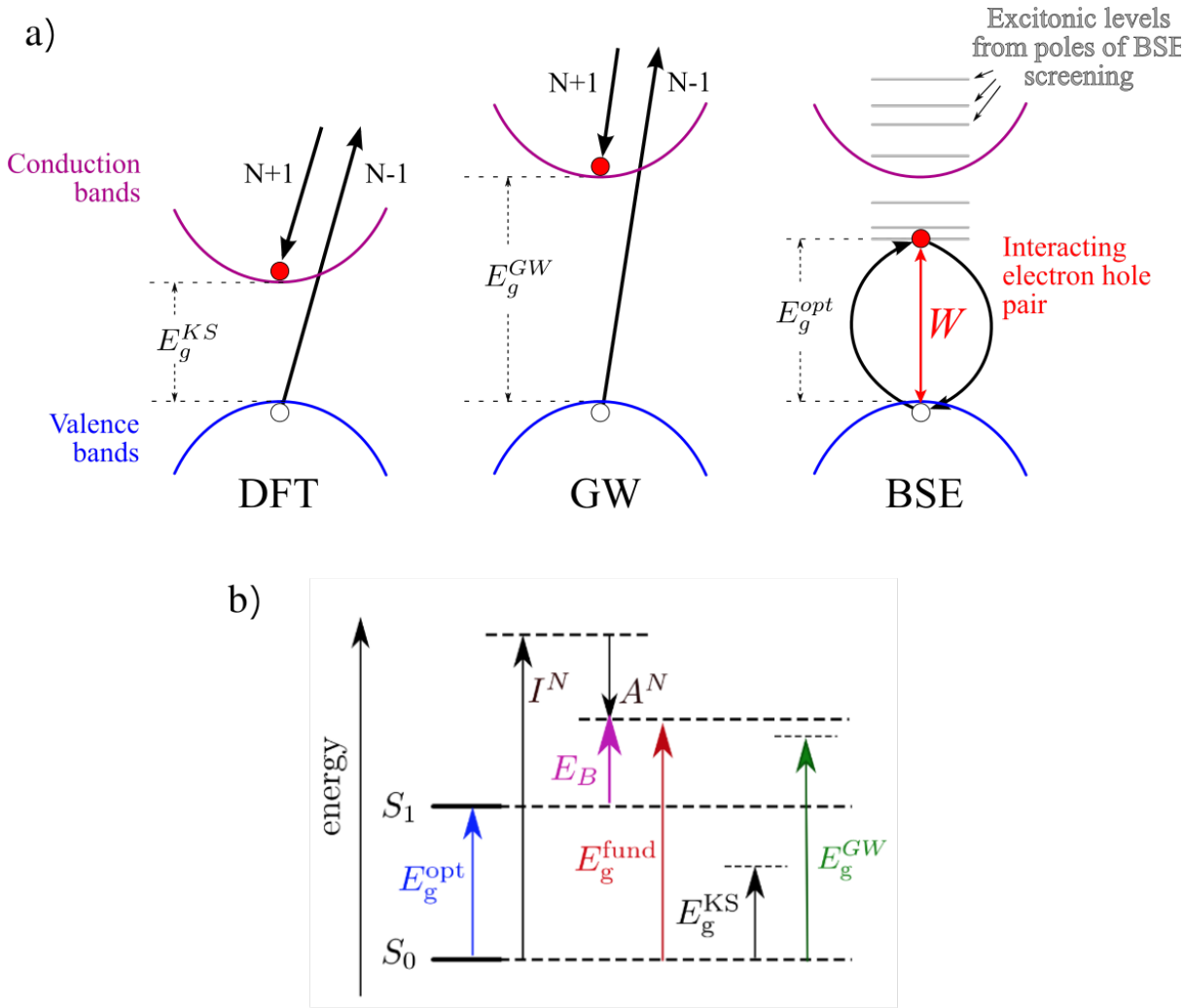

Figure 1.8 – Schema explaining the band gap problem in DFT. a, Definition of the KS, GW, and optical gaps. **b,** Schema showing the difference between these different band gaps [188]. E_B is the electron-hole binding energy, and accounts for the excitonic effect occurred in ABS. While I^N and A^N are the ionization potential and the electron affinity of the N-electrons system (obtained by PES and IPES). Due to the use of the inappropriate theory, the KS gap E_g^{KS} is too small compared to the experimental photoemission fundamental gap E_g^{fund}, which can be almost obtained by GW approximation (see later in 1.4.7). In the ABS experience, the excited electron stays in the system differed from the PES experience, E_g^{fund} is reduced by E_B caused by excitonic effects resulting in optical gap E_g^{opt} (see later in 1.4.8).

where Δ_{xc} is the change exchange-correlation potential when adding one electron, and it varies as a finite constant value so that $\Delta_{xc} = V_{xc}^{N+1}(\mathbf{r}) - V_{xc}^{N}(\mathbf{r}) + \mathcal{O}(1/N)$. This change potential is because V_{xc} with respect to the density n is non-local functional, so the addition electron induces a density variation that influences V_{xc}. It is the so-called band gap problem in DFT [189, 190].

The Eq. (1.59) shows that DFT generally provides a smaller band gap than E_g^{fund} measured by PES and IPES, even if we go up to the highest approximation of the exchange-correlation in Jacob's ladder of DFT. Also, the Kohn-Sham eigenvalues are not excitation energies; they can only be used to probe the ground state properties. It is well-known that Green's function formalism enables the simulation of PES and IPES; in practice, it is called GW approximation, and using this formalism can provide a very accurate band gap to E_g^{fund}. This method will be developed in Sec. 1.4.7. In ABS, an electron is removed from an occupied band to an unoccupied band; an electron-hole pair is created, and the interaction of the electron-hole pair leads to excitonic effects. By attraction, the optical band gap becomes smaller than the fundamental one; this can be simulated by Beth-Salpether equations (BSE) discussed in Sec. 1.4.8.

1.4.7 GW beyond KS-DFT

In this part, we will first briefly introduce the Green's function formalism. We will show why this formalism allows access to the same fundamental band gap measured in the PES experiment. Then, the difference between the green function formalism and DFT will also be discussed. In the second time, we will show how to correct KS eigenvalues using GW approximation developed in Yambo open source.

One-particle Green's function

First, we define the time-ordered one-particle Green's function at zero temperature [191]:

$$G(1,2) = -i \left\langle \Psi_0^N \middle| T\left[\hat{c}(1)\hat{c}^\dagger(2)\right] \middle| \Psi_0^N \right\rangle \tag{1.60}$$

where Ψ_0^N is the exact interacting ground state; $\hat{c}(i), \hat{c}^\dagger(i)$ are annihilation and creation field operators, the number i stands for $(\mathbf{x}_i, t_i)$. From now, we will use shorthand notion: $\langle ... \rangle = \left\langle \Psi_0^N \middle| ... \middle| \Psi_0^N \right\rangle$. Besides, the time ordering operator orders the product of fermionic operators with a greater time argument in the right and adds a sign -1 once the exchange of two operators. The time ordering operator forces the Green's function to be causal in time as [191]:

$$G(1,2) = -i\theta(t_1 - t_2) \left\langle \hat{c}(1)\hat{c}^\dagger(2) \right\rangle + i\theta(t_2 - t_1) \left\langle \hat{c}^\dagger(2)\hat{c}(1) \right\rangle \tag{1.61}$$

where $\theta(t_i - t_j)$ is the Heaviside function. In this relation, for $t_2 > t_1$ (right part), G describes the propagation of an extra hole from $\mathbf{r}_1$ at t_1 to $\mathbf{r}_2$ at t_2, which simulates IPES. While for $t_1 > t_2$ (left part), G describes the propagation of an extra electron from $\mathbf{r}_2$ at t_2 to $\mathbf{r}_1$ at t_1, which simulates PES. Moreover, the full interacting Green's function (1.60) can be expressed in the Lehmann representation [192] in frequency space [191, 193]:

$$G(\mathbf{r_1}, \mathbf{r_2}, \omega) = \sum_n \frac{\varphi_n^{QP}(\mathbf{r_1})\varphi_n^{QP*}(\mathbf{r_2})}{\omega - \epsilon_n^{QP} + i\eta \text{sign}(\epsilon_n^{QP} - E_F)} \tag{1.62}$$

where the excitation energies ϵ_n^{QP} are just introduced:

$$\epsilon_n^{QP} = \begin{cases} E_{N,0} - E_{N-1,n} & \text{if} \quad \epsilon_n^{QP} < E_F \\ E_{N+1,n} - E_{N,0} & \text{if} \quad \epsilon_n^{QP} > E_F \end{cases} \tag{1.63}$$

where electrons are occupied until the chemical potential level E_F. The Lehmann amplitudes ψ_n^{QP}, also called quasi-particle wave functions are defined:

$$\varphi_n^{QP}(\mathbf{r}) = \begin{cases} \left\langle \Psi_0^N \middle| \hat{c}^\dagger(\mathbf{r}) \middle| \Psi_n^{N-1} \right\rangle & \text{if} \quad \epsilon_n^{QP} < E_F \\ \left\langle \Psi_0^N \middle| \hat{c}(\mathbf{r}) \middle| \Psi_n^{N+1} \right\rangle & \text{if} \quad \epsilon_n^{QP} > E_F \end{cases} \tag{1.64}$$

It is shown that they are not orthogonal. On the other hand, G has poles at the electron removal and addition excitation energies ϵ_n^{QP}. In the non-interacting picture, the many-body states $\left|\Psi_0^N\right\rangle$ are Slater determinants, and the non-interacting (or Hartree) Green's function is:

$$G_0(\mathbf{r_1}, \mathbf{r_2}, \omega) = G_H(\mathbf{r_1}, \mathbf{r_2}, \omega) = \sum_n \frac{\varphi_n^H(\mathbf{r_1})\varphi_n^{H*}(\mathbf{r_2})}{\omega - \epsilon_n^H + i\eta \text{sign}(\epsilon_n^H - E_F)} \tag{1.65}$$

where φ_n^H and ϵ_n^H are the non-interacting orthogonal states and energies obtained after a diagonalization of Hartree potential H_H (see later in the following section).

Equation of motion and quasi-particle equation.

In the many-body perturbation theory (MBPT), to study excited states, we focus on the equation of motion of purely one-particle Green's function as below [191, 193, 194]:

$$\left[[\omega - H_H(1)]\, \delta(1,3) - \int d3\Sigma(1,3) \right] G(3,2) = \delta(1,2) \tag{1.66}$$

where $H_H = -\frac{1}{2}\boldsymbol{\nabla}^2 + v_{ext} + v_H$, and v_H is Hartree potential. All the unknown terms are pushed into a single term Σ, called the *self-energy*. Moreover, if the self-energy is turned off ($\Sigma = 0$), the Hamiltonian becomes the Hartree's Hamiltonian, and the system is now in the non-interacting picture. The zeroth order (or non-interacting) Green's function (1.65) is then the solution to the problem. By the way, it is possible to relate the fully interacting Green's function, G, to its non-interacting version, G_H, via the Dyson equation:

$$G(1,2) = G_H(1,2) + \int d34 G_H(1,3)\Sigma(3,4)G(4,2) \tag{1.67}$$

Since the fully-interacting Green's function G depends on the non-interacting one G_H, the self-energy Σ, and itself, G is an infinite sum and can be obtained by the self-consistent method. Additionally, G is the exact solution for the propagation of an electron in the interacting many-electrons system. Nevertheless, because of the differential form of the self-energy [191], the solution of (1.66) is challenging to calculate in practice.

On the other hand, Eq. (1.66) shows that the fully interacting function is the Green's function for the operator $[\omega - H_H(1)]\delta(1,3) - \int d3\Sigma(1,3)$. Thus, this means that it is possible to construct G from the eigenfunction of this operator by transforming it back to the time domain. The time-independent Schrödinger equation of this equation, called quasi-particle equation, is then obtained :

$$H_H(\mathbf{r_1})\psi_n^{QP}(\mathbf{r_1}) - \int d^3\mathbf{r_2}\Sigma(\mathbf{r_1},\mathbf{r_2},\epsilon_n^{QP})\varphi_n^{QP}(\mathbf{r_2}) = \epsilon_n^{QP}\varphi_n^{QP}(\mathbf{r_1}) \tag{1.68}$$

It is worth noting that we re-obtain the Kohn-Sham equation (1.46) if we substitute the self-energy by :

$$\Sigma(\mathbf{r_1},\mathbf{r_2},\epsilon_n^{QP}) = V_{xc}(\mathbf{r_1})\delta(\mathbf{r_1}-\mathbf{r_2}), \tag{1.69}$$

Therefore, the self-energy plays the same role as the exchange-correlation potential V_{xc} in the Kohn-Sham equation, Σ describes the response of the whole system to the propagation of a particle (hole in PES or electron in IPES). On the other hand, Σ is non-local, non-hermitian, energy-dependent, and contains all the differences between the quasi-particle and the non-interacting (or bare) particle. In the ground state, electrons interact via the bare Coulomb interaction, which is naturally long-range. In PES and IPES, in the presence of an additional hole or electron added in the system, the system's electrons polarize, leave their place, and surround the additional particle to interact with it. The additional particle and its surrounding electron cloud form a quasi-particle different from the rest of the system, which is unaffected. So, the interaction between the additional particle and its surrounding electron cloud should be weaker than the strongly bare Coulomb interaction, primarily described by the screened Coulomb interaction instead of the bare Coulomb interaction. The quasi-particles have a finite lifetime, so the

quasi-particle wave functions are not eigenstates of the KS equation.

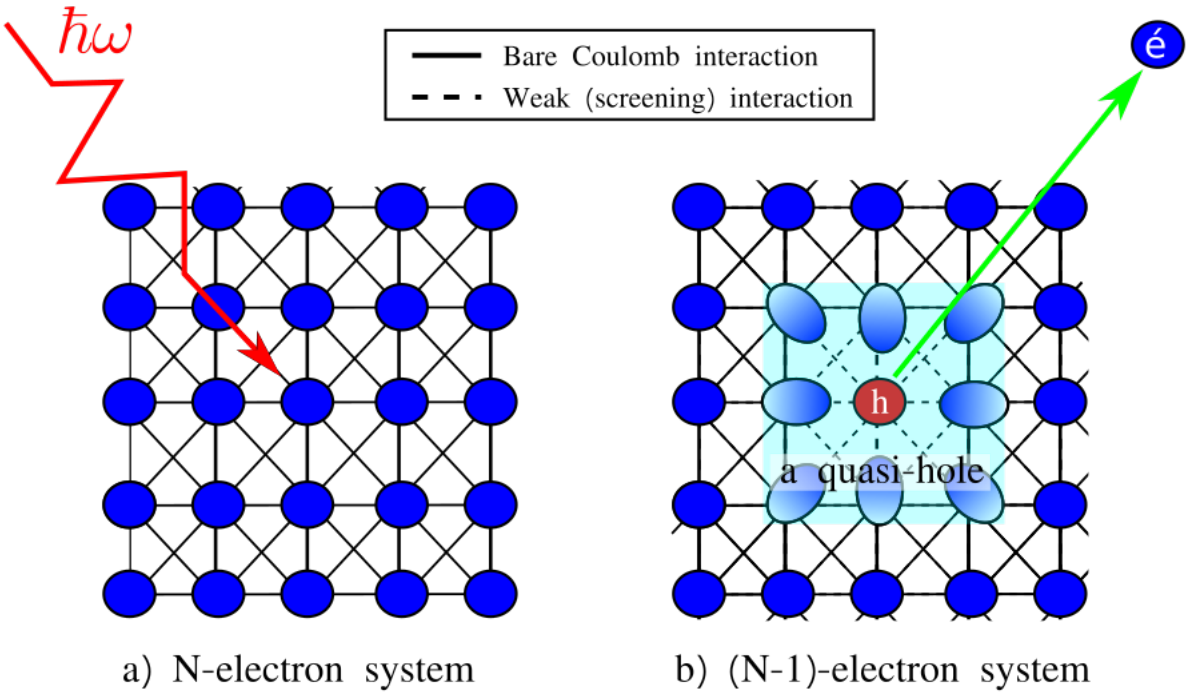

Figure 1.9 – Depiction of the quasiparticle concept a, Before PES, the system contains N-interacting electrons which strongly interact together by the bare Coulomb interaction (continued lines). **b,** After PES, an electron is left, and a hole is just created in the system. Electrons around the new hole are polarized, slightly move away from their cores, then surround and weakly interact (dashed lines) with this hole. By the way, a quasi-hole is created, presented by turquoise zone. Electrons in other regions remains its

Spectrum function

If we assume that both $\hat{G}$ and $\hat{\Sigma}$ are diagonal, the spectrum function can be written as [191, 193]:

$$A_{nn}(\omega) = \frac{1}{\pi}|\mathrm{Im}(G_{nn}(\omega))| = \frac{1}{\pi}\frac{\mathrm{Im}(\Sigma_{nn})}{|\omega - \epsilon_n^H - \mathrm{Re}(\Sigma_{nn}(\omega))|^2 + |\mathrm{Im}(\Sigma_{nn}(\omega))|^2} \tag{1.70}$$

The main peak has shifted $\mathrm{Re}(\Sigma_{nn}(\omega))$ from ϵ_n^H to ϵ_n^{QP}, called quasi-particle peak:

$$\epsilon_n^{QP} = \epsilon_n^H + \mathrm{Re}(\Sigma_{nn}(\epsilon_n^{QP})) \tag{1.71}$$

Its width is given by $\mathrm{Im}(\Sigma_{nn}(\epsilon_n^{QP}))$, which corresponds to the inverse of the excitation lifetime. The farther the excitations go from the Fermi level, the larger the quasi-particle peak and the shorter the lifetime. For this reason, the hole added in a deep energy state can not stay long since the electrons of the upper level subsequently fall to the hole. A hole removed from the highest occupied energy level has an infinite lifetime, and the quasi-particle peak is sharpest as δ-peak. Also, compared to the non-interacting

spectrum function, the interacting spectrum one witnesses some additional peaks, called satellites or sidebands, due to second excitations.

GW approximation in practice

Understanding the vital role of screened interaction, Hedin has used an infinitesimal external perturbation potential to "poke" electrons in the system; the electrons will react by rearranging their density and reaching a new equilibrium in response to the external potential. This external potential is set to 0 at the end of derivation. Hedin has derived a series of equations, which can be self-consistently solved, and order-by-order, the system's screening is described correctly. A good starting point is $\Sigma = 0$ at the top of Hedin's pentagon, and the solving order is presented in Fig. (1.10a). However, the full self-consistency of Hedin's equations is still beyond the computational abilities and resources available nowadays. So, a single iteration of Hedin's equations is usually done with neglecting vertex function, which is like a short-circuit of Hedin's pentagon (see Fig. (1.10b)), called GW approximations (GWA). This method is nothing else than obtaining these equations in the non-interacting picture. For this reason, the resulting quasiparticle energies have not been excellent compared to experiments.

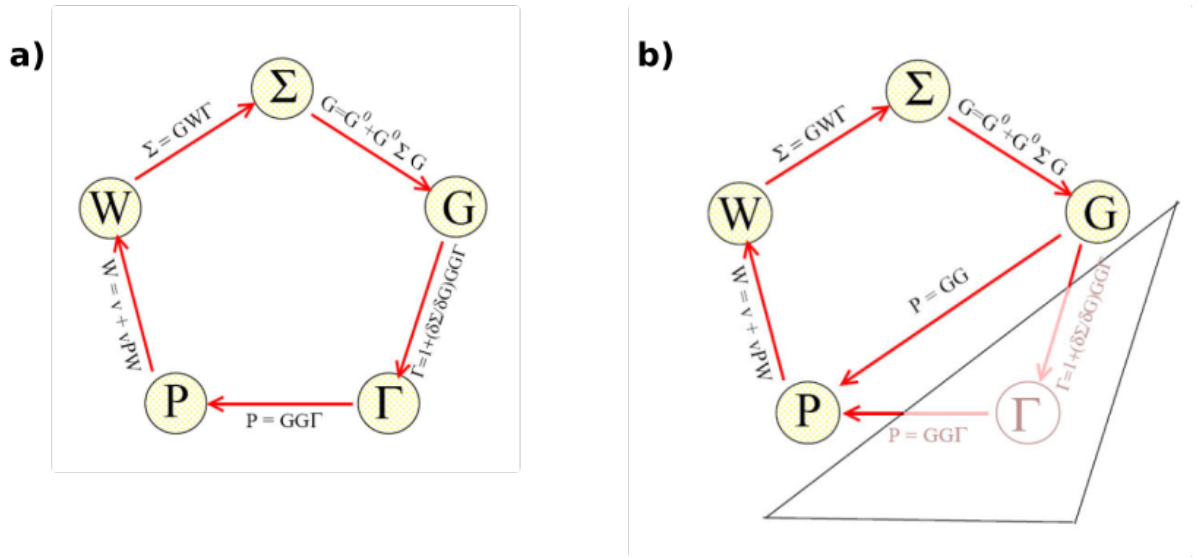

Figure 1.10 – Graphical represention of a, Hedin's pentagon. **b,** a short-circuit of Hedin's pentagon (GWA).

Moreover, the KS eigenvalues and eigenvectors were shown to be closer to the fully self-consistent Green's function than the Hartree ones. The GWA was tried using the KS eigenstates to construct the zeroth order Green's function, and the quasiparticle energies were in excellent agreement with the experiments. In this part, we are showing the main principle of GWA on KS-DFT. We understand that KS Green's function now replaces Hartree Green's function. The independent-particle KS polarizability

χ_{KS} (called Random Phase approximation (RPA) polarizability) is first calculated:

$$\chi_{KS}(1,2) = -iG_{KS}(1,2)G_{KS}(2,1^+), \tag{1.72}$$

Secondly, thanks to the bare Coulomb potential v and KS polarizability χ_{KS}, the independent-particle screening W_{KS} is obtained:

$$W_{KS}(12) = v(1,2) + \int d34 W_{KS}(1,3)\chi_{KS}(3,4)v(4,2), \tag{1.73}$$

Finally, the KS self-energy $\Sigma_{KS}(1,2)$ is achieved by employing KS screening W_{KS} and KS Green's function:

$$\Sigma_{KS}(1,2) = iW_{KS}(1^+,2)G_{KS}(1,2), \tag{1.74}$$

On the other hand, the overlap between LDA and GW wavefunctions has been claimed to be larger than 99.9 $\%$ in simple semiconductors [195], even though more recent calculations have shown that this is not always the case [196]. In the next step, we assume that the KS eigenstates $\varphi^{KS}_{n\mathbf{k}}$ are approximated to the quasi-particle ones $\varphi^{QP}_{n\mathbf{k}}$: $\varphi^{KS}_{n\mathbf{k}} \approx \varphi^{QP}_{n\mathbf{k}}$. If the quasi-particle corrections are assumed to be small, in first order in $\Sigma(\epsilon^{QP}_{n\mathbf{k}})$, the quasi-particle corrections to the Kohn-Sham DFT single-particle energies $\epsilon^{KS}_{n\mathbf{k}}$ is [191, 193, 194]:

$$\epsilon^{QP}_{n\mathbf{k}} - \epsilon^{KS}_{n\mathbf{k}} = Z_{n\mathbf{k}} \left\langle \varphi^{KS}_{n\mathbf{k}} \middle| \Sigma(\epsilon_{n\mathbf{k}}) - V_{xc} \middle| \varphi^{KS}_{n\mathbf{k}} \right\rangle \tag{1.75}$$

where $Z_{n\mathbf{k}}$ is the renormalization factor:

$$Z_{n\mathbf{k}} = \left(1 - \left\langle \frac{\partial \Sigma_{n\mathbf{k}}(\omega)}{\partial \omega} \bigg|_{\omega=\epsilon^{KS}_{n\mathbf{k}}} \right\rangle \right)^{-1} \tag{1.76}$$

This approximation enables us to estimate the quasiparticle correction by calculating $\Sigma(\epsilon^{KS}_{n\mathbf{k}})$ and its derivative at that point. The $Z_{n\mathbf{k}}$ ensures energy conservation when additional excitations are encountered after one-particle excitations that create some satellite peaks in the spectrum function; the renormalization factor moves the intensity of the quasiparticle peaks to the satellite ones. The more important is $Z_{n\mathbf{k}}$, the more significant the satellites are concerning the quasiparticle peaks.

1.4.8 BSE beyond GWA and KS-DFT.

Two particle Green's function.

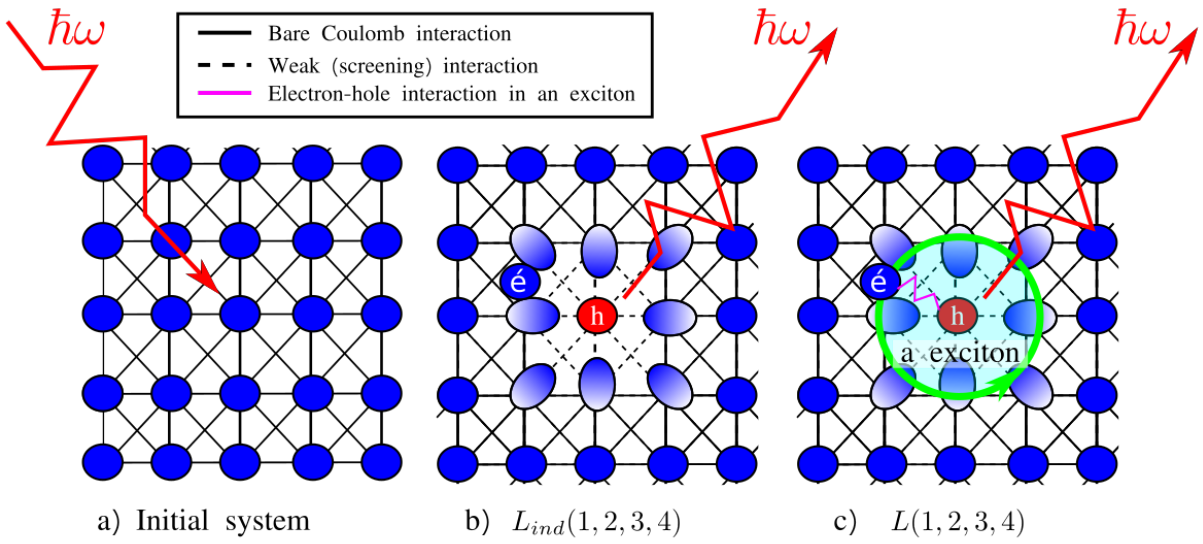

Figure 1.11 – Graphical represention of the absorption phenomena. a, The initial system before absorbing an photon. After absorbing the photon, an electron moves to the conduction band, then it is surrounded by conduction holes to create an quasi-electron. Simultaneously, a hole is created in the valence band, and forms a quasi-hole. **b,** In L_{ind} approach, the quasi-electron and quasi-hole created do not know each other. **c,** In reality, they should interact together and form an exciton. The latter exhibits by L.

In absorption spectra, we deal with neutral excitations due to the creation of a quasi-hole and a quasi-electron, which is different from photoemission, where the monoelectronic vision prevails. Thus, it is necessary to calculate the two-particle Green's function G_2 in this case. The two-particle Green's function can be expressed in this form:

$$G_2(1,2,3,4) = -\left\langle T\left[\hat{c}(1)\hat{c}(3)\hat{c}^\dagger(4)\hat{c}^\dagger(2)\right]\right\rangle \tag{1.77}$$

Now, let us introduce a 4-point reducible polarizability L [191]:

$$L(1,2,3,4) = -i\frac{\delta G(1,2)}{\delta U_{ext}(3,4)} = L_{ind}(1,2,3,4) - G_2(1,2,3,4) \tag{1.78}$$

where the 4-point non-interacting electron-hole polarizability L_0:

$$L_{ind}(1,2,3,4) = iG(1,2)G(3,4) \tag{1.79}$$

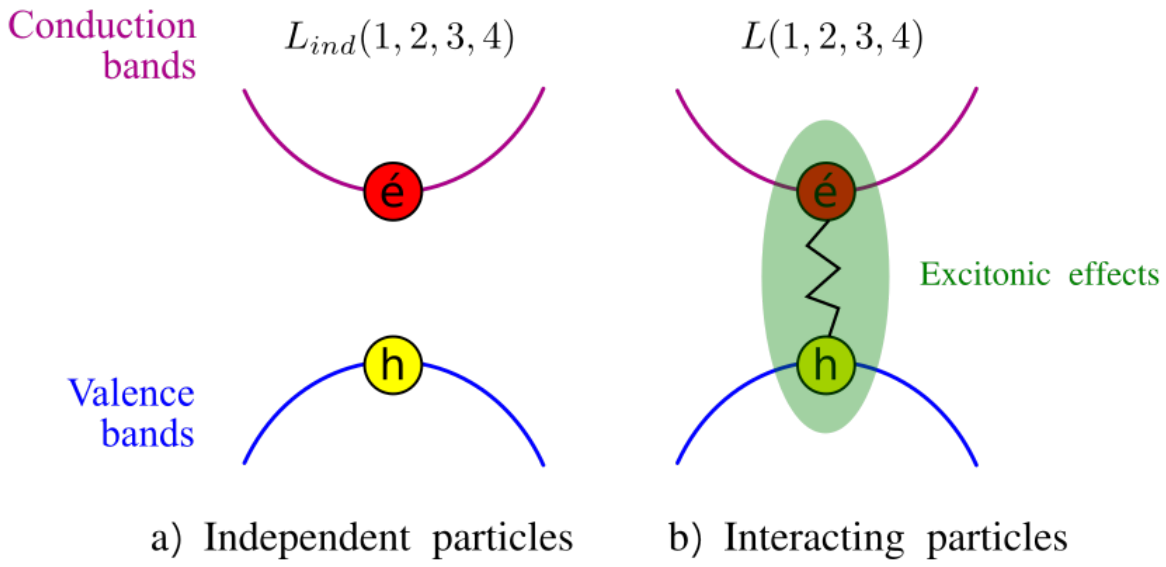

Figure 1.12 – Graphical represention of a, non-interacting electron-hole polarizability L_{ind}. **b,** interacting electron-hole polarizability L.

Bethe-Salpeter equation.

In order to calculate G_2, it is more advantageous to express L as a Dyson-like equation by doing similar works for obtaining Hedin's equations. The Dyson-like equation of a 4-point polarizability L is called *Bethe-Salpeter equation (BSE)* [191]:

$$L(1,2,3,4) = L_{ind}(1,2,3,4) + \int d5678 L_{ind}(1,2,3,4)\left[v(5,7)\delta(5,6)\delta(7,8) + \Xi(5,6,7,8)\right] L(7,8,3,4) \tag{1.80}$$

where 4-point many-body interaction kernel is defined:

$$\Xi(5,6,7,8) = i\frac{\delta\Sigma(5,6)}{\delta G(7,8)} \tag{1.81}$$

In practice, to avoid the divergence of v at $\mathbf{G}_m = 0$ in absorption simulation, modified polarizability $\bar{L}$ is alternatively used and obtained by the modified Coulomb potential $\bar{v}$ so that $v = v_{\mathbf{G}_m=0} + \bar{v}$ [191]. In this case, $\bar{v}$ is responsible for the local effects. Hence, the BSE shows that the first response of the system to the external perturbation is the creation of two independent quasiparticles, a quasi-hole and a quasi-electron, that are expressed by L_{ind} (see Figs. (1.11b) and (1.12a)). After the absorption of the photon, contrary to PES and IPES, the electron still stays in the system, and it can strongly interact with the hole, giving rise to the creation of exciton (see Figs. (1.11c) and (1.12b)). On the other hand, only 2-point polarizability is required to describe the absorption spectra. Thus, we can contract the 4-point

reducible polarizability into the 2-point one [16], to finally calculate the macroscopic dielectric function [17].

GW-BSE in practice.

Although the 4-point polarizability functions depend on four-time variables or, in the absence of the external potential, on three-time differences, the BSE contains much more information than needed; the inversion procedure is costly. In the context of optical excitations, we restrict ourselves to simultaneous creation and simultaneous annihilation, and considering the translational invariance in time, only two of the four-time variables are independent [191]. Additionally, using the static self-energy[18] (1.74) obtained by the GWA to calculate the many-body interaction kernel Ξ[19] (1.81) under these above conditions enables the unique frequency-dependent function $L(\mathbf{x_1}, \mathbf{x_2}, \mathbf{x_3}, \mathbf{x_4}, \omega)$. We note that since G is obtained by GWA, thus $G = G_{KS}$ which are constructed from Kohn-Sham orbitals $\varphi^{QP}_{n\mathbf{k}} = \varphi^{KS}_{n\mathbf{k}}$ and quasi-particle energies $\epsilon^{QP}_{n\mathbf{k}}$. Further, the BSE can be solved by diagonalizing a two-particle excitonic Hamiltonian in the transition basis, which provides information about the excitonic eigenvectors and eigenvalues [200].

In transition space, constituted by couples of quasiparticle wave-functions $\varphi^{QP}_{n_i}\varphi^{QP}_{n_j}$, the BSE (1.80) can be expressed as[20] $L^{n_1n_2,n_3n_4}(\omega) = 2\left[\hat{\mathbf{H}}_{2p} - \mathbb{1}\omega\right]^{-1}_{n_1n_2,n_3n_4}(f_{n_3} - f_{n_4})$, where n_i include the band and wave-vector indexes, the factor 2 is due to spin degeneracy, and f_{n_i} is the occupation number of the state i. Since the two-particle excitonic Hamiltonian H_{2p} contains more information than needed, we are interested only in the first block associated with paired states of type $\left|\varphi^{QP}_{m\mathbf{k}}\varphi^{QP*}_{\mu\mathbf{k}}\right\rangle$ ($m \in$ VB, $\mu \in$ CB), that contributes to the optical spectrum, called excitation of two-particle Hamiltonian $\hat{H}_{exc}$[21] [191]:

$$\hat{\mathbf{H}}^{n_1n_2,n_3n_4}_{2p,exc} = (\varepsilon^{QP}_{n_2} - \varepsilon^{QP}_{n_1})\delta n_1, n_3\delta n_2, n_4 + (f_{n_1} - f_{n_2})(2\bar{v}^{n_1n_2,n_3n_4} - W^{n_1n_2,n_3n_4}) \tag{1.82}$$

where the modified bare Coulomb $\bar{v}$ called un-screened *electron-hole exchange* term is repulsive and controls details of the excitation spectrum, the splitting between spin-singlet and spin-triplet excitations

[16] The 4-point reducible polarizability can be contracted into the 2-point one via $L(1, 1^+, 2, 2^+) = \chi(1, 2)$.

[17] The macroscopic of dielectric function can be obtained as [191]:

$$\epsilon^M(\omega) = 1 - \lim_{\mathbf{q}\to 0}\left[v_{\mathbf{G}_m=0}(\mathbf{q})\int d\mathbf{r}d\mathbf{r}' e^{-i\mathbf{q}(\mathbf{r}-\mathbf{r}')}\bar{L}(\mathbf{r}, \mathbf{r}, \mathbf{r}', \mathbf{r}', \omega)\right]$$

[18] The static self-energy is calculated by using a statically screened instantaneous interaction $W(\mathbf{r_1}, \mathbf{r_2}, t_1 - t_2) = W(\mathbf{r_1}, \mathbf{r_2})\delta(t_1 - t_2)$. This is usually considered as a good approximation for simple semiconductors because dynamical effects in the electron-hole screening W and in the Green's function G tend to cancel [197, 198].

[19] Using GWA, the many-body interaction kernel Ξ (1.81) is [191]:

$$\Xi(5, 6, 7, 8) = i\frac{\delta\Sigma(5, 6)}{\delta G(7, 8)} = -\frac{\delta[G(5, 6)W(5, 6)]}{\delta G(7, 8)} = -W(5, 6)\delta(5, 7)\delta(6, 8) - G(5, 6)\frac{\delta W(5, 6)}{\delta G(7, 8)}$$

Additionally, the latter describing the screening variation due to excitation is neglected. However, the correlation functions are no longer preserving [199].

[20] In transition space, $L^{n_1n_2,n_3n_4}(\mathbf{r_1}, \mathbf{r_2}, \mathbf{r_3}, \mathbf{r_4}, \omega) = \left\langle\varphi^{QP*}_{n_1}(\mathbf{r_1})\varphi^{QP}_{n_2}(\mathbf{r_2})\middle|L(\mathbf{r_1}, \mathbf{r_2}, \mathbf{r_3}, \mathbf{r_4}, \omega)\middle|\varphi^{QP*}_{n_3}(\mathbf{r_3})\varphi^{QP}_{n_4}(\mathbf{r_4})\right\rangle$

[21] The excitation part of two-particle excitonic Hamiltonian H_{2p} contains the on-diagonal blocks called anti-resonant and resonant, which involve negative and positive frequency transitions. While the off-diagonal blocks mix positive and negative ones, they are called coupling parts.

[201]... The screening term W, called *direct electron-hole* interaction term, stems from the variation of an exchange-correlation potential. This term is attractive and responsible for the attractive nature of the electron-hole interaction and the formation of bound electron-hole states, *i.e.*, excitons [201]. If $\hat{H}_{2p,exc}$ uses the quasiparticle eigenvalues ϵ^{QP} and includes the direct interaction term W, the calculation is called GW-BSE. If the latter is excluded, the Random phase approximation (RPA) is used, so the calculation is called GW-RPA if using quasiparticles eigenvalues ϵ^{QP}, and simply called RPA if using KS eigenvalues ϵ^{KS}. Finally, if both electron-hole exchange and direct interaction terms are not used, and the calculation considers KS eigenvalues ϵ^{KS}, thus it is called IP-RPA.

In this thesis, for all our calculations, we will moreover use the Tamm-Dancoff approximation which considers only the diagonal blocks involving negative and positive frequency transitions and neglecting the off-diagonal coupling blocks mixed positive and negative ones. Now, the problem is to solve the Schrödinger equation of two-particle excitonic Hamiltonian [191]:

$$\sum_{n_3,n_4} \hat{\mathbf{H}}_{2p}^{n_1n_2,n_3n_4} A_\lambda^{n_3n_4} = E_\lambda^{2p} A_\lambda^{n_1n_2} \tag{1.83}$$

After diagonalization, the excitonic eigenvalues, eigenstates E_λ and A_λ are employed to calculate $\bar{L}$. Afterward, the 4-point function $\bar{L}$[22] is then contracted into a 2-point one to calculate the dielectric function. The imaginary of macroscopic dielectric function ε_2^M in BSE is finally achieved [191]:

$$\varepsilon_2^M(\omega) = \lim_{\mathbf{q}\to 0} \frac{8\pi}{\mathbf{q}^2} \sum_\lambda \left| \sum_m^{\text{(occ)}} \sum_\mu^{\text{(unocc)}} \sum_{\mathbf{k}}^{\text{1BZ}} A_\lambda^{m\mu\mathbf{k}} \left\langle \varphi_{m\mathbf{k}}^{QP} \middle| e^{-i\mathbf{qr}} \middle| \varphi_{\mu\mathbf{k}}^{QP} \right\rangle \right|^2 \delta(\omega - E_\lambda^{2p}) \tag{1.84}$$

Comparing to the absorption spectra using Fermi's golden rule (1.28), for instance, from the quasiparticle eigenvalues and eigenvectors, the transition energy is now E_λ^{2p} instead of $(\epsilon_{\mu\mathbf{k}}^{QP} - \epsilon_{m\mathbf{k}}^{QP})$. Additionally, thanks to the exciton wave-functions $A_\lambda^{m\mu\mathbf{k}}$, the combination of independent-particle transition $\left\langle \varphi_{m\mathbf{k}}^{QP} \middle| e^{-i\mathbf{qr}} \middle| \varphi_{\mu\mathbf{k}}^{QP} \right\rangle$ is employed instead of just single independent-particle transitions.

1.4.9 STM on Fireball-DFT

Contrary to the ABS and EELS spectroscopies, in which we are interested in the refraction wave, in STM experiments, we are rather interested in the transmission wave. The STM uses a probe tip attached to a piezoelectric drive, which consists of x-, y-, and z-piezoelectric transducers as shown in Fig. (1.13). They expand or contract once a voltage is applied. One controls x-y piezoelectric transducers to scan

[22] Using E_λ and A_λ, L can be calculated as $L^{n_1n_2,n_3n_4}(\omega) = 2\sum_{\lambda,\lambda'} \frac{A_\lambda^{n_1n_2} S^{-1}_{\lambda,\lambda'} A_{\lambda'}^{n_3n_4 *}}{\omega - E_\lambda^{2p} + i\eta}(f_{n_4} - f_{n_3})$. In Tamm-Dancoff approximation $S^{-1}_{\lambda,\lambda'} = \mathbf{1}$

in the x-y plane, whereas the other transducer brings the tip and the sample within a few angstroms. Without an applied bias voltage $V_{bias} = 0$, the system is in equilibrium, the Fermi level of tip and sample is equal, and there is no current between tip and sample. Then, if and only if the tip is brought close enough to the sample in the vacuum region, the electron evanescent functions in the tip overlap electron evanescent functions in the sample surface. An electrical current, called the tunneling current, is thus created between the tip and the sample once $V_{bias} \neq 0$ is applied between those (see Fig. (1.13)). The system is now out of equilibrium. When $V_{bias} > 0$, the electrons in occupied states of the sample tunnel into the unoccupied states of the tip; in this case, the tunneling current contains the information of occupied states of the sample. When $V_{bias} < 0$, the electrons in occupied states of the tip tunnel into the unoccupied states of the sample, and the tunneling current contains the information of the unoccupied states of the sample. There are two imaging modes: constant height imaging ($z - cte$ mode) and constant current imaging ($I - cte$ mode). In $z - cte$ mode, the tip height is conserved as a constant during scanning; thus, we measure the locally changing current mapping. In $I - cte$ mode, the tunneling current is preserved as a constant, and scanning results in a sample topography mapping-dependent tip height. In spectroscopy mode, the tunneling current is measured as a function of voltage V_{bias}.

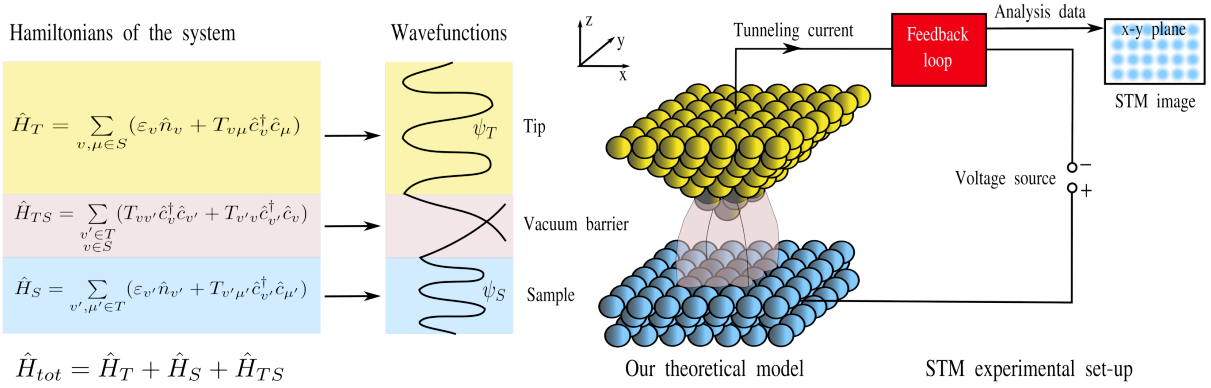

Figure 1.13 – Geometry of Hamiltonian in the local basis formalism. (Left part) Contributions of the total Hamiltonian of the whole system. (Center part) Schematic of wavefunctions in each region. (Right part) Schematic of a STM set-up where our theoretical model is presented in the left part of this panel. Darker atoms represent the active tip and sample sites. The tunneling current witnesses if and only if the tip is brought to close enough to the sample, then there is the overlapping between transmitted wave-functions from the tip, and the ones from the sample in barrier region.

Since then, there have been several theories with different levels of approximation; however, we can categorize them into two main approaches: perturbation and non-perturbation. The methods using perturbation theory have very high calculation speeds, such as Tersoff-Hamman (TH) [159], and Bardeen approaches [202]. In the TH approach, the tip contains only an $s-$orbital apex atom. It means that the electronic structure of the tip is completely disregarded. Consequently, this approach can be used in any DFT and TB codes via local density of states (LDOS) (see the Eq. (1.21)). This method frequently

provides a pretty good qualitative prediction of the experimental observations, for instance, a decoupled single pentacene with a pentacene tip [203], or our novel nanostructures based on graphene, shown later in Chapter 3. Nevertheless, several experiments show that tip effects can be vital in the STM images, such as a decoupled single pentacene with a CO-decorated tip [203]. In the same article, by taking into account the geometry of the tip, the Bardeen method can mimic successfully the STM measurement. Since the surface–tip interactions are considered very weak, the wave functions of the tip and sample are approximately orthogonal. Hence, the Bardeen approach has been limited to large bias voltages or short tip-sample distances. However, these limitations can be solved by using non-perturbation methods based on the Landrauer-Büttiker formula [204] with additional non-equilibrium Green's function formalism (NEGF) [205]. Unfortunately, this method requires costly computation resources; employing a local orbital basis set is necessary to reduce the computational cost. By using a local basis, the problem is reduced to an interaction region, including the vacuum region and the outermost atomic layers of the parts of the sample and tip subsystems. This region connects to a bath of the tip electrons on one side and a bath of the sample electrons on the other side. The following sections will discuss the details of this method developed on Fireball-DFT.

Non-equilibrium Green's functions.

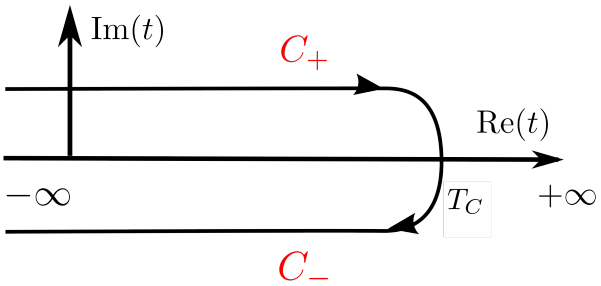

Figure 1.14 – Schema of the time-contour $\mathcal{C}$. It can be seen as comprised between two branches $\mathcal{C}_+$ and $\mathcal{C}_-$ for the case of zero temperature .

The out-of-equilibrium behavior in STM arises from the close proximity of the tip to the sample surface, where quantum mechanical tunneling phenomena dominate and classical equilibrium descriptions are not applicable. Consequently, the theoretical analysis of STM experiments is most suitably approached through the NEGF introduced by Keldysh [205]. In this part, the contour-ordered Green function is defined as:

$$G(1,2) = -i \left\langle T_C[\hat{c}(1)\hat{c}^\dagger(2)] \right\rangle \tag{1.85}$$

wherein C denotes the time-contour such that $t_1, t_2 \in C$; T_C is the time-ordering operator on the time-contour. The Eq. (1.85) comprises four real-time Green's functions: $G^<$, $G^>$, G^{++}, and G^{--} correspond-

ing to "lesser", "greater", time-ordered (or causal), and anti-time-ordered Green's functions, respectively:

$$G(1,2) = \begin{cases} G^{++}(1,2) = -i\left\langle T[\hat{c}(1)\hat{c}^{\dagger}(2)]\right\rangle, & t_1, t_2 \in C_+ \\ G^{--}(1,2) = -i\left\langle \tilde{T}[\hat{c}(1)\hat{c}^{\dagger}(2)]\right\rangle, & t_1, t_2 \in C_- \\ G^{<}(1,2) = i\left\langle \hat{c}^{\dagger}(2)\hat{c}(1)\right\rangle, & t_1 \in C_+, t_2 \in \mathcal{C}_- \\ G^{>}(1,2) = -i\left\langle \hat{c}(1)\hat{c}^{\dagger}(2)\right\rangle, & t_1 \in C_-, t_2 \in C_+ \end{cases} \tag{1.86}$$

where $\tilde{T}$ is the anti time-ordering operator. Here, we note that G^{++}[23] corresponds to the equilibrium one-particle Green's function (1.60) defined in 1.4.7. Additionally, one can define retarded and advanced Green's functions $G^{R/A}$ as:

$$\begin{aligned} G^{R} =& G^{++} - G^{<} = \theta(t_1 - t_2)\big(G^{>}(1,2) - G^{<}(1,2)\big) \\ G^{A} =& G^{--} - G^{>} = \theta(t_2 - t_1)\big(G^{<}(1,2) - G^{>}(1,2)\big) \end{aligned} \tag{1.87}$$

$G^{R/A}$ obeys a separate Dyson equation (1.67) involving a retarded (or advanced) self-energy $\Sigma^{R/A}$, and non-interacting Green's functions $G_0^{R/A}$. Since there is no separate Dyson equation for $G^{>/<}$, it remains coupled to $G^{R/A}$ as [205, 206]:

$$G^{>/<} = (1 + G^{R}\Sigma^{R})G_0^{>/<}(1 + G^{A}\Sigma^{A}) + G^{R}\Sigma^{>/<}G^{A} \tag{1.88}$$

Non-equilibrium Green's function formalism (NEGF)

In this part, the tip and sample are always in their respective thermal equilibrium, *i.e.*, injected hot electrons are instantly thermalized. The Hamiltonian of the whole system can be divided into three parts [207–211]:

$$\hat{H}_{tot} = \hat{H}_S + \hat{H}_T + \hat{H}_{TS}$$

In second quantization, the uncoupled tip and simple Hamiltonians are as follow [207]:

$$\hat{H}_S = \sum_{\nu \in S}(\epsilon_\nu \hat{n}_\nu + T_{\nu\mu}\hat{c}_\nu^{\dagger}\hat{c}_\mu) \tag{1.89}$$

$$\hat{H}_T = \sum_{\nu' \in T}(\epsilon_{\nu'} \hat{n}_{\nu'} + T_{\nu'\mu'}\hat{c}_{\nu'}^{\dagger}\hat{c}_{\mu'}) \tag{1.90}$$

where $\hat{n}_\nu = \hat{c}_\nu^{\dagger}\hat{c}_\nu$ ($\hat{n}_{\nu'}$, respectively) is the number of occupation operator of the sample (tip, respectively). The total number of electrons in the sample (the tip, respectively) is associated with the operator $\hat{N}_S = \sum_\nu \hat{n}_\nu$ ($\hat{N}_T$, respectively). The tip-sample coupling Hamiltonian between active atoms (shown in Fig.

[23] From Eqs. (1.60) and (1.86), G^{++} can be linked to $G^{<}$ and $G^{>}$ as: $G^{++}(1,2) = \theta(t_1 - t_2)G^{>}(1,2) + \theta(t_2 - t_1)G^{<}(1,2)$

(1.13)) in the interaction region, associated with the tunneling currents is [207–212]:

$$\hat{H}_{TS} = \sum_{\substack{\nu' \in T \\ \nu \in S}} \left(T_{\nu\nu'} \hat{c}^{\dagger}_{\nu} \hat{c}_{\nu'} + T_{\nu'\nu} \hat{c}^{\dagger}_{\nu'} \hat{c}_{\nu} \right) \tag{1.91}$$

where the tip-sample hopping elements are $T_{\nu\nu'} = \langle \varphi_{\nu} | \hat{H}_{tot} | \varphi_{\nu'} \rangle$ [24], and describes the transition probability from the ν-th basis function of the surface to the ν'-th basis function of the tip. The change of the number of electrons of the tip induces current flowing between the tip and the sample: $I_{tunnel}(t) = -\frac{\mathrm{d}}{\mathrm{d}t} \left\langle \hat{N}_T \right\rangle$ where $\hat{H}_S$ and $\hat{H}_T$ commute with $\hat{N}_T$, so we have [208–212]:

$$I_{tunnel} = -i \frac{\mathrm{d}}{\mathrm{d}t} \left\langle [\hat{H}_{tot}, \hat{N}_T] \right\rangle (t) = i \sum_{\substack{\nu' \in T \\ \nu \in S}} \left(T_{\nu'\nu} \left\langle \hat{c}^{\dagger}_{\nu'} \hat{c}_{\nu} \right\rangle - T_{\nu\nu'} \left\langle \hat{c}^{\dagger}_{\nu} \hat{c}_{\nu'} \right\rangle \right) \tag{1.92}$$

Thanks to Eq. (1.86), we can identify the non-equilibrium lesser Green's functions $G^{<}_{ij}$[25]. Now, we consider that after receiving (or losing) electrons from (or to) the tip, the system rapidly returns to a steady state (equilibrium). Hence, the Green's function only depends on the time difference $t_1 - t_2$. By the way, their Fourier transform depends only on ω : $G^{<}(t_1, t_1 + 0^+) = \frac{1}{2\pi} \int G^{<}(\omega) d\omega$. In matrix representation, Eq. (1.92) can be rewritten as [208, 209]:

$$I_{tunnel} = \frac{1}{\pi} \int_{-\infty}^{\infty} \mathrm{Tr} \left[T_{TS} G^{<}_{ST}(\omega) - T_{ST} G^{<}_{TS}(\omega) \right] \tag{1.93}$$

Then, $G^{<}_{ST/TS}$ can be obtained thanks to Eq. (1.88). Since the electron-electron and electron-phonon interactions are neglected, the perturbation is considered a single electron perturbation. Thus, in the tip-sample coupling matrix Σ, we have $\Sigma^{R/A}_{TT/SS} = 0$, $\Sigma^{R/A}_{TS} = T_{TS}$, $\Sigma^{R/A}_{ST} = T_{ST}$, and $\Sigma^{>/<} = 0$ [206, 209, 210, 212]. $G^{R/A}$ are the interacting retarded and advanced Green functions of the coupled systems obtained by employing $\Sigma^{R/A}$ and the non-interacting $G^{R/A}_0$ into the Dyson equation (1.67). On the other hand, the $G^{>/<}_0$ is the Green's functions of uncoupled system so that $G^{<}_{SS/TT,0}(\omega) = 2\pi i f_{S/T}(\omega) \rho_{SS/TT}(\omega)$, and $G^{<}_{TS/ST,0} = 0$ [209, 210, 212]. Now, the tunneling current (1.93) becomes [207, 209, 211]:

$$I_{tunnel} = 4\pi \int_{-\infty}^{\infty} d\omega [f_S(\omega) - f_T(\omega)] \mathrm{Tr} [T_{TS} \rho_{SS}(\omega) D^{R}_{SS}(\omega) T_{ST} \rho_{TT}(\omega) D^{A}_{TT}(\omega)] \tag{1.94}$$

[24] The tip-sample hopping elements $T_{\nu\nu'}$ is equal to the Bardeen's transition matrix element [202] with additionally the overlapping between the wave-functions of the uncoupled tip and sample [207]. The latter is set to zero in the Bardeen approach.

[25] In matrix form, G is represented in a basis set, such as the orbital basis, so it no longer depends on $\mathbf{r}$ or $\mathbf{r}'$. Instead, it depends on orbital indexes μ, μ'.

At $T = 0$ K and at a finite bias, the Eq. (1.94) becomes [213]:

$$I_{tunnel} = 4\pi \int_{E_F}^{E_F+V_{bias}} d\omega \mathrm{Tr}[T_{TS}\rho_{SS}(\omega)D^R_{SS}(\omega)T_{ST}\rho_{TT}(\omega - V_{bias})D^A_{TT}(\omega - V_{bias})] \tag{1.95}$$

In the presence of the Fermi-Dirac distribution functions, the Eq. (1.94) includes natural temperature effects. Due to the high Fermi temperatures typical for metals, we expect the temperature dependence to be small in the usual experimental conditions, which occur between 4 K and room temperature. It is then easily incorporated in this formalism through the first term of an expansion around T=0 K. Moreover, the Eq. (1.94) entails tracing the product of several matrices. Physically, this corresponds to a coherent superposition of various channels. Consequently, one can anticipate the emergence of intriguing interference effects under suitable conditions.

On the other hand, we note that, in Bardeen approach [202, 207], the tunneling current is in the lowest order perturbation theory, in which T_{ST} and T_{TS} are obtained by only a single scattering process [202]. The Keldysh-Green's function method allows us to go beyond the Bardeen approximation, in which the effective hopping matrixes T^{eff}_{ST} and T^{eff}_{TS} are used and take into account all the multiple scattering processes (see Fig. (1.15)) [207, 209, 214]:

$$\begin{aligned} T^{eff,R}_{TS} &= T_{TS}[\mathbb{1} - T_{ST}G^{R,0}_{TT}T_{TS}G^{R,0}_{SS}]^{-1} = T_{TS}[\mathbb{1} - X^R_{SS}]^{-1} = T_{TS}D^R_{SS} \\ T^{eff,A}_{ST} &= T_{ST}[\mathbb{1} - T_{TS}G^{A,0}_{SS}T_{ST}G^{A,0}_{TT}]^{-1} = T_{ST}[\mathbb{1} - X^A_{TT}]^{-1} = T_{ST}D^A_{TT} \end{aligned} \tag{1.96}$$

where we defined the denominators $D^{R/A}$ that take into account the multiple scattering effects via the summation up to infinite order of an expansion on the scattering matrixes, $X^{R/A}$ as expressed in Dyson-like equation form. These effects are responsible for the perturbation of the tunneling current found when the tip is brought close to the sample (typically inferior to 4.5 Å). At typical tunneling distances ranging between 5 and 7 Å, these matrices tend to approach the identity matrix, which simplifies the ultimate equation [213]. Thus, the Eq. (1.94)[26] can be written in this form below:

$$I_{tunnel} = 4\pi \int_{-\infty}^{\infty} d\omega [f_S(\omega) - f_T(\omega)]\mathrm{Tr}[T^{eff,R}_{TS}\rho_{SS}T^{eff,A}_{ST}\rho_{TT}] \tag{1.97}$$

This equation is not derived from a perturbation theory expansion limited to a specific order, hence maintaining its validity even at short distances, where multiple scattering effects are crucial, as previously detailed.

[26] In Bardeen approach, the tunneling current can be presented in the local basis, and matrix form as [207]:

$$I_{tunnel} = 4\pi \int_{-\infty}^{\infty} d\omega [f_S(\omega) - f_T(\omega)]\mathrm{Tr}[T_{TS}\rho_{SS}(\omega)T_{ST}\rho_{TT}(\omega)]$$

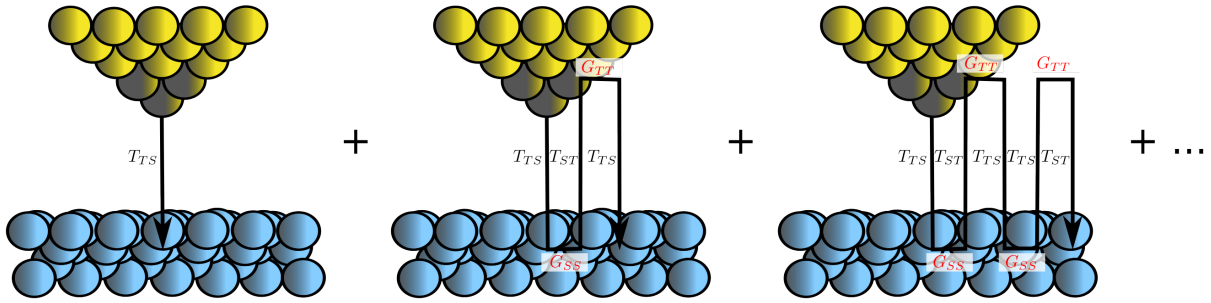

Figure 1.15 – Different order of perturbation theory on tunneling current. From lowest (left) to highest approximation (right).

Furthermore, thanks to the Eq. (1.94), the differential conductance is given by [207, 214]:

$$G_{conductance} = \frac{\partial I_{tunnel}}{\partial V} = 4\pi \mathrm{Tr}[T_{TS}\rho_{SS}(\omega)D^{R}_{SS}(\omega)T_{ST}\rho_{TT}(\omega)D^{A}_{TT}(\omega)] \tag{1.98}$$

NEGF in practice

Based on the Fireball-DFT code, the STM code developed by Cesar *et al.* [215] employs Eq. (1.95) to evaluate the tunneling current. This code does not consider the relaxation between the tip and the sample when the tip and the sample are very close. Since the usual tip-sample distance is around 5-7 Å in the experiment, this approximation is thus relevant. All the ingredients in the Eq. (1.95) can be calculated separately. Since we would like to study the novel low-dimensional graphene material on a metallic surface, both the tip and sample must be connected to an electronic reservoir if a steady state has to be reached. To do so, we consider the tip (sample, respectively) as a cluster of apex atoms (topmost layer atoms, respectively) connected with a bath of other electrons of the tip (sample, respectively), thus [208, 209, 211]:

$$G^{R/A}_{TT/SS,0}(\omega) = \frac{1}{(\omega \pm \eta)\mathbb{1} + \hat{H}^{KS}_{TT/SS,a} + \Sigma^{R/A}_{TT/SS,B}(\omega)} \tag{1.99}$$

where $\hat{H}^{KS}_{a}$ is the Kohn-Sham Hamiltonian matrix of the *active* part of the tip (sample, respectively) electrode (dark region in Fig. (1.13)) and Σ^{R}_{B} is a Bethe lattice self-energy describing the coupling to the semi-infinite periodic bulk (light region in Fig. (1.13)). This latter can be determined iteratively by the decimation technique [216]. The density of states of the uncoupled system can be determined as:

$$\rho_{TT/SS} = -iG^{R}_{TT/SS}(\omega) \tag{1.100}$$

Finally, the dimer approximation determines the hopping elements $T_{ST/TS}$. By the way, the calculated hoppings in this method account for the primary orthogonalization effects between the two respective

atoms, excluding contributions from the rest of the atoms in both the tip and the sample, such as orthogonalization and electrostatic potential effects. This approach has been shown to provide accurate representations of the distance-dependent corrugation behavior with quantitative variations in the estimated corrugation below 2.5% [207]. Additionally, compared to the ordinary Fireball DFT calculation shown in Section 1.4.5, the radius cutoff should increase and be chosen around 15 Å, approximately, to describe correctly the overlap of the tip and sample wave functions. For long distances, the parallel plane approximation will be fitted, using the expression $(A/z^{\alpha})e^{-\Phi_W \cdot z}$. First, the z is the distance between two atoms. The A is the independent value that has to be found in the fitting process. Moreover, the α depends on the orbitals we want to calculate their hopping, and $\alpha = 11 + 12 + 1$ is usually used. However, sometimes it could be changed in some specific conditions, especially when A takes a significant value compared with the $s - s$ case. Finally, the $\Phi_W = \sqrt{(\Phi_T + \Phi_S)/2}$ is the work function of the materials where $\Phi_{T/S}$ are the work function of the tip/sample atom, respectively. [207]. It is essential to highlight that there is no contradiction in employing distinct bases to compute various terms in the conductance. In a similar fashion mentioned in Section 1.4.5, all the necessary interactions are stored in databases. For each value of distance, the code reads these databases to interpolate and adjust various interactions to construct an atom–atom interaction matrix for all possible combinations between the tip's and sample's atoms until the complete matrix $T_{ST/TS}$ is built. All these approximations significantly improve the computation speed of STM calculation.

Applications

Chapter 2

Twisted hexagonal boron nitride bilayers

Before discussing the main applications of new graphene-derived materials, we will present our theoretical studies on the electronic and optical properties of new - close to 30 °- twisted hexagonal boron nitride structures (T-hBN) using the TB and DFT methods. This work can be divided into two steps: reaching TB's validated parameters for small structures and predicting the electronic and optical responses for large structures. In the first step, my collaborators, Dr. Lorenzo Sponza, Dr. Hakim Amara, and Ph.D. student Elisa Serrano Richaud at Laboratoire d'Etude des Microstructures (LEM) laboratory in Chatillon, Paris, have simulated the electronic band structures and absorption spectra of small twisted structures using Quantum Espresso [217, 218] and Yambo codes [174, 175]. At the same time, Dr. Sylvain Latil and I employed the TB method but went beyond the TB scheme for monolayers presented in 1.3 to do the same work. The comparison between the results calculated by these two methods allows us to determine the suitable fit parameters on the TB simulations in order to predict the large structures that ab initio methods may hardly calculate. This chapter will reveal a fascinating, identical bundle of flat conduction states on twisted hexagonal boron nitride bilayer structures.

2.1 Hexagonal boron nitride twisted bilayers (hBN-TBLs)

Van der Waals heterostructures can be formed by stacking 2D atomic layers, and might potentially induce a geometric moiré superlattice. This occurs due to lattice mismatch or a rotational twist between the layers [219]. The resulting pattern causes a modulation in the potential at the supercell scale, leading to alterations in the electronic band structure. This modulation often gives rise to low-dispersion

bands, contributing to the manifestation of distinctive electronic properties in the material, such as twisted bilayer graphene [220], twisted hexagonal boron nitride (hBN) [221–223] or hetero- and homobilayers of transition metal dichalcogenides (TMDs) [224]. The occupancy of these bands serves as a determining factor in the transitions between superconductive and insulating states, offering intriguing possibilities for investigating strong correlation effects in 2D systems [221, 225, 226]. Until now, the scientific community has primarily focused on the small twist angle limit [227, 228]. There were few works restricted to intermediate angles between 15° and 28° [229–231], and even fewer works around 30° [232–235]. But all of these early studies revolves around graphene bilayers. Regarding hBN, Chernozatonskii *et al.* [236] has very recently considered the 30° twisted bilayers. They have revealed that this BN material is a new wide-gap 2D quasicrystal. However, its electronic and optical properties have never been explicitly addressed. In this part, we will find out the characteristics of the band structure and optical response for twist angles in the vicinity of 30° for different stackings of twisted bilayer hBN (TBL-hBN) by employing the TB model and *ab initio* method. We will show that all these structures form a bundle of flat states just above the bottom of the conduction band. We also performed some analyses of the bundle states in view of determining their physical origin.

2.1.1 Tight-Binding model for bilayer structures

In order to study bilayer systems, we must go beyond the second-nearest-neighbor Tight-Binding model (2NN-TB) of monolayer structures discussed in 1.3. First, to better distinguish between intra- and inter-layer parameters, we propose to use additional labels for intralayer parameters "||". In contrast, interlayer parameters will be denoted "⊥". Each atom will have some extra neighbors from another layer in a bilayer system. To include the hopping energy between them, we will reconsider the formula below previously mentioned in the Tab. 1.2:

$$t_{AB} = l_x V_{pp\sigma}(D_{AB}) + (1 - l_x^2) V_{pp\pi}(D_{AB}) \tag{2.1}$$

where $l_x = \sin\phi = \frac{Z_{AB}}{D_{AB}}$ with ϕ, the angle between the first p_z orbital's plane and the axis of quantization (see Fig. (2.1)). The question is how to calculate the Slater and Koster parameters, $V_{pp\pi}$ and $V_{pp\sigma}$. Proposed by Trambly *et al.* [237], these integrals can be explicitly described like:

$$\begin{aligned} V_{pp\pi}(D_{AB}) &= -t^{||}_{AB} \exp\Big\{Q^{||}_{AB}(a_{||} - D_{AB})\Big\} F^{||}_c(D_{AB}) \\ V_{pp\sigma}(D_{AB}) &= \gamma^{\perp}_{AB} \exp\big\{Q^{\perp}_{AB}(a_{\perp} - D_{AB})\big\} F^{\perp}_c(D_{AB}) \end{aligned} \tag{2.2}$$

where $a_{||}$ is the lattice constant in monolayer structure defined in 1.3. $a_{\perp}$ is the interlayer distance, we set $a_{\perp} = 3.22$ Å for hBN-TBLs. $t^{||}$ is the intralayer hopping integral between the first nearest neighbors

defined in 1.3. The prefactor $\gamma_{AB}^{\perp}$ is the interlayer coupling between two p_z orbitals, and Q_{AB} is a semi-empirical decay value. These two parameters can be obtained by fitting with *ab initio* results. In the relation (2.2), to reduce the number of atoms involved in the Slater and Koster integrals, a smooth cutoff function $F_c(D_{AB})$ was introduced by imposing a fitted cutoff radius r_c and a unique cutoff constant $l_c = 0.265$ Å (see the Fig. (2.1)), as:

$$F_c(D_{AB}) = (1 + e^{(D_{AB} - r_c)/l_c})^{-1} \tag{2.3}$$

with

$$r_c = a + \frac{\ln 10^3}{Q_{AB}} \tag{2.4}$$

Finally, to speed up the simulations, in our Tight-Binding model for all twisted bilayer systems, for a given atom, the intralayer interactions are always estimated by the 2NN-TB model defined in 7, and we have only used the Eq. (2.1) to calculate the interlayer interactions.

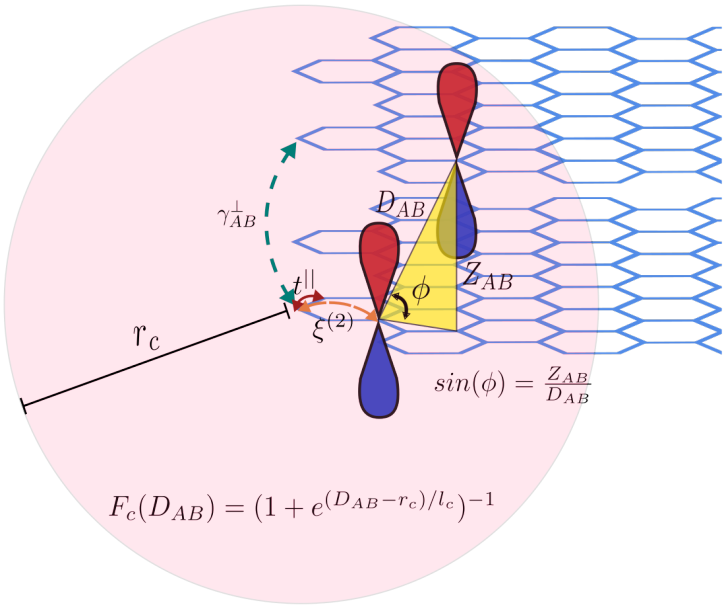

Figure 2.1 – Tight-Binding model for the interlayer hopping intergral t_{AB}. A bilayer structure is depicted in light blue. For a given atom, as shown in the Tab. 1.2, t_{AB} depends on $V_{pp\pi}$, $V_{pp\sigma}$, and an angle ϕ between the axis of quantization and the monolayer plan containing the atom. Proposed by Trambly *et al.* [237], $V_{pp\pi}$ and $V_{pp\sigma}$ can be calculated inside of the globe of a chosen radius cutoff r_c encompassing the given atom, by using the intralayer and interlayer parameters, respectively.

2.1.2 Structure definitions

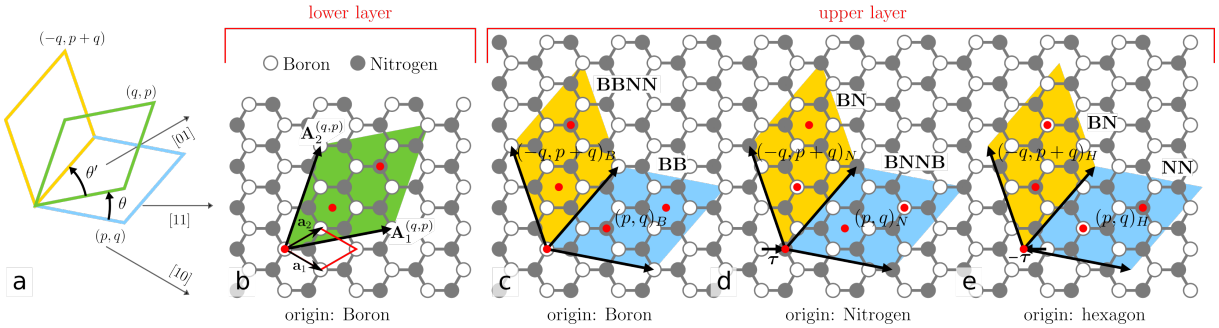

Figure 2.2 – Strategy to build the boron nitride twisted bilayers (TBL-hBNs) [238]. a, Graphical representation of θ and θ' angles according to the $\{p, q\}$ integers. **b,** The lower layer supercell is $(q, p)_B$. **c-e,** The supercells of the upper layer $(p, q)_X$ with X = B, N or H respectively are drawn in blue, and the corresponding $(-q, p + q)_X$ supercells in yellow. High symmetry points are reported as red dots. In the examples $p = 2$ and $q = 1$.

We first introduce our structure definitions of the close to 30° TBL-hBN structures. To simplify, we work on the basis of the two primitive vectors of the boron nitride monolayer $\mathbf{a_1}$ and $\mathbf{a_2}$ defined in the Eq. (1.11). Subsequently, we define the (q, p) hexagonal supercell as resulting from the super-lattice vectors $\mathbf{A}_i^{(q,p)} = \sum_i M_{ij}^{(q,p)} \mathbf{a_j}$, where the matrix M_{ij} can be written as below [238]:

$$M_{ij}^{(q,p)} = \begin{bmatrix} q & p \\ -p & q+p \end{bmatrix} \tag{2.5}$$

where p, and q are integers so that $p \neq q \neq 0$ otherwise they would lead to untwisted structures. Moreover, the difference between p and q is not a multiple of 3 and has no common divisor to define the smallest primitive moire supercell. In a bilayer system, if the lower layer is chosen to be fixed as a (q, p) hexagonal supercell with the origin at a boron atom, denoted $(q, p)_B$; the upper layer can be either $(p, q)_X$ (rotated a θ angle) or $(-q, p + q)_X$ (rotated a $-\theta'$ angle) with the addition of their mirror images, where $X = B, N$ or H (see Fig. (2.2)). However, we obtain only five different twisted bilayer structures[1] by combining these six possible upper layers $(p, q)_X$ or $(-q, p + q)_X$ on the lower layer $(q, p)_B$ (see later in Fig. (2.3)). On the other hand, since the definition of the M matrix is not unique, we restrict ourselves arbitrarily to cases $p > q$, which implies that angles are positive and $\theta + \theta' = 60°$. Moreover, both twist angles can be expressed from p and q with specific formula [238]:

$$\begin{aligned} \tan\theta &= \sqrt{3}\frac{p^2 - q^2}{p^2 + q^2 + 4pq} \\ \tan\theta' &= \sqrt{3}\frac{q^2 + 2pq}{2p^2 - q^2 + 2pq} \end{aligned} \tag{2.6}$$

[1] Because the same structure is obtained by placing $(-q, p + q)_N$ or $(-q, p + q)_H$ on $(q, p)_B$.

Further, since these twisted bilayers are defined by the same values of p, q, thus p and q, they can no longer provide the complete identity of these twisted bilayers. For this reason, we have proposed identifying them by the coincidence of high symmetry points between the upper and lower layers (see the Fig. (2.2)), and we call them by the name of the atoms in the coincident sites (see Tab. 2.1). All other technical details are discussed in [238].

Upper layer	Twist angle	Coincidence type	Stacking sequence	Symmetric group
$(q,p)_B$	$+\theta$	single	BB	$p321$
$(q,p)_N$	$-\theta'$	double	BNNB	$p321$
$(q,p)_H$	$+\theta$	single	NN	$p321$
$(-q,p+q)_B$	$-\theta'$	double	BBNN	$p312$
$(-q,p+q)_{B/H}$	$+\theta$	single	BN	$p3$

Table 2.1 – Geometry of the five stackings of hBN twisted bilayers [238]. The lower layer is chosen to be the $(q,p)_B$ supercell, and to remain unchanged to simplify.

We are only interested in supercells with angles close to 30°, from the Eq. (2.6), we have to choose integer (q,p)-pairs that approximate [239]:

$$p \approx q(1+\sqrt{3}) \tag{2.7}$$

so that θ and θ' tend to 30° asymptotically. The best set of approximants of the Eq. (2.7) are listed in table below:

(q,p)	θ	θ'	N_{atoms}
(1,3)	32.20°	27.80°	52
(5,13)	28.78°	31.22°	1036
(3,8)	29.41°	30.59°	388
(4,11)	30.16°	29.84°	724
(11,30)	29.96°	30.04°	5404

Table 2.2 – Set of the best (q,p)-pairs by employing the Eq. (2.7) [239]. The list is limited to nearly 30° structures containing less than 5404 atoms studied in this Ph.D thesis. Note that other structures close to 30° under 5404 atoms exist but are disregarded. Structures containing more than 5404 atoms are otherwise hardly obtained by the *ab initio* method.

2.1.3 Results for the (1,3), and (3,8) approximants. Limitation of the TB model.

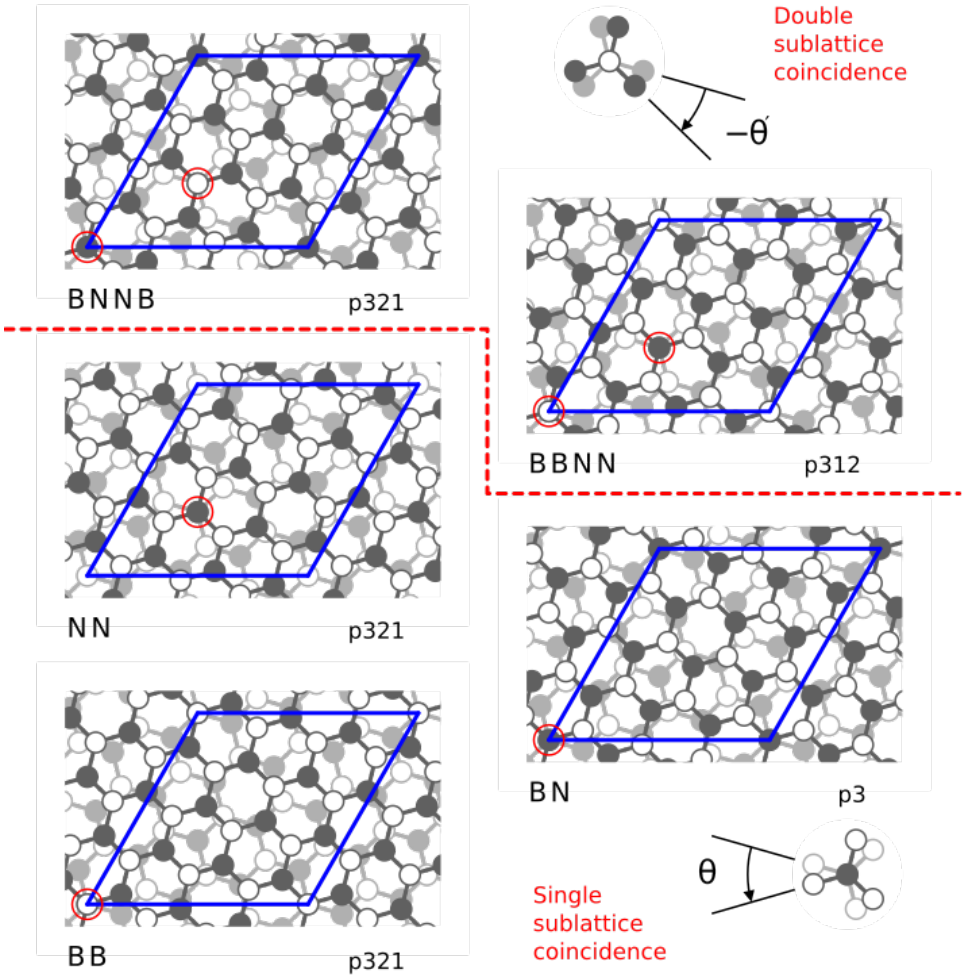

Figure 2.3 – Geometry of the boron nitride twisted bilayers (hBN-TBLs) [239]. The five hexagonal stackings in the (1,3) moire supercell. Red circles highlight the coincidence sites. A red dashed line separates the double-coincidence stackings with twist angle $-\theta'$ (top part) from the single-coincidence once with twist angle θ (bottom part).

As discussed in 1.3, finding the fit parameters that show a good agreement with experimental or *ab initio* data is necessary. It is the major difficulty when using the TB method. Since there are five different structures for each twisted angle and numerous structures close to 30° (as listed in the Tab. 2.2), the parameter qualification becomes tremendously more complex than in the usual case. Thus, the finest parameters are qualified if all the stackings for all twisted angles close to 30° are equally good compared to *ab initio* results. However, it is not always evident that all these issues must be dealt with simultaneously. This part will show how hard it is to reach the finest parameters and our TB limit.

To get reference results, our collaborators calculated the electronic band structures of these stack-

ings using Quantum Espresso code. Because of the size of the systems, they can only attempt the band structures for hBN-TBLs (1,3) (with 32.20° and 52 atoms) and (3,8) (with 29.41° and 388 atoms) structures. They used norm-conserving pseudopotentials, a cutoff energy of 60.0 Ry for the wavefunctions, and 240 Ry for the charge. The exchange-correlation potential has been approximated with the Perdew-Burke-Ernzerhof model [173]. The Brillouin zone has been sampled with shifted Monkhorst-Pack [240] grids of 5 x 5 $\mathbf{k}$-points in the xy plane in the (1,3) supercells and 3 x 3 in the (3,8) supercells. We propose two set parameters for TB calculations, SET 1 and SET 2, listed in Tab. 2.3. It is worth noting that for hBN-TBLs, we included only the σ component[2] in the interlayer hopping (2.1). These sets exhibit a slight difference in parameters related to the boron hoppings, which directly impact conduction bands.

	Intralayers hoppings (||)				Interlayers hoppings ($\perp$)					
	On-site energies (eV)		In-plane hoppings (eV)		Prefactor value (eV)			Decay value (Å^{-1})		
	$\xi_{BB}^{(1)}$	$\xi_{NN}^{(1)}$	$t_{BN}^{\|\|}$ (1st NN)	$\xi_{BB}^{(2)}$ (2nd NN)	$\gamma_{BB}^{\perp}$	$\gamma_{BN}^{\perp}$	$\gamma_{NN}^{\perp}$	$Q_{BB}^{\perp}$	$Q_{BN}^{\perp}$	$Q_{NN}^{\perp}$
SET 1	5.65	0.00	-2.65	0.10	2.45	0.75	0.32	3.0	2.0	1.6
SET 2	4.90	0.00	-2.65	0.00	4.50	0.75	0.32	1.4	2.0	1.6

Table 2.3 – Comparison between two set of parameters SET 1 and SET 2 for the intralayer and interlayer hoppings. All the rest parameters were set to 0. The SET 2 (light gray) was used as the finest input [239]. We include only the σ component in the interlayer hopping t_{AB}.

The performance of these sets on the top valence and bottom conduction bands of all the BB and BN stackings in the (1,3) and (3,8) supercells is illustrated in Fig. (2.4). In this figure, the left part displays the band structures of hBN-TBLs (1,3), whereas the right part displays those of hBN-TBLs (3,8). In the left part of the Fig. (2.4), the QE DFT-GGA predicts the formation of a pretty flat dispersion in the $\mathbf{M}-\mathbf{K}$ region on conduction bands in both systems. The two bands avoid each other in the BB(1,3) presented by (=), even though the splitting is minimal. Instead, they cross at $\mathbf{K}$ in the BN(1,3) presented by (×), consistently with what is simulated at smaller angles. Overall, our TB models catch these features very well, although the BB stacking splitting is somewhat overestimated for both set parameters. These two bands were obtained to be flatter by the SET 1 than by the SET 2. However, the splitting between these bands in BB stacking is too large by the SET 1 and much smaller but still larger by the SET 2 compared to the DFT predictions. Moreover, the form of higher conduction bands calculated by the SET 2 was better at $\mathbf{M}$ and at the middle of $\mathbf{K}-\Gamma$ path. For valence bands, our SET 1 model performs almost perfectly to the DFT bands, whereas although the bands are a little stretched toward lower energy at Γ, our SET 2 model still performs a perfect fit. At a larger angle, like in the BN(3,8) bilayer, the agreement is even

[2] For hBN-TBLs, the interlayer hopping employed is $t_{AB} = l_x V_{pp\sigma}(D_{AB})$.

better, as shown in the right part of the Fig. (2.4). In particular, the model reproduces QE DFT-GGA remarkably well in predicting the emergence of a group of densely packed and low dispersing bands concentrated between 4.37 eV and 4.46 eV on conduction bands, that we have called the $\ll$**bundle**$\gg$ of flat states, located at (#). The latter were caught very efficiently by our TB models. The valence bands were almost perfectly reproduced, thanks to our TB models. Compared to the results obtained by our SET 1 and 2 models, SET 1 provides a slightly better fit for valence bands. However, the bundle of flat states was observed to be formed too tight and located at higher energy. Since the differences between the SET 1 and 2 are only on boron-boron and boron-nitrogen hoppings, it is evident that the valence bands calculated by these models do not change significantly. Hence, we will consider the SET 2 as the finest model in the following section.

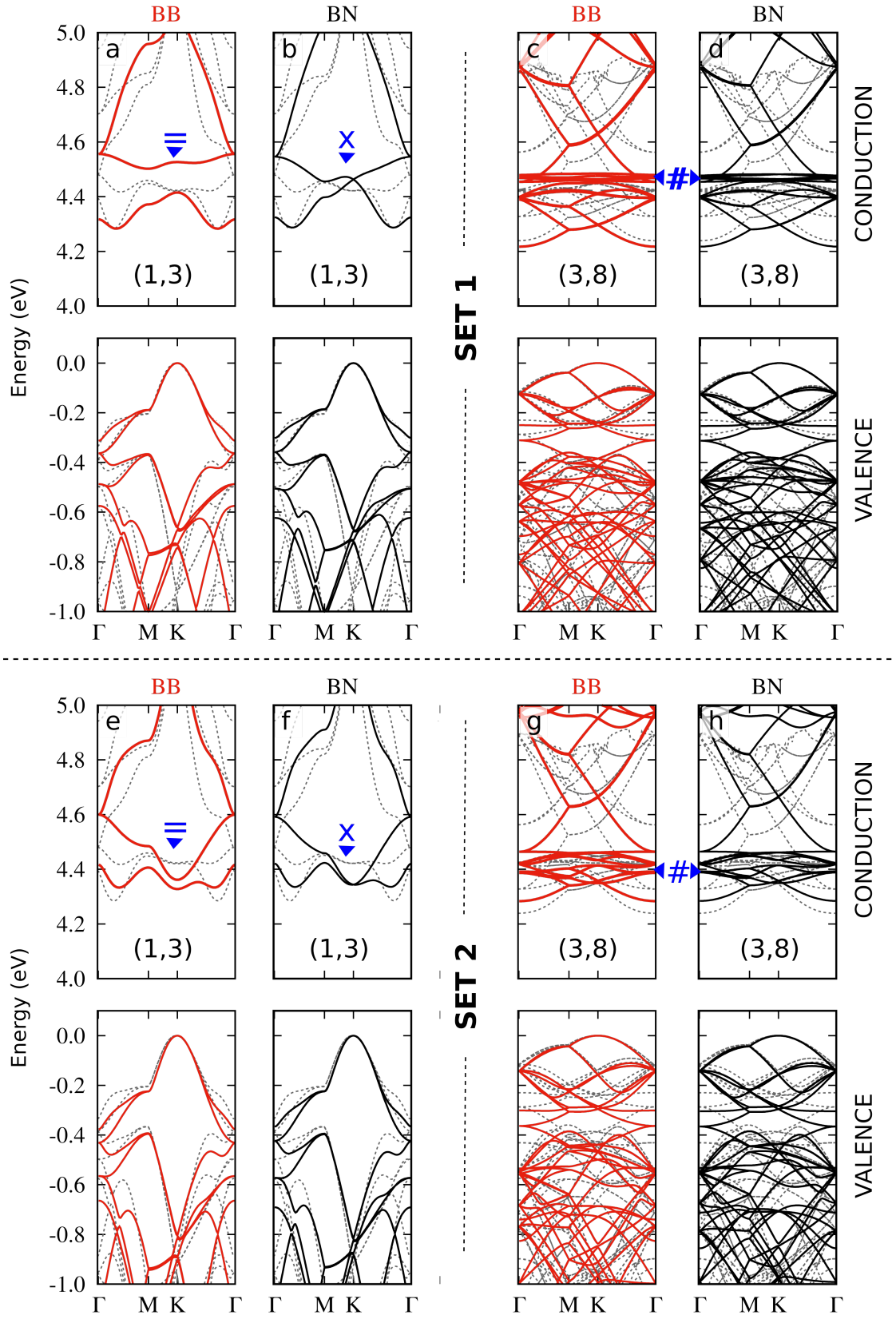

Figure 2.4 – Comparison between two set of parameters SET 1 and SET 2, shown in the Tab. 2.3. a-d, Electronic band-structures of BB, BN(1,3) (left part); those (3,8) (right part) calculated by the TB method withthe SET 1. **e-h,** Electronic band-structures for the same structures calculated by the TB method with the SET 2. The continued curve depicts those calculated by the TB method, whereas the dotted curve depicts those obtained by QE DFT-GGA. The symbol (=) and (×) represents to the avoiding bands and the crossing bands respectively. While the symbol (#) stands for the **bundle** state location.

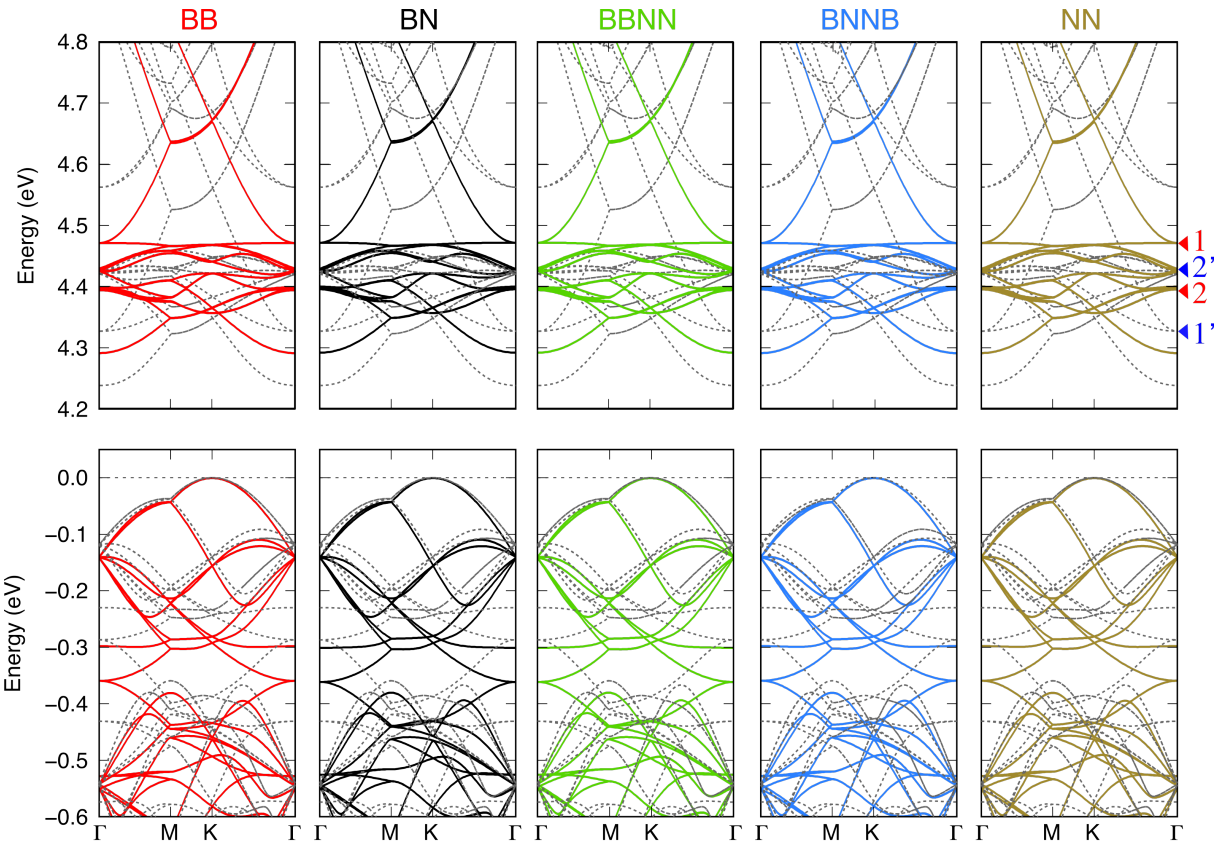

Figure 2.5 – Electronic band-structure of hBN-TBLs (3,8) using the SET 2 parameters [239]. Top valence (bottom panels) and bottom conduction states (top panels) of the (3,8) supercell in the BNNB, BN, NN, BB and BBNN stackings from left to right. Colored solid curves are from our tight-binding model, dotted grey curves from QE DFT-GGA. Red triangles depict the positions of the bundle of flat states obtained by our TB model, whereas blue triangles depict its right positions obtained by QE DFT-GGA.

Before closing this part, we will compare our TB results evaluated by the SET 2 with QE DFT-GGA ones and the limit of our finest model in detail. In Fig. (2.5), we report the electronic band structures of all five (3,8) stackings. We figure out that both the DFT and TB results show that differences between the stackings are negligible, indicating that the band structure and wavefunctions are remarkably similar. As discussed above, our TB model captures pretty well the emergence of the flat states' bundle; our method's limit can only appear once we zoom the bottom conduction bands between 4.2 and 4.8 eV (0.6 eV of energy range only). In the right of the Fig (2.5), we report the position of misplaced bands obtained by our TB model, depicted by red triangles, and its reference position obtained by QE DFT-GGA, depicted by blue triangles. These latters show that the bands at position **1** (position **2**, respectively) should be located at position **1'** (position **2'**, respectively). In Figs. (2.6a-c), we report the two first bottom conduction bands of BB and BN(1,3) stackings into the same energy range from 4.2 to 4.8 eV. The figures show that the conduction bands in the $\mathbf{M}-\mathbf{K}$ path are not as flat as those achieved by QE

DFT-GGA. They are located at too low energy at $\mathbf{K}$, especially since the energy gap becomes direct at $\mathbf{K}$ in BB(1,3), which is in disagreement with DFT predictions. Moreover, as discussed above, the splitting between the two bands in the BB(1,3) is overestimated. However, these limits only appear if we consider a concise energy range of 0.6 eV.

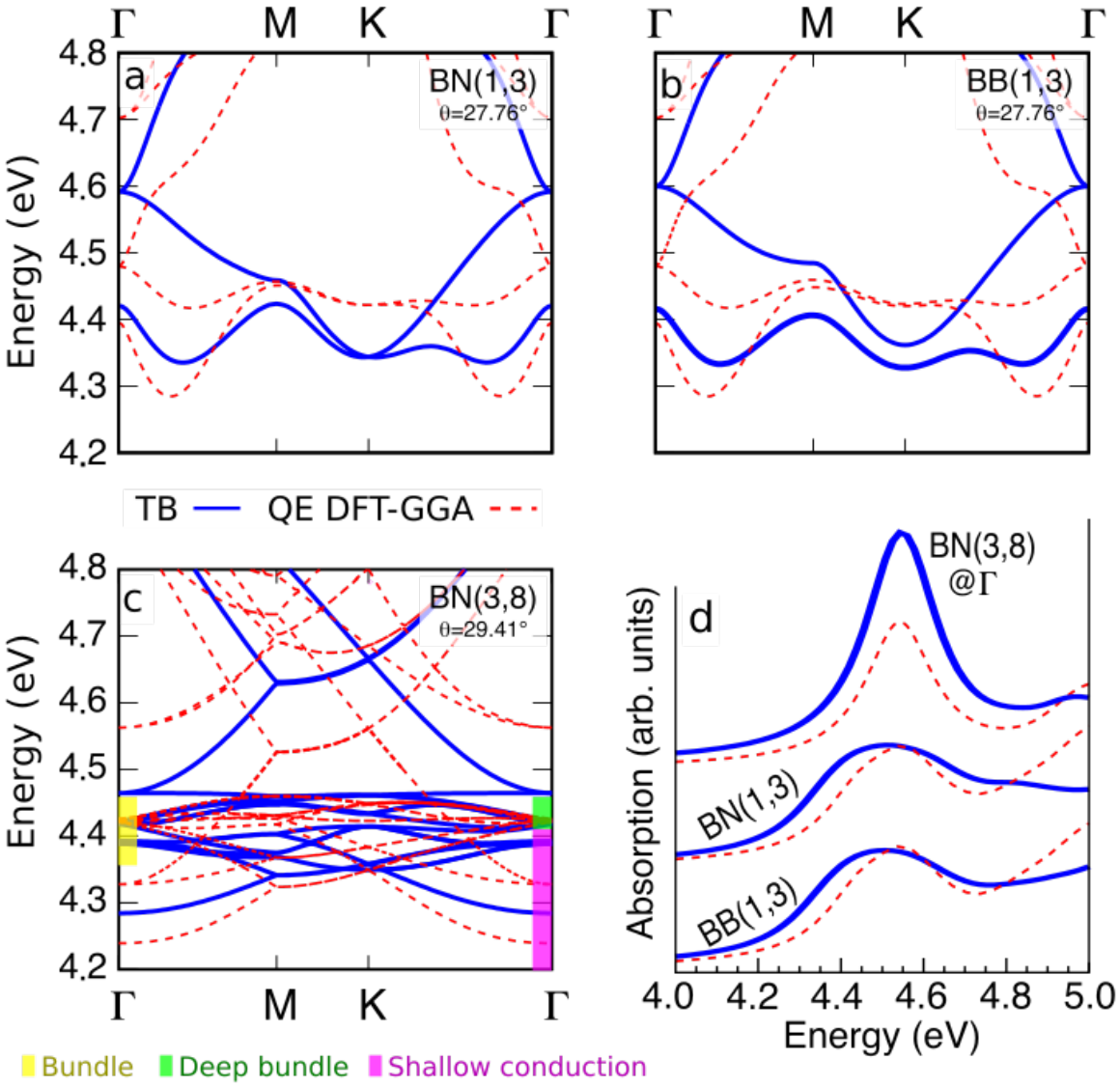

Figure 2.6 – The SET 2 performance on electronic and optical response [239]. **a-c,** Conduction bands of BB(1,3), BN(1,3) and BN(3,8) bilayers from left to right in TB (blue solid) and DFT (red dashed). The top valence of all structures have been aligned to 0.0 eV. In **c**, thick bars on the canvas highlight notable energy intervals: (in yellow) the bundle states (4.37 eV to 4.46 eV); (in green) the deep bundle states (4.39 eV to 4.46 eV); (in violate) shallow conduction states below 4.39 eV. **d,** Onset of independent-particle absorption spectra of the same systems calculated by the TB and Yambo codes. The BN(3,8) spectra are computed only in the Γ point. All spectra have been broadened with a Lorentzian with variance 0.1 eV. In this figure, all TB results were perfomed by using the SET 2 parameters shown in the Tab. 2.3.

Finally, we will show that our TB model's limits do not impact the optical response of those structures.

We have calculated the imaginary part of the independent-particle dielectric function $\varepsilon(\omega)$ in the same systems, using both *ab initio* and our TB model. The results are presented in Fig. (2.6d). *Ab initio* independent-particle absorption spectra have been calculated using the free simulation package Yambo [174]. We sampled the Brillouin zone of the (1,3) supercells with a shifted Monkhorst-Pack [240] grid of 4 x 4 $\mathbf{k}$-points and included 400 bands in the sum over states. Note that this value of band numbers is much higher than required for the absorption onset alone. In the BB(3,8) calculation, because of the larger calculation size (about 1552 electrons), we included bands with an index ranging from 700 to 800, and we computed the sum over states only at the Γ point. We truncated the Coulomb interaction in the z-axis in both cases using the analytic formulation implemented in Yambo [174]. It is neatly exhibited that both methods predict a well-detached peak at 4.5 eV, corresponding to transitions towards the bottom conduction states. Therefore, we conclude that our TB model is good enough and valuable for predicting larger twisted bi-layer structures near 30°, which are hardly attained with DFT.

Also, the Fig. (2.6c) reports the bottom conduction bands of the BN(3,8) bilayer, in which we highlight the ≪**bundle**≫ of flat states by a yellow sidebar. Additionally, it is helpful for the coming part to split the conduction bands into a lower energy region (depicted by a pink bar), called ≪**shallow conduction**≫ and a higher energy region where bands are mainly flat called ≪**deep bundle**≫ region (depicted by a green bar). We note that all energy intervals are given with respect to the top of the valence band.

2.1.4 Predictions for larger twisted bi-layer structures with twist angles closer to 30°

Bundle formation on conduction band and its impact on the optical response

Once the validated TB model is achieved, we extend our investigation to twist angles closer to 30° and systems that are difficult to simulate with DFT. Figs. (2.7a-f) illustrate the bottom conduction states of the BB (red curves) and BN (black curves) stackings in the (5,13), (4,11), and (11,30) supercells, corresponding to twist angles 28.78°, 29.84°, and 29.96°, respectively. The observed tendency, previously noticed in (1,3) and (3,8) supercells, is confirmed and strengthened in this study. All the stackings exhibit the same band structure at a fixed supercell size, as discussed in the reference [239]. In the limit of approaching 30° twist, the BN bilayer displays quasicrystal-like behavior, leading to indistinguishable stacking sequences. A quasicrystal is a structure that exhibits long-range order without translational symmetry, and it can have quasi-periodicity of self-similar patterns. As a result, each supercell has approximate replicas of smaller cells for all five stackings. This self-similarity across different length scales explains the similarity in stacking configurations observed in the electronic band structures at various twist angles. We will discuss another manifestation of this property later on. This is true for any

homobilayer formed of hexagonal monolayers, so we expect a similar behavior to be observed also in close-to-30° twisted graphene, TMDs, silicene, and many of the most popular 2D materials.

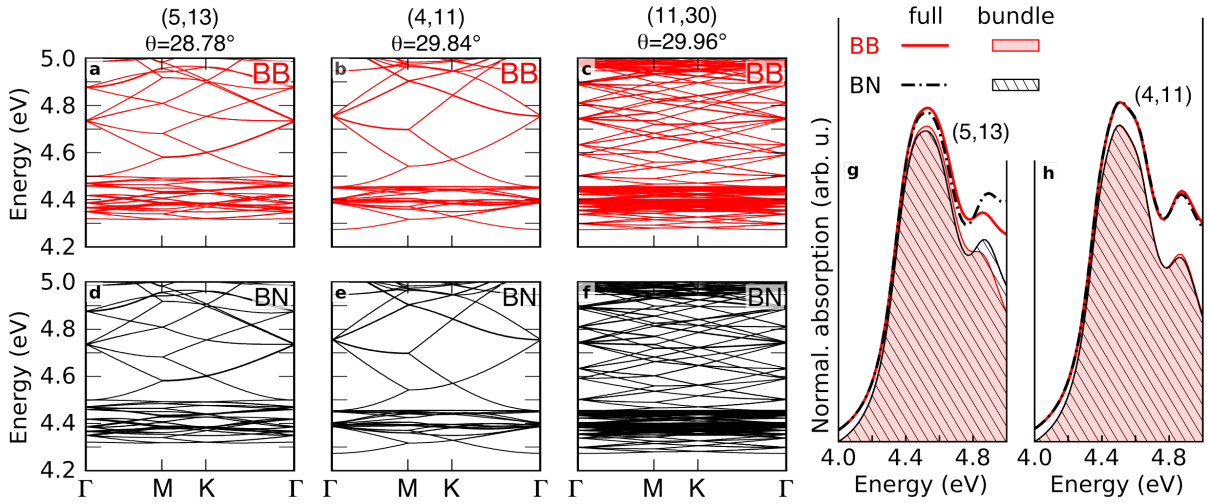

Figure 2.7 – TB predictions on hBN-TBLs close to 30° using the SET 2 series parameters [239]. a-c, Conduction bands of the BB(5,13), BB(4,11) and BB(11,30) bilayers respectively. **d-f,** Same as **a-c** in the BN stacking. The top valence of all structures have been aligned to 0.0 eV. **g-h,** Independent-particle absorption spectra of the BB(5,13) and BB(4,11) (red solid curves) and BN(5,13) and BN(4,11) (black dashed) obtained including all empty and occupied states (full), calculated by the TB method. Shaded and patterned areas correspond to spectra obtained by restricting accessible empty states between 4.34 eV and 4.48 eV.

More appealing, the bundle of flat states forming in the bottom conduction band is observed in all structures at all angles close to 30° and consists of a spare interval (approximately 0.1 eV) centered around 4.40 eV. Such behavior is in contrast with small-angle twisted hBN bilayers where one or more single states are formed directly in the gap and separated in energy by about 0.1 eV [221, 222, 241]. For this reason, it is worth studying the impact of these flat states on their absorption properties. We used the TB method using the SET 2 parameters to calculate the optical response in the (5,13) and (4,11) supercells. Their spectra are presented in Figs. (2.7g-h). The BN and the BB stackings expectedly exhibit quite small differences that are further washed out as the twist angle approaches 30°. Spectral onsets are dominated by the same intense and well-detached peak observed in the Fig. (2.6d). To perceive its origin, we re-evaluated the absorption spectra by considering only transitions toward the bundle (4.34 eV to 4.48 eV), and we recovered almost the same spectra. It is shown that, although they are not the lowest empty bands, the bundle states are principally responsible for the absorption onset. Given the intensity of the onset at the independent-particle level and the low dispersion of the conduction states involved, we predict that hBN bilayers twisted at twist angles near 30° will exhibit intense, robust, and localized electron-hole excitations.

The influence of the boron-boron interlayer interaction on local density of states of the bundle states.

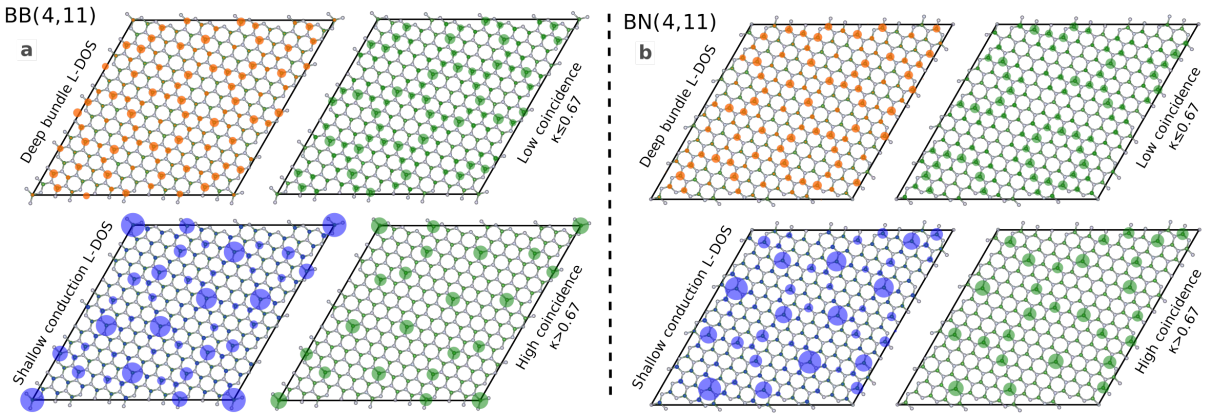

Figure 2.8 – Local density of states of BB and BN(4,11) on the deep and shadow bundle states [239]. a-b, Orange and blue circles: Radius proportional to the LDOS in the deep bundle and shallow conduction interval, respectively. Green circles: Radius proportional to C_{j_B}, where high coincidence occurs when $C_{j_B} > \kappa$, otherwise, low coincidence occurs.

Furthermore, we investigate the spatial distribution of the conduction states by evaluating the local density of states (LDOS) in intervals corresponding to the deep bundle energy and the shallow conduction energy highlighted in the Fig. (2.6c). In Figs. (2.8a-b), we display results in the upper layer of the (4,11) supercells. In these figures, the radius of the orange and blue circles are proportional to the LDOS on the deep bundle energy and shallow conduction energy, respectively, in the upper layer of the BB(4,11) (panel a) and the BN(4,11) (panel b). As expected, no DOS is centered on N sites since they contribute mainly to valence states [157]. It is quite normal for twisted stacks (all angles) to have a greater effect on the conduction bands than on the valence bands, e.g. in 3D crystals [242], in 2D cystalline bilayer stacks [243]. Although both the band structures of the BN(4,11) and BB(4,11) and their optical spectra are similar, the two stacks exhibit pretty different patterns. They may look contradictory at first sight, but these patterns hide fascinating similarities. Inside each structure, one can find infinite rearrangements of smaller cell approximants of all the five stackings, which repeat themselves in a kind of self-similar scheme (see in Supplementary material of Ref. [239]). For instance, inside each (4,11) stacking, we can find some local replicas of all five (3,8) stackings; similarly, inside each (3,8) stacking, we can find some local replicas of all five (1,3) stackings, and so on. Nevertheless, a given approximant can not simply be obtained by repeating lower-size approximants. As a result, it is impossible to tile a given approximant with a lower-order one perfectly (see Supplementary materials in Ref. [239]). Thus, the inclusion and repetition of the smaller cells within a bigger one is not perfect, which gives rise to frustration. The interference resulting from the superposition of this frustrated self-similar repetition of the lower-order

approximants of all stackings is at the origin of the LDOS patterns of the BB(4,11) and BN(4,11) in the Figs. (2.8a-b). We figured out that the LDOS is revealed to be more significant on sites where the B atoms of the two layers are almost vertically aligned. To illustrate this feature, we establish at each B site j_B the coincidence function $C_{j_B}(\mathbf{r}) = 1 - r_{xy}/a_{BN}$, where r_{xy} is the in-plane component of the vector $\mathbf{r}$ connecting the site j_B of one layer to the closest B site of the other layer. Here, $C_{j_B}(\mathbf{r})$ varies from 0 to 1, where $C_{j_B}(\mathbf{r}) = 1$ if two B atoms are perfectly stacked on top of each other, and $C_{j_B}(\mathbf{r}) = 0$ if a B atom of one layer coincides with a N or a hexagon center of the other layer. In the Figs. (2.8a-b), the green circles have radii proportional to $C_{j_B}(\mathbf{r})$ of all B sites of the upper layer for which $C_{j_B}(\mathbf{r}) > \kappa$ with κ = 0.67 if high coincidence is displayed, otherwise, low coincidence is displayed. The resemblance between the high-coincidence patterns and the shallow conduction LDOS is manifestly remarkable, and the same resemblance is observed for the deep bundle states and low coincidence patterns. The latter proves that all the lowest conduction bands stem from B-B interlayer states. For perfect vertical B-B coincidence, the coupling is stronger, and the energy of the corresponding empty state is lower. We verified that these are bonding states by checking that the TB coefficients of coinciding and quasi-coinciding sites have opposite signs in the two layers.

Influence of the boron-boron interlayer interaction on electronic bandstructures of the bundle states

In this part, we will get more insight into the origin of a bundle of flat states by using the TB model to disclose the impact of the B-B interlayer hopping on the formation of the bundle states. Then, we will link to other large-angle twisted bilayers by employing a simple triangular model.

Firstly, we achieved the band structure of the BN(3,8) bilayer, including all parameters of our TB model except for the $\gamma_{BB}^{\perp}$. The resulting states are reported in Fig. (2.9a), in which the blue curves display the conduction bands of the BB(3,8) bilayer with $\gamma_{BB}^{\perp}$ = 0 eV, and the red ones display those of hBN monolayer. We figured out that they are very similar without a flat band. Now, increasing the interlayer B-B coupling and setting $\gamma_{BB}^{\perp}$ = 1.225 eV (50%) (in Fig. (2.9b)), localized states start forming until a bundle of entirely flat bands appears at $\gamma_{BB}^{\perp}$ = 2.45 eV (100%) (in Fig. (2.9c)). It is re-confirmed through the results obtained with $C_{j_B}(\mathbf{r})$ that the bundle states stem from the interlayer B-B coupling and that the interlayer coupling is only due to the B-B interactions. The weakness of the interlayer N-N coupling explains why there is no such a feature in the valence band, contrary to what happens in graphene-twisted bilayers where conduction-conduction and valence-valence couplings are equivalent [244].

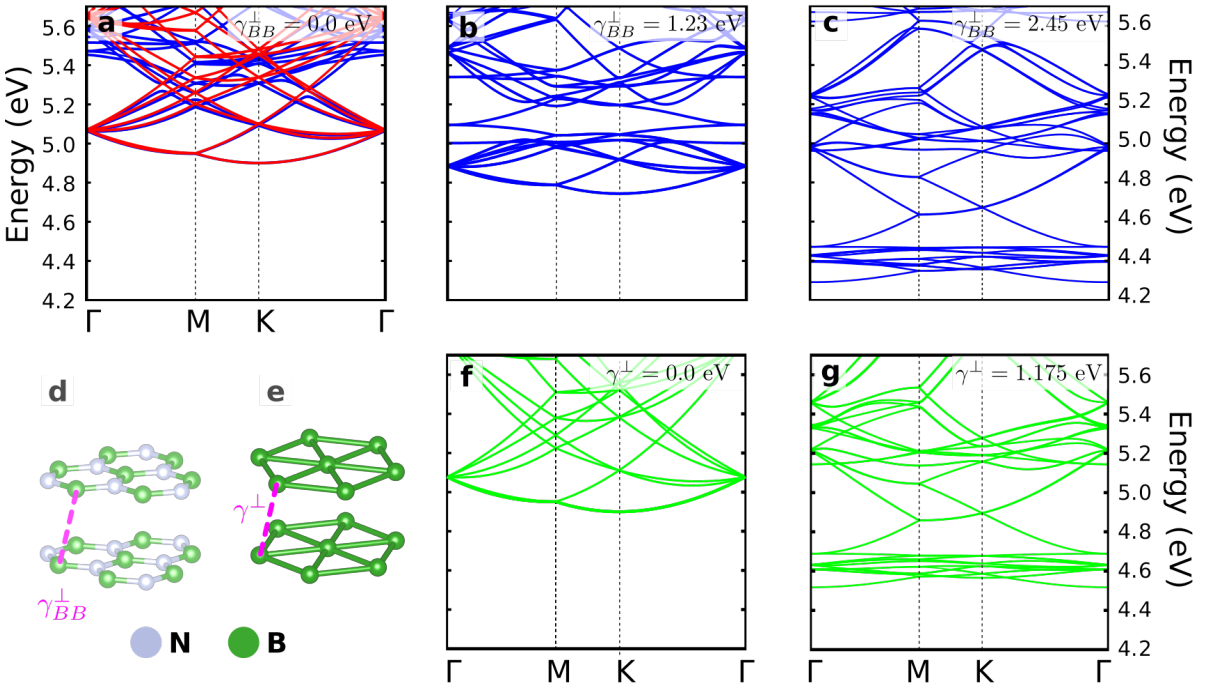

Figure 2.9 – TB investigations on the origin of bundle of flat bands using the SET 2 series parameters [239]. **a,** TB conduction band of the hBN monolayer in the (3,8) supercell (red solid curves) and of the BB(3,8) bilayer with $\gamma^{\perp}_{BB}$ = 0 eV (0%) (blue solid curves). **b-c,** The same bilayer with $\gamma^{\perp}_{BB}$ equal to 1.23 eV (50%) and 2.45 eV (100%) of the correct value. **d,** Ball and stick model of the honeycomb lattice twisted bilayer. Dashed magenta line: the $\gamma^{\perp}_{BB}$ interlayer coupling. **e,** Ball and stick model of the triangular lattice twisted bilayer made only of the B sites. Dashed magenta line: the $\gamma^{\perp}$ interlayer coupling. **f-g,** TB Conduction bands of the triangular model with $\gamma^{\perp}$= 0 eV and 1.715 eV respectively. The top valence of all structures have been aligned to 0.0 eV.

We now derive an even simpler TB model describing bundle states' formation. We select only the B sublattices, obtaining a structure of two triangular lattices where only B-B interactions are considered. To obtain the triangular model, we begin with the conduction band within the monolayer hBN, as discussed in [157]; close to the gap, the conduction eigenstates are mainly localized on boron sites, which is related to the first term expansion:

$$\epsilon_{c\mathbf{k}} \approx \xi^{(1)}_{BB} + \frac{(t^{||}_{BN})^2}{\xi^{(1)}_{BB}} |g_1(\mathbf{k})|^2 \tag{2.8}$$

The Eq. (2.8) is identical to the unique eigenvalue of a first-nearest-neighbor TB model made on the triangular lattice formed by the boron sites. The intralayer B-B hopping integral and the on-site energy of such a triangular lattice model are now replaced respectively by:

$$t_{\Delta} = \frac{(t^{||}_{BN})^2}{\xi^{(1)}_{BB}}, \quad \text{and} \quad \xi^{(1)}_{\Delta} = \xi^{(1)}_{BB} + 3t_{\Delta} \tag{2.9}$$

Moreover, the interlayer B-B hopping integrals follow the same construction rule as that for the honeycomb calculations discussed above in the parameter validation part.

The conduction band structure of this simplified triangular model is reported in Figs. (2.9f-g) respectively for vanishing and non-vanishing interlayer coupling. The model reproduces the isolated honeycomb monolayer at no coupling and gives rise to a bundle of flat bands at full coupling, showing the vital role of the B-B interlayer interaction in localizing the electrons in high-angle twisted boron-nitride bilayers. Also, this model allows us to unravel fundamental mechanisms common to other large-angle twisted bilayers. We deem it probable that a similar bundle of flat states will emerge in the valence band of close to 30° twisted TMDs. As discussed in [245], the interlayer coupling is mostly due to p_z states of chalcogens whose electronic states participate essentially to the top of the valence band.

2.1.5 Conclusion

To conclude, we have investigated the electronic and optical properties of hBN bilayers at twist angles close to 30°, which are calculated in DFT by using our two developed TB models and QE DFT-GGA. Since there are five different stackings for each twist angle, it is necessary to reach the fit parameters for all of these at the same time, so the latter is a highly complex task because it is hard to obtain the fit parameters satisfying all these demands. As a result, none of these TB models have enabled us to achieve results that perfectly match the DFT ones. We made our choice, which may be better for studying the optical responses. Our finest TB model has shown a good agreement with independent particle *ab initio* spectra calculated by Yambo code. We then used our finest TB model to predict the electronic and optical properties of the larger twisted bi-layer structures close to 30° hardly obtained by DFT. We have shown that at twist angles close to 30°, all hBN bilayers encounter the same electronic properties, irrespective of the stacking sequence. This is characterized by the emergence of a bundle of low-dispersing states right above the bottom of the conduction band, causing a significant and intense peak at the onset of the absorption spectrum resulting from a strong coupling between B atoms belonging to different layers. Moreover, this fundamental mechanism has been captured with a very simple triangular-lattice TB model. Additionally, this can be employed further with many other twisted bilayers (*e.g.*, homo-bilayers of TMDs). Our results suggest that 30°-twisted BN bilayers may induce extremely significant excitonic phenomena originated by the bundle of flat bands and independent of the stacking sequence. Besides, the indistinguishability of the band structure with respect to the stacking sequence is expected to be a ubiquitous characteristic in the quasicrystal limit and to occur in twisted bilayers of other 2D materials, including TMDs, antimonide, silicene, transition metal monochalcogenides, and all homo-structures formed of hexagonal single-layers.

Chapter 3

New graphene-derived materials

This chapter presents our complete studies on new graphene-derived material structures' electronic, transport, and optical properties. These new materials are mono- and bilayer graphene quantum dots (GQDs), graphene nanoribbons (GNRs), and graphene nano-meshes (GNMs). This work can be divided into three steps: chemical synthesis, optical and transport characterization, and theoretical simulations. In the first step, our chemists collaborators, Dr. Stéphane Campidelli, Dr. Julien Lavie, and Dr. Daniel Medina-Lopez, at the CEA-NIMBE laboratory in Paris-Saclay, have performed the synthesis of GQDs and precursors. In the second step, Prof. Jean-Sébastien Lauret have studied some GQDs at the LUMIN laboratory at ENS Paris-Saclay by measuring their absorption and photoluminescence spectra. Finally, these systems have been deposited on metallic surfaces under ultra-high vacuum (UHV) in order to build GNRs and GNMs. Prof. Hamid Oughaddou with his Ph.D. student Hamza El-kari at ISMO laboratory, Paris-Saclay, and Dr. Sylvain Clair at IM2NP laboratory at Aix-Marseille University, have performed STM/STS measurments. In the third step, Dr. Sylvain Latil, Dr. Yannick Dappe and I have simulated the electronic band structures, DOS, absorption spectrum, and STM/STS images to compare them with our collaborators' measurements. Our new graphene-derived materials will be divided into four families. To simplify, we will call it as the name of its attached GQD: C42 $D_{6h}(6/mmm)$, C30 $D_{6h}(2mm)$, C96 $D_{3h}(\overline{6}m2)$, and C96 $D_{2h}(mmm)$. As part of this collaboration, I am focusing on the variation of these new graphene-derived material structures on electronic, optical, and transport properties as a function of their size and symmetry. These property changes will be disclosed and highlighted inside of each family.

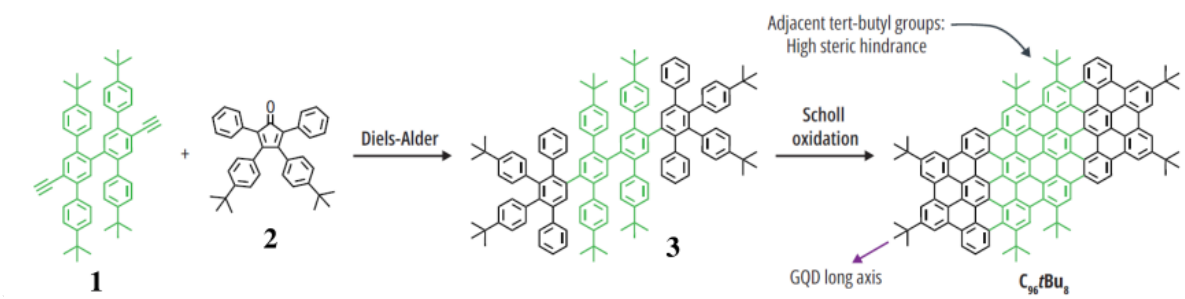

Figure 3.1 – Our chemists' general synthetic strategy to $C_{96}t$Bu$_8$ [246]. The alkyne terphenyl core **1** reacts with the Diels-Alder reaction tert-butyl substituted tetraphenylcyclopentadienone **2** to give dendrimer **3**. The dendrimer **3** are finally oxidized in the presence of $FeCl_3$ in a mixture of dichloromethane and nitromethane under argon flux to give the target GQD $C_{96}t$Bu$_8$. Other GQDs or precursors in this thesis have synthesised under the almost strategy.

3.1 The family of hexagonal-shaped GQD C42 $D_{6h}(6/mmm)$

3.1.1 Hexagonal-shaped GQD C42 $D_{6h}(6/mmm)$

Structural definition

When fully graphitized on a metallic surface, the GQD C42 ($C_{42}H_{18}$) presents a hexagonal form (see Fig. (3.2a)), which is known as the name: *Hexa-peri-hexabenzocoronene* (HBC). To simplify, we call it S1. The GQD S1 belongs to the symmetry point group $(6/mmm)$, so it has sixfold rotational symmetry and three mirror symmetry plans: m_x, m_y, and m_z. As discussed in the introduction , the S1 is easily synthesized, and its optical properties are almost fully understood in experimental and theoretical aspects [247, 248]. For this reason, this GQD can be considered as an excellent approach to check the performance of our set parameters of both Tight-Binding and *ab initio* methods in order to reach the larger GQDs which have better sp^2 hybridization, presented later in 3.3 and 3.4.1.

Optical properties

Its rich symmetry has important effects on the electronic and optical properties. Fig (3.2c) illustrates the imaginary part of the dielectric function (1.29) in terms of incident photon energy by using the 2NN TB method. In this calculation, we used the same set of parameters for graphene presented in Tab. 1.3. The IP RPA-TB absorption spectrum witnesses a major peak at 2.51 eV and minor peaks at 3.75 eV, 4.32 eV, and 4.42 eV. These peaks can be explained by the irreducible representation of frontier orbitals as shown in Fig. (3.2b). The figure shows that the highest occupied molecular orbital (HOMO) and the lowest occupied molecular orbital (LUMO) have double degeneracy. Because of its symmetry,

whether the electric field is along x or y, it belongs to the irreducible representation e_{1u}. As a result, along these two directions, the optical spectrum is the same. Since the HOMO (LUMO, respectively) have the irreducible representation e_{1g} (e_{2u}, respectively), only the transitions between them are allowed by symmetry. These transitions correspond to transition **(1)**, and they are double counted as the double degeneracy of HOMO and LUMO, as demonstrated in Ref. [249].

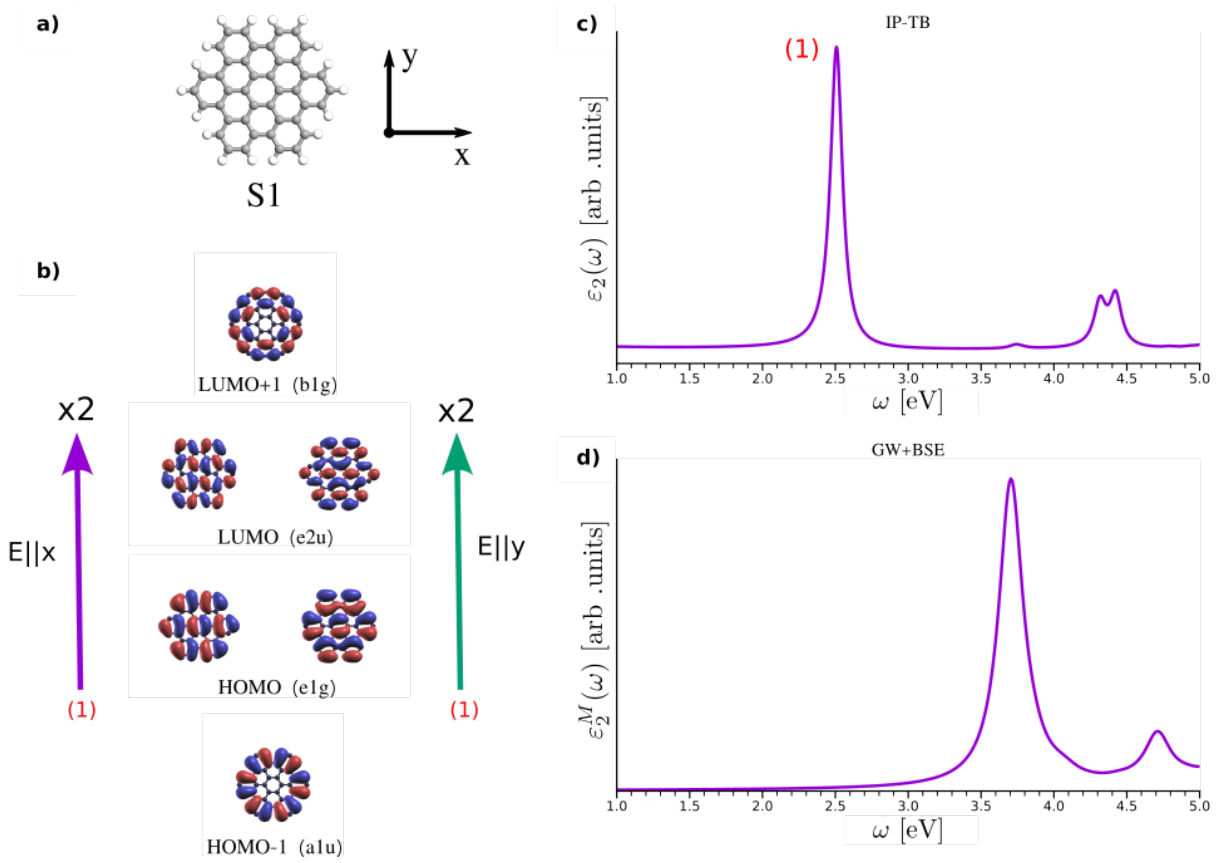

Figure 3.2 – Optical response of the GQD HBC $(6/mmm)$**. a,** Geometry of the GQD HBC $(6/mmm)$ labeled S1. **b,** Frontier orbitals of S1 calculated by TB method, and presented by applying the Eq. (1.22). The violet arrow depicts the allowed transitions by symmetry if the electric field is along the x-axis and a green arrow if the electric field is along the y-axis. **c,** The absorption spectra calculated by 2NN TB model (1.29). The major peak numbered **(1)** corresponds to these allowed transitions in **c**. **d,** The fully absorption spectrum evaluated by GW+BSE scheme (1.84) using Yambo code. All technical details are discussed in Appendix A.

As noted in section 1.3, Tight-Binding results require either experimental or *ab initio* data, or both, to adjust the parameters. Fig. (3.2d) illustrates the fully imaginary part of the dielectric function (1.84) obtained by GW+BSE calculation using YAMBO code [174] over DFT-GGA data calculated by Quantum Espresso [217]. In the incident photon energy range 0-5 eV, our GW+BSE absorption spectrum is in good agreement with that one found by GW+BSE calculations using BerkeleyGW package over DFT-LDA calculations using Quantum Espresso [248]. The first active peak of GQD stems from our GW+BSE

calculations at 3.7 eV, also in excellent agreement with the experimental data at about 3.7 eV in Ref. [247]. Compared to the one in Ref. [248], only a slight difference at a higher energy range subsists, but the main absorption structure is preserved. This little difference can be related to the different choices of exchange-correlation function in DFT simulation, the kinetic cutoff for exchange and correlation self-energy in GWA simulation, the number of bands used to calculate ϵ_2^M in BSE simulation, etc. All our technical details are discussed in Appendix A. However, we only focus on the energy range around the Fermi level from 0-5 eV (where there is no significant difference between our spectra and the reference one) to compare with the absorption spectrum evaluated by our TB method. In comparison with Fig. (3.2c), it clearly shows that we obtain a very comparable structure to the IP RPA-TB absorption spectrum. Further, the calculated energy gap is listed in Tab. 3.1. Our energy gap obtained by QE DFT-GGA, and GWA methods agree with those found in [248]. With the GW correction, the energy gap is 2.29 times greater than the one evaluated by QE-GGA. On the other hand, it is worth noting that the energy gap found by Fireball DFT-LDA is higher than the one found by QE DFT-GGA; it is the effect of the boundary condition of the use of pseudo-atomic orbitals as discussed in 1.4.5.

Simulation methods	E_{gap} (eV)
2NN TB	2.51
Fireball-DFT LDA	2.95
QE DFT-GGA	2.47
GWA	5.66

Table 3.1 – Gap width of S1 evaluated by different methods. All technical details are discussed in Appendix A.

Comparison between STM experiments and simulations.

In this part, we aim to get the signature of the GQD S1 on a gold Au(111) surface in a calculated STM image to help our experimental collaborators identify this signature in their measurements. To do so, we have set the GQD S1 on a five-layer 18 x 18 Å^2 square slab of the fcc Au(111) that was subjected to -0.98% and 1.92% tensile strains along the direction of the in-plane lattice vectors of gold Au(111) (see Fig. (3.3a-b)). The interface was built via geometry matching on the Interface Builder [250] of QuantumATK [251]. Appendix B elaborates all geometry-matching technical details. The reason for using strained gold(111) surface is that firstly, gold(111) surfaces compressed whether greater-5% and lower 5% were observed to preserve the properties of the pristine one; secondly, stretching gold(111) surface allows to obtain a minimized-number-atom resulting interface; thirdly, using strained gold(111)

surfaces exhibited very good agreement with experiments reported by L. Jelver *et al.* [252]. Hence, there are only 285 atoms in the resulting square primitive cell. The simulations were performed under conditions defined in Appendix A.3. After the geometry relaxation of the whole system, the resulting average strain ratios on the topmost Au-Au atoms are between -1.43% to 1.40%. The resulting C-C distance of the GQD is approximately 1.44 Å in its center part and reduced by going toward its edge, about nearly 1.40 Å, but it remains close to the value of graphene (1.43 Å). The C-H distance nearly remains unchanged, close to 1.09 Å. The tip was built from four layers of the fcc gold Au(111) with an 11.54 x 11.54 ($Å^2$) slab coupled to an apex cluster of four gold atoms (see Fig. (3.3b)). This tip has been used throughout the thesis, and only the apex cluster atoms have always been considered in Fireball-STM simulations. In this part, the Fireball-STM simulations have been done with a tip-sample distance of 4.1 Å in z-constant mode, and only the topmost layer of the gold surface and the GQD have been considered to speed up the calculations.

Figure (3.3c) shows that for the GQD S1 in vacuum, the 2NN TB method provides electronic structures (black curve) with an excellent agreement to the one found by Fireball DFT-LDA (red curve), which is not surprising as TB method is usually well suited for sp^2 carbon systems. We note that the top valence of the GQD S1 obtained by the 2NN TB has been aligned to the one obtained by Fireball DFT-LDA. In the presence of the gold surface, the GQD loses 0.9% its charges, so its energy states move to higher energy levels, depicted by the blue curve. The interaction between the GQD and the gold surface leads to new states around the individual peaks of the one in a vacuum; as a result, these have become broader. The energy gap is also reduced to 1.9 eV compared to the GQD S1 in the vacuum. Fig. (3.3d) illustrates the comparison of constant-height currents found by employing the 2NN TB model (1.21) (interpolated by using the Eq. (1.23)) and the Fireball-STM model (1.95). The constant-height current evaluated at -2.5 V, -1.9 V, 1.0 V, and 1.7 V by TB method is nothing else than the LDOS summed up from 0 V to the energy level of HOMO-2, HOMO-1 with HOMO, LUMO with LUMO$+1$, and LUMO$+2$, respectively, in Fig. (3.2b). We have probed only the two first peaks above the Fermi level. In comparison with Fireball-STM simulation images at -1.6 V, 1.0 V, 0.9 V, and 1.3 V, we figure out that in the presence of the gold surface, the density of states at HOMO-1 with HOMO (LUMO with LUMO$+1$, respectively) is moved to the HOMO-2 peak (LUMO$+2$, respectively). Moreover, it is laid out that the TB method yields results that show good agreement with those obtained using the Fireball-STM, especially for negative applied bias voltage, in which the unoccupied states are probed. The anti-bonding and bonding π^* and π states have been probed in these STM images. The dish-like signature of the GQD S1 shown in Fig (3.3d) has already been observed in [78, 87, 253].

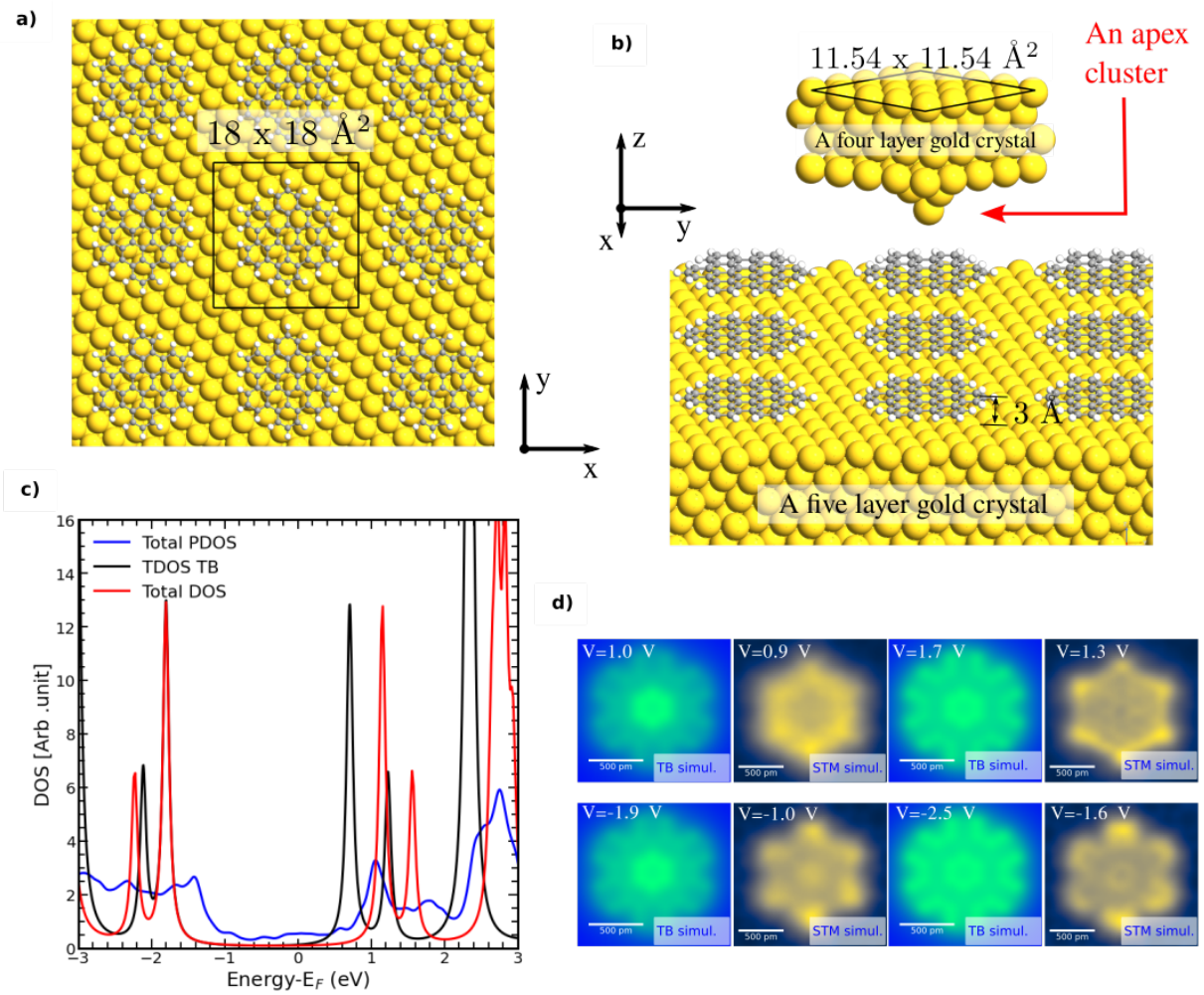

Figure 3.3 – STM simulation images of the GQD S1 on a gold (111) surface . a-b, Top view and side view of the GQD S1 deposited on a five-layer of 18 x 18 Å^2 square slab of the fcc Au(111), used in the Fireball DFT-LDA and -STM simulations. The primitive cell is displayed by a black square in **a**. In the top of **b**, the used tip's geometry in the thesis consists of four layers of a 5 x 5 periodicity crystal of the fcc Au(111) coupled to an apex cluster of four atoms. **c,** The total DOS of the GQD in vacuum achieved by Fireball DFT-LDA (red), TB method (black), and the PDOS of the GQD on the gold surface (blue). **d,** Comparison between the LDOS of the GQD S1 obtained by the 2NN TB model (1.21) and full STM simulations of the GQD S1 on the gold surface obtained by Fireball-STM model (1.95).

Finally, we will present the STM experimental images obtained by Dr. Sylvain Clair and his team from at IM2NP institute (IM2NP) in Marseille. First, in Fig. (3.4a), we display the deposited precursor of the GQD S1, tetrabromo-HBC (S1-4BNP), proposed by Dr. Daniel Medina-Lopez at CEA-NIMBE laboratory in Paris-Saclay. All the concerned synthesis details can be found in his thesis's manuscript [254]. Subsequently, Dr. Sylvain Clair *et al* deposited it on a gold Au(111) surface in an ultra-high vacuum (UHV). The STM experimental images were scanned with a tungsten tip coupled to the surface atoms at the apex.

Fig. (3.4b) illustrates a large-scale of the obtained surface after a deposition flow for 25 minutes

on a gold Au(111) surface at 100ºC, in which we observed the formation of hexagonal phase domains. Fig. (3.4c) depicts a small-scale surface on Fig. (3.4b) showing the hexagonal domains. In these domains, intact molecules are self-assembled and degraded molecules, as shown in Fig. (3.4g). In this figure, bromine atoms are observed to arrange themselves and surround the polycyclic aromatic molecules. Thus, the molecules are locked inside and limit their interactions. Fig. (3.4f) represents an intact molecule's zoomed image, comparable to our constant-height current STM simulation image scanned at 2.8 V (Fig. (3.4e)). The GQD width measured in Fig. (3.4f) is approximately 12 Å, in good agreement with the value of 13.67 Å obtained in the simulation shown in Fig. (3.4e). The main reason for the significant difference between the applied bias voltage in the experiment (5.0 mV) and simulation (2.8 V) is that the monomer has been doped by numerous bromine atoms surrounding it. On the other hand, some further investigations on the degraded molecules were done by our collaborators with a tip functionalized with CO; the measurements were performed on two adjacent molecules: one demonstrating hexagonal symmetry and the other with less symmetry, as shown in Fig. (3.4d). The Fig. (3.4d) suggests that the least symmetric structure aligns with the loss of a phenyl unit, causing the appearance of a degraded molecule.

There are several hypotheses to account for the origin of this degraded molecule. One hypothesis is that the degradation occurred during the deposition step. The sublimation process, part of the deposition, involves harsh conditions. The presence of bromine atoms in close interaction with the hydrogen atoms from the adjacent phenyl groups may cause precursor S1-4BP to be slightly distorted. Thus, it is not expected to give a hexagonal contrast. On the other hand, the more disordered domains stem from intact molecules (molecules whose bromine groups remain). Another possibility is that the degradation occurs once the precursor S1-4BP is adsorbed to the surface. The interaction of the precursor S1-4BP with the surface or other environmental factors after adsorption could contribute to its degradation. Finally, this degraded molecule could form as a byproduct of the Scholl reaction, a chemical reaction involving the oxidative coupling of aromatic compounds. The bromine atoms play a vital role in this experiment; they stabilize the GQD monomers and reduce their reactivity.

Finally, some zigzag areas with limited and uncontrolled GNRs were also observed after annealing the surface at 150ºC. However, only disordered coupling patterns were obtained when the surface was subsequently annealed at 250 ºC. We also observed fused dimers and triangular trimers on more active surfaces, such as a silver Ag(111) surface and a copper Cu(100) surface. The coverage ratio on these surfaces was significantly improved with respect to the one on the gold Au(111) surface. Further attempts at higher temperatures (at 500 ºC on the Ag(111) surface) have shown that messy uncontrolled polymerizations were obtained instead of higher-order polymers.

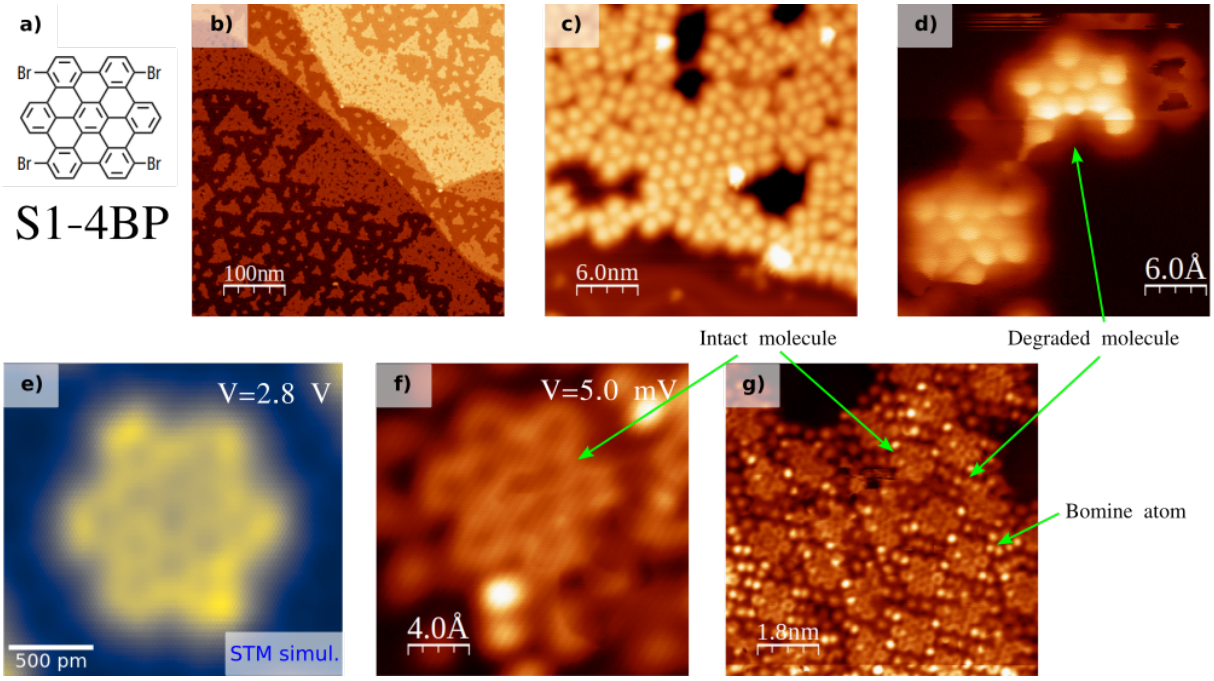

Figure 3.4 – Low temperatures (9 K) STM images on the precursor S1-4BP deposited on a heated Au(111) surface. a, The deposited precursor S1-4BP synthesized by Dr. Daniel Medina-Lopez at CEA-NIMBE laboratory in Paris-Saclay [254]. **b,** Large-scale image obtained after a deposition flow for 25 minutes on a gold Au(111) surface at 100ºC. **c,f,g** Zoom-in on **b**. **d,** Low temperature STM with CO tip image of a degraded molecule in **g**. These experimental STM images have been credited by Dr. Sylvain Clair at IM2NP institute (IM2NP) in Marseille. **e,** Constant-high current on the GQD C42 on the slab of gold Au(111) achieved by Fireball-STM simulation.

3.1.2 GNM C42 $(cmmm)$

Structure definition

As shown in the preceding part, we are not able to obtain a GNM from the precursor S1-4BP. In this part, we will present another precursor of S1, called S1-4BNP. The precursor S1-4BNP has four bromine atoms, as shown in Fig. (3.5). Our strategy is that once the S1-4BNP are deposited on a metallic surface, after the first low-temperature ($\sim$ 200℃) annealing of the surface, the bromine atoms will leave, and the left parts of each GQD will connect at the exact positions of the bromine atoms via the Ullman coupling. After the second higher-temperature ($\sim$ 400-500℃) annealing of the surface, the target GNM will finally be done via cyclodehydrogenation.

In crystallography aspect, the GNM C42 is considered as a centred rectangular lattice, with the superlattice vectors: $\mathbf{A}_1 = 5\mathbf{a}_1 - \mathbf{a}_2$ and $\mathbf{A}_2 = -\mathbf{a}_1 + 5\mathbf{a}_2$, as shown in Fig. (3.6a). In this case, the matrix M_{ij} can be written in this from:

$$M_{ij} = \begin{bmatrix} 5 & -1 \\ -1 & 5 \end{bmatrix} \tag{3.1}$$

in a basis of graphene's lattice vectors $\{\mathbf{a_1}, \mathbf{a_2}\}$ defined (1.11). The lattice parameter is 11.27 Å ($\sim 4.58\ a$ where a defined in 7), and the angle between the superlattice vectors is 81.79°. The GNM belongs to the layer group $cmmm$. It contains a glide reflection plane perpendicular to a crystallographic axis and three mirror plans along the directions $\mathbf{A_1} + \mathbf{A_2}$, $-\mathbf{A_1} + \mathbf{A_2}$, and z-axis. Additionally, it contains also order-two rotations and inversion symmetry.

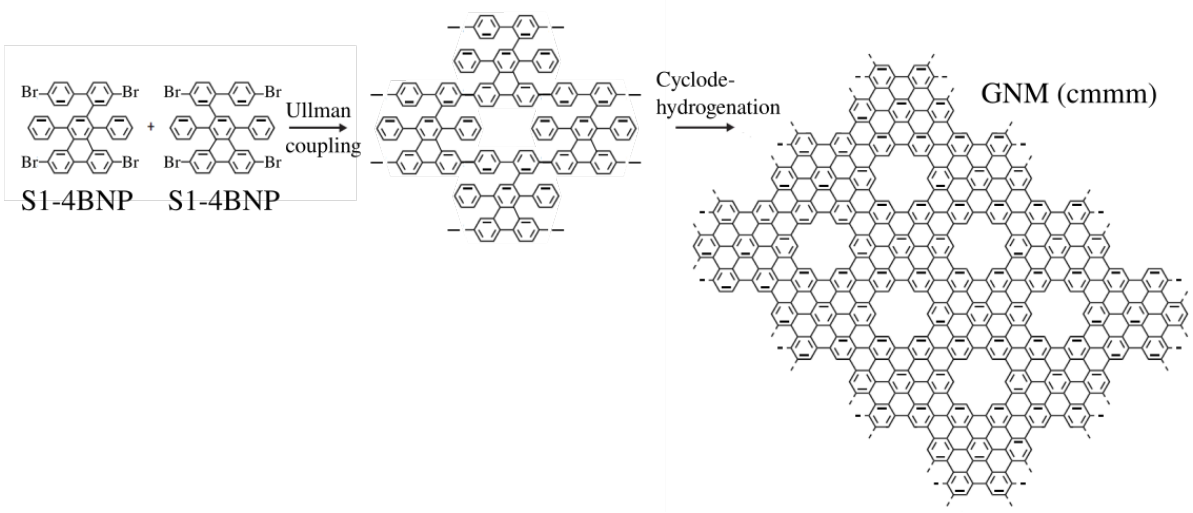

Figure 3.5 – Strategy scheme to achieve the target GNM C42 $(cmmm)$ on a metallic surface from deposited precursors S1-4BNP, proposed by Dr. Stéphane Campidelli at CEA-NIMBE laboratory in Paris-Saclay. All the synthesis details on the precursor S1-4BNP are discussed in [254].

Electronic properties of GNM C42 $(cmmm)$ and influence of the system size

In this part, we will present the electronic properties of GNM C42 and then how they vary as a function of system size.

(a) Infinite-size GNM :

Fig. (3.6b) illustrates the electronic band structure of the GNM obtained QE DFT-GGA (in black), GWA (in turquoise), Fireball-DFT-LDA (in red), and in TB method (in blue). In the presence of a network of holes in graphene, the sixfold rotational symmetry of graphene is destroyed. Thus, the 1BZ no longer has a hexagonal form, as shown in the center part of Fig. (3.6b). Moreover, a direct gap is observed in the GNM at Γ point. The creation of bandgap in GNMs is due to quantum-confinement and Brillouin zone folding that cause Dirac points of pristine graphene to be located at the Γ point, so the intervalley scattering removes the Dirac points and opens a bandgap at the Γ point. This was already observed in [143, 144, 146, 147, 149] . The value of the direct gap is found to be around 1.12 eV, 2.38 eV, 1.29 eV, and 1.09 eV by using QE DFT-GGA, QE DFT-GGA+GW, Fireball DFT-LDA, and TB method, respectively. With this gap width value, the GNM

C42 $(cmmm)$ can be classified as a semiconductor. Thus, this material would require photons with higher energy to excite electrons across the band gap. This means the material would absorb light in the ultraviolet and visible range, extending into the near-infrared region.

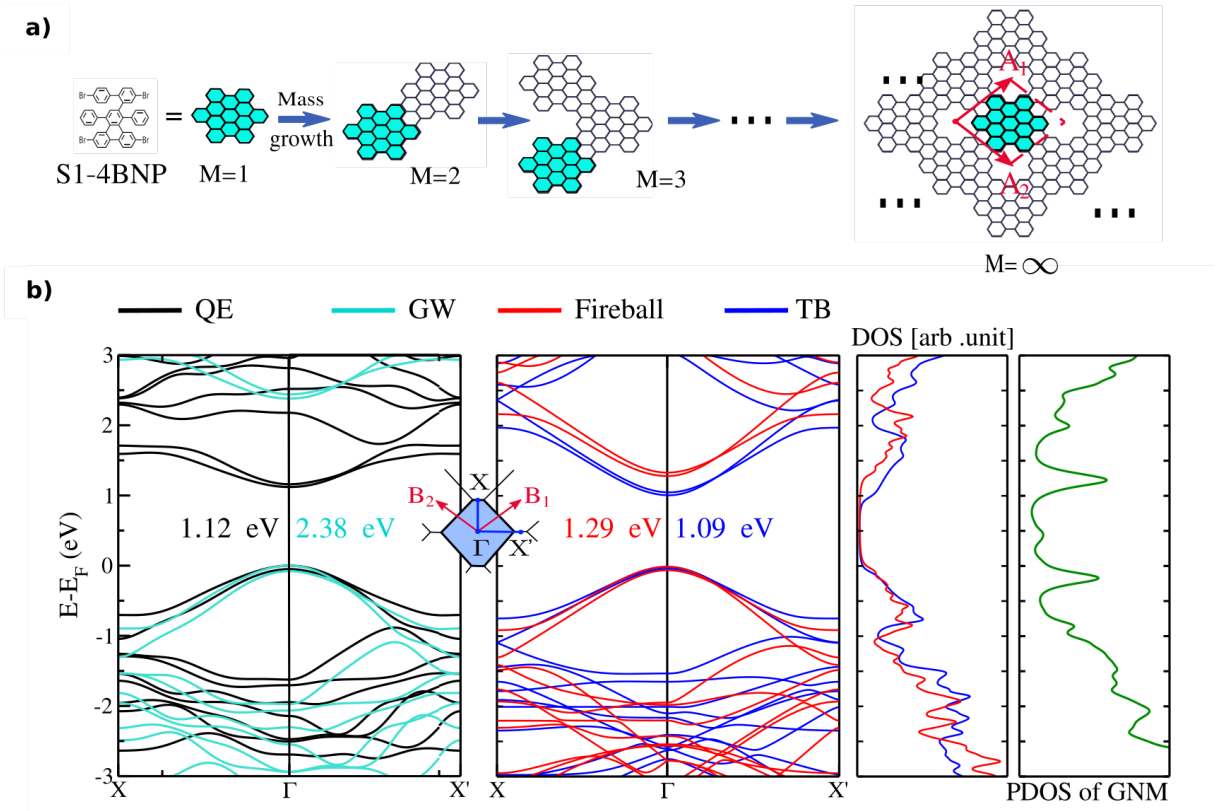

Figure 3.6 – Electronic structure of GNM C42 $(cmmm)$ made from the precursor S1-4BNP. a, Schematic model of the GNM C42 $(cmmm)$. **b,** (Left and center parts) Band structure of the GNM evaluated by Quantum Espresso DFT-GGA (QE) in black, GW Yambo in turquoise, Fireball DFT-LDA DFT in red, and TB method in blue. (Right parts) Total DOS of GNM in vacuum achieved by using Fireball DFT-LDA and projected DOS of GNM on on a five-layer of a 17.04 x 14.76 Å^2 rectangle slab of the fcc Au(111) surface, see later in Fig. (3.9). All the technical details are discussed in Appendix A.

As shown for GQD S1 (Tab. 3.1), the energy gap calculated by Fireball DFT-LDA is more significant than the one calculated by QE DFT-GGA. Besides, after GW corrections, the gap is approximately 2.12 times larger than the one calculated by QE DFT-GGA. Compared to GW band structure, all other methods preserve the behavior around the Fermi level at Γ point, such as the direct gap, no degeneracy, and the form of band structure. Additionally, a crossing between two lowest conduction bands in $\Gamma\mathbf{X}'$ path is respected, where the crossing is nearly at 3/10 of the length of $\Gamma\mathbf{X}'$ path by going towards $\mathbf{X}'$ point from Γ point. The structures of the two highest valence bands without crossing are also remarkably obtained. However, there exist some critical points that are worth pointing out. First, at the Γ point, the slope of the two lowest conduction band structures obtained by 2NN TB and Fireball DFT-LDA is visibly more significant. These bands

obtained by 2NN TB and Fireball DFT-LDA are not as flat near $\mathbf{X}$ and $\mathbf{X}'$. Moreover, the next higher conduction band is located at too high energy at Γ point. It crosses the next lower band near $\mathbf{X}'$ and the next higher band near $\mathbf{X}$, which is not observed in GW band structures. A similar tendency was observed for the next lower conduction bands. On the other hand, the electronic band structures obtained by QE DFT-GGA have the most agreement with GW band structures, which is understandable.

(b) Finite-size GNM :

In this part, we aim to answer the question, "Which size is a structure considered a two-dimensional crystal?". Thus, we want to reveal the change in our GNMs' electronic properties with the system's rising size by progressively adding mass to the precursor S1-4BNP (M).

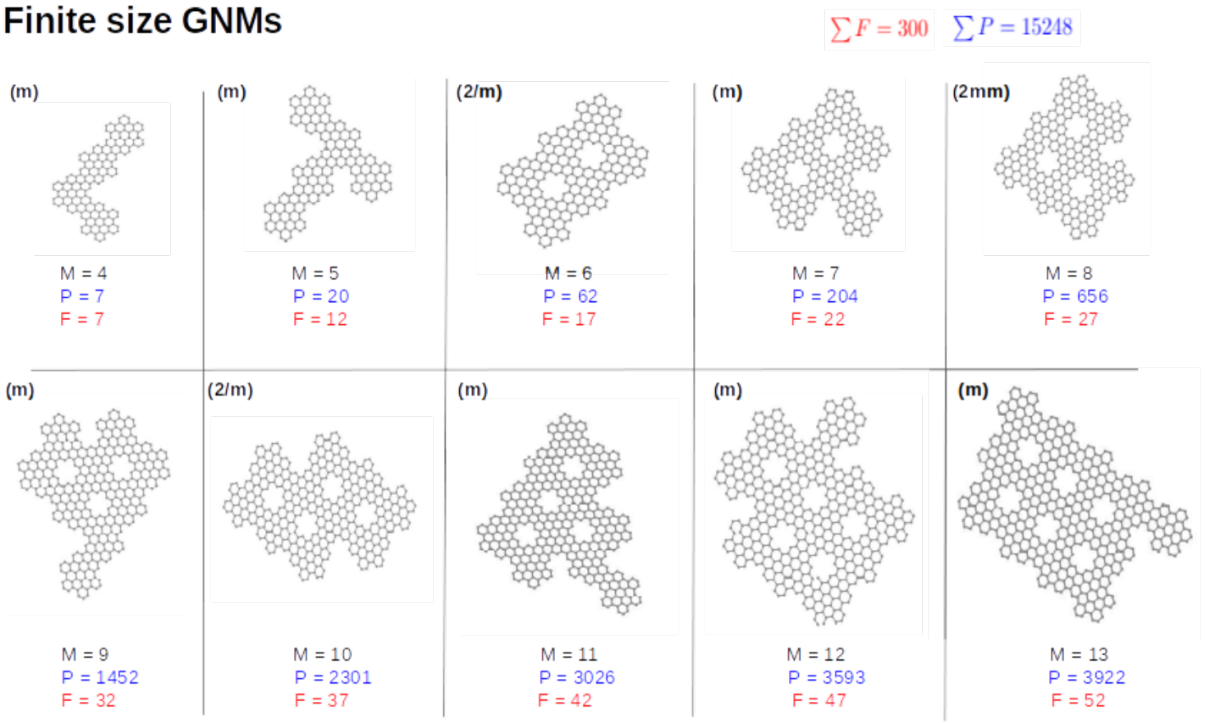

Figure 3.7 – Our studied structures created as function of masses of the precursor S1-4BNP (M) by using the random test. (in blue) **(P)** represents for the total number of possible geometries with respect to each value of mass, whereas (in red) **(F)** is the number of geometries used in our calculation. The geometry is an example for illustrative purpose.

Unlike the case of GNRs, where there is only one way to grow the size of the system, our GNM can be expanded in two different directions along the lattice vectors. As a result, for a given mass, the system can adopt many different geometries; for instance, if M=1 and M=2, there is only one possible structure; if M=3, there are three possible structures; however, the picture changes from M=4; in this case, there are seven possible structures... and so on. In the same manner,

the number of possible structures surges extremely quickly with increasing the mass M, and if we consider a system containing M=13, there are 3922 members of this family, as shown in Fig. (3.7). This issue is very complicated to deal with. For this reason, we created randomness tests for each value of mass in order to detect the repeated structures. First, the precursors will be randomly added using the GNM C42's lattice vectors (3.1) to obtain higher-mass molecules from those of a lower-mass family. Since many ways exist to obtain the same molecule, we count repeated molecule structures and call structure probability. The more a molecule structure is repeated, the higher the probability of obtaining this structure. Then, we considered only the most probable structures for the corresponding mass value in our study. In Fig. (3.7), we report the value of the mass of system M (in black), the number of members in the corresponding M-family (in blue), and the number of selected members in our study (in red). For instance, for M=7, we have considered only 22 structures over 204 possible structures in the 7-family. We stress that the most probable structures are in the sense of geometry, which means the number of structures having the same geometry in space and not in the sense of total energy of the system.

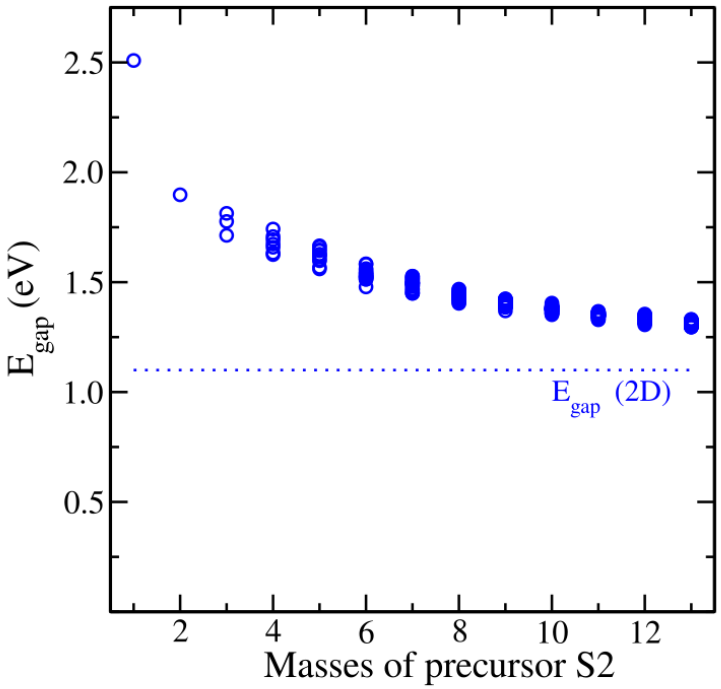

Figure 3.8 – Energy gap (HOMO−LUMO) as function of masses of precursor S1-4BNP (M) by using the random test, obtained by 2NN TB method. We have taken into account ($\mathbf{F}$) systems mentioned in Fig. (3.7).

Fig. (3.8) illustrates the energy gap (HOMO−LUMO) influenced by the mass of the precursor S1-4BNP obtained by the 2NN TB method. We obtain the same trend as Oliver Gröning *et al.* [160] obtained for the variation of electronic properties of armchair graphene nanoribbons (AGNRs) versus their size (in Supplementary materials). The energy gap is maximum at M=1, *i.e.*, when the system is just the GQD S1 shown Fig. (3.2), then rapidly decreasing in growing the number of mass up, and converges to the energy gap of the GNM shown in Fig. (3.6). It is exhibited that a system having thirteen masses of S1-4BNP behaves like a GNM C42 $(cmmm)$.

Comparison between STM experiments and simulations.

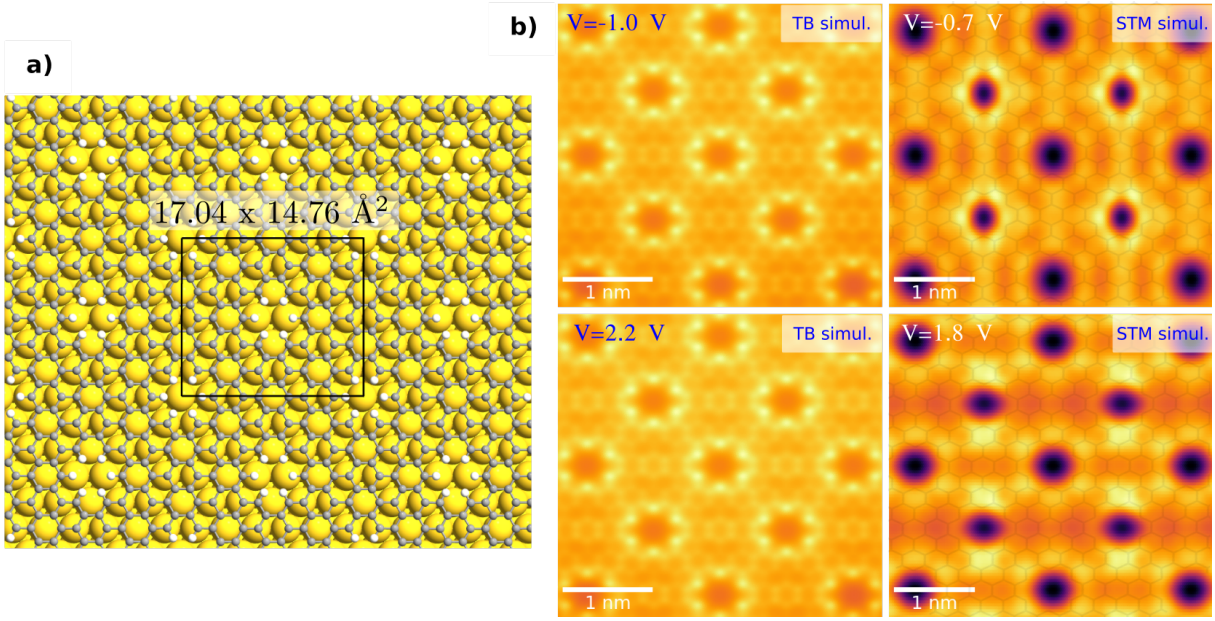

Figure 3.9 – Calculated LDOS and simulated STM images of the GNM C42 $(cmmm)$ on a gold Au(111) surface. a, Geometry of the GNM C42 $(cmmm)$ on a five-layer of a 17.04x14.76 Å^2 rectangle slab of the fcc Au(111). **b,** Comparison between STM simulations (left part) of the GNM on the gold surface, and the 2NN TB-LDOS of the GNM in vacuum (right part).

For STM simulations, we simulated the GNM C42 $(cmmm)$ on a five-layer of a 17.04 x 14.76 Å^2 rectangle slab of the fcc Au(111), achieved by Fireball DFT-LDA (see Fig. (3.9a)). There are 276 atoms in the rectangle primitive cell. The gold surface was compressed by 1.52% along the in-plane lattice vectors of gold Au(111). All our technical details are discussed in Appendix A. After the geometry relaxation processes, we checked that all resulting distances were equally good. The GNM has only lost 0.47% of its charge to the gold sample. Thus, its energy levels have slightly shifted to higher energies, as shown in the right part of Fig. (3.6b).

Fig. (3.9b) shows the constant-height current evaluated by TB and Fireball-STM methods. The

Fireball-STM simulations were done with a tip-sample distance of 4.55 Å. The anti-bonding and bonding (π^* and π) states are represented in this figure. In the presence of a network of pores, electrons tend to localize around each pore, which is captured by both Tight-Binding (TB) and Fireball-STM simulations. However, the gold surface plays a vital role in STM images in this case. As shown in Fireball-STM simulation images at -0.7 V and 1.8 V, one out of every two pores appears brighter than the other along the [100] and [010] directions of the GNM. The TB method does not capture this effect, as evidenced by the Local Density of States (LDOS) at -1.0 V and 2.2 V.

Dr. Sylvain Clair made several attempts at IM2NP Institute in Marseille, by depositing the precursor S1-4BNP on several different surfaces, such as a silver Ag(111) surface, a gold Au(111) surface, and a copper Cu(100) surface. Unfortunately, only disordered structures were produced with no exploitable results, as depicted in Fig. (3.10). Also, the precursor S1-4BNP was observed to have poor adsorption, leading to low coverage ratios. This behavior can be attributed to the inherent three-dimensional asymmetric nature of precursor S1-4BNP, which hinders its adsorption to the surface, leads to asymmetric couplings, and creates multiple configurations on the surface that cannot further link together as anticipated. For this reason, the precursor S1-4BP presented in Fig. (3.4a) has a better coverage ratio than the precursor S1-4BNP because it is more symmetric and "less" three-dimensional (planarized).

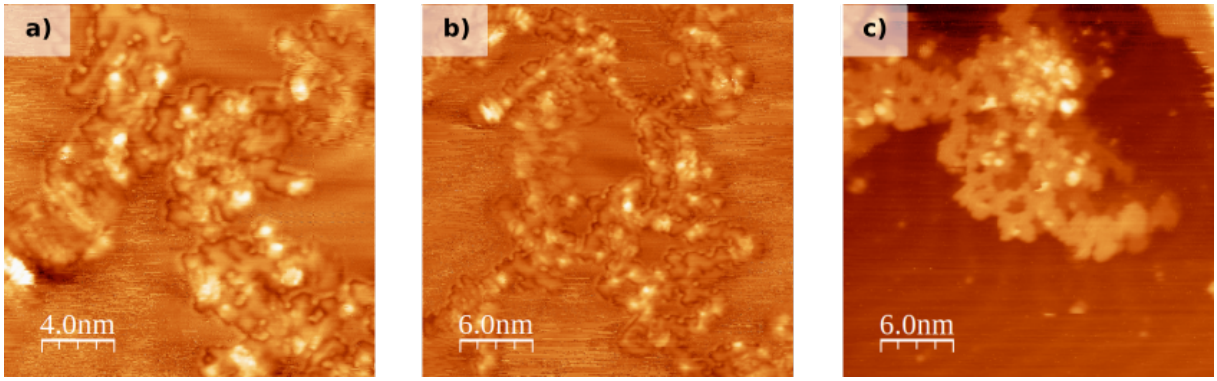

Figure 3.10 – Room temperature STM images of the molecule S1-4BP on Au(111) after a deposition flow for 10 minutes, credited by Dr. Sylvain Clair at IM2NP institute (IM2NP) in Marseille. a,b, Image obtained after a subsequent annealing at 250ºC. **c,** Image obtained after a subsequent annealing at 300ºC.

3.1.3 GNR C42 $(p2mg)$

Chevron-type GNRs from tetraphenyl-triphenylene monomers, named S1-2BNP, have successfully been synthesized by Jinming Cai *et al.* [100]. As shown in the preceding parts, the different precursors (S1-4BP and S1-4BNP) our collaborators tested did not yield the targeted GNRs or GNMs. To better understand whether the encountered synthesis limitations come from their deposition protocol, in this part,

they aim to reproduce previously published GNRs in Ref. [100]. Then, once the GNRs are successfully obtained, the GNM may be obtained by lateral fusion of the GNR. The precursor S1-2BNP was synthesized by Dr. Stephane Campidelli and his team at the CEA-NIMBE Laboratory in Paris-Saclay. All the synthesis details on the precursor S1-2BNP are discussed in [254].

Structure definition

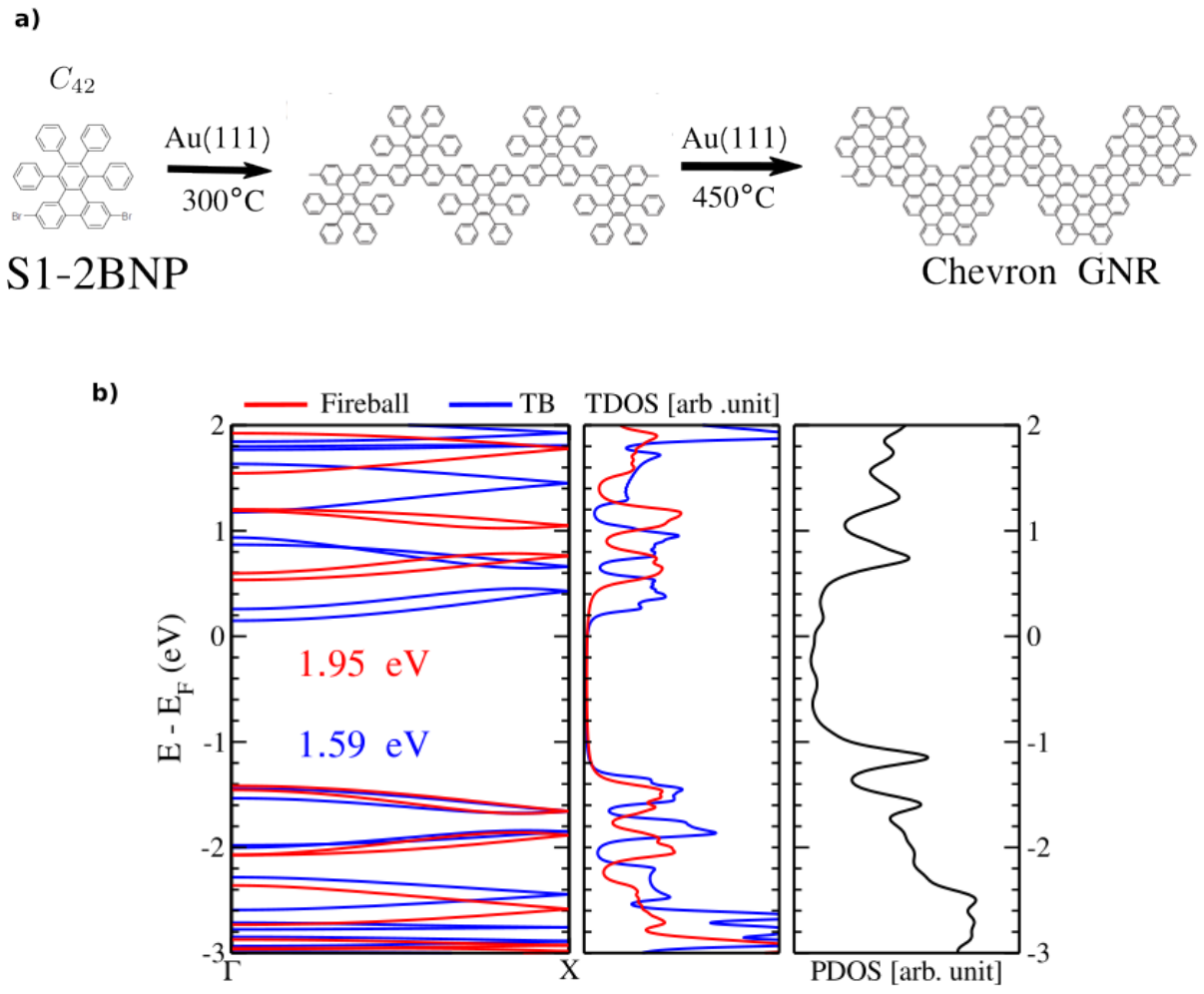

Figure 3.11 – Electronic structure of GNR C42 $(p2mg)$ **made from the precursor S1-2BNP. a,** Schematic representation of on-surface synthesis route from the monomer S1-2BNP to its GNR. **b,** (left and center parts) Band structure and total DOS of GNR calculated with Fireball DFT-LDA and 2NN TB method, and (right part) the projected DOS of GNR on the gold Au(111) surface (see later in Fig. (3.12b)) obtained by Fireball DFT-LDA.

Fig. (3.11a) shows the reaction scheme from S1-2BNP to chevron-type GNRs. Firstly, the dehalogenated intermediates, upon their initial binding to the Au(111) surface at a temperature of 300℃, undergo a colligation process, giving rise to chains. Within these chains, neighboring monomers exhibit a

distinctive feature – their orientations along the polymer main axis are opposite. After a second annealing step at 450℃, this step witnesses the intramolecular cyclodehydrogenation of the polymer chain, leading to complete aromatic GNRs. Our collaborators observed these reactions at IM2NP institute in Marseille and agreed with Ref. [100]. The resulting GNR belongs to the "frieze" group $(p2mg)$, so GNR is a primitive pattern with translational symmetry along the x-axis, two-fold rotational symmetry, mirror symmetry along the z-axis, and glide reflection symmetry along the x-axis. The super-lattice parameter is 17.04 Å ($\sim 6.93\ a$ where a defined in 7).

Electronic properties of GNR C42 $(p2mg)$

The electronic band structure and Total DOS of the GNR C42 $(p2mg)$ in a vacuum, calculated by the 2NN TB method (in blue) and Fireball DFT-LDA (in red), are illustrated in the left and center parts of Fig. (3.11b). The figure shows that the GNR is a semi-conductor, with a direct gap of 1.95 eV calculated by Fireball DFT-LDA and 1.59 eV calculated by the 2NN TB method. The direct gap is found at Γ point. All the technical details are discussed in A. These values are remarkably comparable to the one ($\sim$ 1.6 eV) using QE DFT-GGA obtained by Jinming Cai *et al.* [255] and Mehdi Pour *et al.* [256]. It is worth noting that since the performance of the 2NN TB method depends principally on t_{AB} and $\xi^{(2)}_{AA}$, as shown in 1.3, in this case, we can provide better parameters than the ones (t_{AB} = $-$2.7 eV, $\xi^{(2)}_{AA}$ = 0.27 eV) used in this thesis for all carbon materials, but it is not our goal here.

Comparison between STM experiments and simulations.

For STM simulations, we mismatched the GNR C42 $(p2mg)$ on a five-layer slab of 17.04 x 25.0 (Å^2) rectangle supercell of gold Au(111) (see Fig. (3.12b)). The rectangle primitive cell consists of 408 atoms. The Au-Au distance is compressed by 0.3$\%$ along the first lattice vector of Au(111). All our technical details are discussed in Appendix A. After relaxation, we checked that all resulting distances were equally good. The GNR lost 0.66$\%$ of its charge to the gold surface, which explains why the PDOS of GNR shifted to the higher energy levels, as depicted in the right part of Fig. (3.11b).

Fig. (3.12a) displays the projected band structure of backbone atoms (in green), evaluated by the 2NN TB method via the Eq. (1.19) (interpolated by using the Eq. (1.23)), where the thickness of the lines and the color—black (lower) to light yellow (higher)—denotes the magnitude of PBND$^a_{nj}(\mathbf{k})$. Contrary to preceding works [160, 257], which focused on the edge-extended atoms of GNRs, in this report, we have highlighted the backbone atoms. In this case, the projected band structure into the edge-extended atoms was obtained 19$\%$ of the magnitude less critical than one of the backbone atoms. As a result, this effect has been seen in STM images. Fig. (3.12c) compares constant-height current images calculated

by 2NN TB and Fireball-STM simulations. The Fireball-STM simulations were performed with the tip-distance height constant of 5.05 Å. This figure neatly shows the strong signature of the backbone parts, depicted by its brighter color than the edge parts. Besides, this effect was witnessed in STM experimental images, as depicted in Fig. (3.13).

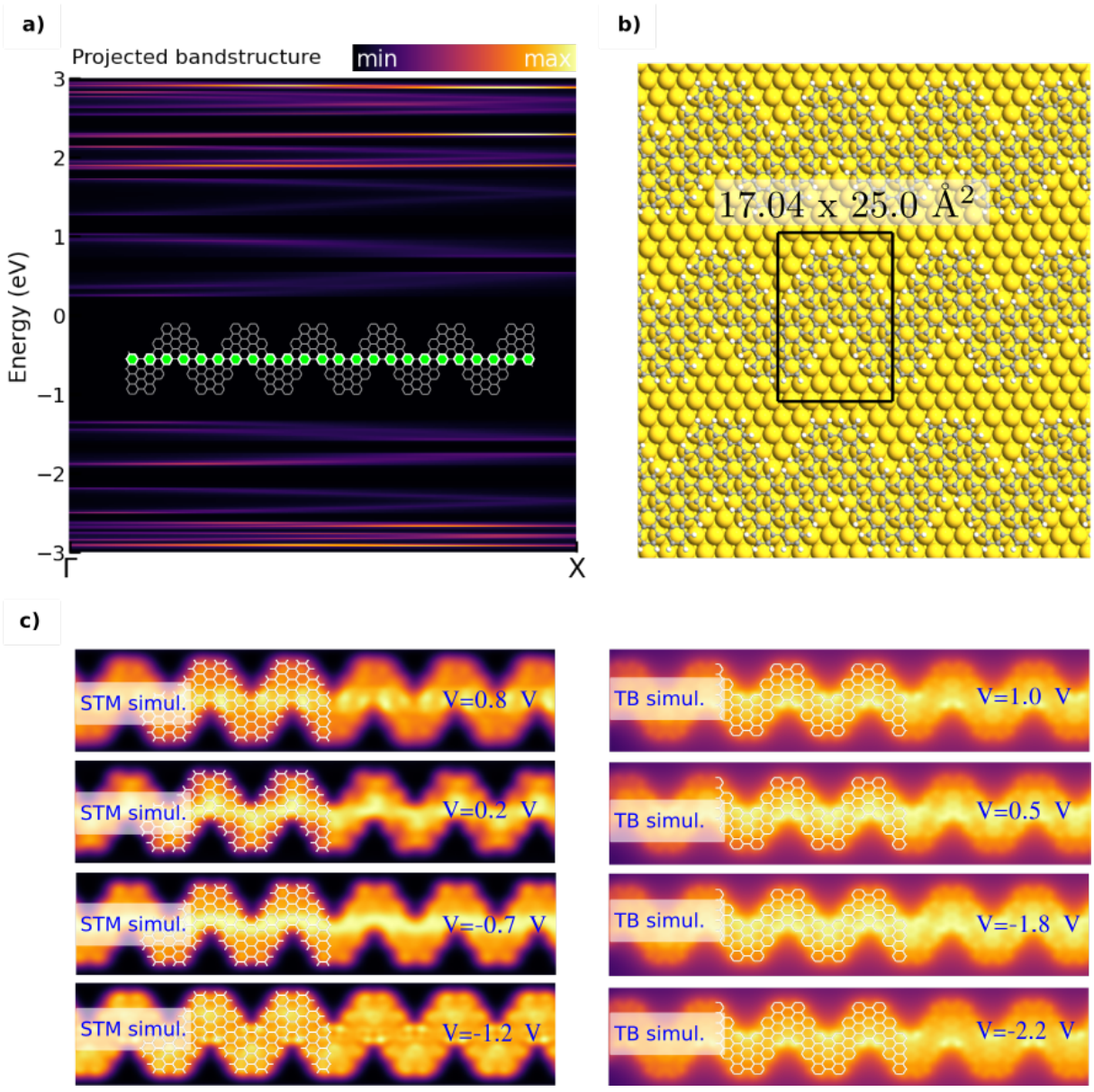

Figure 3.12 – STM simulation images of GNR C42 (p2mg) made from the precursor S1-2BNP. a, Projected band structure of backbone in green shown in center part of **a**. **b,** Geometry model of the GNR C42 $(p2mg)$ on a five-layer of a 17.04 x 25.0 Å^2 rectangle slab of the fcc Au(111). **c,** Comparison between STM simulations of the GNR on the gold surface, and the TB-LDOS of the GNR in vacuum.

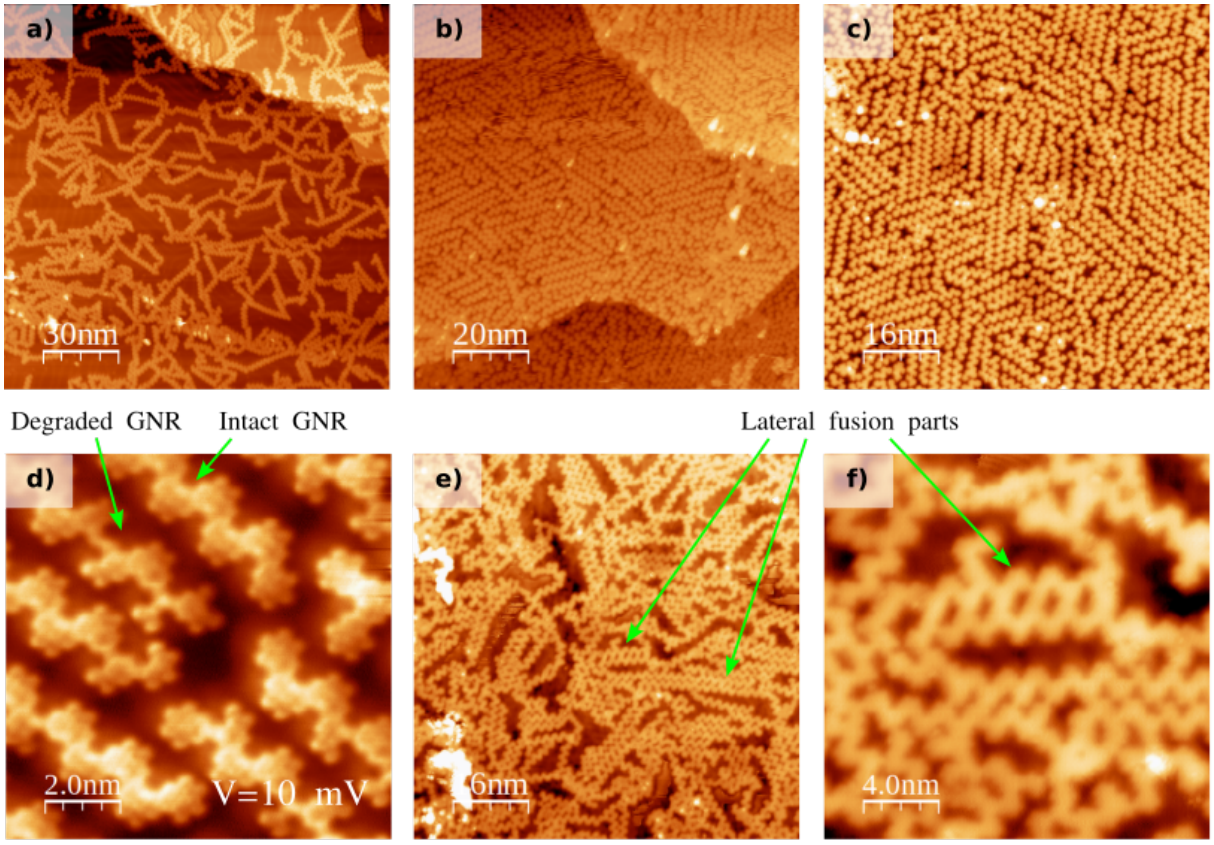

Figure 3.13 – Low-temperature (9 K) STM images of chevron type GNR C42 $(p2mg)$ **obtained from the precursor S1-2BNP, credited by Dr. Sylvain Clair at IM2NP institute (IM2NP) in Marseille. a,** Image obtained after a deposition flow for 5 minutes on an Au(111) room temperature surface followed by three subsequent annealing at 300℃ for 10 minutes, at 450℃ for 10 minutes, and at 500℃ for 20 minutes. **b,** Image obtained after a deposition flow for 10 minutes on an Au(111) room temperature surface followed by annealing at 450℃ for 22 minutes. **c,** Zoom-on on **b**. **d,** Zoom-on on **c**. **e,** Image obtained after a deposition flow for 10 minutes on an Au(111) room temperature surface followed by two subsequent annealing at 450℃ for 22.5 minutes, and at 550℃ for 20 minutes. **f,** Zoom-on on **e**.

Fig. (3.13) displays the low-temperature STM images of complete chevron-type GNRs on a gold Au(111), obtained by our collaborators at IM2NP institute in Marseilles. The Fig. (3.13a) is achieved after a deposition flow for 5 minutes on a gold Au(111) at RT, with following three subsequent annealing at 300℃, at 450℃, and at 500℃ for 40 minutes in total; in which our collaborators observed the long intact GNRs on the surface. Fig. (3.13b-d) illustrate the large- and small-scale STM images obtained after a deposition flow for 10 minutes on a gold Au(111) at RT, with the following three subsequent annealing at 450℃ for 22 minutes. These figures show that, unfortunately, the GNRs are not very long; their average length is approximately 17 nm. On the other hand, we observed the degraded and intact GNRs, as shown in (3.13d). Our collaborators re-obtained the bright signature of backbone atoms as shown in STM simulation images (3.12c). Fig. (3.13) shows that they succesfully recover the chevron-type GNR from S1-2BNP as done in Ref. [100]. In final step, our collaborators attempted to get the

lateral fusion of the GNR by heating at higher temperatures (at 550℃) for longer times. Unfortunately, only localized lateral fusion zones but not the entire length of GNR were observed (see Fig. (3.13e-f)). Uncontrolled graphitization rather than inter-molecular cross-coupling increased the temperature and the deposition time again.

3.1.4 Conclusion

We have studied the change of electronic, optical, and transport properties of the family of C42 D_{6h} $(6/mmm)$ with respect to the system size and symmetry. Compared to graphene $(p6/mmm)$, the translational symmetry is obviously lost in the GQD C42 (S1), and the system behaves like a confined box. As a result, energy levels are discrete leading to a electronic gap. However, the sixfold rotational symmetry is preserved, leading to a sparse absorption spectrum in the S1 GQD. In the presence of a network of pores GNM C42 $(cmmm)$ on graphene, the high symmetry of order six has been lost; thus, a direct gap is open. The GNR C42 $(p2mg)$ is even poorer in symmetry, and a direct gap has similarly been opened. According to the change of their properties concerning the system size, the larger the system is, the smaller the energy gap is. In terms of transport properties, electronic localization varies with the system's changes; for instance, they are mainly localized in the edge for the GQD, whereas around pores for the GNM and in the backbone part for the GNR.

Our TB and Fireball DFT have proven remarkably accurate results around the Fermi levels (from -2 eV to 2 eV, approximately) and provided accurate electronic, optical, and transport structures with good agreement with experimental data. Unfortunately, the production of the targeted GNMs built from the molecule HBC using the molecules S1-4BP, S1-4BNP, and S1-2BNP has not been successful. Since the partially fused precursor S1-4BNP is asymmetric, three-dimensional characteristics hinder its adsorption on the metallic substrate. Thus, S1-4BNP has a bad coverage ratio. Therefore, a complete fusion of S1-4BNP proceeded, and S1-4BP was built. After deposition on different surfaces, S1-4BP was observed to have a better coverage ratio, especially on the more active surfaces than Au(111), such as Cu(100) and Ag(111). An ordered network of the monomers S1 surrounded by the free bromine atoms was observed, in which bromine atoms play a vital role; for instance, they stabilize the monomers and limit their reactivity. Several dimers and trimers were also observed, and the attempts of higher-order polymers failed by raising the annealing temperature and the deposition time. Instead, messy and uncontrolled polymerizations were obtained. Finally, our collaborators deposited S1-2BNP on those three different surfaces; we aimed to obtain chevron-type GNRs in the first step, then fuse the GNRs laterally to get GNMs by heating them at high temperatures for a long time. In the first step, we obtained the desired GNRs seen in the literature. The latter has shown that the experimental setups are good, and

the issue is with the designed molecules. Unfortunately, limited lateral fusion zones were observed after annealing at 550 ℃, and uncontrolled graphitization was unexpectedly witnessed at higher temperatures for longer times. Our attempts to get GNMs using these methods were unsuccessful.

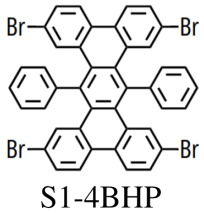

Figure 3.14 – New proposed precursor S1-4BHP proposed by Dr. Daniel Medina-Lopez [254].

In perspective, the symmetric nature of new proposed precursor S1-4BHP may allow for better adsorption and controlled coupling than the ones observed for the precursor S1-4BNP, which differs from S1-4BNP only by a C-C bond (see Fig. (3.14)). Besides, the absence of bonds locking the central phenyl units may diminish the steric hindrance described before and allow for a better coupling at the predefined sites, which leads to the target GMM after the cyclodehydrogenation process.

3.2 The family of trapeze-shaped GQD C30 $C_{2v}(2mm)$

3.2.1 Trapeze-shaped GQD C30 $C_{2v}(2mm)$

Structure definition

In this part, we will show our simulation and experimental studies on the GQD C30 ($C_{30}H_{16}$) labeled S2 (see Fig. (3.15b)). Compared to the GQD S1, the GQD S2 has two carbon rings less, yielding an isosceles trapezium form. So, the symmetry of order six is lost; the GQD belongs to the point group $(2mm)$. It has a rotational invariance of order two around the y-axis and two mirror plans m_x, m_z. By comparison to the previous the GQD C42 (S1), this reduced symmetry has direct effects on its properties.

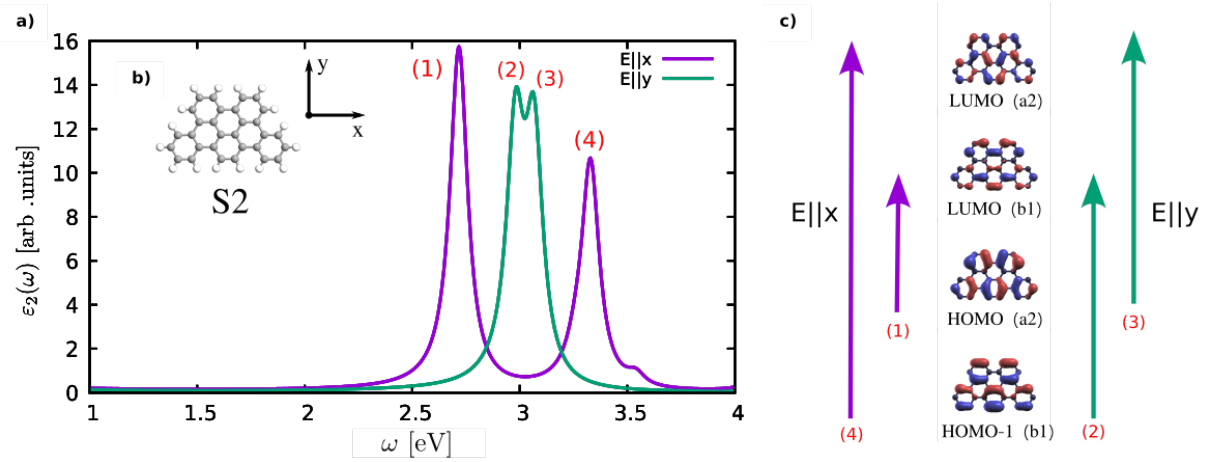

Figure 3.15 – Optical properties of GQD C30 $(2mm)$ **obtained by 2NN TB method using the set of parameters presented in Tab. 1.3. a,** IP RPA-TB absorption spectrum. **b,** Geometry of the GQD C30 $(2mm)$ labeled S2. **c,** Frontier orbitals of the GQD S2.

Optical properties

Fig. (3.15a and c) illustrate the IP RPA-TB absorption spectrum of the GQD S2 (C30) and its irreducible representation of frontier orbitals. Compared to those of the GQD S1 (C42) in Fig. (3.2b and c), the shortened GQD S2 has a pronounced effect induced by symmetry lowering from D_{6h} to C_{2v} point group. The doubly degenerate frontier orbitals of the GQD S1 (both HOMO and LUMO) are split in the GQD S2 (HOMO and HOMO-1, LUMO and LUMO$+1$). Since the geometry of GQD is nonequivalent along $x-$ and y-axes, that induces a different parity for HOMO and HOMO-1, as well as for LUMO and LUMO$+1$, as shown in Fig. (3.15c). The split states result in split peaks in the absorption spectrum in Fig. (3.15a). Moreover, if the electric field $\mathbf{E}$ is polarized along the longitudinal x-axis of the GQD, $\mathbf{E}$ has the irreducible representation b_2. In this case, only the transitions between $a_2 \rightarrow b_1$ and $b_1 \rightarrow a_2$ are allowed by symmetry; hence, they are the transitions HOMO$\rightarrow$LUMO with the energy 2.72 eV, and HOMO$-1\rightarrow$LUMO$+1$ with the energy 3.33 eV, denoted **(1)** and **(4)**, respectively in the Fig. (3.15a). In the same way, if the electric field $\mathbf{E}$ is polarized along the transversal y-axis of the GQD, $\mathbf{E}$ now has the irreducible representation a_1. Thus, the allowed transitions are between $b_1 \rightarrow b_1$ and $a_2 \rightarrow a_2$, such as the transitions HOMO$-1\rightarrow$LUMO with the energy 2.98 eV, and HOMO$\rightarrow$LUMO$+1$ with the energy 3.1 eV, denoted **(2)** and **(3)**, respectively. In the Fig. (3.15a), the distinction between the peaks **(2)** and **(3)** is about 0.12 eV. We stress that, unlike the case of the GQD S1 (C42), the optical response of the GQD S2 (C30) is not the same in changing the direction of polarization.

Comparison between STM experiments and simulations.

To obtain STM simulation images, we deposited the GQD S2 on a five-layer slab of 36 x 16 ($Å^2$) periodicity of Au(111) as shown in Fig. (3.16b). The Au-Au distance has been compressed with the following tensors: 0.42% and -1.11% along the in-plane lattice vectors of Au(111). There are 487 atoms inside the primitive cell depicted by the black rectangle in Fig (3.16b). All relaxation criteria remain unchanged, such as the two bottom layers of gold Au(111) have been fixed, and all the calculations have been performed with Γ point only (see Appendix A). After geometry relaxation, we verified that all the resulting distances are equally good.

Fig. (3.16a) shows the TDOS of the S2 GQD in vacuum, evaluated by the 2NN TB method (in black) and Fireball-DFT method (in red) and the projected DOS of the GQD on the gold Au(111) surface. For the GQD in a vacuum, each Carbon atom contributes four valence electrons, while each Hydrogen contributes only one electron. Thus, the GQD has a total of 136 electrons. In the presence of the gold surface, the GQD has only 134.62 electrons; the GQD thus lost 1.01% its charges to the gold surface. This explains the shift of its PDOS structure towards higher energy compared to the TDOS structure of the GQD in the absence of the gold surface (red curve). On the other hand, the black curve calculated by the 2NN TB method agrees well with the red curve calculated by Fireball DFT-LDA. This agreement has also been seen in STM simulation images of the GQD S2. Fig. (3.16c) illustrates the constant-height current images calculated by 2NN TB and Fireball-STM simulations. The constant-height current images described by the LDOS and calculated by the 2NN TB method probed the first three peaks at -2.8 eV, -2.4 eV, -2.1 eV below, and also at 1 eV, 1.4 eV, 2.0 eV above zero energy level on a black curve in the Fig. (3.16a). These anti-bonding and bonding π, π^* states have been shown in Fireball STM simulations at -1.8 V, -1.6 V, -1.2 V for the negative voltage and at 0.8 V, 1.2 V, 1.8 V for the positive voltage, as shown in the Fig. (3.16c). The energy gap of the GQD C30 was calculated as approximately 2.72 eV by the 2NN TB method and 3.19 eV by Fireball DFT-LDA. The energy gap was reduced to approximately $\lesssim$ 2.0 eV in the presence of the gold surface. We figured out that, likely in the GQD S1 (C42) case, the 2NN TB method provides accurate results, especially for negative bias voltage. In the presence of a gold surface, the density of states of the first peaks above and below zero energy level, respectively, loses a part of its intensity to the subsequent peaks at higher and lower energy levels, respectively

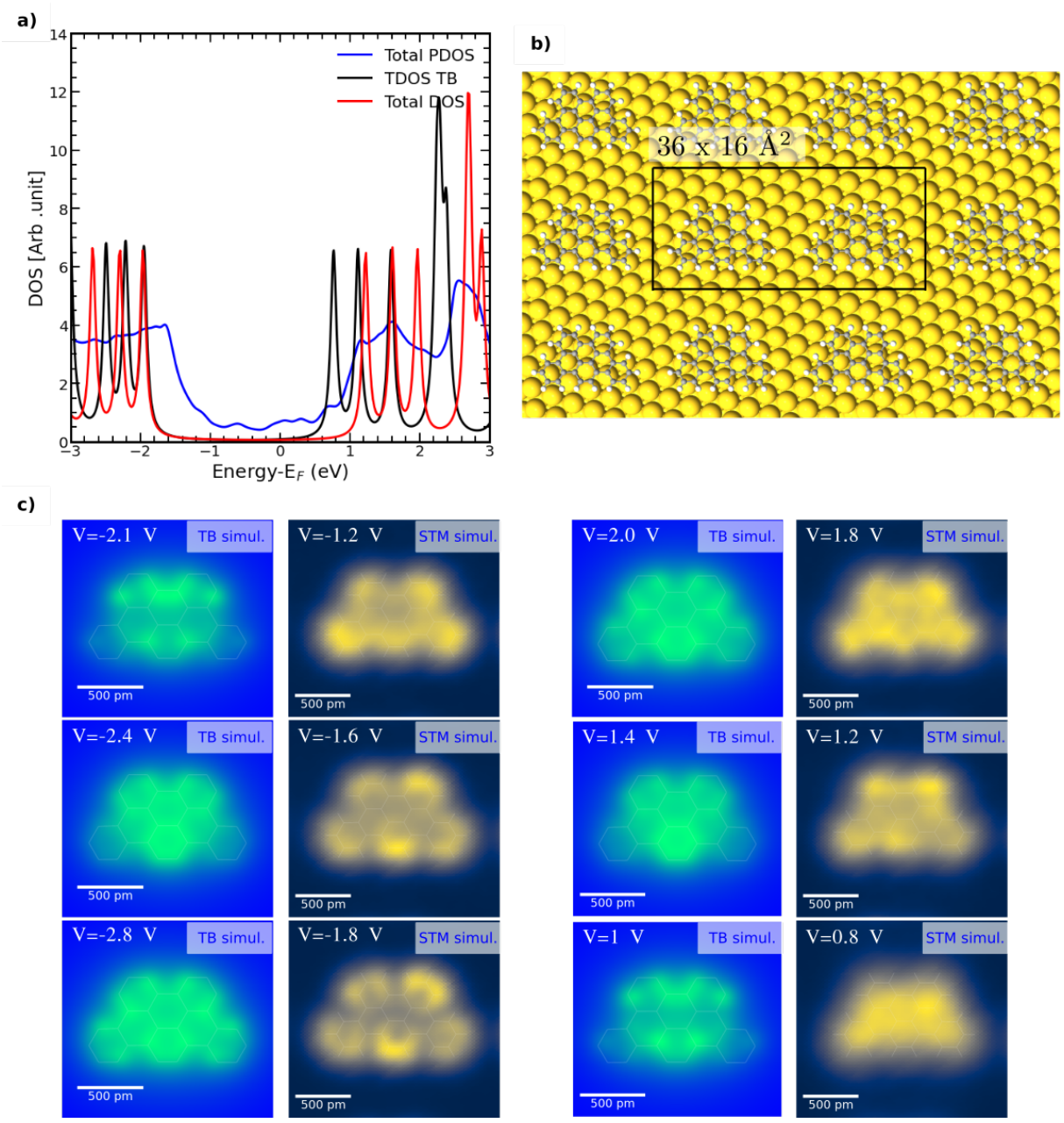

Figure 3.16 – Transport structure of the GQD S2 $(2mm)$**. a,** Total DOS of the GQD in vacuum calculated with Fireball DFT-LDA (in red), 2NN TB method (black), respectively; and PDOS of the GQD on a gold surface Au(111) presented in **b**. **b,** Geometry model of the GQD S2 $(2mm)$ on a five-layer slab of 36 x 16 (Å^2) periodicity of Au(111). **c,** Comparison between the LDOS of the GQD obtained by 2NN TB method and constant-height-current images obtained by Fireball-STM simulations of the GQD on the gold surface.

Our collaborators, Dr. Sylvain Clair and his team at IM2NP in Marseille deposited precursor S2-2INP on a Cu(100) surface to explore its behavior on this reactive surface. The precursor S2-2INP was synthesized by Dr. Daniel Medina-Lopez at CEA-NIMBE laboratory in Paris-Saclay [254].

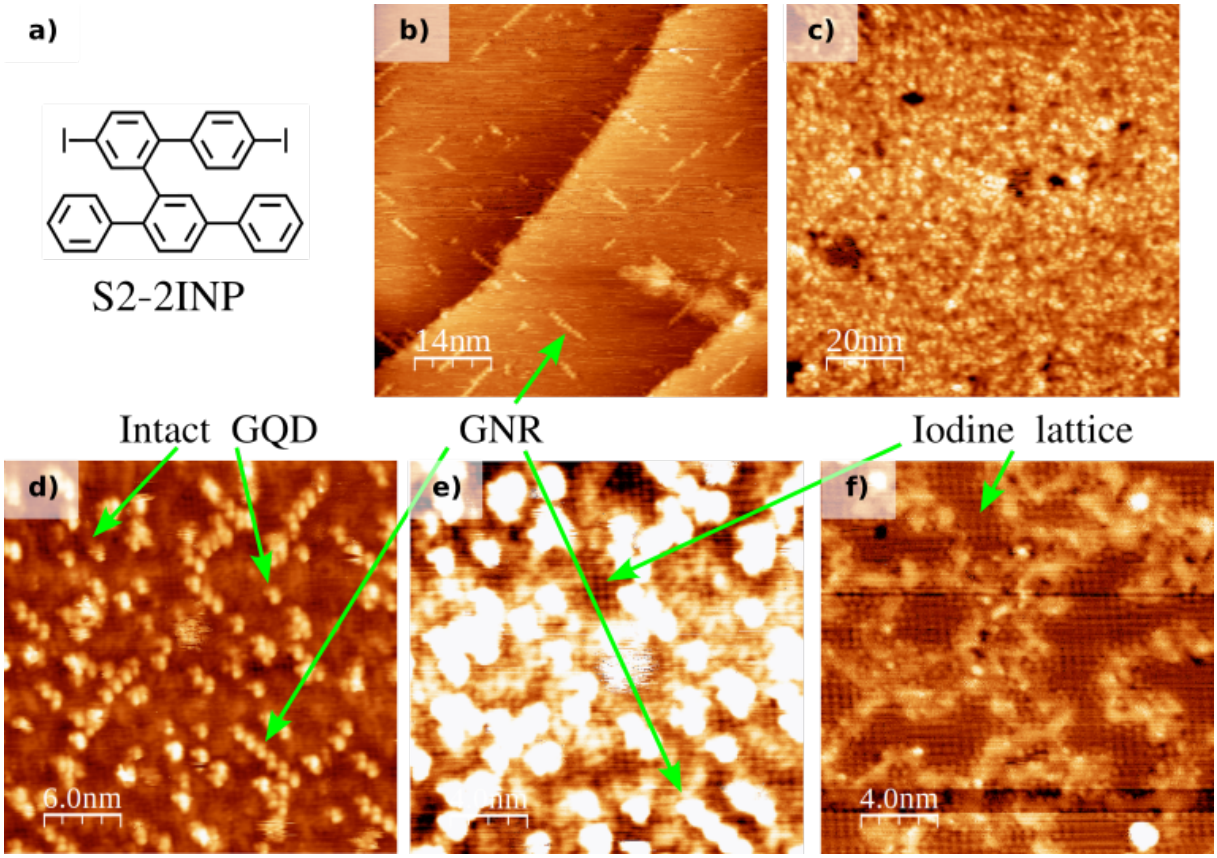

Figure 3.17 – Room temperature STM images of precursor S2-2INP on copper Cu(100) surface, credited by Dr. Sylvain Clair at IM2NP institute (IM2NP) in Marseille. a, Geometry of precursor S2-2INP. **b,** Image obtained after 2 minutes of deposition on a surface at room temperature. **c,** Image obtained after 10 minutes of deposition on a surface at room temperature. **d,** Image obtained after 4 minutes of deposition on a hot surface at 200ºC. **e,** Zoom in on a small surface of **d** with increased contrast. **f,** Image after annealing the surface at 300ºC.

The first depositions took place on a surface at room temperature. Low coverage was achieved after 2 minutes of deposition. Nevertheless, the C-C coupling reaction occurred even at room temperature, as shown in Fig. (3.17b). In this figure, limited nanoribbons formed by a few monomers were observed, and they are smaller than 10 nm with a periodicity of 1.1 nm. Fig. (3.17c) shows the surface obtained after 10 minutes of deposition; full coverage was achieved but without any supramolecular arrangement of molecules. The cyclodehydrogenation was attempted by annealing the surface to 300ºC. However, only disordered planarization was obtained.

Further attempts were made on a hotter surface, at 200ºC (instead of RT). The resulting surfaces are presented in Fig. (3.17d-e). In these figures, a disordered network of intact GQDs S2 was observed. Unfortunately, since the temperature of the room was not as low as used in the previous experiments (at 4 K) for the family of C42 $D_{6h}(6/mmm)$, it has not been possible to obtain an atomic image of the GQD S2. However, even at these large scanned surfaces, we can still identify the similar signatures

calculated by Fireball-STM simulations shown in Fig. (3.16c). Moreover, only small nanoribbons with a length of 5-6 nm and a periodicity of 1.1 nm were also observed, as depicted in the Fig. (3.17d-e). In the Fig. (3.17e), some lattices of iodine atoms appeared on the surface. The significant excess of iodine atoms indicates that the precursors principally desorb from the surface, and full coverage is not possible, which is not beneficial to the growth of large GNRs. Upon further annealing of the surface at 300ºC, planarization is only achieved in a disordered fashion (Fig. (3.17f)).

These studies demonstrated that it is possible to reassemble the precursors S2-2INP to chevron nanoribbons on the copper Cu(100) surface. However, deposition at higher temperatures promotes the desorption of the precursor, leaving behind its iodine atoms. No additional surfaces were tested for this precursor, as even less reactive surfaces may allow for additional control of the reaction; the friability of the carbon-iodine bond makes similar results possible.

3.2.2 GNR C30 $(p2mg)$

Structure definition

Our chemist collaborators, Dr. Stéphane Campidelli and Dr. Daniel Medina-Lopez, at the CEA-NIMBE laboratory in Paris-Saclay, decided to switch to the synthesis of brominated precursors because carbon-bromine bonds are more robust than carbon-iodine bonds. They proposed the precursor S2-2BNP containing two bromine atoms laying in its longitudinal x-axis, as shown in Fig. (3.18). Once the precursors S2-2BNP are deposited on a metallic surface, the target chevron-type GNR will be obtained via on-surface Ullmann coupling and cyclodehydrogenation after multiple annealing cycles in a similar way to form the GNR C42 $(p2mg)$ shown in (3.11a).

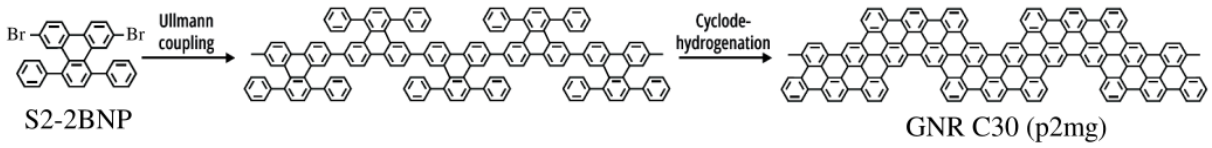

Figure 3.18 – Strategy scheme to obtain the target GNR C30 $(p2mg)$ on a metallic surface from deposited precursors S2-2BNP, proposed by Dr. Stéphane Campidelli at CEA-NIMBE laboratory in Paris-Saclay. All the synthesis details on the precursor S1-4BNP are discussed in [254].

The GNR C30 belongs to the same "frieze" group as the GNR C42 $(p2mg)$. Additionally, the superlattice parameter remains unchanged with respect to the one of the GNR C42 (p2mg); it is equal to 17.04 Å ($\sim 6.93\ a$ where a defined in 7). We remind that in this thesis, we always choose the longitudinal direction along the x-axis.

Electronic properties of GNR C30 $(p2mg)$ and influence of the system size

In this part, we will perform the same studies as for the GNM C42 $(cmmm)$ to explore the variation of electronic properties of the GNR C30 $(p2mg)$ with the system size.

(a) Infinite-size GNR :

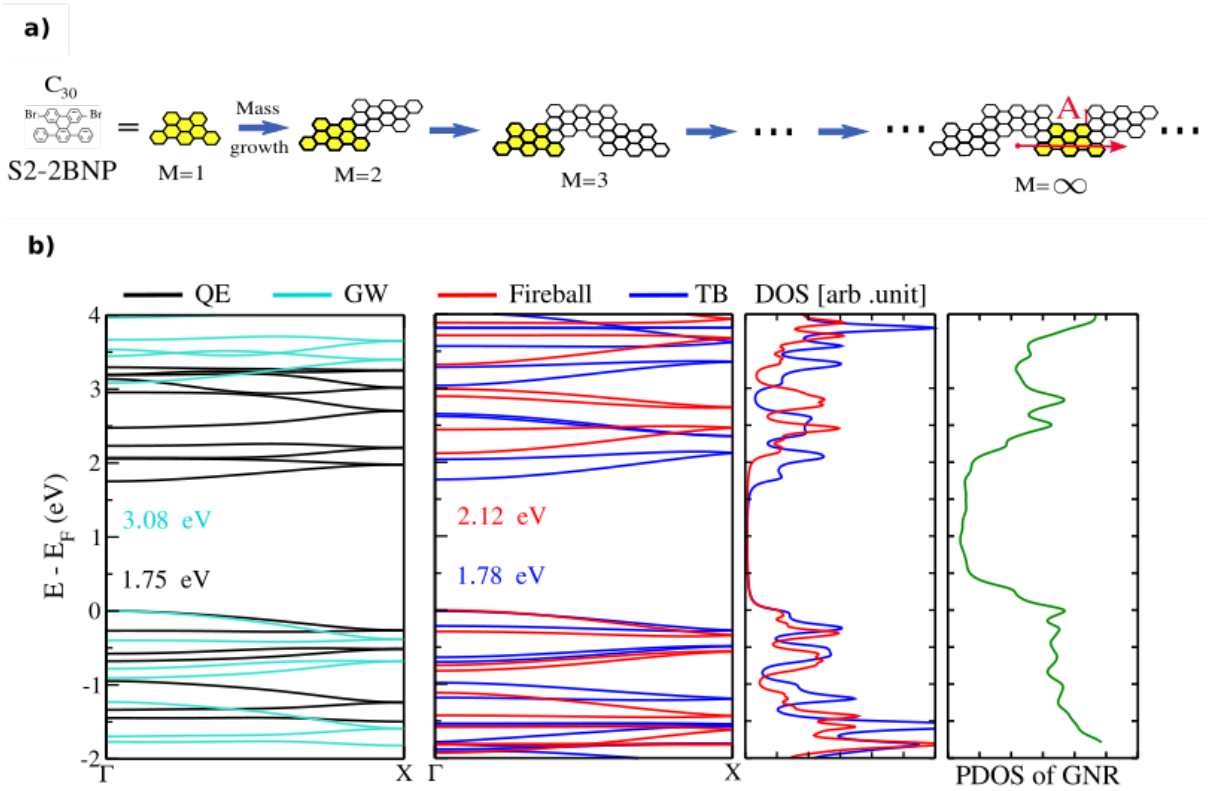

Figure 3.19 – Electronic structure of the GNR C30 $(p2mg)$**. a,** Schema of masses growth from a precursor S2-2BNP to an infinite GNR C30 $(p2mg)$. **b,** (Left parts) Band structure of the GNRs calculated by GWA method (in turquoise), Quantum Espresso DFT-GGA (in black), LDA-Fireabll DFT (in red), and 2NN TB method (in blue). (Right Parts) Total DOS of GNR in vacuum achieved by using Fireball DFT-LDA and projected DOS of the GNR on the gold Au(111) surface presented later in Fig. (3.21a).

The left part of Fig (3.19b) illustrates the electronic band structure of the GNR C30 $(p2mg)$ calculated by QE DFT-GGA (in black), GWA (in turquoise), Fireball DFT-LDA (in red), and 2NN TB (in blue) methods. This figure shows that these methods lead to a direct gap at Γ. Differently to the case of GQDs, although the precursor S2-2BNP has two carbon rings less than the precursor S1-2BNP, the chevron GNR C30 $(p2mg)$ has very similar electronic band structures with the chevron GNR C42 $(p2mg)$ shown in Fig. (3.11b). By reducing just two carbon rings less in the transversal direction, the former exhibits a more significant band gap (1.78 eV on 2NN TB band gap) than the latter (1.59 eV on 2NN TB band gap). On the other hand, the energy gap value is equal to 1.75

eV by QE DFT-GGA, 3.08 eV by GWA, 2.12 eV by Fireball DFT-LDA, and 1.78 eV by the 2NN TB method. Compared to the QE DFT-GGA gap, the corrected GWA gap is about 1.76 times bigger. This correction ratio is observed to be accurate for GNRs, compared to one published by Mehdi Pour *et al.* [256] on the chevron GNR C42 ($p2mg$). The TB gap is close to the QE DFT-GGA one, whereas the Fireball DFT-LDA gap is the closest to the corrected one, with an error of 31.17%. In terms of band structure's geometry, since the corrected GWA gap was calculated based on QE DFT-GGA data, the QE DFT-GGA band structure is the most accurate compared with the TB and Fireball DFT-LDA ones. The TB and Fireball DFT methods again provide very consistent occupied bands. On the other hand, these methods work well for energy below 2.5 eV and get worse for energy above 2.5 eV.

(b) Finite-size GNRs :

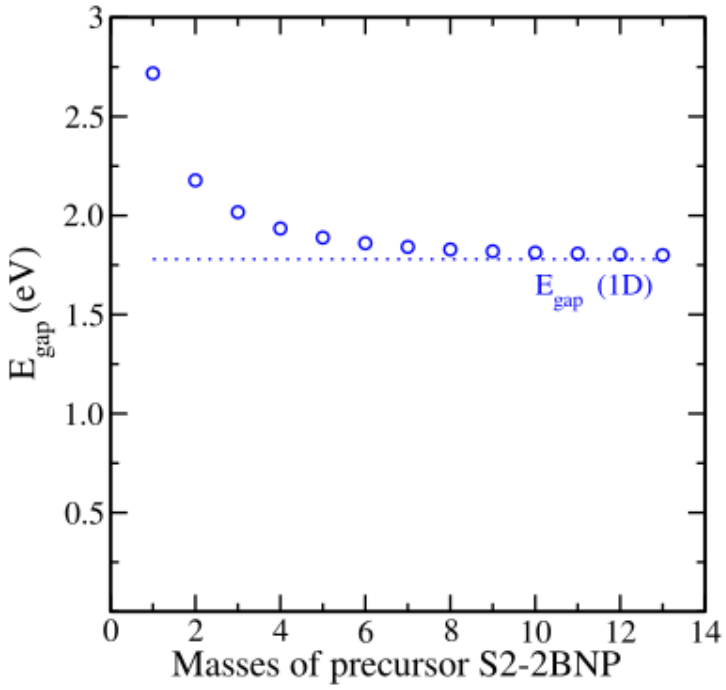

Figure 3.20 – Energy gap (HOMO−LUMO) as function of masses of precursor S2-2BNP (M) obtained by 2NN TB method.. In the case of GNRs, the masses can only be added in a unique direction.

Fig. (3.19a) represents the schematic model of the GNR in increasing the mass of precursor S2-2BNP (M). Fig. (3.20) represents the evolution of the energy gap (HOMO−LUMO) with respect to the mass of precursor S2-2BNP evaluated by the 2NN TB method. This case is different from the

case of GNM C42 in the Fig. 3.1.2 since we can add the mass in only one direction, there is only one possible structure for a given mass, as shown in (3.19a). In this case, the energy of the gap of M-order of polymer converges very fast to the one of an infinite GNR; for instance, if the system is 8-order polymer ($\sim$ 6.8 nm), that can be nearly considered as the infinite GNR, as its energy gap is close to that of the infinite GNR C30.

Comparison between STM experiments and simulations.

To characterize the transport properties of GNR C30 $(p2mg)$, we theoretically deposited it on a five-layer slab of 34.64 x 16 (Å^2) supercell of the fcc gold Au(111) (see Fig. (3.21a)). In this case, we compressed the gold surface by 1.13$\%$ and 0.51$\%$ along the in-plane lattice vectors of gold Au(111). The primitive cell consists of 555 atoms in total. After the geometry relaxation processes, all resulting distances were verified to be equally good. In the presence of the gold surface, the GNR has only lost 0.69$\%$ of its charges to the gold sample. Thus, its energy levels have slightly shifted to higher energies, as shown in the right part of Fig. (3.19b).

Fig. (3.21b) exhibits constant-height-current STM simulation images obtained by the 2NN TB method (right part) and the Fireball-STM method (left part). These images were obtained under a tip-sample height constant of 5 Å. In the 2NN TB simulations, we probed the first two peaks of the blue curve TDOS in the Fig. (3.19b) at -0.98 eV and -0.48 eV below and 2.22 eV, 2.82 eV above the zero energy level. In the presence of the gold surface, these states can be retrieved at -0.55 V and -0.15 V for the negative bias voltage and 2.45 V and 3.25 V for the positive voltage. Contrary to the case of GNR C42 discussed in 3.1.3, this figure shows that the 2NN TB method can only cover the main feature of the full STM simulation results. We note that the presence of the gold surface and, especially, the contribution of extended-edge atoms of the GNR play a nonneglected role in this case. The reason is probably due to the reduction of the extended-edge atoms along the transversal direction from the GNR C42 to the GNR C30.

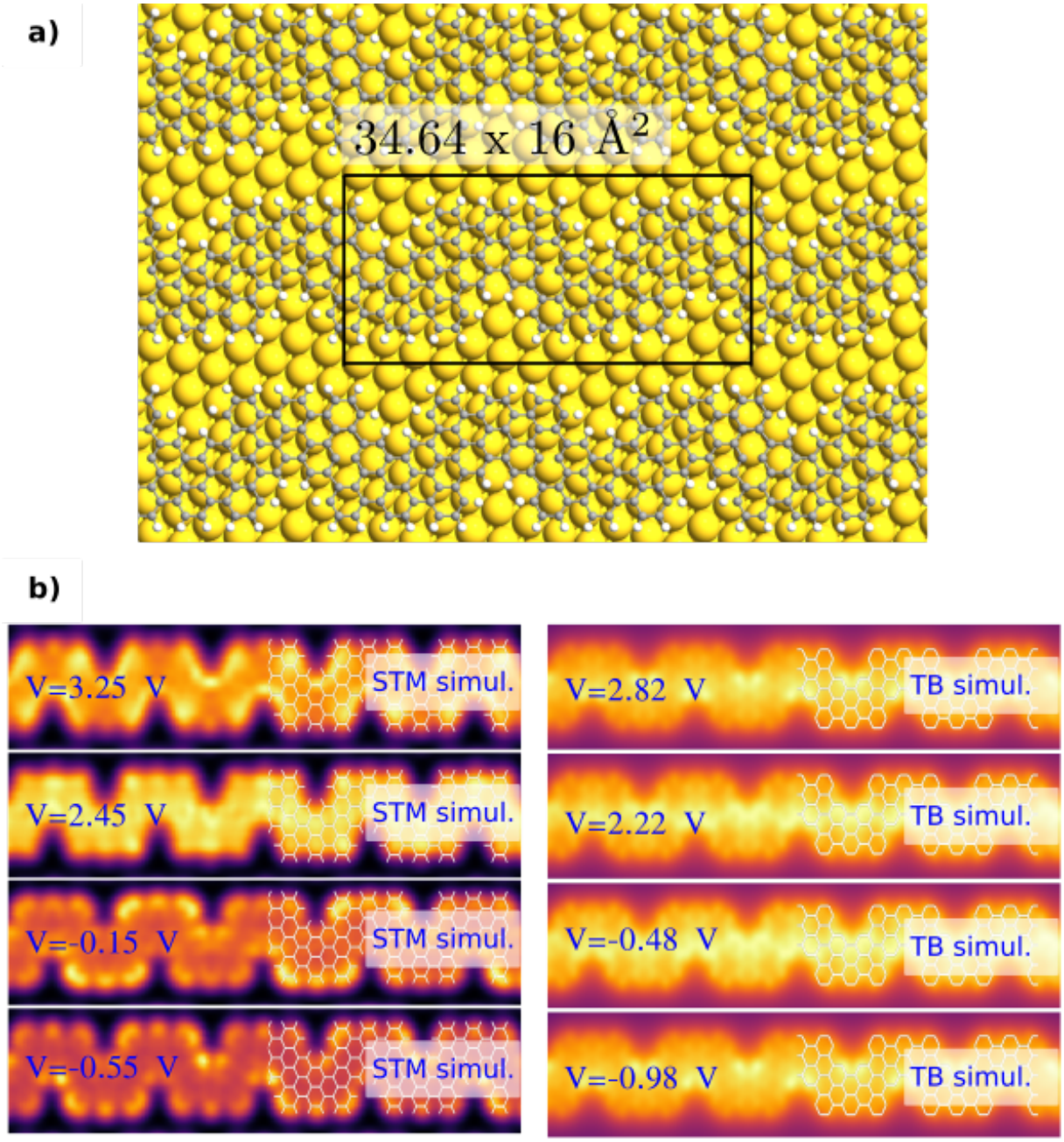

Figure 3.21 – Transport structure of the GNR C30 $(p2mg)$**. a,** Schematic model of the GNR C30 $(p2mg)$ on a five-layer slab of 34.64 x 16 (Å^2) supercell of the fcc gold Au(111). **b,** Constant height current achieved by 2NN TB simulation (right part) and Fireball-STM simulation (left part).

Fig. (3.22) shows low-temperature STM images obtained after the physical deposition of precursor S2-2BNP on the gold Au(111) surface, performed by our collaborators at IM2NP institute in Marseille. Initial deposition at room temperature resulted in low coverage, as shown in Fig. (3.22a). Precursors were arranged in monomers and supramolecular dimers or trimers, and limited organization and coverage were achieved at this temperature. In order to promote C-C coupling, precursor S2-2BNP was deposited on a hotter gold surface at 200ºC, as depicted in Fig. (3.22b). As a result, we observed higher

coverage compared to room temperature deposition. Nevertheless, small linear arrangements were observed, with a width limited to the size of one stacking phase of the herringbone reconstruction of the gold surface. Furthermore, our collaborators also attempted to deposit precursor S2-2BNP on a slightly hotter surface at 250ºC, as presented in (3.22c). In this case, uncontrolled polymerizations and small domains showed chevron-like configurations, especially limited to the size of one stacking phase of the herringbone reconstruction. Fig. (3.22d) illustrates the surface obtained after a long deposition flow for 100 minutes on a hot gold surface at 150 ℃ with a subsequent annealing at 400 ℃. Since only disordered planarization was observed, the expected cyclodehydrogenation or lateral fusion did not occur, as presented in this figure. There is the possibility of achieving larger nanoribbons by using a more reactive surface, such as Ag(111). However, in general, our results seem to diverge significantly from previous reports of on-surface GNR synthesis [255, 258–260], in which long nanoribbons with high coverage and a small number of defects were achieved.

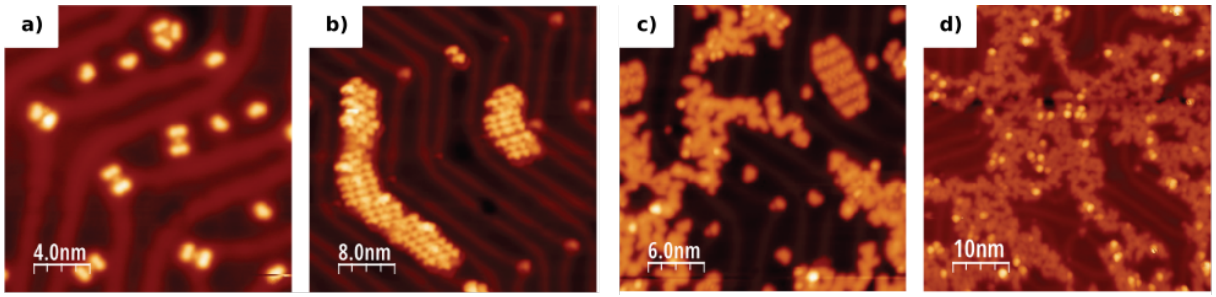

Figure 3.22 – Low-temperature (9 K) STM images of compound S2-2BNP on the gold Au(111) surface, credited by Dr. Sylvain Clair at IM2NP institute (IM2NP) in Marseille. a, Image obtained after a deposition flow for 1 minute on an Au(111) surface at room temperature. **b,** Image obtained after a deposition flow for 1 minute on a gold Au(111) surface at 200 ℃. **c,** Image obtained after a deposition flow for 30 minutes on a gold Au(111) surface at 250 ℃. **d,** Image obtained after a deposition flow for 100 minutes on a gold Au(111) surface at 150 ℃ and subsequent annealing at 400 ℃.

3.2.3 Conclusion

We have shown evidence of the change in the electronic, optical, and transport properties of the C30 family with respect to size and symmetry of superstructures. Compared to GQD C42 (S1), the GQD C30 (S2) has two carbon rings less, and its symmetry group does not contain the sixfold rotational symmetry of the system. This reduced symmetry directly affects the optical properties of GQD; for instance, the double degeneracy of frontier orbitals of GQD C42 does not exist anymore, leading to the split of two different states in the GQD C30 system. Since the geometry of GQD C30 is not identical along the longitudinal and transversal directions, these split states were moved to different energy levels. The latter explains the split peaks in the absorption spectrum of GQD C30. We have also shown that by increasing the mass of the precursor of GQD C30 progressively, the energy gap decreases progressively

to the one of an infinite GNR; this behavior was observed in the case of GNM C42. Contrary to the case of GQD, which depicts having two carbon rings less, the GNR C30 still belongs to the same symmetry group as the GNR C42, and it has electronic band structures that are remarkably similar to the GNR C42. In terms of transport response, the GNR C30 has shown very similar features to the GNR C42. Since the GNR C30 is a semi-conductor with a direct gap, thus it is also very promising. Unfortunately, in the experiment, the deposition of precursors S2-2INP and S2-2BNP on copper Cu(100) and gold Au(111) surfaces showed that the reaction is complicated, in which only small domains of GNRs are obtained co-existing with the disordered domain. The GNRs were observed to be significantly shorter than those in references, even on the active surface like copper. The tested precursors have a bad coverage ratio on these surfaces, the attempts of longer GNRs were fruitless, and only disordered planarization was achieved.

3.3 Triangular-shaped GQDs T C96 $D_{3h}(\overline{6}m2)$

Structure definition

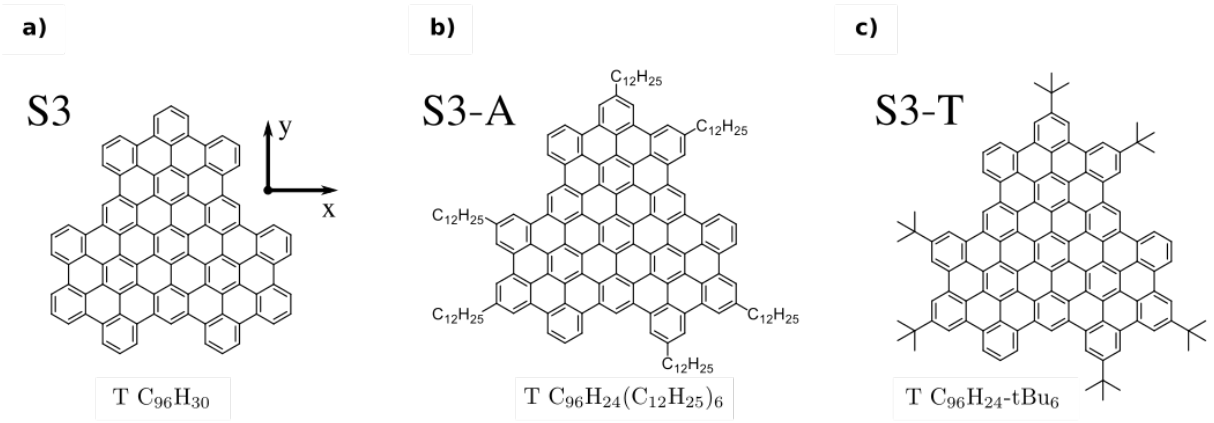

Figure 3.23 – Geometry of the studied triangular-shaped GQDs. **a,** Non-functionalized GQD T $C_{96}H_{30}$ (S3). **a** Functionalized GQD with six tert-butyl groups $C_{96}H_{24}$-tBu_6 (S3-T). **c,** Functionalized GQD with six alkyl chains $C_{96}H_{24}(C_{12}H_{25})_6$ (S3-A).

Our collaborators, Dr. Stéphane Campidelli, Dr. Julien Lavie, and Daniel Medina-Lopez at CEA-NIMBE laboratory in Paris-Saclay area, proposed to study bigger-size GQDs which are the triangular-shaped GQDs (T): non-functionalized GQD $C_{96}H_{30}$ (labeled S3); the functionalized GQDs $C_{96}H_{24}$-tBu_6 (labeled S3-T) and $C_{96}H_{24}(C_{12}H_{25})_6$ (labeled S3-A), as shown in Fig. (3.23). The S3 belongs to the point group $(\overline{6}m2)$ and has an improper rotation "$\overline{6}$" concerning the z-axis, a mirror plan along transversal direction m_y, and a twofold rotational symmetry concerning the y-axis. At the same time, the GQDs S3-T and

S3-A have six functionalized tert-butyl groups and alkyl chains, respectively, placed strategically as presented in Fig. (3.23). All synthesis details were discussed in [254, 261].

Optical properties

The first experiment was done with the GQD S3 on different solvents such as toluene, N-methyl pyrrolidone (NMP), 1,2,4-trichlorobenzene (TCB), and surfactants like sodium cholate (SC) or sodium deoxycholate (SDC). We figured out that the best dispersants are TCB and SDC, but because of the large size of S3, GQDs were observed to form aggregates in solution, reducing the absorption measurement performance. Therefore, we tested the functionalized GQD C96 (S3-A and -T). They exhibited apparent solubility in usual solvents like dichloromethane, chloroform, toluene, and tetrahydrofuran; although aggregate forms still occurred in solution [261], they proved better sp^2 behaviors.

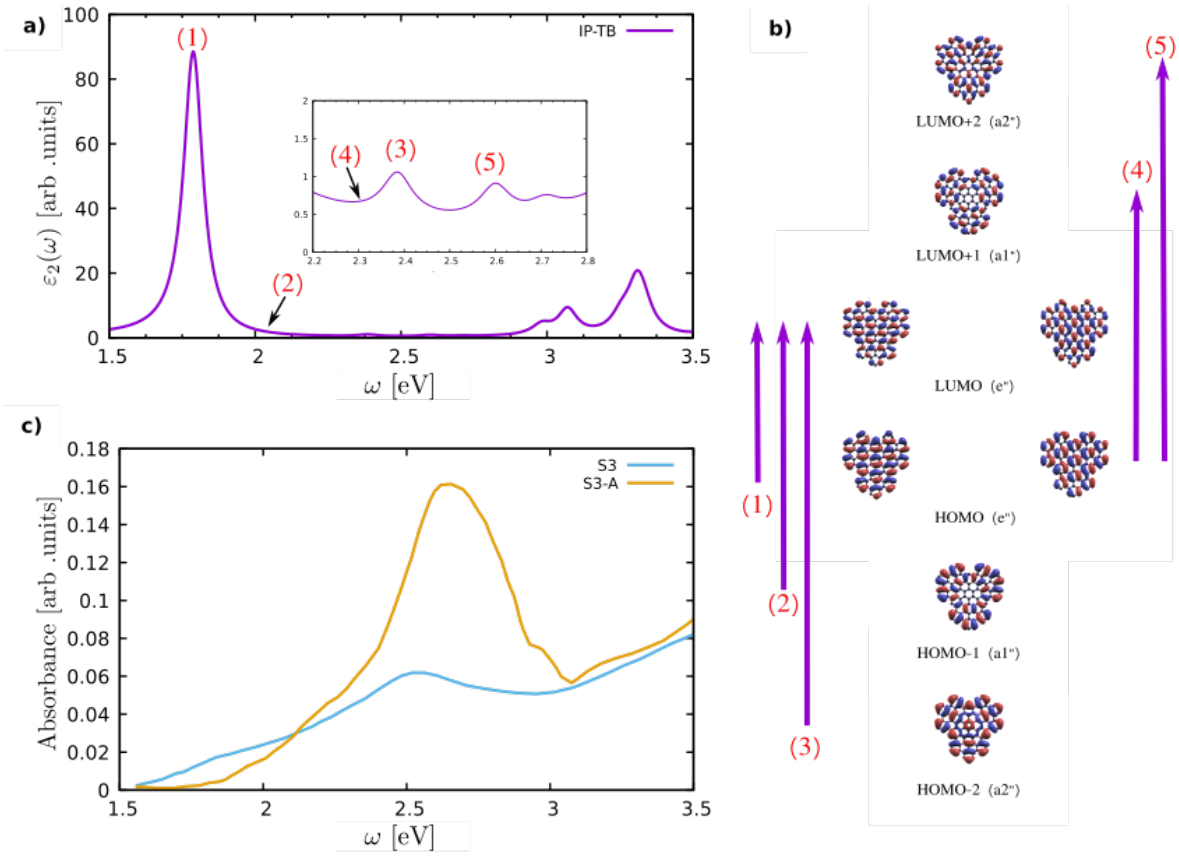

Figure 3.24 – Optical response of GQDs T C96 $(\overline{6}m2)$**. a,** IP RPA-TB absorption spectrum of the GQD S3. **b,** Irreducible representation of frontier orbitals of the GQD S3 calculated with our 2NN TB model. **c,** UV-Vis absorption spectrum of S3, S3-A in 1,2,4-trichlorobenzene (TCB) [261].

Fig. (3.24c) depicts the absorption spectrum of S3 (in turquoise) and S3-A (in orange) in 1,2,4-trichlorobenzene (TCB) solution. Our collaborator, Dr. Jean-Sébastien Lauret at LUMIN laboratory in ENS Paris-Saclay, measured the absorption spectra. The solutions of these GQDs are prepared at 0.1

mg/ml in TCB, sonicated in an ultrasonic bath for 30 seconds, and stirred for 24 hours. Because of the poor solubility of S3, we observed a weaker absorption intensity than S3-A. The absorption spectrum of S3 witnesses a weak absorption band at 2.61 eV, with a shoulder peak at 1.9 eV. The spectrum of S3-A shows a large band at 2.75 eV with shoulder peaks at around 1.97 eV and 2.14 eV. It is shown that the absorption spectrum of S3-A was not shifted compared to the S3 one; this shift could be witnessed by chemical functionalization of the edges with $C_{12}H_{25}$ alkyl chains [93, 261]. As shown in the Fig. (3.24c), the absorption spectrum was significantly improved in the presence of the alkyl chains. Furthermore, in Refs. [93, 261], the photoluminescence-excitation spectrums (PLE) in varying the emission wavelength have confirmed the existence of the main peak at 2.61 eV, as well as shoulders at 1.97 eV and 2.14 eV. Furthermore, the experiment on the S3-T was successfully done in TCB by Medina *et al.* [246]. Significantly, the absorption spectra were greatly improved, even better than one with S3-A, and exhibited narrower maxima at 2.62 eV, and shoulder at 2.33 eV. Nevertheless, the S3-T still forms aggregates or at least dimers, as in the case of T C96 GQDs substituted with six metyl groups [262]. Thus, further experimental investigations are needed to eliminate the aggregation issues.

Fig. (3.24a-b) illustrate the independent particle absorption spectrum and the irreducible representation of frontier orbitals calculated by our 2NN TB method. As depicted in the Fig. (3.24b), the HOMO and LUMO have double degeneracy, and they both belong to irreducible presentations e", whereas further states belong to irreducible representations a_1" or a_2". The absorption does not change whether the electric field is polarized along x or y because both electric field operators belong to the irreducible representation e'. In this case, only the transitions between a_1" or a_2" $\rightarrow a_1$" or a_2" are forbidden by symmetry, and all the other transitions are allowed. Thus, the allowed transitions are between HOMO$\rightarrow$LUMO, HOMO$-1\rightarrow$LUMO, HOMO$-2\rightarrow$LUMO, HOMO$\rightarrow$LUMO$+1$, and HOMO$\rightarrow$LUMO$+2$ denoted **(1) - (5)**, respectively in the Fig. (3.24b). The absorption spectrum exhibits a prominent peak at 1.78 eV **(1)** and shoulders at 2.15 eV **(2)**, 2.33 eV **(4)**, 2.39 eV **(3)**, and 2.6 eV **(5)**. Nevertheless, the intensity of absorption at the peaks is pretty tiny at **(2)** and **(4)**, approximately 1420 times smaller than the peak **(1)**. For this reason, these transitions can not be seen in the absorption spectrum in the Fig. (3.24a). The peak **(1)** seems to capture the first shoulder peak at 1.97 eV in the experimental absorption spectrum. However, we have shown in 1.3.3 that the 2NN TB method has not considered gap correction and exciton effects; thus, the IP RPA-TB spectrum can not be directly compared to the experimental one. Therefore, further theoretical investigations like GW+BSE, or maybe GW+BSE including phonon effects, are needed to explain the experimental absorption spectrum.

Comparison between STM experiments and simulations.

This section will present a comparative analysis between the experimental and simulated surfaces resulting from the deposition of the GQDs. Firstly, we will discuss the key experimental observations. Subsequently, we will showcase our anticipated surfaces based on the primary simulations. Thirdly, we will delve into the detailed examination of the structures that are thoroughly understood. Lastly, we will make predictions for the unknown structures that require further elucidation.

(a) Primary observations :

These triangular-shaped GQDs T C96 $(\bar{6}m2)$ (shown in the Fig. (3.23)) were deposited on a gold Au(111) surface at room temperature in UHV by Prof. Hamid Oughaddou and his Ph.D. student Hamza El-Kari at ISMO institute in Paris-Saclay area. All of those molecules were observed to have a poor coverage ratio. Unexpectedly, it appears that an ordered network of S3 monomers, even with S3-A or S3-T precursors, and some columnar zones were achieved on the gold surface after a deposition flow for 10 minutes at room temperature (RT), as shown in Fig. (3.25a). Each monomer was found to be flat with 15 Å of length and 1.4 Å of height, oriented in the direction [110] of Au(111) (see Fig. (3.25b)). A columnar zone was highlighted in Fig. (3.25c), with each column evaluated to be around 15 Å long and a distance of about 4 Å between two columns. The columnar structure was measured to be flat and to have 1.2 Å of height. These measured heights indicate that both those columns and monomers are monolayer structures. This observation disagrees with one observed in Refs. [96, 261] the GQDs S3-A were observed to be vertically stacked in 1-phenylacetate on HOPG (highly oriented pyrolytic graphite).

Additionally, the system was observed to be unstable, as seen in Fig. (3.25d), which shows the image of the surface achieved after a deposition flow for 1 hour on a gold Au(111) at RT and subsequent annealing for 1 hour at 100℃. Uncontrolled disordered S3 monomers and columnar structures were observed, as shown in Figs. (3.25d-f). A zoom-in on Fig. (3.25d) is depicted in Fig. (3.25e), which shows that the disordered columnar structures exhibit different lengths. Attempts at heating at higher temperatures become even worse. Fig. (3.25f) represents the small-scale STM experimental image obtained after a deposition flow for 20 minutes on the gold surface at room temperature (RT) and subsequent heating of the surface up to 150℃ for 1 hour. Disordered structures of S3 monomers were achieved again, with plenty of groups of three S3 monomers frequently observed. Additionally, many GQDs of different shapes were unexpectedly observed on the surface, such as **square-shaped** GQDs with four bright spots and **hexagonal-shaped** GQDs with five bright spots.

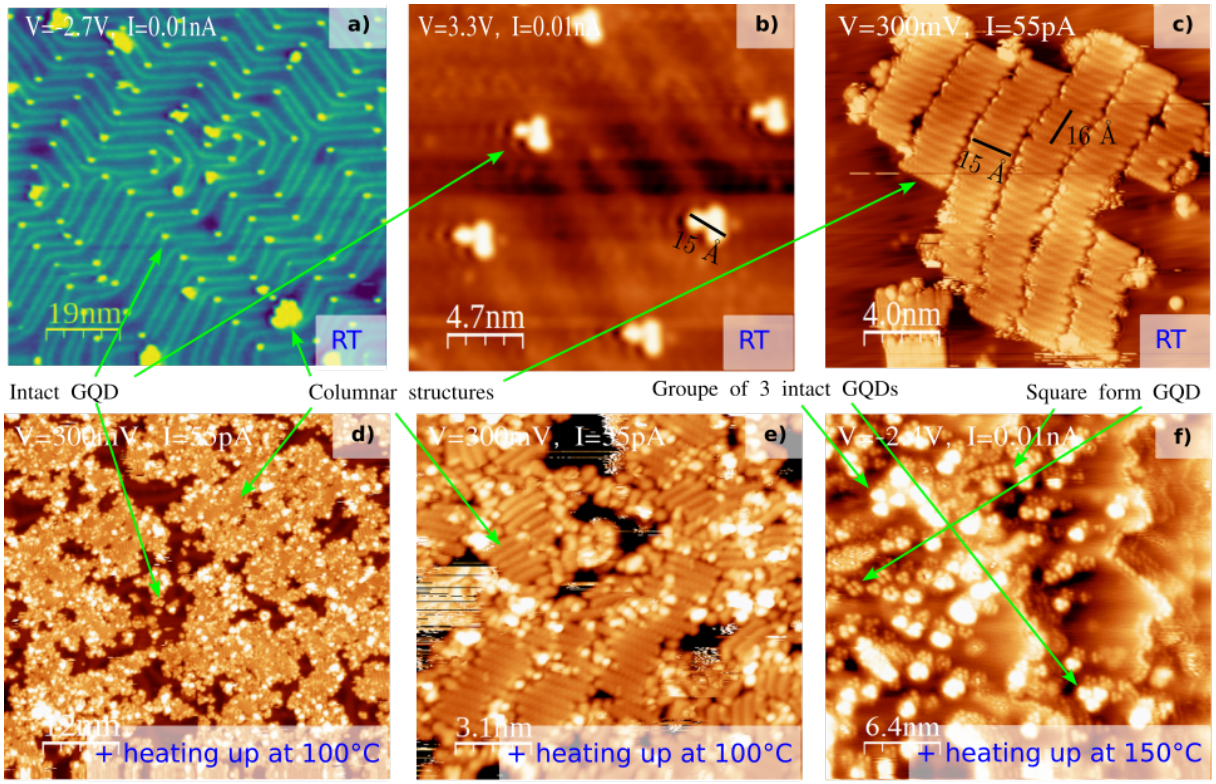

Figure 3.25 – Low-temperature (77 K) STM experimental images obtained after depositing molecules S3-A on the gold Au(111) surface. a, Large-scale image obtained after a deposition flow for 10 minutes on the gold surface at room temperature (RT), in which ordered network of S3 monomers, and ordered columnar unknown structures are observed. **b,** Zoom-in on **a**. **c,** Small-scale image of an ordered columnar zone obtained after a deposition flow for 20 minutes on the gold surface at RT. **d,** Image achieved after a deposition flow for 1 hour on the gold surface at RT and a subsequent heating the surface up to 100℃ for 1 hour. **e,** Zoom-in on disordered columnar zone on **d**. **f,** Image of disordered monomers S3 achieved after a deposition flow for 20 minutes on the gold surface at RT and a subsequent heating the surface up to 150℃ for 1 hour.

(b) Primary simulations :

At the same time, first, we theoretically deposited the S3-A on a gold Au(111) surface to have an idea of the obtained surface (see Fig. (3.26a)). Fig. (3.26b) depicts a Fireball-STM simulation image of the S3-A molecule on a five-layer slab of 37.68 x 37.34 ($Å^2$) periodicity of gold Au(111) surface. We compressed the gold surface by 1.19% and 0.39% along the in-plane lattice vectors of gold Au(111). The resulting superlattice contains 1187 atoms. Although the resulting surface was already as optimized as possible on the number of atoms, the calculations were very cumbersome. The STM simulation result (3.26b) exhibits that the signature of the alkyl chains is always significant, and it depends very little on the bias voltage. Compared to the obtained surface (3.25b) in the experiment, it is proved that the alkyl chains were really separated from the center part of the S3-A molecule on the gold surface.

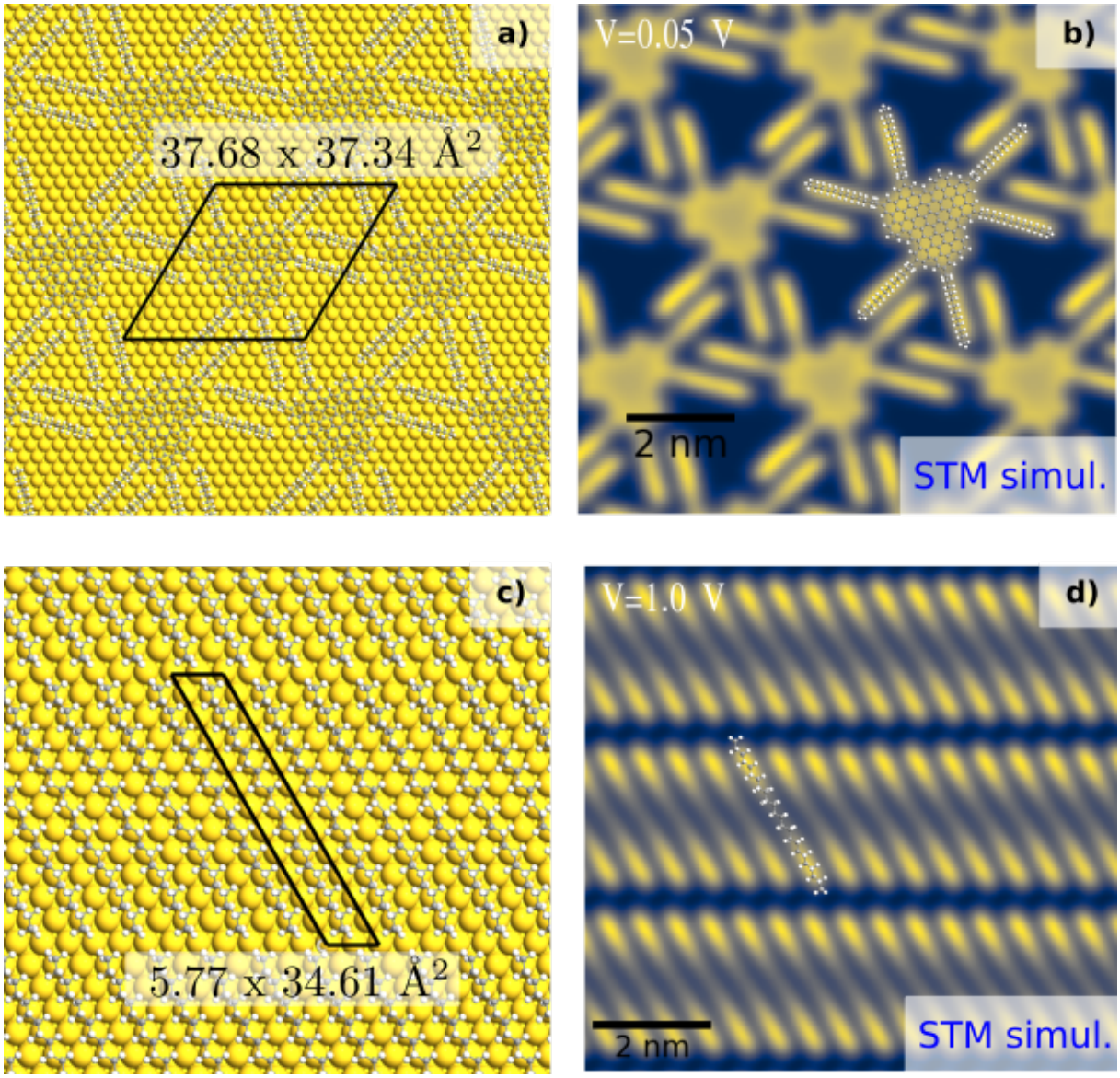

Figure 3.26 – Fireball-SIM simulation images obtained after depositing the GQD S3-A and an alkyl chain $C_{24}H_{50}$ on gold Au(111) surfaces. a, Geometry model of the GQD S3-A on a five-layer of 37.68 x 37.34 (Å^2) periodicity of pristine gold Au(111) surface. **b,** STM image of the model **a** shows a strong signature of alkyl chains. **c,** Geometry model of a self-assembly of two alkyl chains $C_{12}H_{25}$ on a five-layer of 5.77 x 34.61 (Å^2) periodicity of gold Au(111) surface. **d,** STM image of the resulting alkyl chain $C_{24}H_{50}$ on the gold Au(111) surface.

The question to be answered is whether the alkyl chains have stayed on the gold surface after leaving their PAH core and then formed an ordered structure of alkyl chains on the gold surface, which allows us to explain the surface (3.25c). András Pálinkás *et al.* [263] reported that the $C_{32}H_{66}$ alkyl chains can be successfully obtained by PVD on different Van der Waals materials such as graphene, graphite, hexagonal boron nitride (hBN) and molybdenum disulfide (MoS_2). The corresponding experimental STM images also exhibited a similar signature to the ordered

columnar structures observed in the Fig. (3.25c). Therefore, we aim to achieve the signature of the ordered structure of alkyl chains on the gold Au(111) surface on STM images to first verify if their signature on the gold surface is the same as observed on the other different surfaces in [263]; and to secondly compare with the experimental surface (3.25c). To do so, we deposited two $C_{12}H_{25}$ alkyl chains on a five-layer of 5.77 x 34.61 ($Å^2$) periodicity of pristine gold Au(111) surface. After separating the center part of the S3-A molecule, each alkyl chain contains a free bond that allows to connect with another one or the gold surface. After the geometry relaxation processes, we observed that these two alkyl chains were assembled to form a longer $C_{24}H_{50}$ alkyl chain (see Fig. (3.26c)). Fig. (3.26d) illustrates an STM simulation image on a periodic structure of the $C_{24}H_{50}$ alkyl chains on the gold surface. We figured out that the electrons are strongly localized at the edges of each alkyl chain; the signature was not observed at those different materials as mentioned in [263]. Moreover, compared to Figs. (3.25c and e), these figures do not seem to exhibit the structures made from alkyl chains. Since our collaborators observed the same order on the gold surface after depositing the S3 and S3-T molecules, the alkyl chains were probably not absorbed on the gold surface in those three experiments.

(c) Single monomer S3

This part will prove that the GQD S3 was observed on the gold Au(111) surface instead of S3-A or S3-T. First, we would like to know the preferred orientation of the resulting GQD S3 on the gold Au(111) surface. The GQD S3 was rotated progressively on the five-layer 40.58 x 40.22 ($Å^2$) gold Au(111) surface periodicity. At each orientation, we achieved the geometry relaxation and calculated the total energy of the system in order to determine the system with the lowest total energy. The gold surface was compressed by 1.19% and 0.39% along the in-plane lattice vectors of gold Au(111). The resulting superlattice contains 1106 atoms. Fig. (3.27) illustrates the evolution of total energy of the system versus rotation angles of molecule θ with respect to the direction [110] of Au(111). The bottom-left part of the Fig. (3.27) explains the definition of the rotation angle θ with respect to the origin axis as the direction [110] of Au(111). In the right part of the Fig. (3.27), we conclude that the system's total energy depends marginally on the orientation of the S3 molecule. This figure shows that the minimum total energy of the system is when the molecule is aligned to the direction [110] of Au(111), about $\lesssim$ -816.97 eV/atom, approximately. This result is shown in good agreement with the observation in the STM experiment image in the Fig. (3.27). However, the difference between the system's maximum and minimum total energies is not significant (order meV/atom), which explains why, even after annealing at 150℃, the S3 molecule can easily change its orientation, as shown in the Fig. (3.25f).

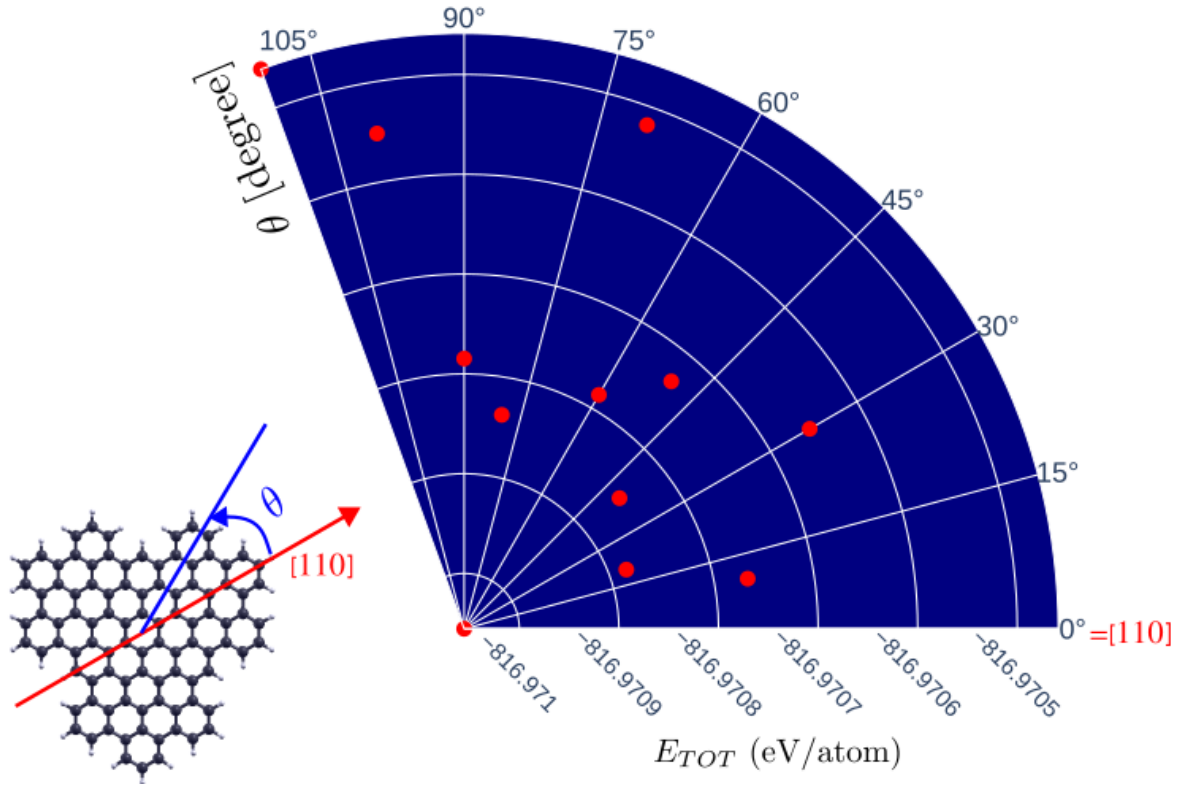

Figure 3.27 – Total energy of the system versus the rotation angle of the GQD S3. Made from five-layer of 40.58 x 40.22 ($Å^2$) periodicity of gold Au(111) surface, with respect to the direction [110] of gold surface.

Secondly, we simulated the STM images of the GQD S3 with the 2NN TB and Fireball-STM methods and then compared them to experimental results. Figs. (3.28a and e) illustrate small-scale surface images, obtained by depositing the S3-A and S3 molecules on the gold Au(111) surface at RT, respectively. They show the atomic resolution of the GQD S3 on the gold (111). We recognized its triangle form; its highlighted signature is displayed like three globes at the vertex of the GQD. Figs. (3.28b, c, f, and g) depict our Fireball-STM simulation images of the S3 molecule on five-layer of 26.09 x 25.85 ($Å^2$) periodicity of gold Au(111) surface. The gold surface was compressed by 1.19% and 0.39% along the in-plane lattice vectors of gold Au(111). The resulting superlattice contains 531 atoms in total (see Fig. (3.28i)). The tip-sample distance was set to 4.5 Å in Fireball-STM simulations. The Figs. (3.28b and c) are obtained for negative bias voltage, directly comparable to the Fig. (3.28a). While the Figs. (3.28f and g) are obtained for positive voltage and can be directly compared to the Fig. (3.28e). It is neatly exhibited that the Fireball-STM simulations perfectly covered the specific signature of the S3 molecule. Nevertheless, in terms of molecular size, there is a significant gap between experiment and simulation; for instance, in the Fig. (3.28a), the red line represents the width of the molecule, and measured to be approximately

equal to 15 Å. In contrast, this distance is 2.42 Å greater in the Fig. (3.28b).

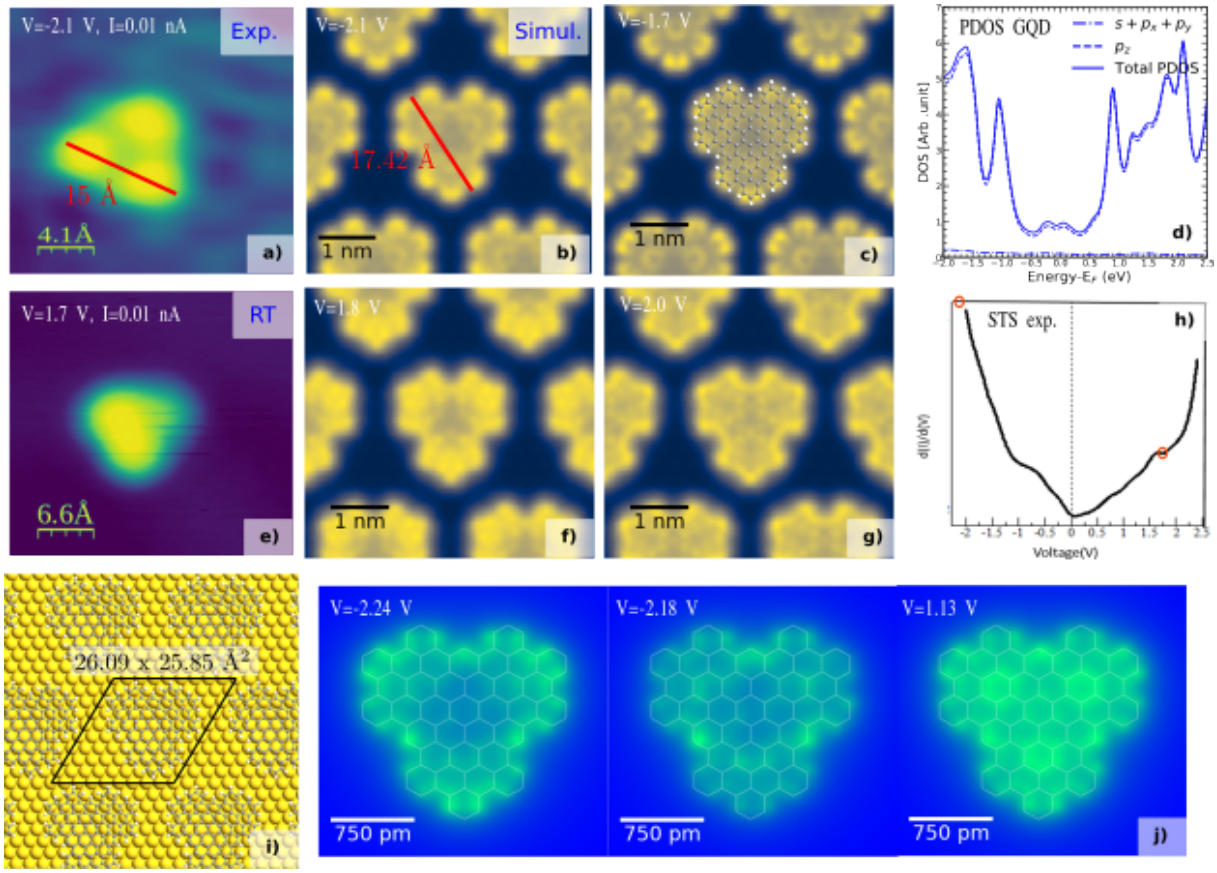

Figure 3.28 – Comparison between experimental and simulation results on the S3 molecule on gold Au(111). a, e, STM experimental images of the GQD S3 on herringbone gold surface at RT, at the bias voltages presented by red circles in the STS experiment spectrum presented in **h**. The surface **a** obtained after depositing the S3-A, while the surface **e** obtained after depositing the S3. **i,** Geometry model of the GQD S3 on five-layer of 26.09 x 25.85 ($Å^2$) periodicity of gold Au(111) surface in Fireball-DFT and -STM simulations. **b,c,f,g,** Constant-height current images of model **i** obtained with Fireball-STM simulations. **d,** The projected density of states (PDOS) of the isolated molecule calculated by Fireball DFT-LDA. **j,** Constant-height current images achieved by 2NN TB method.

Moreover, Fig. (3.28h) displays the STS experimental spectrum of the S3 molecule on gold Au(111). This figure surprisingly exhibits a small gap. Nevertheless, the band gap of the S3 molecule calculated by Fireball DFT-LDA is around 2.1 eV, as shown in PDOS of S3 (3.28d). Thus, the STS spectrum needs to be improved in further measurement. Although the STS experimental spectrum is imperfect, it is still possible to compare with the PDOS of the S3 molecule. As depicted in Eq. (1.98), the dI/dV spectrum is obtained by a convolution product of the DOS of the sample and the DOS of the tip through the tip-sample interaction and the scattering matrices. The scattering matrices are approximate to identity at the set tip-sample distance (~ 4.5 Å). Additionally, since the gold sample is more distant from the gold's tip than the S3 molecule, the

interaction between the gold's tip and the gold's sample is multiple times smaller than between the molecule and the gold's tip. Therefore, the contribution of the density of states of the GQD powerfully dominates. In this case, the Figs. (3.28d and h) show that the PDOS of the GQD S3 is very comparable to the STS experimental spectrum.

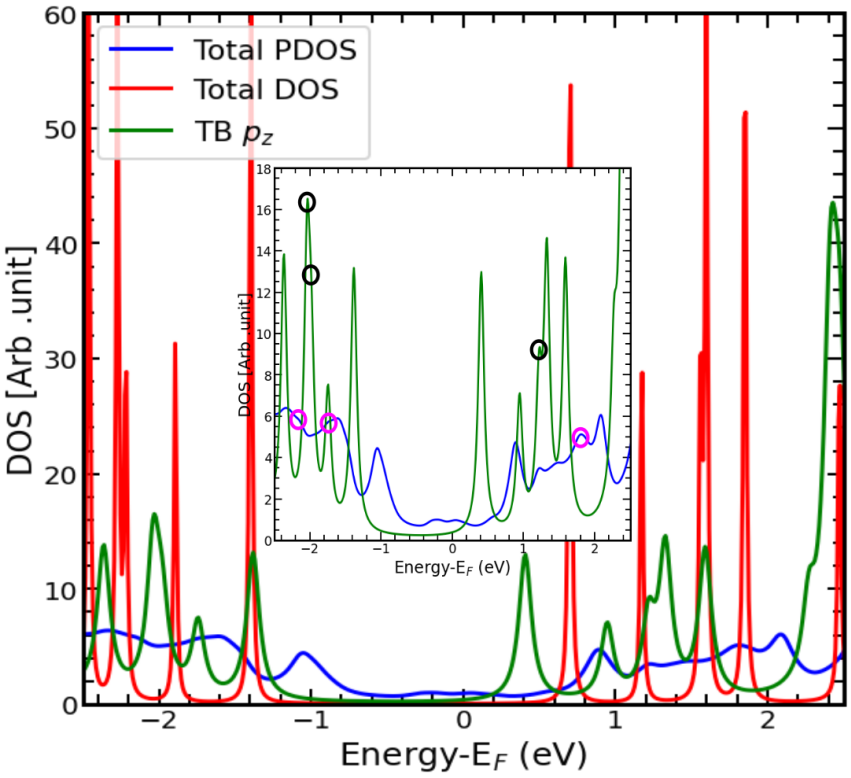

Figure 3.29 – Comparison between the PDOS (3.28d) (in blue), total DOS of the S3 molecule in vacuum calculated by Fireball DFT-LDA method (in red), and by 2NN TB method (in green). a, Continued circles represent the energy levels where the frontier orbitals in the Fig. (3.28j) are found by the 2NN TB method, respectively. In contrast, pink circles represent the voltage values where the three-spot signature observed in the Figs. (3.28a and e) can be retrieved by STM simulation.

In the Fig. (3.28d), the PDOS of p_z orbitals is denoted by a dashed curve, whereas the dotted dashed curve presents that of $s + p_x + p_y$ orbitals. Similarly to benzene, carbon-carbon bonds in the S3 molecule are considered purely sp^2 hybridized, so the PDOS of p_z orbitals dominates that of $s + p_x + p_y$ orbitals. The sp^2 origin of the S3 GQD signature found in the Figs. (3.28a and e) are successfully retrieved in the Fig. (3.28j) by using 2NN TB method. On the other hand, Fig. (3.29) shows a comparison between the total DOS of the S3 GQD in vacuum, evaluated by TB method (in green), Fireball DFT-LDA (in red) and the projected DOS of the S3 GQD presented in the Fig. (3.28d). The energy gap of the S3 GQD in the vacuum is 1.79 eV by the TB method and 2.1 eV by Fireball DFT-LDA. In the presence of the gold surface, the energy gap is reduced to 1.9 eV. This observation was also made in the cases GQD C30 (S2) 3.2.1 and GQD C42 (S1) 3.1.1. In the

presence of the gold surface, the S3 molecule lost 0.74% of its charge.

(d) Finite structure built from the monomers S3

As the unknown ordered column structure constitutes a monolayer arrangement, our strategy involves simulating a finite network composed of S3 monomers, which are the most frequently observed experimentally. By comprehensively understanding the formation of this structure, we can subsequently offer predictions for achieving the desired ordered column configuration

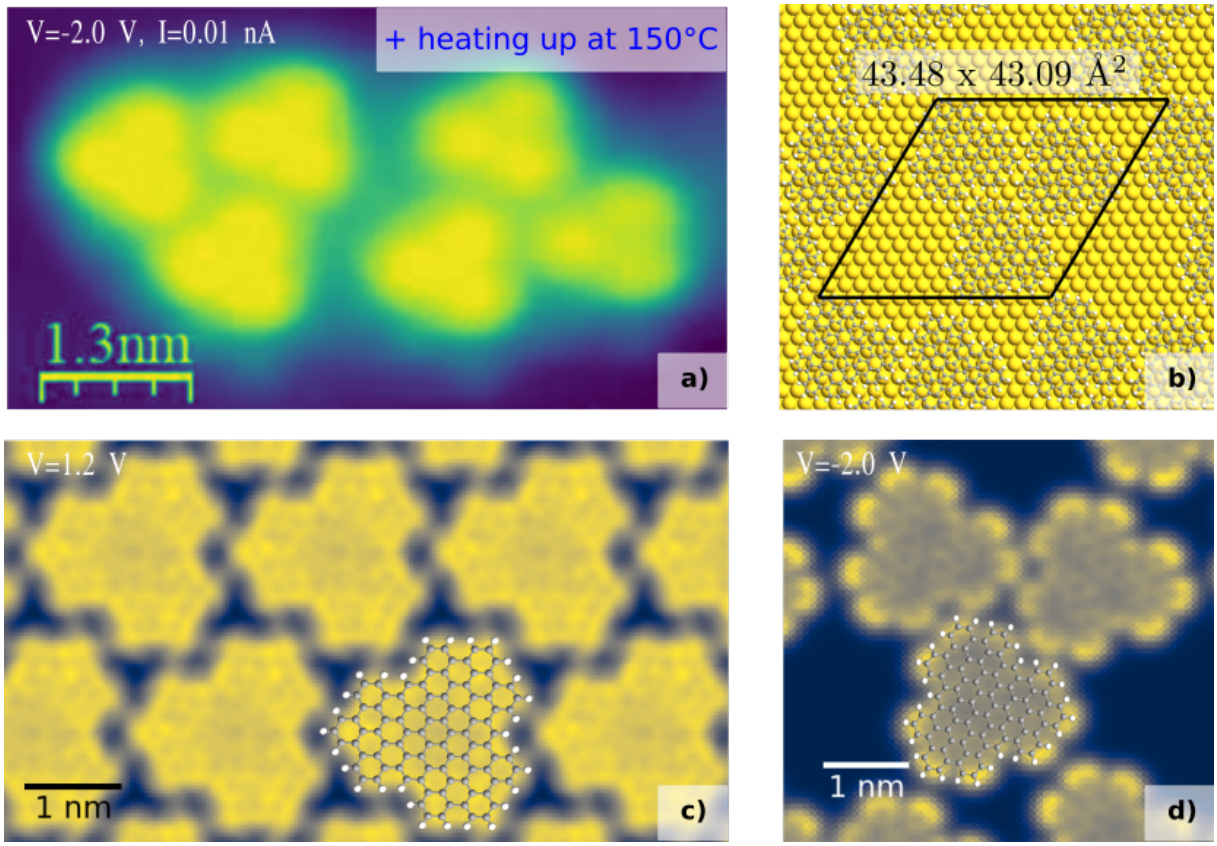

Figure 3.30 – Comparison between experimental and simulation results on finite networks of the monomers S3 on gold Au(111). a, Zoom-in on the Fig. (3.25f). **b,** Geometry model of three S3 molecule system on five-layer of 43.48 x 43.09 (Å^2) periodicity of gold Au(111) surface. **d,** STM simulation image of the model **b**. **c,** STM simulation image of a 2D network of the GQDs S3 shown later in Fig. (3.31h), on a five-layer of 21.0 x 21.0 (Å^2) periodicity of gold Au(111) surface.

Fig. (3.30a) shows an atomic resolution image of two groups of three S3 monomers on the gold surface. This figure shows that the S3 monomers were attracted together to form triple S3 monomer groups, and it is confirmed that the alkyl chains were separated from the center part of the S3-A GQD. Fig. (3.30d) illustrates an STM simulation image of a triple S3 monomer group on a five-layer of 43.48 x 43.09 (Å^2) periodicity of gold Au(111) surface. In this study, we compressed the gold surface by 1.19% and 0.39% along the in-plane lattice vectors of gold Au(111). The resulting

primitive cell contains 1503 atoms in total. We can only simulate the left triple monomer group with our computational capability compared to the Fig. (3.30a). For the same reason, we neglected the contribution of the gold surface in the tip-sample interaction in the Fireball-STM simulation. The tip-sample distance was set to 4.35 Å. Although the gold's tip and gold's sample interaction was not considered, we can still obtain again the typical signature of the GQD S3 (3.28) as depicted in the Fig. (3.30a). In this case, since a large gold surface was taken into account, each monomer averagely lost 0.7% of its charge to the gold surface, *i.e.* 0.04% less than the lost ratio of a single monomer presented in the Fig. (3.28).

Moreover, we are supposed to grow up to a 2D network of S3 monomers from the triple group to see if this typical signature is still present. For this reason, we studied the hexagonal S3-B1 network on a five-layer of 21.0 x 21.0 ($Å^2$) periodicity of gold Au(111) surface (see later in Fig. (3.31j). This study compressed the gold surface by -0.98% along the in-plane lattice vectors of gold Au(111). The resulting primitive cell contains 386 atoms in total. The tip-sample distance was set to 3.2 Å, and the topmost layer of the gold surface was considered in the tip-sample interaction. Fig. (3.30c) presents the STM simulation image of the S3-B1 on the gold surface. In this figure, the three-globe signature of the S3 was recovered. We note that in the presence of a periodicity of the S3, its signature changes a bit, and also, the scattering effects were 1.7 times more important than scanning at 4.5 Å of tip-sample height. On the other hand, the S3-B1 was observed to have lost 0.66% of its charges to the gold surface.

(e) Infinite structure built from the S3 monomers and theoretical prediction for columnar structures.

Until now, both experimental and simulation results agree that the alkyl chains are somehow separated from the center part of the S3 and were probably not absorbed on the gold surface. Thus, the columnar structure may be a two-dimensional planar structure made from the S3 GQD.

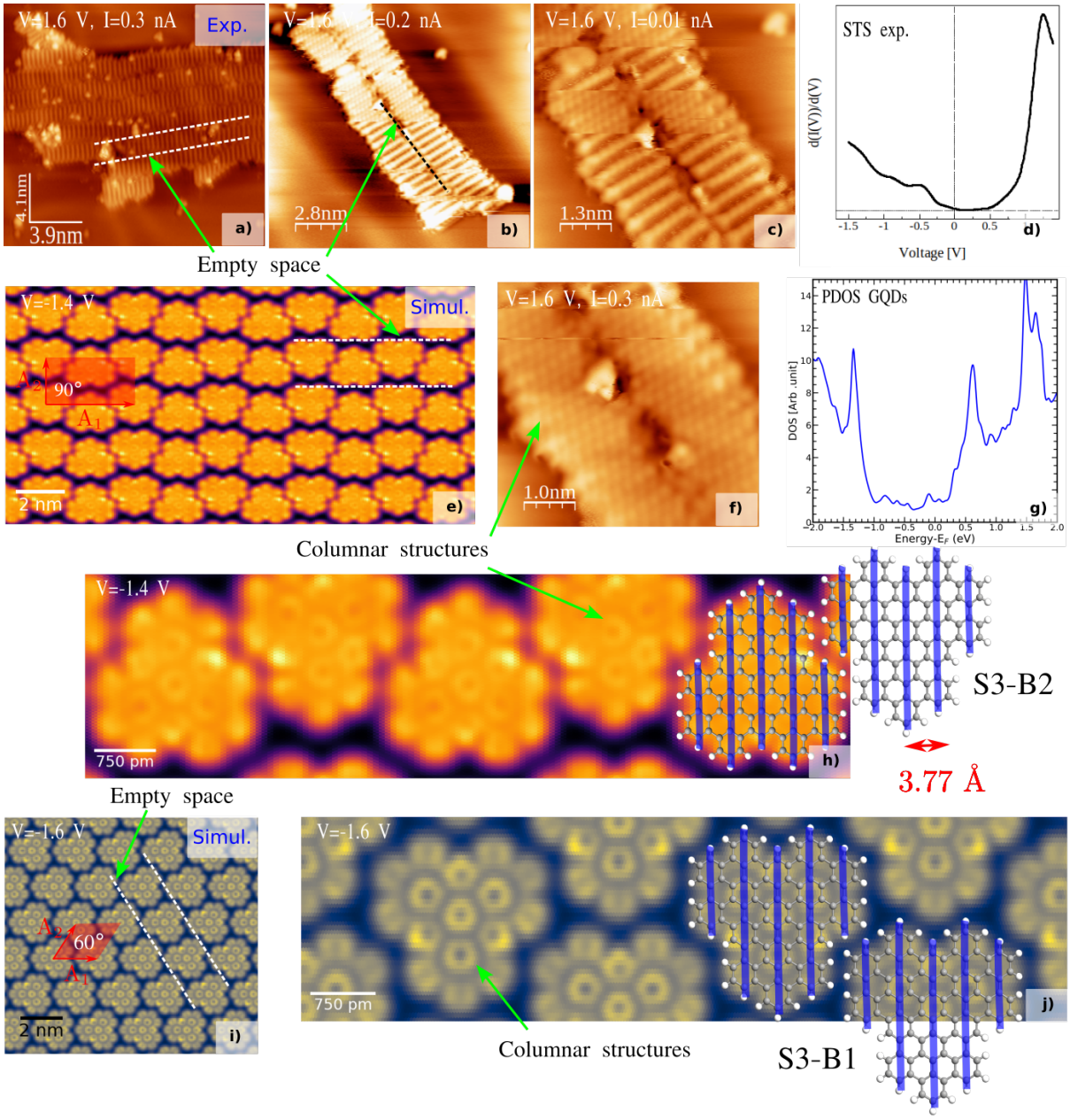

Figure 3.31 – Proposed model for the ordered columnar structures. a,b, Image of a columnar zone obtained after a deposition flow of the S3 for 1 hour on the gold surface at RT. **c,** Zoom-in on **b**. **f,** Zoom-in on **c**. **d,** STS experimental spectrum of the ordered columnar structure. **e,** STM simulation image of a proposed monomer network (S3-B2) on five-layer of 35.5 x 20.65 ($Å^2$) periodicity of gold Au(111) surface. **g,** Projected DOS of the S3-B2. **h,** Atomic resolution image and the schematic geometry of the S3-B2 model. The columnar signature is represented by blue continued lines. **i,** STM simulation image of another monomer network (S3-B1) on five-layer of 21.0 x 21.0 ($Å^2$) periodicity of gold Au(111) surface. **j,** Atomic resolution image and the geometry schematic of the S3-B1 model. In **i**, the superlatice vectors $\{\mathbf{A}_1, \mathbf{A}_2\}$ are exactly equal to the ones of the gold (111) superlattice.

Figs. (3.31a and b) represent two distinct columnar zones obtained after a deposition flow of S3 for 1 hour on a gold surface at room temperature (RT). Zoomed-in views of the Fig. (3.31b) are

shown in Figs. (3.31c and f), revealing enhanced resolution of the columnar structure, with each column closely resembling pentacene on a Ni(111) substrate [264]. Fig. (3.31d) illustrates the STS experimental spectrum of the structure presented in the Fig. (3.31f). The STS spectrum exhibits a maximum peak at $\sim$ 1.3 eV and a shoulder at -0.5 eV. In contrast, the PDOS of the S3 GQD, as demonstrated previously in Fig. (3.28h), exhibits a similar trend to the STS curve of the columnar structure, with a peak at 2.1 eV and shoulder peaks at 0.8 eV and 1.1 eV. Furthermore, according to experimental data, the length of each columnar structure precisely matches that of a single S3 monomer, with both displaying a closely similar STS spectrum. These observations support the hypothesis that the columnar structure is built from the S3 GQD could be a good approximation.

In the following part, we will propose two simulation models from the S3 GQDs that may resemble the columnar structure. First, Figs. (3.31i and j) display STM images obtained by simulating the S3-B1 on a five-layer of 21.0 x 21.0 (Å^2) periodicity of gold Au(111) surface, as discussed recently in the Fig. (3.30c). The columnar signature is considered to be created along each armchair ring of the S3, and the columns are formed in the direction [-110] of the hexagonal lattice vectors of graphene as presented by blue continued lines in the Fig. (3.31j). The distance between each blue continued line is around 3.77 Å, which is very close to the distance between columns measured in the experiment (see the Fig. (3.25c)). The S3-B1 model contains a single S3 monomer in the primitive cell, and the S3 is repeated periodically in space thanks to hexagonal superlattice vectors presented in the Fig. (3.31i). In this case, each monomer is orientated in the same direction as others. We note that empty space (or unoccupied space) between each column pack (represented by white dashed lines) observed in STM experimental images is not highlighted in this model, as shown in the large-scale image (3.31i). Since the signature shown in the Figs. (3.31i and j) were also obtained without the gold surface by using the 2N TB method, this issue can adequately be solved by using the more significant lattice vector in the direction perpendicular to the direction of the empty space to increase the width of the empty space.

Figs. (3.31e and h) depict STM simulation images obtained by performing the S3-B2 model on a five-layer of 35.5 x 20.65 (Å^2) periodicity of gold Au(111) surface. The schematic geometry of the S3-B2 model is presented in the Fig. (3.31h). There are two S3 monomers in the centered rectangular primitive cell, and they are oriented in opposite directions. For this case, the gold surface was compressed by 1.08% and 0.74% along the in-plane lattice vectors of gold Au(111). The resulting primitive cell contains 812 atoms in total. Learned from the case of the S3-B1, we added a larger space between each column pack, as shown in the Fig. (3.31e). The projected DOS of the S3-B2 is displayed in Fig. (3.31g). Compared to the STS spectrum in the Fig. (3.31d),

we figure out that they are very comparable as expected. Furthermore, the S3-B2's PDOS is very close to that of the S3 monomer in the Fig. (3.28d). This latter shows a good agreement with experimental measurements once we compare the STS spectrum (3.28h) to (3.31d). It is worth noting that the S3-B1's PDOS is not as comparable to the STS spectrum (3.31d) as that of the S3-B2. Since the columns are formed in the direction [100] of its centered rectangular lattice vectors, the STM simulations images of the S3-B1 have been found to have better agreements with the surface (3.31b). However, two phases seem to co-exist in the Fig. (3.31a): a straight network of columns at the center part and a crossing network of the columns at the edge. The S3-B1 is more comparable to the latter network, whereas the S3-B1 is more likely to be the former. However, further experimental studies are needed to conclude the columnar structure. Another possibility to explain the difference between experimental data and simulation results is that in our simulations, we do not use the chevron gold surface used in the experiment. In this case, this difference is considered as the computational limitation that we can hardly go beyond.

3.3.1 Conclusion

Since the triangle-shaped GQD S3 was observed not to be perfectly soluble in the TCB solvent, we decided to investigate not only the pristine S3 GQD but also the functionalized GQDs with alkyl chains and tert-butyl groups such as the S3-A and -T.

For the optical response, the functionalized GQDs were shown to improve significantly the absorption spectra. However, they still have poor solubility and can hardly disperse, which causes the apparition of extra peaks stemming from the aggregate of GQDs in the solvent. Our collaborators did further experiments on the S3-T. Since these bulky functional groups appear to reduce π-stacking interactions partially, sharper and more resolved absorption lines than in the case of the GQD S3 and the GQD S3-A were successfully observed. However, these GQDs still form aggregates (or at least dimers) as in the case of C96 GQDs substituted with six mesityl groups [262]. On the other hand, although the 2NN TB method can detect the main feature of the absorption spectra, further theoretical studies are needed to fully understand the practical absorption and PL measurements, such as GW+BSE or GW+BSE with electron-phonon coupling.

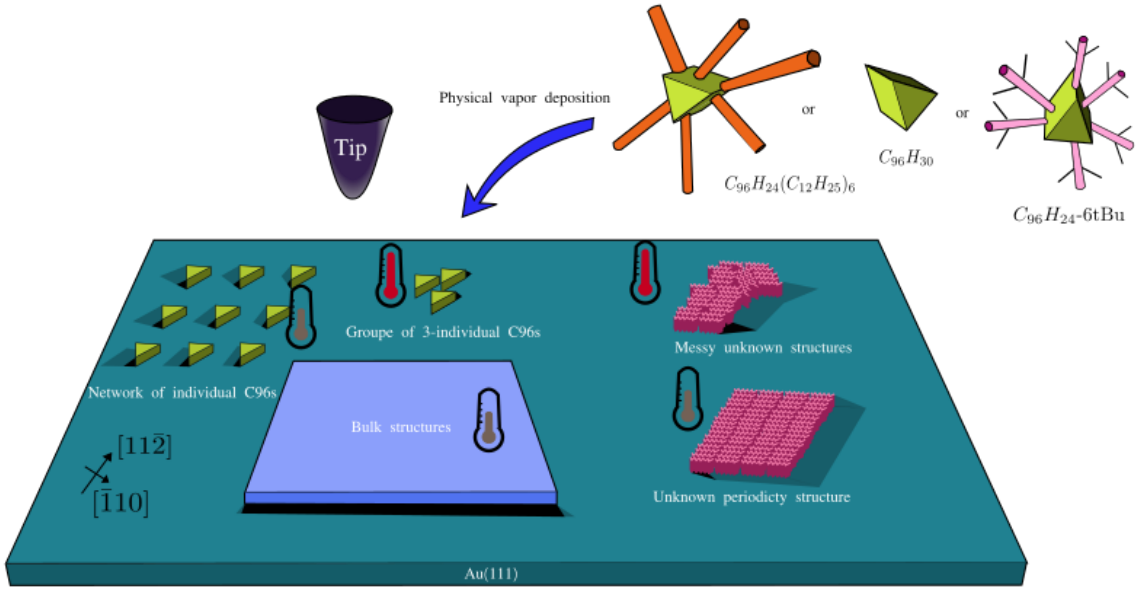

Figure 3.32 – Schema of the surface experiment obtained after depositing S3, S3-A, and S3-T molecules on gold Au(111) surface. The first experiment was performed with the S3-A molecule, the second with the S3 molecule, and the third with the S3-T molecule. Nevertheless, the same structures were obtained on the gold surface.

Regarding STM simulations, the functionalized GQDs did not improve the results of the pristine S3 molecule. Unexpectedly, our collaborators observed the same phenomena when using those three GQDs: S3, S3-T, and S3-A. They all show very bad coverage ratios. Our collaborators achieved an ordered network of the S3 GQDs and an ordered columnar unknown structure for all those deposited molecules. These structures were unstable as they became disordered after annealing only at 150℃ (see the Fig. (3.32)). The ordered network of the S3 GQD on gold was proved by comparing experimental and simulation and was almost fully understood. After annealing only at 150℃, our collaborators obtained an uncontrolled disordered structure of the S3 and the columns. Unexpectedly, the multiple edge-shaped GQDs and chains of multiple lengths were also obtained on the gold surface. Until now, we have no convincing reasons for what occurred after the last heating. Thus, we disregarded these multiple edge-shaped GQDs in this manuscript. Comparing the different experiments and simulation results, the alkyl or tert-butyl chains were questioned not to be absorbed on the gold surface at room temperature. They were separated from the PAH core of the GQDs. For this reason, initially, we hypothesize that all the structures, including the columnar one obtained on the gold surface, were built from the S3 monomers. The first hypothesis is that the columnar structure may be created by vertically stacking the S3 GQDs; nevertheless, the columns were observed to have mono-layer height. The second hypothesis is that the S3 GQDs form a two-dimensional planar structure. Following the second hypoth-

esis, we simulated the equilateral triangle-shaped triple monomer group that was frequently observed. Subsequently, we attempted to create a new two-dimensional nanostructure. In this case, we proposed two different models: S3-B1 and S3-B2. The former was our first trial that reproduced the exact geometry of the triple GQD group with hexagonal lattices. Compared to the experimental data, we proved that the columnar signature can be approximately represented by each armchair ring of the S3, with the coherent length and separation distance. In this model, the columns have followed the direction of its hexagonal lattice vectors [-110]. In contrast, the column network of the latter is formed in the direction [100] of its centered rectangular lattice vectors. Thus, the resulting STM simulation image of the latter is closer to the experimental one than the one of the former. However, they both can co-exist on the experimental surface. Until now, we hypothesize that the Hydrogen atoms in the room saturate the core of the S3-A after leaving the alkyl chains, which enables us to obtain those comparable results with the measurements. However, we still need to provide more convincing results that can explain the columnar structures. One possibility to explain the difference between experimental data and simulation results is that the compressed-under-2$\%$ gold surfaces were used instead of the real chevron gold surface in the Fireball-STM simulation. In this case, this difference is considered as the computational limitation that we can hardly go beyond. On the other hand, our recent Fireball-STM simulations on a radical S3-A (without the alkyl chains) on a gold surface show that the radical molecule exhibits the three-globe signature observed in the Figs. (3.28a-e) but at height constant mode instead of current constant mode as measured in experiments. On the other hand, another possibility to explain columnar structures is that molecules like water vapor, carbon-based contaminants (e.g., hydrocarbons from the air), and other airborne pollutants can adsorb and then form a contamination layer onto a gold surface [263]. Those recent results make us even more confused. Further experimental investigations with better resolution (for instance, depositing these molecules on a more active surface or a hot surface or reducing the temperature of the room from 77 K to 7 K like the case of GQD C30 (S2) and GQD C42 (S1)) are needed to

1. Confirm whether the same surfaces were observed in both experiments with the S3, S3-A, and S3-T GQDs;
2. The columnar structures appear in both experiments; if yes, are they constructed from an alkyl chain network or a network of the S3 monomers or a contamination structure ?;
3. Compare them with our simulation models to better understand what is encountered in those experiences.

As demonstrated, both alkyl and tBu chains leave the center part of the S3-A or -T. Our recent Fireball-STM simulations show that the radical S3-A or -T molecules may be observed on the gold sur-

face. For this reason, it may be possible to have a new GNM after depositing the S3-A or -T. To close this section, we would like to propose an imaginary GNM model, denoted S3-B3, made from the PAH cores of the S3-A or -T (radical molecules), which connect to the others in the exact position of the functionalized groups left, as depicted in Fig. (3.33a). The S3-B3 is a 19.52 x 19.52 ($Å^2$) hexagonal lattice, on which there are two kinds of pores with different shaped forms, such as a circle and a triangle. These pores' presence causes an opening direct gap at Γ point, as shown in its electronic band-structures depicted in Fig. (3.33b). Additionally, the value of the gap is small enough, inside of our gap target, to be equal to 1.55 eV by the TB method (in blue) and 1.88 eV by Fireball DFT-LDA (in red).

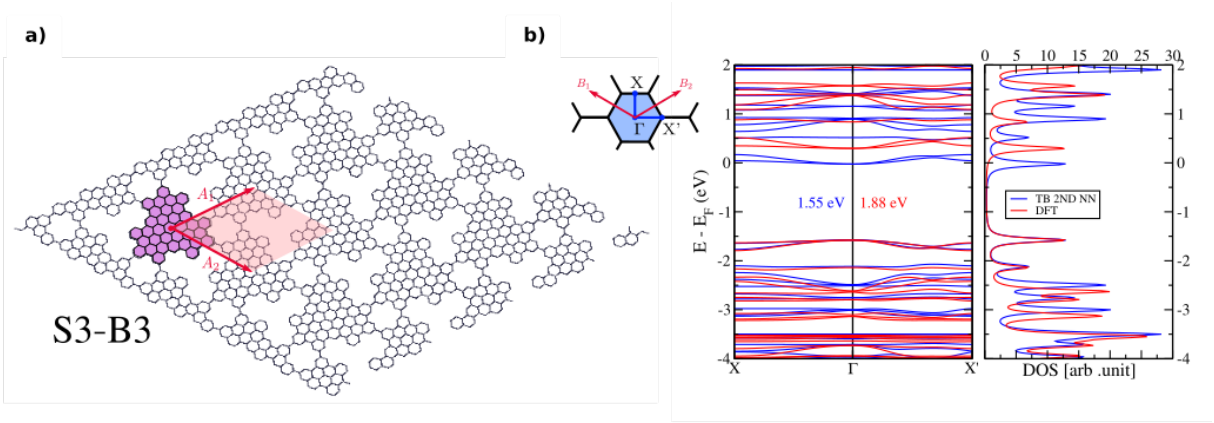

Figure 3.33 – Imaginary graphene nano-mesh (GNM) obtained once the alkyl or tBu chains leave the center part of the S3-A or -T molecule in absence of hydrogen atoms in the room. a, Geometry model of the GNMs made of the center part of the S3-A or -T GQDs with free bonds in the place of the chains left. **b,** Band-structures of this GNMs calculated by TB method (in blue) and Fireball-DFT (in red).

3.4 Family of rectangular-shaped R GQDs $D_{2h}(mmm)$.

3.4.1 Rectangular-shaped R GQDs $D_{2h}(mmm)$.

Structure definition

In this section, we will show the change of electronic and optical properties of rectangular-shaped (R) GQDs in D_{2h} family in changing the width and length of the GQD, and also the symmetry by adding a second layer. Proposed by our collaborators, Dr. Stéphane Campidelli, Dr. Julien Lavie, and Daniel Medina-Lopez at the CEA-NIMBE laboratory in Paris-Saclay area, the studied D_{2h} family contains four GQDs: $C_{78}H_{26}$ (S4), $C_{96}H_{30}$ (S5), $C_{132}H_{34}$ (S6) and $C_{162}H_{38}$ (S7). The GQDs share similar armchair edges but vary in the number of rows of benzene rings, as shown in Fig. (3.34a). The S5 displays a longitudinal expansion with one additional row of benzene rings in red compared to the S4. Similarly, the S7 exhibits a longitudinal expansion with one extra row of red and purple benzene rings compared

to the S6. Additionally, the S6 and S7 showcase a lateral expansion, with two extra rows of benzene rings, compared to the S4 and S5. They both can be compared two by two. Undeniably, the rows of benzene rings cannot be extended starting from the previous GQDs; re-considering the synthesis process is required. All synthesis details were discussed in [254, 265].

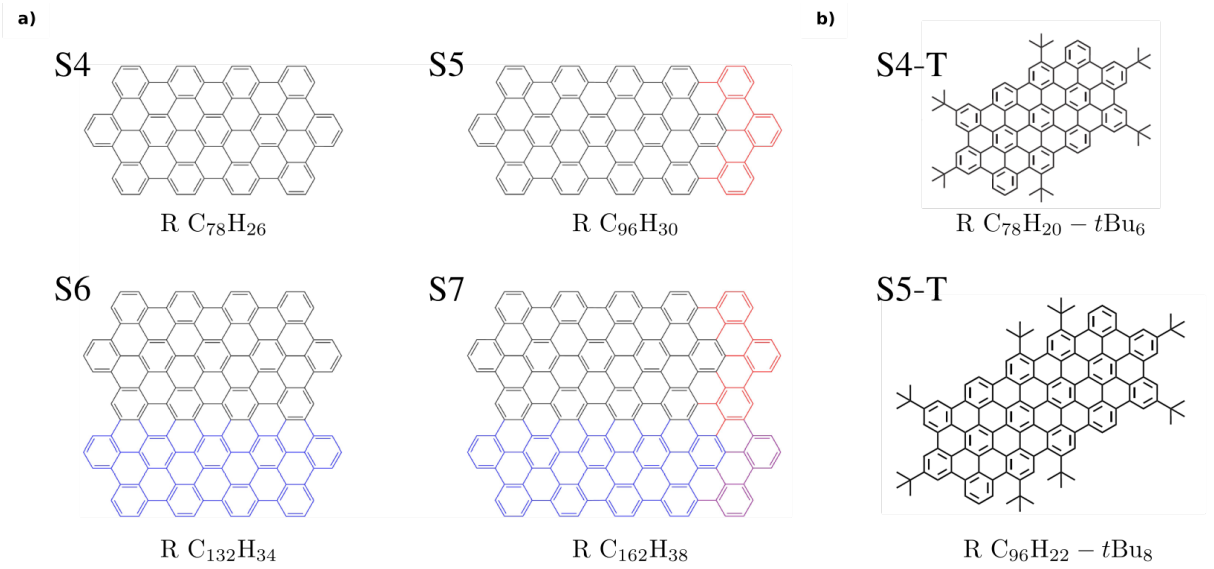

Figure 3.34 – Geometry of the studied molecules of D_{2h} family [246, 265]. a, Structure of the $C_{78}H_{26}$, $C_{96}H_{30}$, $C_{132}H_{34}$ and $C_{162}H_{38}$ GQDs, denoted S4-S7, and structural relationship between them. **b,** The S4 and S5 molecules functionalized with multiple tert-butyl chains (tBu), called S4-T and S5-T, respectively, were used to improve the solubility in organic solvents [246, 265].

For optical investigations, these GQDs were dispersed in sodium deoxycholate (SDOC) 2% solution at pH 12 using tip sonication, and large aggregates were removed by ultracentrifugation at 120000 g for one hour. As shown in 3.3, in the absence of functional groups, these GQDs were observed to have poor solubility and be difficult to disperse, especially for small GQDs such as the S4 and S5 (see Fig. 3.34); optical responses yielded a better dispersion of the large GQDs (S6 and S7) by deoxycholate surfactant. For this reason, it is necessary to functionalize those GQDs, especially for the S4 and S5. Fig. (3.34b) illustrates S4-T and S5-T, which are the functionalized molecules of the S4 and S5, respectively, with tert-butyl chains (tBu). The S4-T contains six tBu chains, whereas the S5-T has eight tBu chains. The S4- and S5-T synthesis followed a nearly similar process to the unfunctionalized ones [246, 254].

Optical properties

The PAH core of the S4-S7 molecules belongs to the rectangular D_{2h} group of symmetry that contains three mirror planes along the three x, y, and z axes. As a result, there are no degeneracies (for electronic or vibronic states) induced by symmetry (see later in Tab. 3.2). As the other sp^2 GQDs presented in

previous sections, we separate σ and π electronic eigenstates, which are symmetric and anti-symmetric, under the $+z/-z$ mirror operation. The former contribute to the chemical backbone of the molecules but are energetically located far from HOMO and LUMO. In contrast, the latter contains only combinations of carbon p_z orbital and are much more relevant for low energy electronic properties. We assume the PAH cores lie in the xy plane and the x axis is longitudinal. Since they are antisymmetric under the action of the xy mirror plane, all the π molecular states belong exclusively to the a_u, b_{1u}, b_{2g} or b_{3g} irreducible representations of the D_{2h} group, as depicted in the Tab. 3.2.

GQD / state	HOMO-1 (b_{3g})	HOMO (b_{2g})	LUMO (b_{1u})	LUMO$+1$ (a_u)
S4	-1.77709	-1.53748	+0.17302	+0.47535
S5	-1.75979	-1.46276	+0.07192	+0.44514
S6	-1.75979	-1.41444	+0.01141	+0.09855
S7	-1.48070	-1.34029	+0.10917	+0.09855

Table 3.2 – Energy level of the four frontier orbitals of the GQDs (in eV) obtained by 2NN TB model [265].

In the Tab. 3.2, we report the calculated electronic TB energies around the HOMO and LUMO levels. First, one can notice that the energy gap reduces as the size of the GQD increases. This observation is in agreement with optical measurements performed on the S6 and S7 GQDs but is not reliable for the behavior of the S4 and S5 GQDs, probably because of the poor quality of their dispersion [265]. It is worth noticing that since the molecules have the same rectangular symmetry, it implies similarity in their electronic structure. Indeed, we have noticed that the four states (respectively HOMO-1, HOMO, LUMO and LUMO$+1$) have always the same representation (b_{3g}, b_{2g}, b_{1u} and a_u, respectively) for all the GQD geometries from S4 to S7. The wave functions of HOMO-1 to LUMO$+1$ frontier orbitals were plotted in Fig. (3.35a). We can affirm that the transitions HOMO to LUMO and HOMO-1 to LUMO$+1$, labeled transitions **(1)** and **(2)**, are always allowed by symmetry when the electric field is along x (and forbidden otherwise), and the transitions HOMO-1 to LUMO and HOMO to LUMO$+1$, labeled **(3)** and **(4)**, are allowed only when the field is along y. These transitions are listed in Tab. 3.3. Compared to the GQD C42 (S1), the S4 (C78) and S5 (C96) have more benzene rings in the longitudinal direction, whereas the S6 (C132) and S7 (C162) have more benzene rings in both longitudinal and transversal directions. Therefore, their symmetry do not contain the sixfold rotational symmetry. As a result, the doubly degenerate frontier orbitals of the GQD C42 (S1) (both HOMO (e_{1g}) and LUMO (e_{2u})) are split in the GQDs S4-S7 (HOMO (b_{2g}) and HOMO-1 (b_{3g}), LUMO (b_{1u}) and LUMO$+1$ (a_u)). This is already observed in 3.2.1 for the GQD C30 (S2). Consequently, the energy gap is significantly reduced.

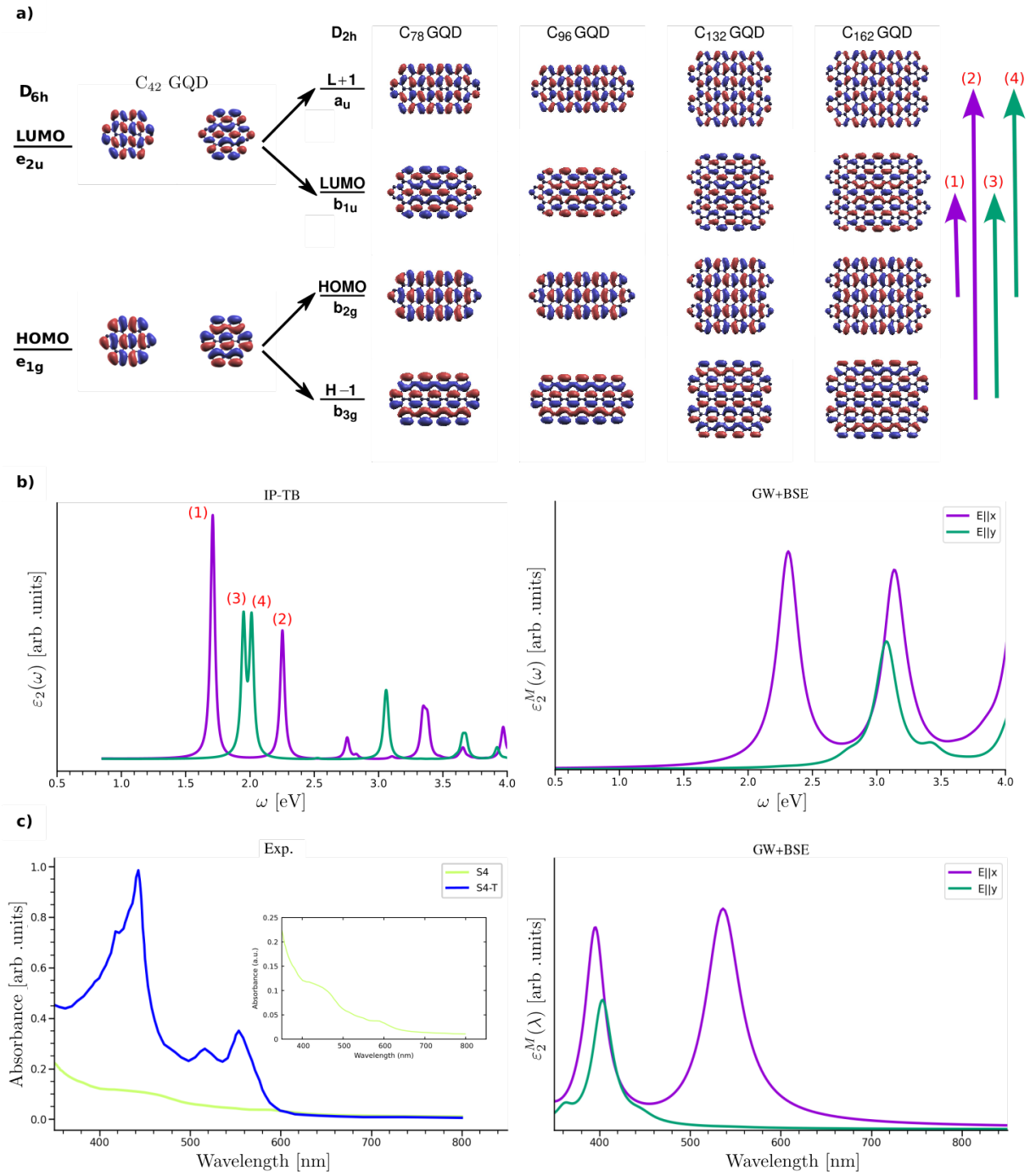

Figure 3.35 – Optical response of S4 ML GQD. a, Comparison between frontier orbitals of the GQD C42 (S1) and the S4-S7 GQDs calculated with our TB model. **b,** (Left part) Independent-particle spectrum calculated by 2NN TB method [265]. Peaks **(1) - (4)** represent allowed transitions in **a**. (Right part) Full spectrum calculated by GW+BSE represented in photon energy unit. Violet curve represents the optical response if electric field is polarized to x, whereas turquoise curve represents the optical response if electric field is polarized to y. **c,** (Left part) UV-Vis absorption spectrum of S4 (blue curve) in sodium deoxycholate (SDOC), S4-T (light-green curve) in 1,2,4-trichlorobenzene (TCB); credited by Dr. Jean-Sébastien Lauret at LUMIN laboratory in ENS Paris-Saclay, Dr. Julien Lavie, and Daniel Medina-Lopez at CEA-NIMBE laboratory in Paris-Saclay area [246, 265]. (Right part) Full spectrum calculated by GW+BSE represented in wavelength unit.

Peak	x Polarization (E||x)	y Polarization (E||y)	S4 (C78)	S5 (C96)	S6 (C132)	S7 (C162)
1	HOMO $\rightarrow$ LUMO	–	1.71050	1.53468	1.40303	1.23112
2	HOMO$-1\rightarrow$ LUMO$+1$	–	2.25244	2.20494	1.61139	1.52948
3	–	HOMO$-1\rightarrow$ LUMO	1.95011	1.83171	1.50143	1.37153
4	–	HOMO$\rightarrow$LUMO$+1$	2.01282	1.90791	1.51299	1.38908

Table 3.3 – Allowed transitions (in eV) between frontier orbitals of the S4-S7 GQDs calculated with 2NN TB model [265].

Fig. (3.35b) displays IP RPA-TB absorption spectra (left part) and fully GW+BSE absorption spectra (right part) of the S4 GQD (C78). All the technical details of the *ab initio* calculations are discussed in Appendix A. The direct gap is calculated and presented in Tab. 3.4. The corrected gap is 2.5 times larger than the one without correction found by the QE DFT-GGA method. This observation shows a good agreement with the case of the GQD C42 (S1) in 3.1.1. In the left part of the Fig. (3.35b), we can identify the allowed transitions **(1) - (4)** listed in Tab. 3.3. The Tab. 3.3 shows the possibility of tuning the optical transitions by more than 0.48 eV ($\gtrsim$ 283 nm) (from S4 to S7), and it is a great asset for using GQD in optoelectronic devices. Since the longitudinal size is bigger than the transversal one, the optical response is not identical if the polarization direction changes from the longitudinal x-axis to the transversal y-axis. Compared to the absorption spectra of the GQD C42 (S1) (see the Fig. (3.2)), several new peaks appeared, and the energy levels were changed due to the loss of order six symmetry. As listed in the Tab. 3.3, when the electric field is polarized to the longitudinal x-axis, the IP RPA-TB absorption spectrum exhibits a maximum peak at 1.71 eV and a shoulder at 2.25 eV stemmed from transition **(1)** and **(2)**, respectively. The corresponding transitions were also achieved at 2.32 eV for the maximum and 3.14 eV for the shoulder in the GW+BSE spectrum. Moreover, when the electric field is polarized to the transversal y-axis, these peaks **(1)** and **(2)** collapsed, and a maximum and shoulder peaks appeared at 1.95 eV and 2.01 eV stemmed from transitions **(3)** and **(4)**, respectively. In the GW+BSE spectrum, the absorption spectrum change was also captured, compared to the IP-TB spectrum; the difference was that the shoulder peak was first observed at 2.78 eV and after the maximum at 3.08 eV. We conclude that the TB method provides a reliable absorption spectrum for the S4 GQD (C78) and agrees well with the GW+BSE method.

Simulation method	E_{gap} (eV)
2NN TB	1.71
QE DFT-GGA	1.62
GWA	4.02

Table 3.4 – Gap width of the S4 GQD (C78) evaluated by different methods. All technical details are discussed in Appendix A.

In the following part, we compare theoretical and experimental absorption spectra. In Fig. (3.35c), we report the absorbance measurement in the left figure, and the full GW+BSE absorption spectrum is presented as a function of wavelength in the right figure. In the left figure, the light-green curve displays the experimental absorption spectra of the S4 GQD (C78) in sodium deoxycholate 2% (ca. 50 mM) [265]. Without functional groups on the GQD, the S4 GQD was poorly soluble and difficult to disperse. Only weak and broad transitions are observed with maxima at 569 and 635 nm for the S4 GQD. We suggested that the suspension is mainly composed of aggregates. We obtained similar absorption spectra for the S5 (C96) with maxima at 569 and 635 nm, whereas, for the S6 (C132) and S7 (C162), the spectra shifted to 541 and 590 nm as the gap decreased with the size of the molecules [265]. On the absorption spectra, one can observe that the transitions are more pronounced in the case of the S6 (C132) and S7 (C162) GQDs, despite these particles exhibiting a more significant number of sp^2 carbon atoms compared to the S4 (C78) and S5 (C96) GQDs. We attributed this result to a better dispersion of the large nanoparticles by the deoxycholate surfactant. The blue curve depicts the experimental absorption spectra of the S4-T in 1,2,4-trichlorobenzene (TCB) solvent. Compared to the absorption spectra of the pristine S4, since the intensity of the S4-T's spectrum is four times greater than that of the pristine S4, the tert-butyl chains did improve the absorption spectra. The blue curve shows a maximum at 449 and shoulders at 418, 433, 516, and 554 nm. We noticed that the peaks at 449 and 554 nm are consistent with those of the pristine S4 GQD with redshifts. This red shift was due to the change in the solvent. The solubility of this small GQD was observed to be significantly influenced by the choice of solvent by testing also with toluene, tetrahydrofuran (THF), and dichloromethane (DCM) [254]. Moreover, S4-T was still poorly soluble and had lower solubility than S5-T due to the lack of adjacent tert-butyl groups. It is worth noting that GQD S5-T reaches an exceptionally high value of 94%, which is one of the highest reported for GQDs, thus highlighting the great potential of GQDs as emitters for optoelectronic applications [254].

Recently, Medina *et al.* [246] reported that the absorption peaks at 554 nm, 449 nm, and 433 nm could be re-obtained at 554 nm, 449 nm, and 433 respectively by Time-dependent DFT (TDDFT) simulations, and they correspond to the three first transitions according to TDDFT analyses. The absorption

bands at 554 nm and 433 nm occur if the electric field is polarized to x-axis while one at 449 nm occurs if the electric field is polarized to y-axis. However, they cannot explain to the absorption bands at 478, and 516 nm. Moreover, it seems that they do not stem from the aggregation because they also appear at absorbance spectra of larger GQDs S5-T ($C_{78}H_{20}tBu_6$), $C_{114}tBu_{10}$, and S6-T ($C_{132}tBu_{12}$), where these larger GQDs were exhibited to be almost excellent solubility in the same report. However, they showed the origin of aggregation on the S4-T and S5-T by simulation. The positioning of the tert-butyl groups along the x-axis creates possible conformers for the GQDs. The calculations reveal that the steric hindrance caused by the tert-butyl groups creates an energetic barrier that inhibits the aggregation of the S5-T GQD. This barrier is sufficiently high to prevent aggregation, leading to the high solubility of the S5-T GQD in solution. In contrast, the S4-T GQD possesses conformers that all exist in solution and allow for aggregation.

On the other hand, in the GW+BSE absorption spectra (3.35c), when the electric field is polarized to x-axis, the violet absorption curve shows maxima at 395 and 536 nm, whereas when the electric field is polarized to x axis, the green absorption curve presents maxima at 362, 403, and 444 nm. The sum of these absorption spectra shows an excellent agreement with the experimental absorbance (blue curve). Since the peaks can be shifted by changing the solvent, the red shift between experimental and simulation absorption spectra is thus not a problem. Thanks to the full GW+BSE spectrum, we conclude that the other peaks on the blue curve stem from the aggregation of the GQDs. Later, the impact of the aggregation of the GQDs on the optical response will also be discussed in 3.4.2.

Comparison between STM experiments and simulations.

Since the small size S4 GQD (C78) was observed to have the worst resolution of measurements, the big GQDs like the S6 (C132) and S7 (C162) are so significant to be calculated with full correction; the S5 (C96) and its functionalized molecules seem to be the best option to simulate the STM images of the D_{2h} family. Thus, the S5-T molecules were studied on gold Au(111) surface in UHV by Prof. Hamid Oughaddou and his Ph.D. student Hamza El-Kari at ISMO Institute in the Saclay area. As shown in 3.3, the physical vapor deposition (PVD)[1] has not succeeded with a bad coverage ratio. Therefore, in this case, our collaborators utilized in addition liquid solution deposition (LSD)[2].

In Fig. (3.36), we report the comparison between experimental and simulation STM and STS results on the S5 GQD on the gold Au(111) surface. Figs. (3.36a-b) display the surface's large- and small-scale images obtained after a PVD flow for 10 minutes on the gold surface at RT. Similarly to the case of the

[1] During the physical vapor deposition (PVD), the materials to be deposited are heated to vaporize in a UHV room and then condensed onto the surface of the substrate, forming a thin, uniform layer. The substrate is then characterized directly with STM in the same room.

[2] Liquid Solution Deposition (LSD) is a method used to deposit thin films of materials onto a substrate from a liquid solution. The substrate is then placed in a UHV room to be studied by STM.

triangular-shaped T GQDs S3-A and -T GQDs in 3.3, the tert-butyl chains (t-Bu) were separated from the center part of the S5-T. Also, a bad coverage ratio was reached after depositing the S5-T. The resulting surface was similar to the one in the Fig. (3.25); it consists of an ordered network of the S5 GQDs (see the Fig. (3.36a)) and an ordered networks of columns (see later in Fig. (3.37a)). The height of these structures on the gold surface nearly remains unchanged (~ 1.2 Å).

(a) Monomer S5:

We first focus on the S5 molecule signature on gold Au(111). The S5 GQD exhibits various signatures on the gold surface, such as **a single ellipse-shaped spot** (see the Fig. (3.36b)), **two circle-shaped spots** (see Fig. (3.36c)), and **triple columnar spots** along the longitudinal axis (see Fig. (3.37c)). Since the former signature does not contain as much information as the latter, we investigated theoretical studies on the second and third signatures to compare them to the experimental measurements.

The Fig. (3.36c) shows a low-temperature STM image obtained after an LSD flow for 10 ms on a gold Au(111) surface at RT. This figure highlights the **two circle-shaped spot** signatures of the S5 GQD at 1.1 eV. In Figs. (3.36e and f), we report constant-height current simulation images evaluated by the 2NN TB and Fireball-STM methods, respectively. In Fireball DFT-LDA simulations, the S5 GQD was deposited on a pristine five-layer slab of 28.84 x 20.19 ($Å^2$) superlattice of gold Au(111). The resulting primitive cell consists of 476 atoms in total. The tip-sample height was set to 5.2 Å. These figures show that the **two circle-shaped spots** signature of the monomer S5 is remarkably obtained in both experiment and simulation. The STM experimental image (3.36c) at 1.1 V (red continued circle in Fig. (3.36d)) can be directly compared to the LDOS-TB simulation image at 1.23 V (black continued circle in Fig. (3.36i)), and the Fireball-STM simulation at 1.8 V (black dash circle in Fig. (3.36h)). It also means that this signature stems from a π state. Nevertheless, there is a significant gap in the size of the molecule because of the resolution of experimental images. The S5 GQD width is approximately 20 Å experimentally, while it is 24.54 Å in the simulation.

The Figs. (3.36d and h) illustrate the STS experimental spectrum and the projected DOS of the S5 calculated by the Fireball DFT-LDA method, respectively. We figured out that the PDOS of S5 has shown a good agreement with the STS experimental spectrum. Moreover, the Fig. (3.36i) depicts a comparison between the PDOS of the S5 and the total DOS of the S5 in vacuum calculated by the 2NN TB method (in green) and by Fireball DFT-LDA (in red) (shown in the Fig. (3.36h)). The 2NN TB method provided a very accurate TDOS with a gap of 1.53 eV compared to Fireball DFT-LDA with a gap of 1.79 eV. In the presence of the gold surface, the S5 GQD lost 0.74% of its

charges for the gold surface, which explains why the blue curve shifted to a higher energy level than the red one.

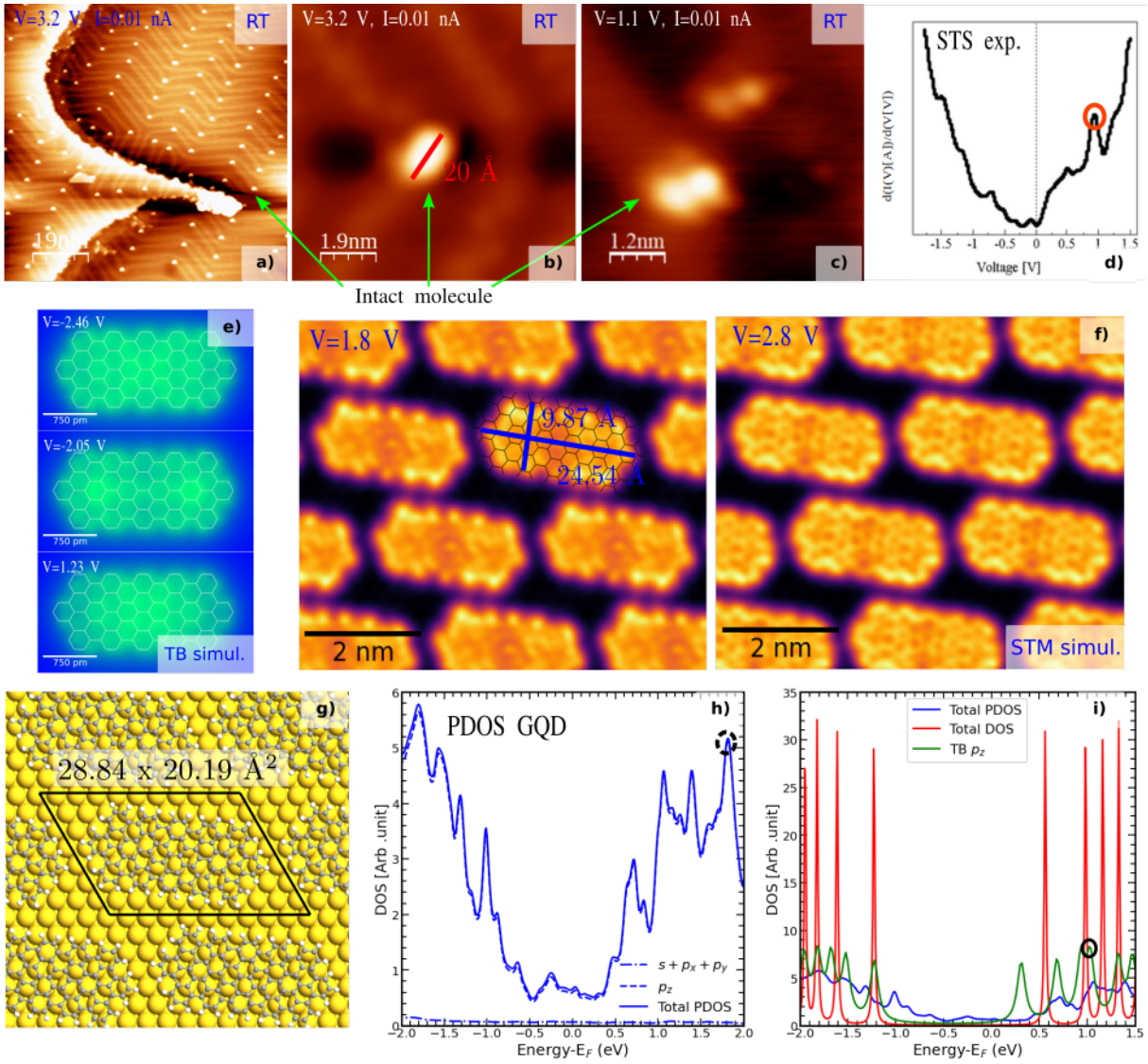

Figure 3.36 – Comparison between experimental and simulation results on the S5 GQD on gold Au(111) surface. a-b, Low-temperature (77K) STM experiment images of substrate after a PVD flow for 10 minutes on the gold surface at room temperature (RT). **c,** Images obtained after a LSD flow for 10 ms on gold surface at RT. **d,** STS experiment spectrum of **c**, with the red continued circle representing the voltage where **c** is found. **e,** LDOS obtained by 2NN TB method which have shown the same signature as in **c**. **f,** STM simulations images of model **g**. **g,** Geometry model of the S5 GQD on a five-layer slab of 28.84 x 20.09 ($Å^2$) periodicity of gold Au(111) surface. **h,** PDOS of the S5 GQD, black dash circle represents to the voltage where **f** is found. **i,** Comparison between the PDOS of the GQD on the gold surface calculated by Fireball-DFT method (blue line) and the total DOS of the GQD in vacuum evaluated by 2NN TB method (green line) and Fireball-DFT method (red line). Black continued circle represents to the voltage where **e** is found.

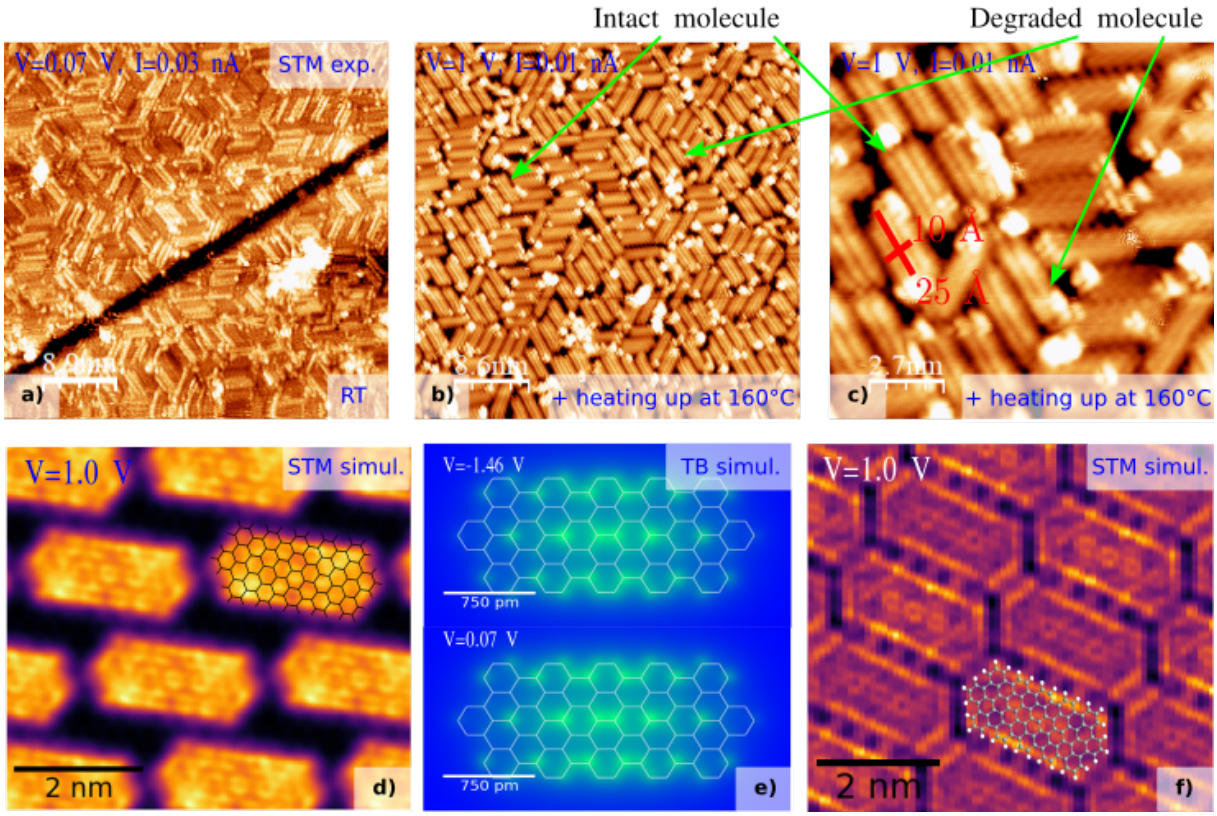

Figure 3.37 – Higher-coverage surfaces obtained after the LSD flow. **a,** Large-scale surface after an LSD flow for 60 mns on a gold Au(111) surface at RT. **b-c,** Surfaces obtained by heating up the surface **a** to 160℃ for 15 minutes, in which a disordered network of the S5 GQDs is observed. **d,** STM simulation image of the model (3.36g). **e,** LDOS of the S5 GQD calculated by 2NN TB method. **f,** STM simulation image of a 2D network of S5 monomers presented later in Fig. (3.38f).

Besides, the monomer S5 also exhibits other highlighted signatures, **triple columnar spots**, which is a stronger argument to confirm the presence of the S5 monomer. In Fig. (3.37a), we report the image of the surface obtained after an LDS flow for 60 ms on a gold surface at RT. Compared to the surface obtained by PVD in the Fig. (3.36a), we notice that the LSD significantly improved the coverage ratio. Figs. (3.37b-c) display the images of the surface obtained after annealing the surface at 160℃ for 15 minutes. In these figures, at 1 V, we observed a disordered network of the intact S5 GQDs with a **triple columnar** signature and, unexpectedly, the degraded GQDs with a **double columnar** signature. The **triple columnar** signature of the S5 monomer is exhibited by the 2NN TB method at 0.07 V and the Fireball-STM method at 1.0 V (see Figs. (3.37d-e)). In this case, the columnar structure is proved again to be created along each armchair ring of the GQD, which was already observed in the Fig. (3.31) for the triangular-shaped GQDs T C96 (S3). The transversal and longitudinal lengths of the S5 GQD are approximately equal to 10 and 25 Å experimentally (see the Fig. (3.37c)). They are close to those calculated by simulation, equal

to 9.87 and 24.54 Å, as shown in the Fig. (3.36f). Additionally, both experiment and simulation results exhibit a similar separation distance between the two columns, which was measured to be approximately equal to 4 Å experimentally and 3.77 Å by simulation (see later in the Fig. (3.38d)). Since the coverage ratio is significant, each intact GQD was influenced by many others. In order to consider this effect that appeared in these experimental surfaces (3.37a-c), we simulated a two-dimensional periodicity of the S5 GQDs on the gold surface, which is discussed more in detail in the next part. We recover the **triple columnar** signature of the S5 monomer, as shown in Fig. (3.37f), and this surface is comparable to the large-scale image of the experimental surface (3.37a). We conclude that theoretical simulations successfully revealed the signature of the S5 monomer on the gold surface, and similarly to the case of the triangular-sharped GQDs T C96, the formation of uncontrolled degraded GQDs was inexplicable.

(b) 2D network of the monomers S5 and theoretical prediction for the ordered column structures:

The exposure of the **triple columnar** signature of S5 GQD plays a vital role in understanding the origin of ordered column networks that appear on gold Au(111) surface for both triangular- and rectangular-sharped GQDs C96. A two-dimensional network of S5 GQDs probably gives an ordered column network. In this part, we introduce a 2D planar network of the S5 GQDs, called S5-B1, presented in the Fig. (3.38f). This network can be obtained by a S5 GQD with the superlattice vectors $\{\mathbf{A}_1, \mathbf{A}_2\}$ where $|\mathbf{A}_1| = 26.08$ Å, $|\mathbf{A}_2| = 13.8$ Å. These vectors form an angle of 74.38°.

Fig. (3.38a) depicts an STM experimental image obtained after a PVD flow for 20 minutes on a gold Au(111) surface at room temperature. Compared to the surface (3.36a) obtained after shorter deposition time, we noticed that there were more materials deposited on the surface (3.38a), and they formed several columnar islands. In Fig. (3.38b), we report an STM experimental image on a columnar island measured after an LSD flow for 30 ms on a gold Au(111) surface at RT. The ordered columnar network made from the S5 GQDs has the same signature as shown in the Fig. (3.31a) in the case of the triangular-shaped GQDs T C96 (S3). The only difference is that the length of each column is longer in this case than in the triangular-shaped GQDs T C96 (S3) case; it is evident that the S5 GQD is longer than the S3 GQD along the longitudinal axis. In Fig. (3.38d and g), we report constant-height current maps of the S5-B1 model on gold Au(111) surface and in a vacuum obtained by the Fireball-STM simulation and the 2NN TB simulation, respectively. It is worth noting that since our 2NN TB method has taken into account only second nearest neighbors, the resulting LDOS maps presented in the Fig. (3.38g) are equal to those of the S5 monomer (3.37e) but duplicating in space thanks to superlattice vectors $\{\mathbf{A}_1, \mathbf{A}_2\}$. For the Fireball STM method, we used a five-layer slab of 83.02 x 32.62 ($Å^2$) periodicity of gold Au(111) surface

compressed with strain ratios of -1.56 and 0.45 $\%$ along the in-plane pristine lattice vectors of Au(111). The resulting primitive cell consists of 727 atoms in total. In the Fireball-STM simulation, the contribution of the gold surface on tip-sample interaction was neglected, and the tip-sample distance was set to 4 Å. Compared to the STM experimental image (3.38b), we obtained identical column signatures by using 2NN TB and Fireball-STM methods. We note that firstly since the ordered column structures were successfully modeled by using only p_z orbitals without surface, the empty space (or unoccupied space) between each column pack (white dash line in the Fig. (3.38d)) can be perfectly reproduced if we set a longer $\mathbf{A}_1$ vector. Secondly, the gold surface plays a vital role since the distance gap between each GQD in each column pack is visibly seen in the STM simulation images, which has not appeared in the STM experiment images. This may be due to the resolution of the experiment images or the use of a compressed gold surface instead of a pristine chevron gold surface, as mentioned in 3.3 for the triangular-shaped C96 GQDs.

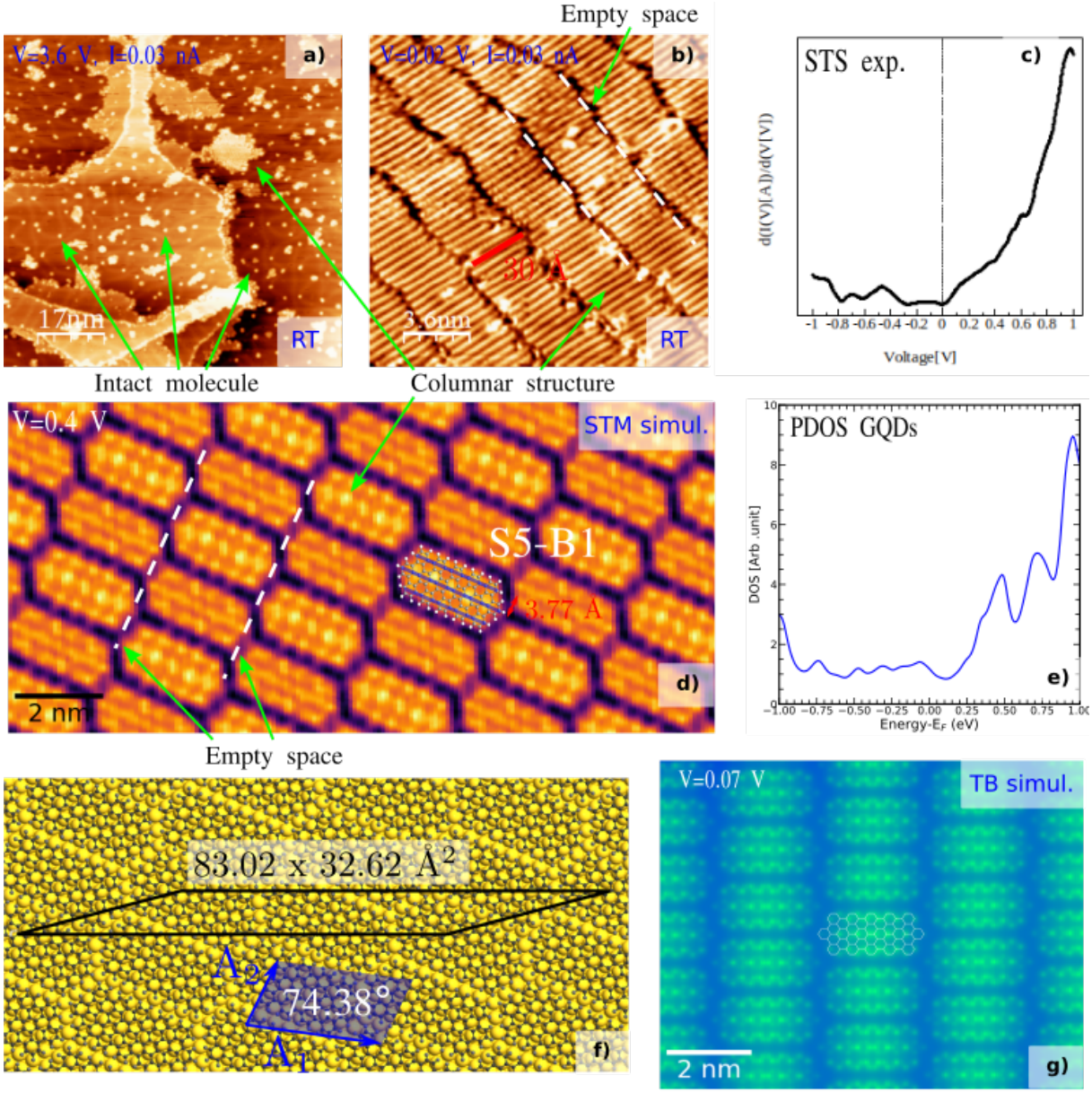

Figure 3.38 – Two-dimensional periodicity network of the S5 GQDs on gold Au(111) surface. a, Image obtained after a PVD flow for 20 minutes on a gold Au(111) at RT. **b,** Image achieved after a LSD flow for 30 ms on a gold Au(111) surface at RT. **c,** STS experiment measurement of **b**. **f**. Geometry model of a 2D 26.08 x 13.8 ($Å^2$) periodicity of the S5 GQDs (blue cell), labeled S5-B1, on five-layer slab of 83.02 x 32.62 ($Å^2$) gold Au(111) surface (black cell). **d-e,** STM simulation image and PDOS of the model **f**. **g,** LDOS of LUMO state of the S5-B1 calculated by 2NN TB method.

Further, in Fig. (3.38c and e), we report the STS experimental spectrum and the projected DOS of the S3-B1 calculated by Fireball DFT-LDA. We notice that these figures are strongly comparable. All these theoretical proofs convince us to believe that the ordered column network is nothing else than a two-dimensional planar network of S5 GQDs. Unfortunately, in this study, the experiment was performed in a low-temperature room at 77 K; thus, we could obtain a better resolution of the

STM experimental image. Further experimental investigations are needed to compare with these theoretical results.

3.4.2 Twisted bilayer molecules.

As shown in 3.4.1, the GQDs mostly stack together onto clusters in the solvent because of their large size and poor solubility. Optical measurements are consequently not performed on a solution of purely isolated molecules. Therefore, it is interesting to question the impact of such stacking of molecules on their electronic and optical properties.

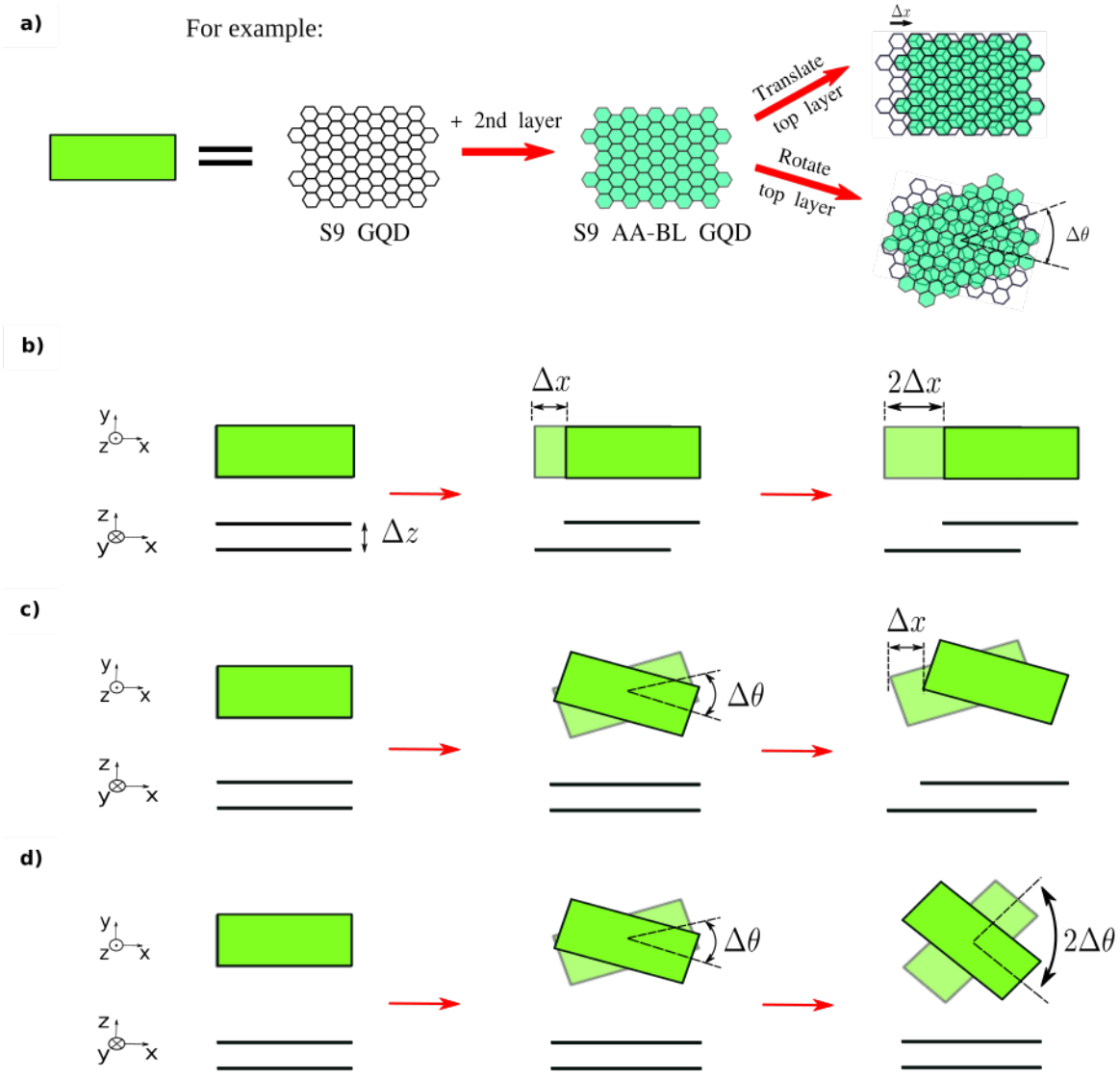

Figure 3.39 – Schematic geometry of bi-layer GQDs studies. a, Guide to understanding the following schematic. **b,c,d,** Schema showing our studies by purely translating along the longitudinal axis, by rotating with a default angle, then translating along the longitudinal axis, and by purely rotating.

In order to estimate the changes induced by the aggregation effect in the electronic structure, we have performed a systematic theoretical study of the electronic properties of clusters made from two stacked molecules called bilayer graphene quantum dots (BL-GQDs). Then, we compare the electronic properties of BL-GQDs with those of pristine molecules.

First, for studying bilayer GQD structures, we have used a very similar Tight-Binding model as described in 2.1.1. In the case of graphene-derived materials, the lattice constant $a_{||}$ is now equal to 2.456 Å, and $a_{\perp}$ is set to the interplane distance in bilayer graphite, 3.35 Å. The most significant difference in the Tight-Binding scheme used in this case is that the cutoff functions $F_c(D_{AB})$ were removed entirely, $F_c(D_{AB}) = 1$. The set of parameters is presented in Tab. 3.5.

Intralayers hoppings (||)			Interlayers hoppings ($\perp$)			
On-site energies (eV)	In-plane hoppings (eV)		Prefactor value (eV)		Decay value (Å^{-1})	
$\xi_{AA}^{(1)}$	$t_{AB}^{\|\|}$ (1st NN)	$\xi_{AA}^{(2)}$ (2nd NN)	$t_{AB}^{\|\|}$	$\gamma_{AB}^{\perp}$	$Q_{AB}^{\|\|}$	$Q_{AB}^{\perp}$
0.00	-2.70	0.27	-2.70	0.48	2.218	2.218

Table 3.5 – Set of parameters for the intralayer and interlayer hoppings [265]. In this case, the cutoff functions $F_c(D_{AB})$ were completely removed, $F_c(D_{AB}) = 1$.

In order to obtain geometries of BL-GQD, we did three different studies presented in Figs. (3.39b-d). We locate two molecules on top of each other, and then either we apply relative translations along the x-axis by using a distance step Δx (see the Fig. (3.39b)) or rotations with a default angle along the z-axis, then subsequently translations along the $x-$axis (see the Fig. (3.39c)), or purely rotations angle along the z-axis by using an angle step $\Delta\theta$ (see the Fig. (3.39d)). Thanks to these strategies, we can span various stacked molecular architectures. The vertical separation is 3.5 Å, close to the interlayer distance in graphite and relative compounds.

Since direct atom-on-atom AA stacking is energetically disadvantaged, rotated geometries with an angle close to 0 or 60° are excluded, as they are not representative of the geometries that may occur in the samples. For the same reason, the translated geometries we considered always have a local AB stacking (atom located above a hexagon center). Since the results obtained by the first and second cases presented in Figs. (3.39b-c) have the same trend, in this report, we will only show the results of the former. The evolution of the HOMO–LUMO gap as a function of the relative translation and rotation is plotted in Fig. (3.40). In this figure, dashed curves represent the change in the gap of the pristine ML-GQDs, whereas continued curves represent the change of one of its corresponding BL-GQDs. The gap of the BL-GQDs is always smaller than the gap of its corresponding isolated molecule, and the reduction

is in the range of ca. 200 meV. Additionally, no magic angle was observed because of the limited size of GQDs.

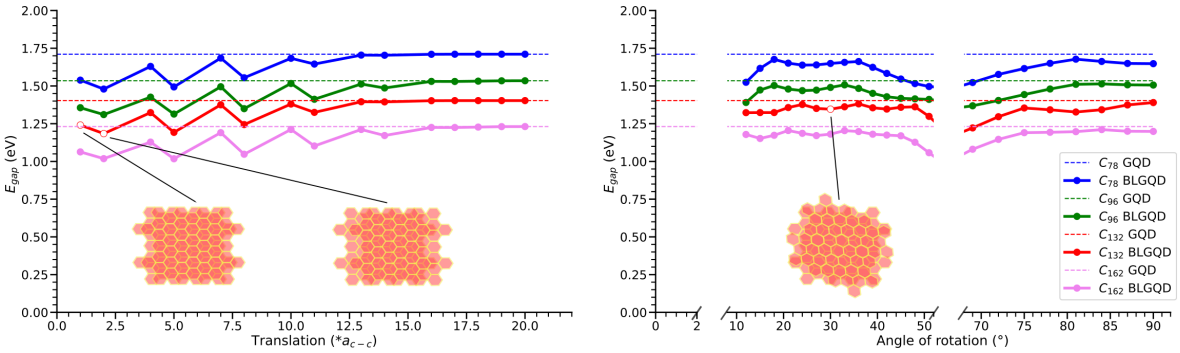

Figure 3.40 – Effects of stacking of two D_{2h} GQDs on their HOMO–LUMO gap [265]. (Left part) evolution when translating two stacked molecules. (Right part) evolution with the rotation angle. In both cases, the reduction of the gap is small (lower that 200 meV).

The physical origin of this reduction is easy to understand if we analyze the first AB stacked geometry. When we stack the two molecules that are shifted by a distance of Δx=1.42 Å, the D_{2h} symmetry of the isolated GQD is lost. Since the relative displacement is along x, the y mirror symmetry operation is preserved. The group symmetry of AB stacked BL-GQD is then the C_{2h}, which contains inversion and a twofold rotational symmetric rotation along y-axis in addition to the mirror. Due to the weak interaction between molecules, each isolated GQD energy level gives rise to two distinct states according to the bonding or antibonding combination of molecular functions. As shown in Fig. (3.41a), when mixing the former LUMO (b_{1u}) levels of the pristine ML GQD, we can obtain either a bilayer state of irreducible representation a_g (if the character of the rotation is +1) or b_u (if it is - 1). One is a bonding state between the two molecules, and the other is antibonding. We understand that each transition peak (*e.g.*, HOMO to LUMO denoted **(1)**) of the monolayer corresponds now two transitions (HOMO to LUMO denoted **(1)** and HOMO$-$2 to LUMO$+$2 denoted **(3)**) in the bilayer system, implying a reduction of the HOMO–LUMO gap. The electronic transitions allowed by the C_{2h} symmetry of the bilayer system are depicted in the Fig. (3.41a) in the case of the AB bilayer made from two S6 GQDs. Moreover, since each allowed transition induces the emergence of a peak in the absorption spectrum, the subsequent impact of the aggregation of GQDs is thus the apparition of extra peaks compared to the absorption spectrum of the pristine ML GQD (see Figs. (3.41b-c)). In addition, the distinction between two peaks due to the aggregates is very significant with respect to the photon energy. For instance, the transition **(1)** in the monolayer system corresponds to a peak at 1.4 eV. Due to the aggregates, this transition corresponds to **(1)** at 1.2 eV and **(3)** at 1.6 eV in the bilayer system; thus, the distinction between these two peaks is 0.4 eV, which is

remarkably distinguishable in the absorption spectrum.

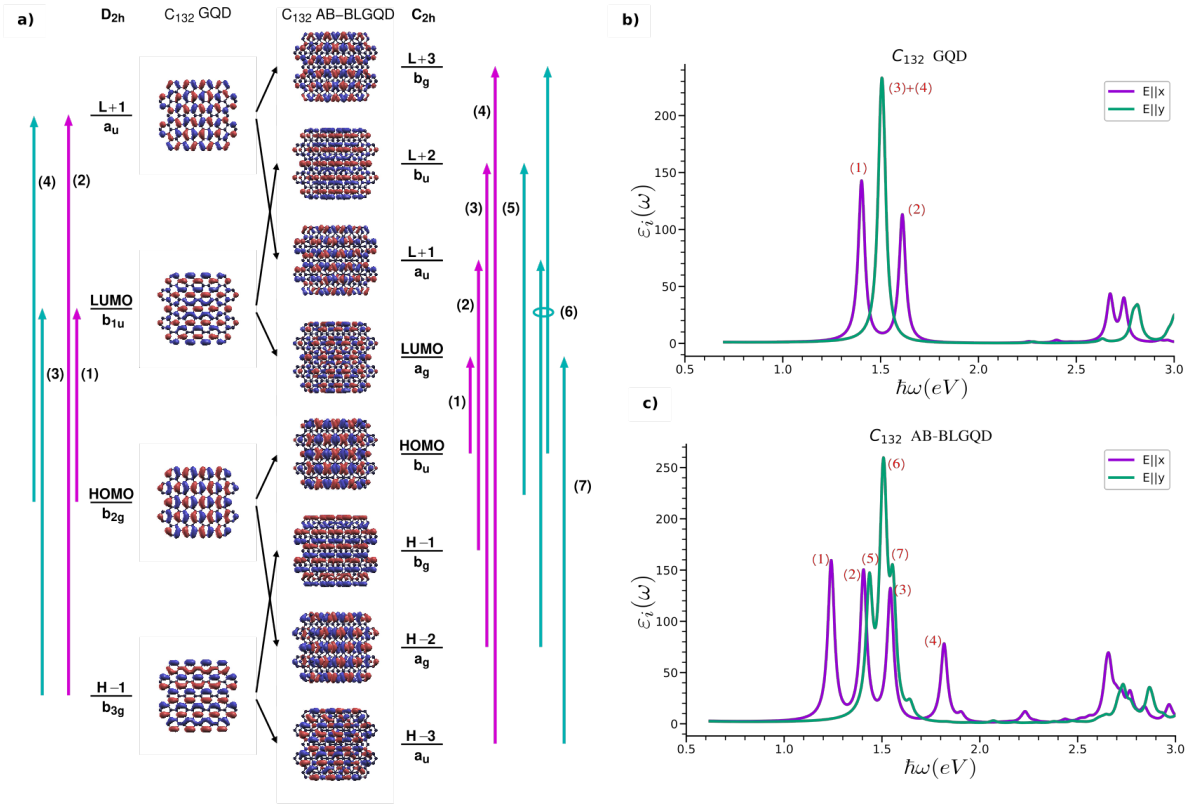

Figure 3.41 – IP-TB absorption spectrum of the S6 ML GQD (C132) and S6 AB-BL-GQD [265]. a, (left part) Frontier orbitals of the S6 calculated with our TB model. The symmetry group D_{2h} implies that allowed transitions when the field is along $x-$axis (violet) give rise to peaks **(1)** and **(2)** in **b** or **(3)** and **(4)** when the field is along $y-$axis (turquoise) in **b**. Right part of **a** the first AB stacked bilayer architecture, made from two S6 GQDs; the AB stacked BL-GQD belongs to the C_{2h} group. Due to intermolecular interactions, each individual level of the isolated molecule split onto two levels. Therefore, each transition peak is separated onto two parts. **b,** Peaks corresponding to the transitions listed in **a** for the S6 ML-GQD. **c,** Peaks corresponding to the transitions listed in **a** for an AB stacked bilayer of the S6 GQDs.

3.4.3 Conclusion

Here, we described a series of graphene quantum dots containing up to 162 sp^2 carbon atoms. The GQDs exhibit the extension of benzene rings along longitudinal (for S4 – $C_{78}H_{26}$ and S5 – $C_{96}H_{30}$) and transversal (for S6 – $C_{132}H_{34}$ and S7 – $C_{162}H_{38}$) axes. As a result, their symmetry no longer contains the rotational invariance of order six as the GQD C42 (S1). The GQDs were synthesized using the bottom-up approach, which allows our collaborators to control the structure of the materials perfectly. First, they were not functionalized with solubilizing groups on their periphery to keep the maximum similarity with nanoparticles of pure graphene. These GQDs are, thus, insoluble in organic solvents, and our collaborators use surfactants to prepare dispersions. The sodium deoxycholate is

known as an efficient surfactant to solubilize carbon nanotubes and graphene, and here we showed that the larger GQDs (S6 and S7) are better dispersed in SDOC solution than the smallest ones (S4 and S5). The optical studies showed broad transitions in absorption and photoluminescence spectra, characteristic of the presence of aggregates in solution; for instance, the smaller S4 and S5 GQDs have very bad absorbance, PL, and PLE spectra. Nevertheless, for S6 and S7, we observed, as expected, a redshift of the transitions as the size of the GQDs increases. Subsequently, the functionalized $C_{78}tBu_6$, $C_{96}tBu_8$, $C_{132}tBu_{12}$ GQDs were tested to reduce the aggregation effects by our collaborators, in different solvents: 1,2,4-trichlorobenzene (TCB); toluene; tetrahydrofuran (THF); and dichloromethane (DCM) [246]. These functionalized groups were observed to make the GQDs better solubilized, and substantial improvement was shown in both spectra. The biggest GQDs were pretty well solubilized; they remained highly individualized in solution at the dilute concentrations needed for optics experiments. Thus, well-defined spectra were performed with perfect matching between the absorption and excitation spectra for all emission peaks, no dependence of the absorption spectrum to concentration, high quantum yields, and monoexponential lifetimes [246]. However, the solubility challenges of the smallest GQD, S4, arise from its limited functionalized groups, impacting its imperfect solubilization compared to the larger GQDs. This issue results in the formation of aggregates, affecting the absorbance, photoluminescence (PL), and photoluminescence excitation (PLE) spectra. Furthermore, the solubility of the S4 GQD appears notably influenced by the solvent choice. In TCB, monomers coexist with other species, including dimers or higher aggregates. These aggregates undergo a bathochromic shift in absorption within the 500 nm – 600 nm range and display a red-shifted emission compared to the monomer [246]. Further synthesis and experimental studies are needed to obtain the finest spectroscopy and thoroughly explore these rectangular-shaped GQDs' optical properties.

Theoretically, these target properties of the pristine GQD can be determined if we calculate the absorption spectrum of the pristine GQD, understand influences arising from aggregate formation, and finally, juxtapose these findings with empirical observations. First, we simulated the absorption spectra of the pristine GQDs using the TB and GW+BSE methods. Compared to GQD C42 (S1), the doubly degenerate frontier orbitals of the S1 are split in the S4-S7 systems, which induced the apparition of new peaks in the absorption spectra and reduced energy gap. Comparing these GQDs, we observed that the energy gap decreased when the GQD's size increased. The optical response differs since the GQDs no longer have the same geometry along longitudinal and transversal axes. Although the 2NN TB method disregarded the gap correction exciton effect,..., it can detect this feature, and surprisingly, the accurate spectra compared to the full GW+BSE one. Subsequently, we corrected the gap and included the exciton effect using GW and BSE methods. The GW+BSE spectrum successfully showed a good agreement with experimental results. Moreover, to understand the impact of aggregates on

the absorption spectra, we also did theoretical investigations on twisted bilayer GQDs using the 2NN TB method. Our goals were to create aggregates that could strategically form in the solvent and then compare their absorption spectrum to that of pristine mono-layer GQD. Electronic and optical properties were also studied as a function of the translation and the rotation angle between the molecules. The theoretical results obtained after these case studies were very similar. We conclude that if we choose the example of AB stacking bilayer of the S6 GQDs obtained by translation, the aggregates cause the change of the symmetry point group from the higher symmetry group, D_{2h}, to the lower one, C_{2h}; only the mirror along the displacement axis is persevered. As a result, the energy levels of the isolated GQD were split into those of the BL-GQD system, which induced the band-gap reduction and a significant change in the absorption spectrum. In all cases, the band gap reduction due to aggregation is smaller than 200 meV.

Our collaborators tested additional liquid solution deposition for the STM part to improve this ratio since the coverage ratio was very bad with physical vapor deposition for the triangular-shaped GQDs T C96 (S3). Our collaborators experimented only with the S5-T GQD; in this case, they used these two deposition methods. We observed that this latter deposition method significantly improved the coverage ratio. Unexpectedly, we achieved a similar surface to the one obtained after depositing the triangular-shaped GQDs T C96 (S3). From the STM experimental image of the isolated S5 GQD, the origin of the columnar structure on STM experimental image insight, each column stems from an armchair ring of the GQD. This argument is consistent with the one discussed in the triangular-shaped GQDs T C96 (S3) case. On the other hand, uncontrolled degraded GQDs were obtained on the surface after annealing at 160℃. This surface was also observed on the surface after heating up at 150℃ for the case of triangular-shaped GQDs T C96 (S3). However, we do not have a convincing answer for this phenomenon. As discussed in 3.3, radical GQDs may be formed on the gold surface instead of the GQDs saturated by Hydrogen atoms. Thus, further simulations must be performed on a radical S5-T GQD (without the tert-butyl chains) on the gold surface to confirm whether the radical molecule has the same signatures observed in STM experimental images. On the other hand, we can still not provide a more convincable structure for the columnar structures, and very probably, these are combination structures as reported by András Pálinkás *et al.* [263]. Additionally, the reason why the tert-butyl chains are breaking, though done by the LSD, is still uncomprehensive. Thus, further experimental studies with better precision and control are needed.

Conclusions

As mentioned in the introduction, this thesis work aims at evaluating theoretically the electronic band structures, absorption, and STM/STS spectroscopies of new graphene-derived materials proposed by collaborators within the frameworks of **GANESH** and **BOGART** projects, and then to compare them with the corresponding experimental measurements. Thanks to this collaboration, we can explore the change in optical and electronic properties of these target materials as a function of their size and symmetry.

Unfortunately, the first year of this PhD thesis was directly affected by the pandemic Covid 19 since all the collaborators' experiments were delayed; therefore, we lacked experimental data to evaluate in simulations. For this reason, we decided to participate in the theoretical studies on electronic and optical properties of new close to 30° twisted hexagonal boron nitride (T-hBN) proposed by Dr. Sylvain Latil in collaboration with theoreticians at the LEM laboratory. Before this work, it was well-known that low-dispersion bands were found at small angles of twisted bilayers of numerous hexagonal structures, such as graphene, hBN, and TMDs. In this collaboration, we observed that these low-dispersion bands occur in bilayer systems of hBN near 30°, and they cause a significant absorption band in the ultraviolet region. The Tight-Binding model allowed us to obtain electronic and optical band structures with very good agreement with the ones evaluated by *ab initio* method. Moreover, we explained that boron-boron interlayer interaction plays a vital role in forming these bundle bands and their local density of states. Therefore, we predicted the potential existence of these bundle bands on all homo-structures formed of hexagonal single-layers, such as TMD, antimonide, and silicene... This work may interest researchers studying close to 30° twisted hexagonal systems within the research community. On the other hand, the closer the twist angle is to 30°, the bigger the unit cell of the system becomes. Hence, this work only yielded the absorption spectra at the independent particle level. Further, it will be more intriguing if exciton effects are included. Because of large system sizes, it is impossible to evaluate the absorption spectra, including exciton effects in *ab initio* calculations; including these effects on the Tight-Binding model could be an excellent option to answer the problem. However, as shown in 1.3, in the Tight-Binding approach, the many-body effects were completely disregarded; moreover, only kinetic integrals and spherically symmetric atomic-like hopping integrals between nearest-neighbors are considered. Therefore, including the exciton effects in the Tight-Binding method is challenging and even more complicated than in DFT. Thus, adapting this potential to the Tight-binding model for twisted bilayer systems is worth it.

In this thesis, our studied graphene-derived materials can be divided into five families concerning the correspondent GQDs below: hexagonal-shaped GQD C42 (S1), trapeze-shaped GQD C30 (S2), triangular-shaped GQDs T C96 (S3), and rectangular-shaped GQDs R C78 up to C162 (S4-S7).

Concerning GQDs, contrary to the observations published by the research community (see the introduction), our collaborators surprisingly observed that the larger unfunctionalized rectangular-shaped

GQDs, C132 (S6) and C162 (S7), were better soluble and individualized in solution than the others despite their large size. However, all these unfunctionalized GQDs showed a behavior that could be explained by aggregation in solution. Later, they showed that the functionalized groups improved their absorbance spectrum significantly. The GQDs with the tert-butyl groups exhibit better improvement in solubility than with the alkyl chains [246]. The large GQDs with the tert-butyl groups, such as S5-T, were almost perfectly solubilized. However, aggregates and impurities were still present in the smallest GQD, S4-T, which blurs the intrinsic properties of GQDs. Nevertheless, no experimental evidence of aggregates in solution was detected. By simulations, S5-T GQD exhibits high solubility due to the energetically unfavorable conformers for aggregation, while S4-T GQD possesses conformers that allow for aggregation. TDDFT predictions matched the experimental data for only three first absorption bands. However, several peaks on the experimental spectra do not relate to the aggregates because they appear for larger GQDs that have proven remarkably soluble, and the TDDFT predictions could not explain these peaks.

Therefore, we decided to evaluate the absorption spectra of these GQDs by using full GW+BSE simulation. Since the optical properties of the S1 GQD (C42) are almost fully understood, thus we first evaluated the absorption spectra of S1 and then compared them to one calculated in reference. We aimed to achieve the best parameters for the large GQDs in the GW+BSE simulation. Secondly, these parameters were adapted to obtain the absorption spectra of the S4 GQD (C78). The resulting spectra of the S1 showed outstanding agreements with those evaluated about the interest energy range 0-5 eV; the difference between them was related to the different used packages and exchange-correlation functionals... Moreover, the resulting spectra of the S4 exhibited better agreement with experimental data than the one obtained by TDDFT simulations. Thanks to the full GW+BSE simulation, we can identify two more absorption bands that TDDFT simulations cannot explain, and we can eliminate other bands originating from the aggregates and impurities. On the other hand, using the Tight-Binding method, we got insight into the impact of aggregates on electronic and optical properties by creating all possible stacking bilayers of GQDs. The simulation results showed that the aggregates cause the creation of numerous additional energy levels and changes of all energy levels, which reduce a band gap smaller than 200 meV. Thus, the absorption spectrum of a single GQD changed significantly due to these changes, such as the appearance of new adsorption peaks and a red shift of peaks, which challenges the determination of intrinsic properties of the target GQDs.

Unlikely the rectangular-shaped R C96 GQDs with highly soluble, the triangular T C96 GQDs were badly solubilized and still formed aggregates even with functionalized groups. These GQDs with tert-butyl groups showed an apparent improvement in solubility accompanied by sharper absorption and emission bands concerning alkyl chains, but not enough to determine their intrinsic properties. However,

in this case, we only evaluated the optical properties using the Tight-Binding method, and the resulting spectrum could only help a little in understanding the experimental data. In perspective, further GW+BSE simulations are needed for this case.

Studying the change of properties of these GQDs as a function of system size and symmetry allows us to reveal many intriguing phenomena. For instance, in the rectangular-shaped family of GQDs, it was possible to tune the absorption by more than 283 nm by changing the size from S4 (C78) to S7 (C162). Moreover, the changing size of GQDs induces a change in the band gap; the band gap decreases as the size of GQDs increases. A band gap reduction is about 0.48 eV from S4 to S7. This observation was already made about what was discussed in the introduction. This family of GQDs also exhibited very high quantum yields, up to 94$\%$. This is one of the highest reported for GQDs. These GQDs promise great potential as emitters for optoelectronic applications. The symmetry of GQDs also greatly impacts their electronic and optical properties. For instance, if we consider unfunctionalized rectangular- and triangular-shaped C96 GQDs, S5 and S3, they have the same system size. Nevertheless, they belong to two different symmetry groups: D_{2h} and D_{3h} respectively. These symmetrical groups have the same number of symmetry operations; thus, these GQDs have the same level of symmetry richness. Their different symmetries lead to different edge structures and quantum confinement effects. Therefore, even though these GQDs have the same system size, the S5 GQD has different energy levels than the S3 GQD with a smaller band gap ($\sim$0.25 eV less) and different absorption structures.

Our collaborators did prior on-surface studies before this PhD time. They deposited functionalized triangular-shaped S3-A GQDs with alkyl chains in 1-phenyloctane on HOPG (highly oriented pyrolytic graphite) by liquid solution deposition (LSD). STM images showed no organization of individual molecules, and only vertically columnar structures of the S3-A GQDs were observed. Afterward, the unfunctionalized S3 GQDs, S3-A, and S3-T GQDs functionalized with alkyl chains, and the tert-butyl groups were studied on gold Au(111) surface by physical vapor deposition (PVD). Surprisingly, our collaborators observed that the resulting surfaces were the same for all these deposited GQDs, which showed bad coverage ratios. For all the experiments, only horizontally planar structures were observed on the gold surface instead of the vertically structure ones, as mentioned in the prior work. Compared to the expected STM simulation surface, the functionalized groups left the PAH core on the gold surface. Instead, a network of isolated GQDs was obtained on the gold surface. All the experimental surfaces were observed to be identical for all the experiments, including with the unfunctionalized S3 GQDs. Based on the latter experimental observation, our collaborators assumed that the functionalized groups were not absorbed on the gold surface. Simultaneously, unknown horizontal columnar structures have existed, which are hardly explained. Besides the columnar signature, experimental data allow us to measure the length of each column, the distance gap between two columns, and the STS spectrum. The

only option that respects all this information is for a 2D network of isolated S3 GQDs to form columnar structures. The STM simulation results of the 2D network of the isolated S3 GQDs almost aligned with the experimental observations of the columnar structures.

To confirm this work, our collaborators deposited the rectangular-shaped S5-T GQD functionalized with tert-butyl groups on the gold Au(111) surface by PVD and later LSD. The resulting surfaces also showed very bad ratios by PVD, while LSD entirely covered the resulting surfaces. The experimental data showed that the tert-butyl groups left the PAH core of the GQD on the gold surface, even by LSD. The latter is consistent with previous experiments on the family of the triangular-shaped S3 GQDs. The individual S5 GQDs and similar horizontally columnar structures were observed in this case. Following these experimental observations, the STM simulations of the individual S5 GQDs and a 2D network of individual S5 GQDs can explain that the origin of each columnar signature comes from each armchair ring of GQD formed by each column signature. This exposure is validated for the triangular-shaped GQDs. Nevertheless, in both the triangular- and rectangular-shaped cases, these simulation models for the columnar structures did not enable us to obtain the STM simulation images perfectly aligned with the experimental ones. Additionally, our recent STM simulations show that the radical S3-A molecule can exhibit the three-globe signature on the gold surface but in the constant height mode instead of the constant current mode, as measured in experiments. On the other hand, it is also possible that molecules like water vapor, carbon-based contaminants (e.g., hydrocarbons from the air), and other airborne pollutants can form a contamination layer onto a gold surface as reported by András Pálinkás [263]. Besides, there are many questions that we could not answer, such as why were the functionalized groups not absorbed, even by LSD ?... Further experiments with better precision and control will allow us to answer these questions and gain insight into these experiments. As discussed, the functionalized groups left the PAH core, and the radical molecules may be formed on the gold surface, which is a positive revelation for producing new GNM. It is worth testing on more active surfaces (copper and silver) or a hot surface following higher heating (over 450 ℃) to see if forming a GNM from the S5-T, S3-A, and S3-T is possible.

Concerning GNRs and GNM, our collaborators showed that after deposition of the precursors of the C30 GQD (S2), S2-2INP and S2-2BNP, on the surface Au(111), Cu(100), and Au(111), the reaction is very complicated; there were only small domains of very short GNRs ($\sim$ 5-6 nm) co-existing with the disordered domains. The tested precursors have a bad coverage ratio on these surfaces, the attempts of longer GNRs were unsuccessful, and only disordered planarization was achieved. There were no exploitable results. The attempts of our collaborators with the precursor of the C42 GQD (S1), S1-2BNP, showed a much better coverage ratio, and long GNRs ($\sim$ 17 nm) were achieved. Nevertheless, these resulting GNRs were much shorter than those published in prior articles for the same experience.

Moreover, the attempts to get a GNM by fusing laterally the GNRs were unsuccessful; only localized lateral fusion zones but not the entire length of GNR were encountered. After higher heating for a longer time, uncontrolled graphitization was achieved instead of intermolecular cross-coupling as expected. Finally, the desired GNM was not obtained via Ullmann coupling and cyclodehydrogenation by deposing the precursors S1-4BNP and S1-4BP. The S1-4BNP showed a very bad coverage ratio on all these study surfaces, Au(111), Cu(100), and Ag(111), because of its partially asymmetric form. The S1-4BP has a better coverage ratio on these surfaces with very nice supramolecular assemblies. However, the GQDs did not couple together to form the expected GNM, which was attributed to poor accessibility to the coupling sites due to the steric hindrance from adjacent hydrogen atoms. In perspective, new precursors with different symmetries are being developed by our collaborators, for instance, S1-4BHP with the free rotation of the central phenyl groups, which may diminish the steric hindrance in order to allow better access to the predefined coupling sites carrying the bromine atoms.

Since only limited-length GNRs and limited-size GNM were obtained in the experiments, studying the change of properties of the expected GNRs and GNM as a function of system size can answer the question below: "Up to what length (size, respectively) can a finite GNR (GNM, respectively) be considered as an infinite GNR (GNM, respectively)?". In this work, the band gap of finite GNRs C30 $(p2mg)$ decreases very quickly as a function of the size, and a finite GNR is considered an infinite GNR if it contains more than eight masses of precursor S2-2BNP ($>$ 6.8 nm). The band gap of finite GNM C42 $(cmmm)$ decreases more slowly following a similar trend, and a finite GNM is considered an infinite GNR if it contains more than thirteen masses of precursor S1-4BNP. On the other hand, STM simulations showed excellent agreement with the experiment data and revealed a similar signature of GNRs $(p2mg)$ made from both S1-2BNP and S2-2BNP.

Theoretically, the biggest problem encountered in this Ph.D. thesis is related to the system size that challenges the computational cost. For optical response, the target GQDs have a large size to get better sp^2 hybridization. Their optical simulations require extremely high precision under the set effort criteria. Additionally, to compare with the experimental data, we need to perform the GW and then BSE simulations, which are cumbersome, even for small nanoparticles. Therefore, we could not perform these simulations for all the studied GQDs during this thesis. The calculations were even more complicated for STM simulations because we needed to consider the gold surface, which must be large enough to behave like a better elecron reservoir. However, instead of considering pristine chevron gold Au(111) surfaces as in reality in STM experiments, we can only consider generic gold Au(111) surfaces. In most cases, the gold surface was compressed under 2%. Although we used these $\ll$ *unreal* $\gg$ gold surfaces, the *ab initio* simulations needed to perform under the effortless criteria. If not, they cannot be done, reducing the precision. In perspective, to go beyond this problem, as mentioned at the beginning

of the conclusion, it would be interesting to create the exciton effects in the Tight-Binding model in order to achieve the absorption spectrum which is hardly or impossibly obtained by the *ab initio* method, to compare with the experiment data directly. On the other hand, the Non-equilibrium Green's function formalism (NEGF) developed on the *ab initio* Tight-Binding model has been considered one of the best choices in STM simulation for these large systems, and it is hard to go beyond. However, in the last few years, Machine Learning algorithms have allowed crossing this limitation with lower computational cost and significantly higher accuracy, such as STM simulation with Tersoff-Hamman approach [266], identification of impurities in the STM images [267], denoising experimental STM images [268], STM simulation based on a generative adversarial model [269]. Among them, the latter is the most impressive work because it permits the prediction of STM images of self-assemblies of the desired molecule from the training set without using the "true" STM formalism as before. The training set just contains some typical STM images with the corresponding molecular structures built from the target molecule optimized via DFT. This exciting topic is worthy of further development in STM simulation.

Appendices

Appendix A

Technical calculation details

A.1 Simulations in Quantum Espresso

The free simulation package Quantum Espresso is well-known for accurately providing DFT results because it uses a plane wave basis. For this reason, we used this code to get the reference results on relaxation geometry and especially to get an excellent first step on Kohn-Sham eigenvalues and eigenvectors in order to correct them later by using Yambo code, as discussed later in A.2.

The structural optimization of the GQD was carried out under DFT-GGA conditions, free from symmetry constraints. Convergence was ensured by imposing strict criteria: the total energy difference was required to be less than 10^{-6} (a.u), and forces acting on individual atoms were constrained to be below 10^{-4} (a.u). Employing the Perdew, Burke, and Ernzerhof (PBE) functional facilitated the accurate treatment of exchange-correlation effects in electron interactions. Following geometry optimization, the resultant structures maintained a planar geometry. The computational methodology included norm-conserving pseudopotentials and a plane-wave basis set with a kinetic energy cutoff set at 60 Ry. A vacuum region of about 20 Å (approximately 37.8 Ry) in the non-periodic directions was introduced to prevent from an interaction between periodic replicas. The calculations were limited to the Γ point for GQDs, while 13 symmetric $\mathbf{k}$-points in the first Brillouin zone (1BZ) were used for the GNM C48 $(cmmm)$.

A.2 Simulations in Yambo.

A.2.1 GWA simulations.

In this PhD thesis, we evaluated the GW corrections for S1 GQD $(6/mmm)$, S4 GQD (mmm), and GNM C42 $(cmmm)$

For S1 GQD $(6/mmm)$ and S4 GQD (mmm), respectively, a set of 500 (700, respectively) bands was utilized to construct the dielectric matrix and the correlation self-energy operator in the computational study. A kinetic cutoff of 30 Ry was applied for the exchange self-energy operator, and the exchange-correlation potential was reconstructed from DFT. The dielectric matrix and correlation part cutoffs were individually set to the energy of the highest unoccupied orbital. Because of the limit of our super-calculator, we are only able to set the dimension of the inverse dielectric matrix to 2 Ry in order to employ the Plasmon Pole approximation (PPA) [270] to treat the frequency dependence of self-energy operator. For simulating low-dimensional material in both GW and subsequent BSE calculations, the Coulomb potential was truncated at the edges of the Wigner-Seitz cell to avoid numerical instabilities close to $\mathbf{q} = 0$ and $\mathbf{G} = 0$ for non-3D systems and speed up the convergence with respect to the vacuum [271]. To do so, we chose a box with the cutoff volume 55 x 55 x 35 Ry^3 (70 x 50 x 35 Ry^3, respectively) and additionally employed the terminator corrections on the response function (X-terminator) proposed by Bruneval and Gonze (BG) [175]. Using the X terminator allows the acceleration of GW convergence by reducing the sensible number of virtual orbitals required to calculate both polarizability and self-energy.

For GNM C42 $(cmmm)$, since the GNM is a two-dimensional system, we just chose a box with a cutoff 33 Ry along the perpendicular direction of the system in order to evaluate the truncated Coulomb potential. Moreover, a set of 400 bands was employed to build the dielectric matrix and self-energy operator. All the rest of the used parameters for GQDs were preserved.

A.2.2 BSE simulations.

The BSE simulations were only performed for S1 GQD $(6/mmm)$ and S4 GQD (mmm). We have considered the Hartree and the screened exchange kernel for the exchange and screened interaction. Also, only the resonant part of the two-particle Hamiltonian has been considered. In this case, we have used the inverse dielectric matrix obtained by PPA in the previous GW calculation, the same box-shaped truncated Coulomb interaction, and a kinetic cutoff of 30 Ry for bare interaction in the electron-hole exchange part. Then, for similar limitation reasons, we have set the kinetic cutoff to 2 Ry to build a screened interaction matrix. Finally, 20 occupied and 100 unoccupied bands (20 occupied and 31 unoccupied bands, respectively) were employed to get converged absorption spectra in 0-5 eV (0-4 eV, respectively) range for S1 GQD $(6/mmm)$ and S4 GQD (mmm) respectively.

A.3 Simulations in Fireball.

A.3.1 DFT-LDA simulations.

Since our target materials have huge sizes, and we aim to study their properties as a function of system size, additionally, these materials have been studied on a five-layer slab of the fcc gold Au(111), we have chosen to set effortless convergence criteria as less than 10^{-4} eV for the total energy difference and 0.1 eV/Å for the force tolerance. Moreover, we used 99 Å of vacuum thickness along the z-axis. For the system without gold surface, we reduced the force tolerance to 0.05 eV/Å to improve the precision. Except for the network of alkyl chains on the gold surface (Fig. (3.26c-d)), which were performed with a grid of 4x2 symmetry $\mathbf{k}$-points, all the other structures on the gold surface were calculated at Γ point. The two bottom layers of gold surface are fixed in the geometry relaxation process. For GNRs (both GNR C30 $(p2mg)$ and GNR C42 $(p2mg)$) and GNM C42 $(cmmm)$ in a vacuum, respectively, a grid of 4 (32) symmetric $\mathbf{k}$-points. Additionally, all the GQDs studied in vacuum were performed at Γ point.

A.3.2 STM simulations.

Guided by the developer of the STM code in Fireball DFT, Cesar Gonzalez, the STM simulations were performed with the same grid of $\mathbf{k}$-points used for the system in Fireball DFT-LDA simulations. The tip was built from four layers of the fcc gold Au(111) with an 11.54 x 11.54 ($Å^2$) slab coupled to an apex cluster of four gold atoms. This tip has been used throughout the thesis, and only the apex cluster atoms have always been considered in Fireball-STM simulations. Concerning the sample, the topmost layer of gold structure and the target graphene-derived structure were taken into account in tip-sample interaction simulations, except for the network of alkyl chains (Fig. (3.26c)), the three S3 molecule system (3.30), and the S5-B1 structure (Fig. (3.38f)). The second and latter were done by neglecting the contribution of the gold surface entirely in tip-sample interaction, while the former was performed by considering the three most gold layers.

A.4 Simulations in Tight-Binding.

In Tight-Binding simulations, the vacuum thicknesses along non-periodic direction have no meaning. For GQDs, the simulations were evaluated at Γ point. For GNRs (both GNR C30 $(p2mg)$ and GNR C42 $(p2mg)$), a vacuum thickness of 10.0 Å was added along y-axis. and the simulations were performed with 18 $\mathbf{k}$-points in the 1BZ. Finally, for GNM C42 $(cmmm)$, a grid of 1024 $\mathbf{k}$-points in the 1BZ were employed.

Appendix B

Determination of low-strain, small interfaces through geometry matching

In this thesis, we expect to obtain low-dimension graphitic materials (GODs, GNRs, GNMs) on the gold(111) surface. Matching these surfaces to build a stable interface is complicated in the simulation aspect. The reason is that they have different lattice constants and lattice structures, and it is challenging to align their atomic structures. If not, the resulting interface is tremendous and incalculable. It is necessary to apply a significant strain to build up at the interface if the materials are not commensurate, which results in defects and unstable interface geometries affecting the electronic properties of the interface. Moreover, the prediction of the stability of an interface is very challenging; the most conventional way to find out is to study numerous possible interfaces to determine the stable one. To deal with these issues, we employed the Interface Builder [250] of QuantumATK [251] using a generic method reported by L. Jelver *et al.* [252, 272]. One of the most impressive advantages of this tool is that a list of all possible interface supercells constructed starting from the two surface unit cells is returned. These resulting interfaces are built by varying the size of the two surfaces (controlling through a given number of unit cell repetitions), the strain of the desired surface among the two surfaces, and the rotation between the two surfaces given thresholds predefined by the user. Finally, since our study objects (GQDs, GNRs, GNMs) are on the upper surface, we aimed to keep them unstrained (pristine). Instead, we strained or compressed the lower surface, the gold(111) surface. Before doing it, we studied the dependence properties of gold(111) surface on compression and strain. Fig. (B.1) illustrates the change of total density of states (TDOS) of a five-layer 1 x 1 periodicity gold(111) surface with respect to compression ratios along its lattice vectors $\{\mathbf{a_1}, \mathbf{a_2}\}$. Since this surface is a hexagonal lattice structure, it only needs to compress (or strain) along one and both lattice vectors. Compared to the TDOS of the pristine gold surface (Fig.

(B.1c)), the one of strained, compressed, and both strained and compressed surfaces vary very slightly with respect to compression ratios except to the surface compressed with -5% and 5%. While the TDOS of the others is preserved, one of the latter witnesses additionally states. Therefore, we have the right to compress or strain or both compress and strain greater -5% and lower 5%. Thanks to the Interface Builder [250] of QuantumATK [251], for all our study structures presented in chapter 3, we chose the resulting interfaces that have the least number of atoms (to reduce computational cost), under 5% of absolute compression ratios (to preserve the gold(111) surface's properties), and are stable.

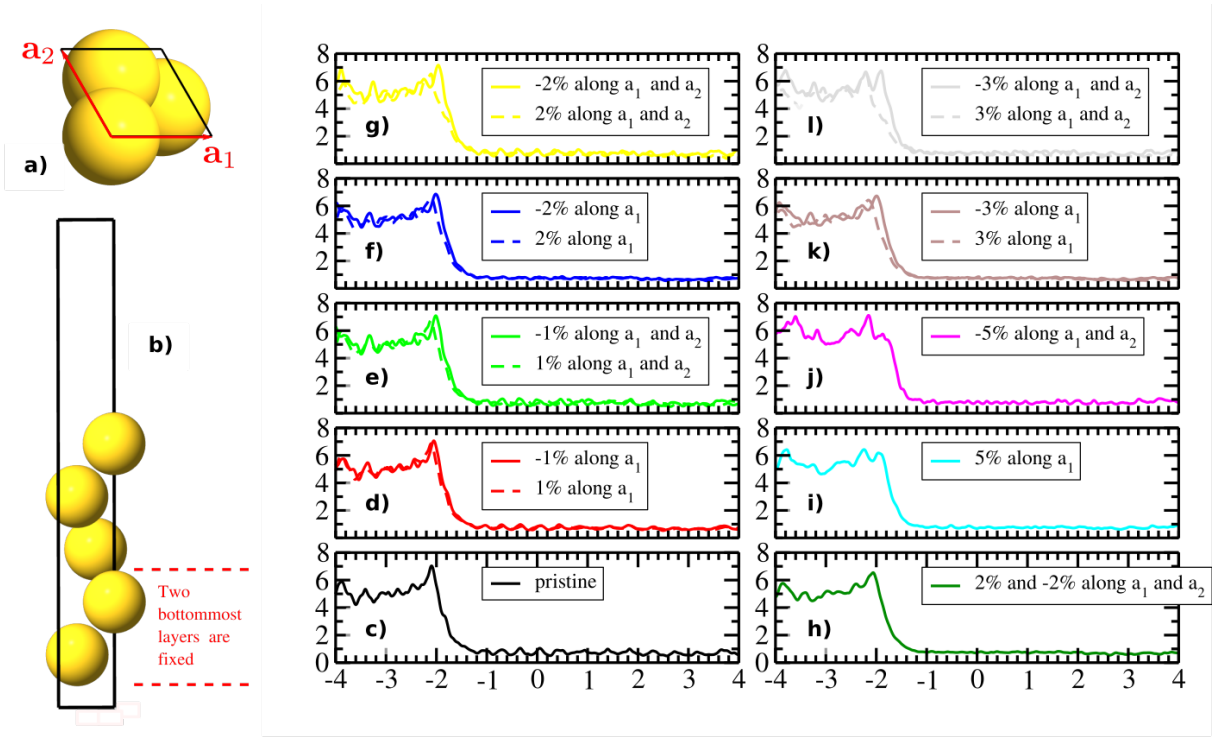

Figure B.1 – The change of total density of states (TDOS) of a five-layer 1 x 1 periodicity gold(111) with respect to compression ratios along its lattice vectors $\{\mathbf{a_1}, \mathbf{a_2}\}$. a-b, Top and side view of the primitive cell. **c,** TDOS of the pristine five-layer 1 x 1 periodicity gold(111) surface. **d-h** TDOS of the gold(111) surface compressed/stretched along its lattice vectors $\{\mathbf{a_1}, \mathbf{a_2}\}$. The simulations were performed under the similar conditions mentioned in A.3.

List of Publications

- **Graphene/aluminum oxide interfaces for nanoelectronic devices.**
  Van Binh VU, J. L. Bubendorff, L. D. N Mouafo, S. Latil1, A. Zaarour, J-F Dayen, L. Simon and Y. J. Dappe
  Electron. Struct. 5 045005 (2023)

- **Emergence of flat bands in the quasicrystal limit of boron nitride twisted bilayers.**
  Lorenzo Sponza, Van Binh Vu, Elisa Serrano Richaud, Hakim Amara, and Sylvain Latil
  Phys. Rev. B 109, L161403 (2024)

- **Bottom-Up Synthesis, Dispersion and Properties of Rectangular-Shaped Graphene Quantum Dots.**
  Julien Lavie, Van Binh Vu, Daniel Medina-Lopez, Yannick Dappe, Thomas Liu, Loïc Rondin, Jean-Sébastien Lauret, Sylvain Latil, and Stéphane Campidelli
  Helv. Chim. Acta, 106, e202300034 (2023)

- **Synthesis of rod-shaped R GQDs C96 on Au(111) surface.**
  Van Binh Vu, Hamza El-kari, Daniel Medina-Lopez, Yannick Dappe, Hamid Oughaddou, Sylvain Latil, and Stéphane Campidelli
  [in preparation]

- **Synthesis of triangular-shaped T GQDs C96 on Au(111) surface.** Van Binh Vu, Hamza El-kari, Daniel Medina-Lopez, Yannick Dappe, Hamid Oughaddou, Sylvain Latil, and Stéphane Campidelli
  [in preparation]

- **Photophysics of individualized rod-shaped R GQD C78.**
  Van Binh Vu, Daniel Medina-Lopez, Yannick Dappe, Jean-Sébastien Lauret, Sylvain Latil, and Stéphane Campidelli
  [in preparation]

Bibliography

[1] P. R. Wallace. The Band Theory of Graphite. *Physical Review*, 71(9):622–634, May 1947.

[2] K. S. Novoselov, A. K. Geim, S. V. Morozov, D. Jiang, Y. Zhang, S. V. Dubonos, I. V. Grigorieva, and A. A. Firsov. Electric Field Effect in Atomically Thin Carbon Films. *Science*, 306(5696):666–669, October 2004.

[3] K. S. Novoselov, D. Jiang, F. Schedin, T. J. Booth, V. V. Khotkevich, S. V. Morozov, and A. K. Geim. Two-dimensional atomic crystals. *Proceedings of the National Academy of Sciences*, 102(30):10451–10453, July 2005.

[4] Changgu Lee, Xiaoding Wei, Jeffrey W. Kysar, and James Hone. Measurement of the Elastic Properties and Intrinsic Strength of Monolayer Graphene. *Science*, 321(5887):385–388, July 2008.

[5] William E. Luecke, Joseph D. McColskey, Christopher N. McCowan, Stephen W. Banovic, Richard J. Fields, Timothy J. Foecke, Thomas A. Siewert, and Frank W. Gayle. Mechanical Properties of Structural Steels. Federal Building and Fire Safety Investigation of the World Trade Center Disaster (NIST NCSTAR 1-3D) ***DRAFT for Public Comments***. *NIST*, September 2005.

[6] Md Abdullah Al Faruque, Md Syduzzaman, Joy Sarkar, Kadir Bilisik, and Maryam Naebe. A Review on the Production Methods and Applications of Graphene-Based Materials. *Nanomaterials*, 11(9):2414, September 2021.

[7] Baoyan Fu and Jianxin Gao. Study on the Application of Graphene Polymer Material in Sports Equipment. *Journal of Physics: Conference Series*, 1676(1):012044, November 2020.

[8] Nurul Husna Othman, Mokhtar Che Ismail, Mazli Mustapha, Nabihah Sallih, Kok Eng Kee, and Rafida Ahmad Jaal. Graphene-based polymer nanocomposites as barrier coatings for corrosion protection. *Progress in Organic Coatings*, 135:82–99, October 2019.

[9] K. S. Novoselov, A. K. Geim, S. V. Morozov, D. Jiang, M. I. Katsnelson, I. V. Grigorieva, S. V. Dubonos, and A. A. Firsov. Two-dimensional gas of massless Dirac fermions in graphene. *Nature*, 438(7065):197–200, November 2005.

[10] K. I. Bolotin, K. J. Sikes, Z. Jiang, M. Klima, G. Fudenberg, J. Hone, P. Kim, and H. L. Stormer. Ultrahigh electron mobility in suspended graphene. *Solid State Communications*, 146(9):351–355, June 2008.

[11] R. R. Nair, P. Blake, A. N. Grigorenko, K. S. Novoselov, T. J. Booth, T. Stauber, N. M. R. Peres, and A. K. Geim. Fine Structure Constant Defines Visual Transparency of Graphene. *Science*, 320(5881):1308–1308, June 2008.

[12] Shanshan Chen, Arden L. Moore, Weiwei Cai, Ji Won Suk, Jinho An, Columbia Mishra, Charles Amos, Carl W. Magnuson, Junyong Kang, Li Shi, and Rodney S. Ruoff. Raman Measurements of Thermal Transport in Suspended Monolayer Graphene of Variable Sizes in Vacuum and Gaseous Environments. *ACS Nano*, 5(1):321–328, January 2011.

[13] Yang Chen, Yuan-Yuan Yue, Shi-Rong Wang, Nan Zhang, Jing Feng, and Hong-Bo Sun. Graphene as a Transparent and Conductive Electrode for Organic Optoelectronic Devices. *Advanced Electronic Materials*, 5(10):1900247, 2019.

[14] Xuan Wang, Linjie Zhi, and Klaus Müllen. Transparent, Conductive Graphene Electrodes for Dye-Sensitized Solar Cells. *Nano Letters*, 8(1):323–327, January 2008.

[15] Mingyu Sang, Jongwoon Shin, Kiho Kim, and Ki Jun Yu. Electronic and Thermal Properties of Graphene and Recent Advances in Graphene Based Electronics Applications. *Nanomaterials*, 9(3):374, March 2019.

[16] Dong Hae Ho, Qijun Sun, So Young Kim, Joong Tark Han, Do Hwan Kim, and Jeong Ho Cho. Stretchable and Multimodal All Graphene Electronic Skin. *Advanced Materials*, 28(13):2601–2608, 2016.

[17] Pradip Kumar, Faisal Shahzad, Seunggun Yu, Soon Man Hong, Yoon Hyun Kim, and Chong Min Koo. Large-area reduced graphene oxide thin film with excellent thermal conductivity and electromagnetic interference shielding effectiveness. *Carbon*, 94:494–500, August 2015.

[18] Haoxue Han, Yong Zhang, Nan Wang, Majid Kabiri Samani, Yuxiang Ni, Zainelabideen Y. Mijbil, Michael Edwards, Shiyun Xiong, Kimmo Sääskilahti, Murali Murugesan, Yifeng Fu, Lilei Ye, Hatef Sadeghi, Steven Bailey, Yuriy A. Kosevich, Colin J. Lambert, Johan Liu, and Sebastian

Volz. Functionalization mediates heat transport in graphene nanoflakes. *Nature Communications*, 7(1):11281, April 2016.

[19] Jakub Kedzierski, Pei-Lan Hsu, Paul Healey, Peter Wyatt, Craig Keast, Mike Sprinkle, Claire Berger, and Walt Heer. Epitaxial Graphene Transistors on SiC Substrates. *Electron Devices, IEEE Transactions on*, 55:2078–2085, September 2008.

[20] Taisuke Ohta, Aaron Bostwick, Thomas Seyller, Karsten Horn, and Eli Rotenberg. Controlling the Electronic Structure of Bilayer Graphene. *Science*, 313(5789):951–954, August 2006.

[21] Eryin Wang, Xiaobo Lu, Shijie Ding, Wei Yao, Mingzhe Yan, Guoliang Wan, Ke Deng, Shuopei Wang, Guorui Chen, Liguo Ma, Jeil Jung, Alexei V. Fedorov, Yuanbo Zhang, Guangyu Zhang, and Shuyun Zhou. Gaps induced by inversion symmetry breaking and second-generation Dirac cones in graphene/hexagonal boron nitride. *Nature Physics*, 12(12):1111–1115, December 2016.

[22] S. Y. Zhou, G.-H. Gweon, A. V. Fedorov, P. N. First, W. A. de Heer, D.-H. Lee, F. Guinea, A. H. Castro Neto, and A. Lanzara. Substrate-induced bandgap opening in epitaxial graphene. *Nature Materials*, 6(10):770–775, October 2007.

[23] D. Usachov, O. Vilkov, A. Grüneis, D. Haberer, A. Fedorov, V. K. Adamchuk, A. B. Preobrajenski, P. Dudin, A. Barinov, M. Oehzelt, C. Laubschat, and D. V. Vyalikh. Nitrogen-Doped Graphene: Efficient Growth, Structure, and Electronic Properties. *Nano Letters*, 11(12):5401–5407, December 2011.

[24] Cheng-Kai Chang, Satender Kataria, Chun-Chiang Kuo, Abhijit Ganguly, Bo-Yao Wang, Jeong-Yuan Hwang, Kay-Jay Huang, Wei-Hsun Yang, Sheng-Bo Wang, Cheng-Hao Chuang, Mi Chen, Ching-I Huang, Way-Faung Pong, Ker-Jar Song, Shoou-Jinn Chang, Jing-Hua Guo, Yian Tai, Masahiko Tsujimoto, Seiji Isoda, Chun-Wei Chen, Li-Chyong Chen, and Kuei-Hsien Chen. Band Gap Engineering of Chemical Vapor Deposited Graphene by in Situ BN Doping. *ACS Nano*, 7(2):1333–1341, February 2013.

[25] Toma Susi, Trevor P. Hardcastle, Hans Hofsäss, Andreas Mittelberger, Timothy J. Pennycook, Clemens Mangler, Rik Drummond-Brydson, Andrew J. Scott, Jannik C. Meyer, and Jani Kotakoski. Single-atom spectroscopy of phosphorus dopants implanted into graphene. *2D Materials*, 4(2):021013, February 2017.

[26] Quentin M. Ramasse, Che R. Seabourne, Despoina-Maria Kepaptsoglou, Recep Zan, Ursel Bangert, and Andrew J. Scott. Probing the Bonding and Electronic Structure of Single Atom

Dopants in Graphene with Electron Energy Loss Spectroscopy. *Nano Letters*, 13(10):4989–4995, October 2013.

[27] Toma Susi, Jannik C. Meyer, and Jani Kotakoski. Manipulating low-dimensional materials down to the level of single atoms with electron irradiation. *Ultramicroscopy*, 180:163–172, September 2017.

[28] Alex W. Robertson, Barbara Montanari, Kuang He, Judy Kim, Christopher S. Allen, Yimin A. Wu, Jaco Olivier, Jan Neethling, Nicholas Harrison, Angus I. Kirkland, and Jamie H. Warner. Dynamics of Single Fe Atoms in Graphene Vacancies. *Nano Letters*, 13(4):1468–1475, April 2013.

[29] Pin-Cheng Lin, Renan Villarreal, Simona Achilli, Harsh Bana, Maya N. Nair, Antonio Tejeda, Ken Verguts, Stefan De Gendt, Manuel Auge, Hans Hofsäss, Steven De Feyter, Giovanni Di Santo, Luca Petaccia, Steven Brems, Guido Fratesi, and Lino M. C. Pereira. Doping Graphene with Substitutional Mn. *ACS Nano*, 15(3):5449–5458, March 2021.

[30] Hongtao Wang, Qingxiao Wang, Yingchun Cheng, Kun Li, Yingbang Yao, Qiang Zhang, Cezhou Dong, Peng Wang, Udo Schwingenschlögl, Wei Yang, and X. X. Zhang. Doping Monolayer Graphene with Single Atom Substitutions. *Nano Letters*, 12(1):141–144, January 2012.

[31] Jeremy T. Robinson, James S. Burgess, Chad E. Junkermeier, Stefan C. Badescu, Thomas L. Reinecke, F. Keith Perkins, Maxim K. Zalalutdniov, Jeffrey W. Baldwin, James C. Culbertson, Paul E. Sheehan, and Eric S. Snow. Properties of Fluorinated Graphene Films. *Nano Letters*, 10(8):3001–3005, August 2010.

[32] Rahul R. Nair, Wencai Ren, Rashid Jalil, Ibtsam Riaz, Vasyl G. Kravets, Liam Britnell, Peter Blake, Fredrik Schedin, Alexander S. Mayorov, Shengjun Yuan, Mikhail I. Katsnelson, Hui-Ming Cheng, Wlodek Strupinski, Lyubov G. Bulusheva, Alexander V. Okotrub, Irina V. Grigorieva, Alexander N. Grigorenko, Kostya S. Novoselov, and Andre K. Geim. Fluorographene: A Two-Dimensional Counterpart of Teflon. *Small*, 6(24):2877–2884, 2010.

[33] S.-H. Cheng, K. Zou, F. Okino, H. R. Gutierrez, A. Gupta, N. Shen, P. C. Eklund, J. O. Sofo, and J. Zhu. Reversible fluorination of graphene: Evidence of a two-dimensional wide bandgap semiconductor. *Physical Review B*, 81(20):205435, May 2010.

[34] Nina I. Kovtyukhova, Patricia J. Ollivier, Benjamin R. Martin, Thomas E. Mallouk, Sergey A. Chizhik, Eugenia V. Buzaneva, and Alexandr D. Gorchinskiy. Layer-by-Layer Assembly of Ultrathin Composite Films from Micron-Sized Graphite Oxide Sheets and Polycations. *Chemistry of Materials*, 11(3):771–778, March 1999.

[35] Songfeng Pei and Hui-Ming Cheng. The reduction of graphene oxide. *Carbon*, 50(9):3210–3228, August 2012.

[36] Yiqian Jin, Yiteng Zheng, Simon G. Podkolzin, and Woo Lee. Band gap of reduced graphene oxide tuned by controlling functional groups. *Journal of Materials Chemistry C*, 8(14):4885–4894, April 2020.

[37] Amirhasan Nourbakhsh, Mirco Cantoro, Tom Vosch, Geoffrey Pourtois, Francesca Clemente, Marleen H. van der Veen, Johan Hofkens, Marc M. Heyns, Stefan De Gendt, and Bert F. Sels. Bandgap opening in oxygen plasma-treated graphene. *Nanotechnology*, 21(43):435203, October 2010.

[38] Haiming Huang, Zhibing Li, Juncong She, and Weiliang Wang. Oxygen density dependent band gap of reduced graphene oxide. *Journal of Applied Physics*, 111(5):054317, March 2012.

[39] Hamze Mousavi and Rostam Moradian. Nitrogen and boron doping effects on the electrical conductivity of graphene and nanotube. *Solid State Sciences*, 13(8):1459–1464, August 2011.

[40] Goki Eda, Giovanni Fanchini, and Manish Chhowalla. Large-area ultrathin films of reduced graphene oxide as a transparent and flexible electronic material. *Nature Nanotechnology*, 3(5):270–274, May 2008.

[41] Xiaolin Li, Xinran Wang, Li Zhang, Sangwon Lee, and Hongjie Dai. Chemically Derived, Ultrasmooth Graphene Nanoribbon Semiconductors. *Science*, 319(5867):1229–1232, February 2008.

[42] Xiaoming Sun, Zhuang Liu, Kevin Welsher, Joshua Tucker Robinson, Andrew Goodwin, Sasa Zaric, and Hongjie Dai. Nano-graphene oxide for cellular imaging and drug delivery. *Nano Research*, 1(3):203–212, September 2008.

[43] Thomas G. Pedersen, Christian Flindt, Jesper Pedersen, Niels Asger Mortensen, Antti-Pekka Jauho, and Kjeld Pedersen. Graphene Antidot Lattices: Designed Defects and Spin Qubits. *Physical Review Letters*, 100(13):136804, April 2008.

[44] Lingling Li, Gehui Wu, Guohai Yang, Juan Peng, Jianwei Zhao, and Jun-Jie Zhu. Focusing on luminescent graphene quantum dots: Current status and future perspectives. *Nanoscale*, 5(10):4015–4039, May 2013.

[45] William S. Jr. Hummers and Richard E. Offeman. Preparation of Graphitic Oxide. *Journal of the American Chemical Society*, 80(6):1339–1339, March 1958.

[46] Jianhua Shen, Yihua Zhu, Cheng Chen, Xiaoling Yang, and Chunzhong Li. Facile preparation and upconversion luminescence of graphene quantum dots. *Chemical Communications*, 47(9):2580–2582, February 2011.

[47] Dengyu Pan, Jingchun Zhang, Zhen Li, and Minghong Wu. Hydrothermal Route for Cutting Graphene Sheets into Blue-Luminescent Graphene Quantum Dots. *Advanced Materials*, 22(6):734–738, 2010.

[48] Jianhua Shen, Yihua Zhu, Xiaoling Yang, and Chunzhong Li. Graphene quantum dots: Emergent nanolights for bioimaging, sensors, catalysis and photovoltaic devices. *Chemical Communications*, 48(31):3686–3699, March 2012.

[49] Satyaprakash Ahirwar, Sudhanshu Mallick, and Dhirendra Bahadur. Electrochemical Method To Prepare Graphene Quantum Dots and Graphene Oxide Quantum Dots. *ACS Omega*, 2(11):8343–8353, November 2017.

[50] Hyunwoong Kang, Dong Yeong Kim, and Jaehee Cho. Top-Down Fabrication of Luminescent Graphene Quantum Dots Using Self-Assembled Au Nanoparticles. *ACS Omega*, 8(6):5885–5892, February 2023.

[51] Enamul Haque, Jeonghun Kim, Victor Malgras, Kakarla Raghava Reddy, Alister C. Ward, Jungmok You, Yoshio Bando, Md. Shahriar A. Hossain, and Yusuke Yamauchi. Recent Advances in Graphene Quantum Dots: Synthesis, Properties, and Applications. *Small Methods*, 2(10):1800050, 2018.

[52] Ahmadreza Ghaffarkhah, Ehsan Hosseini, Milad Kamkar, Ali Akbari Sehat, Sara Dordanihaghighi, Ahmad Allahbakhsh, Colin van der Kuur, and Mohammad Arjmand. Synthesis, Applications, and Prospects of Graphene Quantum Dots: A Comprehensive Review. *Small*, 18(2):2102683, 2022.

[53] Liying Jiao, Li Zhang, Xinran Wang, Georgi Diankov, and Hongjie Dai. Narrow graphene nanoribbons from carbon nanotubes. *Nature*, 458(7240):877–880, April 2009.

[54] Dmitry V. Kosynkin, Amanda L. Higginbotham, Alexander Sinitskii, Jay R. Lomeda, Ayrat Dimiev, B. Katherine Price, and James M. Tour. Longitudinal unzipping of carbon nanotubes to form graphene nanoribbons. *Nature*, 458(7240):872–876, April 2009.

[55] Liang Ma, Jinlan Wang, and Feng Ding. Recent Progress and Challenges in Graphene Nanoribbon Synthesis. *ChemPhysChem*, 14(1):47–54, 2013.

[56] Melinda Y. Han, Barbaros Özyilmaz, Yuanbo Zhang, and Philip Kim. Energy Band-Gap Engineering of Graphene Nanoribbons. *Physical Review Letters*, 98(20):206805, May 2007.

[57] Xiaolin Li, Xinran Wang, Li Zhang, Sangwon Lee, and Hongjie Dai. Chemically Derived, Ultrasmooth Graphene Nanoribbon Semiconductors. *Science*, 319(5867):1229–1232, February 2008.

[58] Jingwei Bai, Xing Zhong, Shan Jiang, Yu Huang, and Xiangfeng Duan. Graphene nanomesh. *Nature Nanotechnology*, 5(3):190–194, March 2010.

[59] Xiaogan Liang, Yeon-Sik Jung, Shiwei Wu, Ariel Ismach, Deirdre L. Olynick, Stefano Cabrini, and Jeffrey Bokor. Formation of Bandgap and Subbands in Graphene Nanomeshes with Sub-10 nm Ribbon Width Fabricated via Nanoimprint Lithography. *Nano Letters*, 10(7):2454–2460, July 2010.

[60] Zhiyuan Zeng, Xiao Huang, Zongyou Yin, Hong Li, Yang Chen, Hai Li, Qing Zhang, Jan Ma, Freddy Boey, and Hua Zhang. Fabrication of Graphene Nanomesh by Using an Anodic Aluminum Oxide Membrane as a Template. *Advanced Materials*, 24(30):4138–4142, 2012.

[61] Omid Akhavan. Graphene Nanomesh by ZnO Nanorod Photocatalysts. *ACS Nano*, 4(7):4174–4180, July 2010.

[62] Qinfeng Xu, Qi Zhou, Zheng Hua, Qi Xue, Chunfeng Zhang, Xiaoyong Wang, Dengyu Pan, and Min Xiao. Single-Particle Spectroscopic Measurements of Fluorescent Graphene Quantum Dots. *ACS Nano*, 7(12):10654–10661, December 2013.

[63] Shujuan Zhuo, Mingwang Shao, and Shuit-Tong Lee. Upconversion and Downconversion Fluorescent Graphene Quantum Dots: Ultrasonic Preparation and Photocatalysis. *ACS Nano*, 6(2):1059–1064, February 2012.

[64] Shoujun Zhu, Junhu Zhang, Shijia Tang, Chunyan Qiao, Lei Wang, Haiyu Wang, Xue Liu, Bo Li, Yunfeng Li, Weili Yu, Xingfeng Wang, Hongchen Sun, and Bai Yang. Surface Chemistry Routes to Modulate the Photoluminescence of Graphene Quantum Dots: From Fluorescence Mechanism to Up-Conversion Bioimaging Applications. *Advanced Functional Materials*, 22(22):4732–4740, 2012.

[65] Kiran Lingam, Ramakrishna Podila, Haijun Qian, Steven Serkiz, and Apparao M. Rao. Evidence for Edge-State Photoluminescence in Graphene Quantum Dots. *Advanced Functional Materials*, 23(40):5062–5065, 2013.

[66] Stephen R. Power and Antti-Pekka Jauho. Electronic transport in disordered graphene antidot lattice devices. *Physical Review B*, 90(11):115408, September 2014.

[67] V. Hung Nguyen, M. Chung Nguyen, Huy-Viet Nguyen, and P. Dollfus. Disorder effects on electronic bandgap and transport in graphene-nanomesh-based structures. *Journal of Applied Physics*, 113(1):013702, January 2013.

[68] Shengjun Yuan, Rafael Roldán, Antti-Pekka Jauho, and M. I. Katsnelson. Electronic properties of disordered graphene antidot lattices. *Physical Review B*, 87(8):085430, February 2013.

[69] Xiang Ji, Jinyu Zhang, Yan Wang, He Qian, and Zhiping Yu. Influence of edge imperfections on the transport behavior of graphene nanomeshes. *Nanoscale*, 5(6):2527–2531, 2013.

[70] Mitchell Bacon, Siobhan J. Bradley, and Thomas Nann. Graphene Quantum Dots. *Particle & Particle Systems Characterization*, 31(4):415–428, 2014.

[71] Xin Ting Zheng, Arundithi Ananthanarayanan, Kathy Qian Luo, and Peng Chen. Glowing Graphene Quantum Dots and Carbon Dots: Properties, Syntheses, and Biological Applications. *Small*, 11(14):1620–1636, 2015.

[72] Xin Hai, Ji Feng, Xuwei Chen, and Jianhua Wang. Tuning the optical properties of graphene quantum dots for biosensing and bioimaging. *Journal of Materials Chemistry B*, 6(20):3219–3234, May 2018.

[73] Liying Jiao, Xinran Wang, Georgi Diankov, Hailiang Wang, and Hongjie Dai. Facile synthesis of high-quality graphene nanoribbons. *Nature Nanotechnology*, 5(5):321–325, May 2010.

[74] Wentao Xu and Tae-Woo Lee. Recent progress in fabrication techniques of graphene nanoribbons. *Materials Horizons*, 3(3):186–207, May 2016.

[75] Khaiwal Ravindra, Ranjeet Sokhi, and René Van Grieken. Atmospheric polycyclic aromatic hydrocarbons: Source attribution, emission factors and regulation. *Atmospheric Environment*, 42(13):2895–2921, April 2008.

[76] Frank Morgenroth, Erik Reuther, and Klaus Müllen. Polyphenylene Dendrimers: From Three-Dimensional to Two-Dimensional Structures. *Angewandte Chemie International Edition in English*, 36(6):631–634, 1997.

[77] Christopher D. Simpson, J. Diedrich Brand, Alexander J. Berresheim, Laurence Przybilla, Hans Joachim Räder, and Klaus Müllen. Synthesis of a Giant 222 Carbon Graphite Sheet. *Chemistry – A European Journal*, 8(6):1424–1429, 2002.

[78] Jishan Wu, Wojciech Pisula, and Klaus Müllen. Graphenes as Potential Material for Electronics. *Chemical Reviews*, 107(3):718–747, March 2007.

[79] Željko Tomović, Mark D. Watson, and Klaus Müllen. Superphenalene-Based Columnar Liquid Crystals. *Angewandte Chemie International Edition*, 43(6):755–758, January 2004.

[80] Vivekanantan S. Iyer, Kimihiro Yoshimura, Volker Enkelmann, Rebekka Epsch, Jürgen P. Rabe, and Klaus Müllen. A Soluble C60 Graphite Segment. *Angewandte Chemie International Edition*, 37(19):2696–2699, 1998.

[81] Markus Müller, Christian Kübel, and Klaus Müllen. Giant Polycyclic Aromatic Hydrocarbons. *Chemistry – A European Journal*, 4(11):2099–2109, 1998.

[82] Vivekanantan S. Iyer, Mike Wehmeier, J. Diedrich Brand, Menno A. Keegstra, and Klaus Müllen. From Hexa-peri-hexabenzocoronene to "Superacenes". *Angewandte Chemie International Edition in English*, 36(15):1604–1607, 1997.

[83] Florian Dötz, Johann Diedrich Brand, Shunji Ito, Lileta Gherghel, and Klaus Müllen. Synthesis of Large Polycyclic Aromatic Hydrocarbons: Variation of Size and Periphery. *Journal of the American Chemical Society*, 122(32):7707–7717, August 2000.

[84] Xin Yan, Xiao Cui, and Liang-shi Li. Synthesis of Large, Stable Colloidal Graphene Quantum Dots with Tunable Size. *Journal of the American Chemical Society*, 132(17):5944–5945, May 2010.

[85] Zhe Sun, Sangsu Lee, Kyu Hyung Park, Xiaojian Zhu, Wenhua Zhang, Bin Zheng, Pan Hu, Zebing Zeng, Soumyajit Das, Yuan Li, Chunyan Chi, Run-Wei Li, Kuo-Wei Huang, Jun Ding, Dongho Kim, and Jishan Wu. Dibenzoheptazethrene Isomers with Different Biradical Characters: An Exercise of Clar's Aromatic Sextet Rule in Singlet Biradicaloids. *Journal of the American Chemical Society*, 135(48):18229–18236, December 2013.

[86] Stephen E. Stein and R. L. Brown. .pi.-Electron properties of large condensed polyaromatic hydrocarbons. *Journal of the American Chemical Society*, 109(12):3721–3729, June 1987.

[87] J. Marguerite Hughes, Yenny Hernandez, Damian Aherne, Lukas Doessel, Klaus Müllen, Ben Moreton, Thomas W. White, Cerianne Partridge, Giovanni Costantini, Aleksey Shmeliov, Mervyn Shannon, Valeria Nicolosi, and Jonathan N Coleman. High Quality Dispersions of Hexabenzocoronene in Organic Solvents. *Journal of the American Chemical Society*, 134(29):12168–12179, July 2012.

[88] Jan M. Englert, Frank Hauke, Xingliang Feng, Klaus Müllen, and Andreas Hirsch. Exfoliation of hexa-peri-hexabenzocoronene in water. *Chemical Communications*, 46(48):9194–9196, December 2010.

[89] Philipp Haines, David Reger, Johannes Träg, Volker Strauss, Dominik Lungerich, Dirk Zahn, Norbert Jux, and Dirk M. Guldi. On the photophysics of nanographenes – investigation of function-

alized hexa-peri-hexabenzocoronenes as model systems. *Nanoscale*, 13(2):801–809, January 2021.

[90] Michael G. Debije, Jorge Piris, Matthijs P. de Haas, John M. Warman, Željko Tomović, Christopher D. Simpson, Mark D. Watson, and Klaus Müllen. The Optical and Charge Transport Properties of Discotic Materials with Large Aromatic Hydrocarbon Cores. *Journal of the American Chemical Society*, 126(14):4641–4645, April 2004.

[91] Yuan-Zhi Tan, Bo Yang, Khaled Parvez, Akimitsu Narita, Silvio Osella, David Beljonne, Xinliang Feng, and Klaus Müllen. Atomically precise edge chlorination of nanographenes and its application in graphene nanoribbons. *Nature Communications*, 4(1):2646, November 2013.

[92] Hans Riesen, Christian Wiebeler, and Stefan Schumacher. Optical Spectroscopy of Graphene Quantum Dots: The Case of C132. *The Journal of Physical Chemistry A*, 118(28):5189–5195, July 2014.

[93] Shen Zhao, Julien Lavie, Loïc Rondin, Lucile Orcin-Chaix, Carole Diederichs, Philippe Roussignol, Yannick Chassagneux, Christophe Voisin, Klaus Müllen, Akimitsu Narita, Stéphane Campidelli, and Jean-Sébastien Lauret. Single photon emission from graphene quantum dots at room temperature. *Nature Communications*, 9(1):3470, August 2018.

[94] Igor Aharonovich, Dirk Englund, and Milos Toth. Solid-state single-photon emitters. *Nature Photonics*, 10(10):631–641, October 2016.

[95] L. J. Martínez, T. Pelini, V. Waselowski, J. R. Maze, B. Gil, G. Cassabois, and V. Jacques. Efficient single photon emission from a high-purity hexagonal boron nitride crystal. *Physical Review B*, 94(12):121405, September 2016.

[96] Xiaoyin Yang, Xi Dou, Ali Rouhanipour, Linjie Zhi, Hans Joachim Räder, and Klaus Müllen. Two-Dimensional Graphene Nanoribbons. *Journal of the American Chemical Society*, 130(13):4216–4217, April 2008.

[97] Akimitsu Narita, Xinliang Feng, Yenny Hernandez, Søren A. Jensen, Mischa Bonn, Huafeng Yang, Ivan A. Verzhbitskiy, Cinzia Casiraghi, Michael Ryan Hansen, Amelie H. R. Koch, George Fytas, Oleksandr Ivasenko, Bing Li, Kunal S. Mali, Tatyana Balandina, Sankarapillai Mahesh, Steven De Feyter, and Klaus Müllen. Synthesis of structurally well-defined and liquid-phase-processable graphene nanoribbons. *Nature Chemistry*, 6(2):126–132, February 2014.

[98] Akimitsu Narita, Ivan A. Verzhbitskiy, Wout Frederickx, Kunal S. Mali, Soeren Alkaersig Jensen, Michael Ryan Hansen, Mischa Bonn, Steven De Feyter, Cinzia Casiraghi, Xinliang Feng, and

Klaus Müllen. Bottom-Up Synthesis of Liquid-Phase-Processable Graphene Nanoribbons with Near-Infrared Absorption. *ACS Nano*, 8(11):11622–11630, November 2014.

[99] Akimitsu Narita, Zongping Chen, Qiang Chen, and Klaus Müllen. Solution and on-surface synthesis of structurally defined graphene nanoribbons as a new family of semiconductors. *Chemical Science*, 10(4):964–975, January 2019.

[100] Jinming Cai, Pascal Ruffieux, Rached Jaafar, Marco Bieri, Thomas Braun, Stephan Blankenburg, Matthias Muoth, Ari P. Seitsonen, Moussa Saleh, Xinliang Feng, Klaus Müllen, and Roman Fasel. Atomically precise bottom-up fabrication of graphene nanoribbons. *Nature*, 466(7305):470–473, July 2010.

[101] Leopold Talirz, Pascal Ruffieux, and Roman Fasel. On-Surface Synthesis of Atomically Precise Graphene Nanoribbons. *Advanced Materials*, 28(29):6222–6231, 2016.

[102] Christopher Bronner, Stephan Stremlau, Marie Gille, Felix Braußе, Anton Haase, Stefan Hecht, and Petra Tegeder. Aligning the Band Gap of Graphene Nanoribbons by Monomer Doping. *Angewandte Chemie International Edition*, 52(16):4422–4425, 2013.

[103] Ryan R. Cloke, Tomas Marangoni, Giang D. Nguyen, Trinity Joshi, Daniel J. Rizzo, Christopher Bronner, Ting Cao, Steven G. Louie, Michael F. Crommie, and Felix R. Fischer. Site-Specific Substitutional Boron Doping of Semiconducting Armchair Graphene Nanoribbons. *Journal of the American Chemical Society*, 137(28):8872–8875, July 2015.

[104] Shigeki Kawai, Shohei Saito, Shinichiro Osumi, Shigehiro Yamaguchi, Adam S. Foster, Peter Spijker, and Ernst Meyer. Atomically controlled substitutional boron-doping of graphene nanoribbons. *Nature Communications*, 6(1):8098, August 2015.

[105] R. S. Koen Houtsma, Joris de la Rie, and Meike Stöhr. Atomically precise graphene nanoribbons: Interplay of structural and electronic properties. *Chemical Society Reviews*, 50(11):6541–6568, June 2021.

[106] Pascal Ruffieux, Shiyong Wang, Bo Yang, Carlos Sánchez-Sánchez, Jia Liu, Thomas Dienel, Leopold Talirz, Prashant Shinde, Carlo A. Pignedoli, Daniele Passerone, Tim Dumslaff, Xinliang Feng, Klaus Müllen, and Roman Fasel. On-surface synthesis of graphene nanoribbons with zigzag edge topology. *Nature*, 531(7595):489–492, March 2016.

[107] Li Yang, Cheol-Hwan Park, Young-Woo Son, Marvin L. Cohen, and Steven G. Louie. Quasiparticle Energies and Band Gaps in Graphene Nanoribbons. *Physical Review Letters*, 99(18):186801, November 2007.

[108] Patrick B. Bennett, Zahra Pedramrazi, Ali Madani, Yen-Chia Chen, Dimas G. de Oteyza, Chen Chen, Felix R. Fischer, Michael F. Crommie, and Jeffrey Bokor. Bottom-up graphene nanoribbon field-effect transistors. *Applied Physics Letters*, 103(25):253114, December 2013.

[109] Ahmad N. Abbas, Gang Liu, Akimitsu Narita, Manuel Orosco, Xinliang Feng, Klaus Müllen, and Chongwu Zhou. Deposition, Characterization, and Thin-Film-Based Chemical Sensing of Ultra-long Chemically Synthesized Graphene Nanoribbons. *Journal of the American Chemical Society*, 136(21):7555–7558, May 2014.

[110] Ute Zschieschang, Hagen Klauk, Imke B. Müeller, Andrew J. Strudwick, Tobias Hintermann, Matthias G. Schwab, Akimitsu Narita, Xinliang Feng, Klaus Müellen, and R. Thomas Weitz. Electrical Characteristics of Field-Effect Transistors based on Chemically Synthesized Graphene Nanoribbons. *Advanced Electronic Materials*, 1(3):1400010, 2015.

[111] Zongping Chen, Wen Zhang, Carlos-Andres Palma, Alberto Lodi Rizzini, Bilu Liu, Ahmad Abbas, Nils Richter, Leonardo Martini, Xiao-Ye Wang, Nicola Cavani, Hao Lu, Neeraj Mishra, Camilla Coletti, Reinhard Berger, Florian Klappenberger, Mathias Kläui, Andrea Candini, Marco Affronte, Chongwu Zhou, Valentina De Renzi, Umberto del Pennino, Johannes V. Barth, Hans Joachim Räder, Akimitsu Narita, Xinliang Feng, and Klaus Müllen. Synthesis of Graphene Nanoribbons by Ambient-Pressure Chemical Vapor Deposition and Device Integration. *Journal of the American Chemical Society*, 138(47):15488–15496, November 2016.

[112] Juan Pablo Llinas, Andrew Fairbrother, Gabriela Borin Barin, Wu Shi, Kyunghoon Lee, Shuang Wu, Byung Yong Choi, Rohit Braganza, Jordan Lear, Nicholas Kau, Wonwoo Choi, Chen Chen, Zahra Pedramrazi, Tim Dumslaff, Akimitsu Narita, Xinliang Feng, Klaus Müllen, Felix Fischer, Alex Zettl, Pascal Ruffieux, Eli Yablonovitch, Michael Crommie, Roman Fasel, and Jeffrey Bokor. Short-channel field-effect transistors with 9-atom and 13-atom wide graphene nanoribbons. *Nature Communications*, 8(1):633, September 2017.

[113] Leonardo Martini, Zongping Chen, Neeraj Mishra, Gabriela Borin Barin, Paolo Fantuzzi, Pascal Ruffieux, Roman Fasel, Xinliang Feng, Akimitsu Narita, Camilla Coletti, Klaus Müllen, and Andrea Candini. Structure-dependent electrical properties of graphene nanoribbon devices with graphene electrodes. *Carbon*, 146:36–43, May 2019.

[114] Richard Denk, Alberto Lodi-Rizzini, Shudong Wang, Michael Hohage, Peter Zeppenfeld, Jinming Cai, Roman Fasel, Pascal Ruffieux, Reinhard Franz Josef Berger, Zongping Chen, Akimitsu Narita, Xinliang Feng, Klaus Müllen, Roberto Biagi, Valentina De Renzi, Deborah Prezzi, Alice

Ruini, and Andrea Ferretti. Probing optical excitations in chevron-like armchair graphene nanoribbons. *Nanoscale*, 9(46):18326–18333, November 2017.

[115] Richard Denk, Michael Hohage, Peter Zeppenfeld, Jinming Cai, Carlo A. Pignedoli, Hajo Söde, Roman Fasel, Xinliang Feng, Klaus Müllen, Shudong Wang, Deborah Prezzi, Andrea Ferretti, Alice Ruini, Elisa Molinari, and Pascal Ruffieux. Exciton-dominated optical response of ultra-narrow graphene nanoribbons. *Nature Communications*, 5(1):4253, July 2014.

[116] B. V. Senkovskiy, M. Pfeiffer, S. K. Alavi, A. Bliesener, J. Zhu, S. Michel, A. V. Fedorov, R. German, D. Hertel, D. Haberer, L. Petaccia, F. R. Fischer, K. Meerholz, P. H. M. van Loosdrecht, K. Lindfors, and A. Grüneis. Making Graphene Nanoribbons Photoluminescent. *Nano Letters*, 17(7):4029–4037, July 2017.

[117] Michael C. Chong, Lydia Sosa-Vargas, Hervé Bulou, Alex Boeglin, Fabrice Scheurer, Fabrice Mathevet, and Guillaume Schull. Ordinary and Hot Electroluminescence from Single-Molecule Devices: Controlling the Emission Color by Chemical Engineering. *Nano Letters*, 16(10):6480–6484, October 2016.

[118] S. Zhao, L. Rondin, G. Delport, C. Voisin, U. Beser, Y. Hu, X. Feng, K. Müllen, A. Narita, S. Campidelli, and J. S. Lauret. Fluorescence from graphene nanoribbons of well-defined structure. *Carbon*, 119:235–240, August 2017.

[119] Xuemei Zhang, Qingdao Zeng, and Chen Wang. On-surface single molecule synthesis chemistry: A promising bottom-up approach towards functional surfaces. *Nanoscale*, 5(18):8269–8287, 2013.

[120] Florian Klappenberger, Yi-Qi Zhang, Jonas Björk, Svetlana Klyatskaya, Mario Ruben, and Johannes V. Barth. On-Surface Synthesis of Carbon-Based Scaffolds and Nanomaterials Using Terminal Alkynes. *Accounts of Chemical Research*, 48(7):2140–2150, July 2015.

[121] Kunal S. Mali, Nicholas Pearce, Steven De Feyter, and Neil R. Champness. Frontiers of supramolecular chemistry at solid surfaces. *Chemical Society Reviews*, 46(9):2520–2542, 2017.

[122] Marco Di Giovannantonio and Giorgio Contini. Reversibility and intermediate steps as key tools for the growth of extended ordered polymers via on-surface synthesis. *Journal of Physics: Condensed Matter*, 30(9):093001, February 2018.

[123] Payam Payamyar, Benjamin T. King, Hans Christian Öttinger, and A. Dieter Schlüter. Two-dimensional polymers: Concepts and perspectives. *Chemical Communications*, 52(1):18–34, December 2015.

[124] Sylvain Clair, Mathieu Abel, and Louis Porte. Growth of boronic acid based two-dimensional covalent networks on a metal surface under ultrahigh vacuum. *Chemical Communications*, 50(68):9627–9635, 2014.

[125] Sylvain Clair and Dimas G. de Oteyza. Controlling a Chemical Coupling Reaction on a Surface: Tools and Strategies for On-Surface Synthesis. *Chemical Reviews*, 119(7):4717–4776, April 2019.

[126] Nathaniel S. Safron, Myungwoong Kim, Padma Gopalan, and Michael S. Arnold. Barrier-Guided Growth of Micro- and Nano-Structured Graphene. *Advanced Materials*, 24(8):1041–1045, 2012.

[127] Insub Jung, Ho Young Jang, and Sungho Park. Direct growth of graphene nanomesh using a Au nano-network as a metal catalyst via chemical vapor deposition. *Applied Physics Letters*, 103(2):023105, July 2013.

[128] Leonhard Grill, Matthew Dyer, Leif Lafferentz, Mats Persson, Maike V. Peters, and Stefan Hecht. Nano-architectures by covalent assembly of molecular building blocks. *Nature Nanotechnology*, 2(11):687–691, November 2007.

[129] Marco Bieri, Matthias Treier, Jinming Cai, Kamel Aït-Mansour, Pascal Ruffieux, Oliver Gröning, Pierangelo Gröning, Marcel Kastler, Ralph Rieger, Xinliang Feng, Klaus Müllen, and Roman Fasel. Porous graphenes: Two-dimensional polymer synthesis with atomic precision. *Chemical Communications*, (45):6919–6921, November 2009.

[130] Marco Bieri, Stephan Blankenburg, Milan Kivala, Carlo A. Pignedoli, Pascal Ruffieux, Klaus Müllen, and Roman Fasel. Surface-supported 2D heterotriangulene polymers. *Chemical Communications*, 47(37):10239–10241, 2011.

[131] Jia Liu, Pascal Ruffieux, Xinliang Feng, Klaus Müllen, and Roman Fasel. Cyclotrimerization of arylalkynes on Au(111). *Chemical Communications*, 50(76):11200–11203, 2014.

[132] Johanna Eichhorn, Damian Nieckarz, Oliver Ochs, Debabrata Samanta, Michael Schmittel, Pawel Jerzy Szabelski, and Markus Lackinger. On-Surface Ullmann Coupling: The Influence of Kinetic Reaction Parameters on the Morphology and Quality of Covalent Networks. *ACS Nano*, 8(8):7880–7889, August 2014.

[133] Christian Steiner, Julian Gebhardt, Maximilian Ammon, Zechao Yang, Alexander Heidenreich, Natalie Hammer, Andreas Görling, Milan Kivala, and Sabine Maier. Hierarchical on-surface synthesis and electronic structure of carbonyl-functionalized one- and two-dimensional covalent nanoarchitectures. *Nature Communications*, 8(1):14765, March 2017.

[134] Luis Cardenas, Rico Gutzler, Josh Lipton-Duffin, Chaoying Fu, Jaclyn L. Brusso, Laurentiu E. Dinca, Martin Vondráček, Yannick Fagot-Revurat, Daniel Malterre, Federico Rosei, and Dmitrii F. Perepichka. Synthesis and electronic structure of a two dimensional π-conjugated polythiophene. *Chemical Science*, 4(8):3263–3268, 2013.

[135] Wei Liu, Xin Luo, Yang Bao, Yan Peng Liu, Guo-Hong Ning, Ibrahim Abdelwahab, Linjun Li, Chang Tai Nai, Zhi Gang Hu, Dan Zhao, Bin Liu, Su Ying Quek, and Kian Ping Loh. A two-dimensional conjugated aromatic polymer via C–C coupling reaction. *Nature Chemistry*, 9(6):563–570, June 2017.

[136] Mathieu Abel, Sylvain Clair, Oualid Ourdjini, Mireille Mossoyan, and Louis Porte. Single Layer of Polymeric Fe-Phthalocyanine: An Organometallic Sheet on Metal and Thin Insulating Film. *Journal of the American Chemical Society*, 133(5):1203–1205, February 2011.

[137] Elena Nardi, Long Chen, Sylvain Clair, Mathieu Koudia, Luca Giovanelli, Xinliang Feng, Klaus Müllen, and Mathieu Abel. On-Surface Reaction between Tetracarbonitrile-Functionalized Molecules and Copper Atoms. *The Journal of Physical Chemistry C*, 118(47):27549–27553, November 2014.

[138] César Moreno, Manuel Vilas-Varela, Bernhard Kretz, Aran Garcia-Lekue, Marius V. Costache, Markos Paradinas, Mirko Panighel, Gustavo Ceballos, Sergio O. Valenzuela, Diego Peña, and Aitor Mugarza. Bottom-up synthesis of multifunctional nanoporous graphene. *Science*, 360(6385):199–203, April 2018.

[139] Zafer Mutlu, Peter H. Jacobse, Ryan D. McCurdy, Juan P. Llinas, Yuxuan Lin, Gregory C. Veber, Felix R. Fischer, Michael F. Crommie, and Jeffrey Bokor. Bottom-Up Synthesized Nanoporous Graphene Transistors. *Advanced Functional Materials*, 31(47):2103798, 2021.

[140] Salim Berrada, Viet Hung Nguyen, Damien Querlioz, Jérôme Saint-Martin, Alfonso Alarcón, Christophe Chassat, Arnaud Bournel, and Philippe Dollfus. Graphene nanomesh transistor with high on/off ratio and good saturation behavior. *Applied Physics Letters*, 103(18):183509, October 2013.

[141] Jingwei Bai, Xing Zhong, Shan Jiang, Yu Huang, and Xiangfeng Duan. Graphene nanomesh. *Nature Nanotechnology*, 5(3):190–194, March 2010.

[142] Xiluan Wang, Liying Jiao, Kaixuan Sheng, Chun Li, Liming Dai, and Gaoquan Shi. Solution-processable graphene nanomeshes with controlled pore structures. *Scientific Reports*, 3(1):1996, June 2013.

[143] O. V. Sedelnikova, S. G. Stolyarova, A. L. Chuvilin, A. V. Okotrub, and L. G. Bulusheva. Holey graphene with enhanced near-infrared absorption: Experimental and DFT study. *Applied Physics Letters*, 114(9):091901, March 2019.

[144] Babak Sakkaki, Hassan Rasooli Saghai, Ghafar Darvish, and Mehdi Khatir. Electronic and optical properties of passivated graphene nanomeshes: An ab initio study. *Optical Materials*, 122:111707, December 2021.

[145] Babak Sakkaki, Hassan Rasooli Saghai, Ghafar Darvish, and Mehdi Khatir. A new photodetector structure based on graphene nanomeshes: An ab initio study. *Beilstein Journal of Nanotechnology*, 11(1):1036–1044, July 2020.

[146] Marc Dvorak, William Oswald, and Zhigang Wu. Bandgap Opening by Patterning Graphene. *Scientific Reports*, 3(1):2289, July 2013.

[147] Wei Liu, Z. F. Wang, Q. W. Shi, Jinlong Yang, and Feng Liu. Band-gap scaling of graphene nanohole superlattices. *Physical Review B*, 80(23):233405, December 2009.

[148] Aihua Zhang, Hao Fatt Teoh, Zhenxiang Dai, Yuan Ping Feng, and Chun Zhang. Band gap engineering in graphene and hexagonal BN antidot lattices: A first principles study. *Applied Physics Letters*, 98(2):023105, January 2011.

[149] Fangping Ouyang, Shenglin Peng, Zhongfan Liu, and Zhirong Liu. Bandgap Opening in Graphene Antidot Lattices: The Missing Half. *ACS Nano*, 5(5):4023–4030, May 2011.

[150] Thomas G. Pedersen, Christian Flindt, Jesper Pedersen, Antti-Pekka Jauho, Niels Asger Mortensen, and Kjeld Pedersen. Optical properties of graphene antidot lattices. *Physical Review B*, 77(24):245431, June 2008.

[151] J. A. Sobota, S.-L. Yang, A. F. Kemper, J. J. Lee, F. T. Schmitt, W. Li, R. G. Moore, J. G. Analytis, I. R. Fisher, P. S. Kirchmann, T. P. Devereaux, and Z.-X. Shen. Direct Optical Coupling to an Unoccupied Dirac Surface State in the Topological Insulator Bi 2 Se 3. *Physical Review Letters*, 111(13):136802, September 2013.

[152] Aaron Bostwick, Taisuke Ohta, Thomas Seyller, Karsten Horn, and Eli Rotenberg. Quasiparticle Dynamics in Graphene. *Nature Physics*, 3, January 2007.

[153] Giuseppe Grosso and Giuseppe Pastori Parravicini. *Solid State Physics*. Academic Press, an imprint of Elsevier, Amsterdam, second edition edition, 2014.

[154] Elke Scheer Juan Carlos Cuevas. *Molecular Electronics: An Introduction to Theory and Experiment*, volume 1 of *World Scientific Series in Nanoscience and Nanotechnology*. World Scientific Publishing Co Pte Ltd, 5 Toh Tuck Link, Singapore 596224, June 2010.

[155] D A Papaconstantopoulos and M J Mehl. The Slater Koster tight-binding method: A computationally efficient and accurate approach. *Journal of Physics: Condensed Matter*, 15(10):R413–R440, March 2003.

[156] J. C. Slater and G. F. Koster. Simplified LCAO Method for the Periodic Potential Problem. *Physical Review*, 94(6):1498–1524, June 1954.

[157] Thomas Galvani, Fulvio Paleari, Henrique P. C. Miranda, Alejandro Molina-Sánchez, Ludger Wirtz, Sylvain Latil, Hakim Amara, and François Ducastelle. Excitons in boron nitride single layer. *Physical Review B*, 94(12):125303, September 2016.

[158] A. H. Castro Neto, F. Guinea, N. M. R. Peres, K. S. Novoselov, and A. K. Geim. The electronic properties of graphene. *Reviews of Modern Physics*, 81(1):109–162, January 2009.

[159] J. Tersoff and D. R. Hamann. Theory of the scanning tunneling microscope. *Physical Review B*, 31(2):805–813, January 1985.

[160] Oliver Gröning, Shiyong Wang, Xuelin Yao, Carlo A. Pignedoli, Gabriela Borin Barin, Colin Daniels, Andrew Cupo, Vincent Meunier, Xinliang Feng, Akimitsu Narita, Klaus Müllen, Pascal Ruffieux, and Roman Fasel. Engineering of robust topological quantum phases in graphene nanoribbons. *Nature*, 560(7717):209–213, August 2018.

[161] Stephen L. Adler. Quantum Theory of the Dielectric Constant in Real Solids. *Physical Review*, 126(2):413–420, April 1962.

[162] Nathan Wiser. Dielectric Constant with Local Field Effects Included. *Physical Review*, 129(1):62–69, January 1963.

[163] P. Hohenberg and W. Kohn. Inhomogeneous Electron Gas. *Physical Review*, 136(3B):B864–B871, November 1964.

[164] W. Kohn and L. J. Sham. Self-Consistent Equations Including Exchange and Correlation Effects. *Physical Review*, 140(4A):A1133–A1138, November 1965.

[165] Elliott H. Lieb. Density functionals for coulomb systems. *International Journal of Quantum Chemistry*, 24(3):243–277, 1983.

[166] Mel Levy. Electron densities in search of Hamiltonians. *Physical Review A*, 26(3):1200–1208, September 1982.

[167] Mel Levy. Universal variational functionals of electron densities, first-order density matrices, and natural spin-orbitals and solution of the v-representability problem. *Proceedings of the National Academy of Sciences*, 76(12):6062–6065, December 1979.

[168] O. Gunnarsson, M. Jonson, and B. I. Lundqvist. Descriptions of exchange and correlation effects in inhomogeneous electron systems. *Physical Review B*, 20(8):3136–3164, October 1979.

[169] A. D. Becke. Density-functional exchange-energy approximation with correct asymptotic behavior. *Physical Review A*, 38(6):3098–3100, September 1988.

[170] Chengteh Lee, Weitao Yang, and Robert G. Parr. Development of the Colle-Salvetti correlation-energy formula into a functional of the electron density. *Physical Review B*, 37(2):785–789, January 1988.

[171] John P. Perdew, J. A. Chevary, S. H. Vosko, Koblar A. Jackson, Mark R. Pederson, D. J. Singh, and Carlos Fiolhais. Atoms, molecules, solids, and surfaces: Applications of the generalized gradient approximation for exchange and correlation. *Physical Review B*, 46(11):6671–6687, September 1992.

[172] Kieron Burke, John P. Perdew, and Yue Wang. Derivation of a Generalized Gradient Approximation: The PW91 Density Functional. In John F. Dobson, Giovanni Vignale, and Mukunda P. Das, editors, *Electronic Density Functional Theory: Recent Progress and New Directions*, pages 81–111. Springer US, Boston, MA, 1998.

[173] John P. Perdew, Kieron Burke, and Matthias Ernzerhof. Generalized Gradient Approximation Made Simple. *Physical Review Letters*, 77(18):3865–3868, October 1996.

[174] Andrea Marini, Conor Hogan, Myrta Grüning, and Daniele Varsano. Yambo: An ab initio tool for excited state calculations. *Computer Physics Communications*, 180(8):1392–1403, August 2009.

[175] D Sangalli, A Ferretti, H Miranda, C Attaccalite, I Marri, E Cannuccia, P Melo, M Marsili, F Paleari, A Marrazzo, G Prandini, P Bonfà, M O Atambo, F Affinito, M Palummo, A Molina-Sánchez, C Hogan, M Grüning, D Varsano, and A Marini. Many-body perturbation theory calculations using the yambo code. *Journal of Physics: Condensed Matter*, 31(32):325902, August 2019.

[176] Otto F. Sankey and Roland E. Allen. Atomic forces from electronic energies via the Hellmann-Feynman theorem, with application to semiconductor (110) surface relaxation. *Physical Review B*, 33(10):7164–7171, May 1986.

[177] Otto F. Sankey and David J. Niklewski. *Ab Initio* multicenter tight-binding model for molecular-dynamics simulations and other applications in covalent systems. *Physical Review B*, 40(6):3979–3995, August 1989.

[178] J. Harris. Simplified method for calculating the energy of weakly interacting fragments. *Physical Review B*, 31(4):1770–1779, February 1985.

[179] James P. Lewis, Kurt R. Glaesemann, Gregory A. Voth, Jürgen Fritsch, Alexander A. Demkov, José Ortega, and Otto F. Sankey. Further developments in the local-orbital density-functional-theory tight-binding method. *Physical Review B*, 64(19):195103, October 2001.

[180] Alexander A. Demkov, José Ortega, Otto F. Sankey, and Matthew P. Grumbach. Electronic structure approach for complex silicas. *Physical Review B*, 52(3):1618–1630, July 1995.

[181] James Lewis, Pavel Jelinek, José Ortega, Alex Demkov, Daniel Trabada, Barry Haycock, Hao Wang, Gary Adams, John Tomfohr, Enrique Abad, Hong Wang, and D. Drabold. Advances and applications in the FIREBALL ab initio tight-binding molecular-dynamics formalism. *PHYSICA STATUS SOLIDI B-BASIC SOLID STATE PHYSICS*, 248:1989–2007, August 2011.

[182] W. Matthew C. Foulkes and Roger Haydock. Tight-binding models and density-functional theory. *Physical Review B*, 39(17):12520–12536, June 1989.

[183] M. A. Basanta, Y. J. Dappe, P. Jelínek, and J. Ortega. Optimized atomic-like orbitals for first-principles tight-binding molecular dynamics. *Computational Materials Science*, 39(4):759–766, June 2007.

[184] Pavel Jelínek, Hao Wang, James P. Lewis, Otto F. Sankey, and José Ortega. Multicenter approach to the exchange-correlation interactions in *ab initio* tight-binding methods. *Physical Review B*, 71(23):235101, June 2005.

[185] Andrew P. Horsfield. Efficient ab initio tight binding. *Physical Review B*, 56(11):6594–6602, September 1997.

[186] C.-O. Almbladh and U. von Barth. Exact results for the charge and spin densities, exchange-correlation potentials, and density-functional eigenvalues. *Physical Review B*, 31(6):3231–3244, March 1985.

[187] Matteo Gatti. *Ab-Initio Calculations of Many Body Effects in Electronic Spectre.* PhD thesis, Ecole Polytechnique X, December 2007.

[188] Xavier Blase, Ivan Duchemin, Denis Jacquemin, and Pierre-Francois Loos. The Bethe-Salpeter Equation Formalism: From Physics to Chemistry. *Journal of Physical Chemistry Letters*, 11(17):7371–7382, 2020.

[189] John P. Perdew and Mel Levy. Physical Content of the Exact Kohn-Sham Orbital Energies: Band Gaps and Derivative Discontinuities. *Physical Review Letters*, 51(20):1884–1887, November 1983.

[190] L. J. Sham and M. Schlüter. Density-Functional Theory of the Energy Gap. *Physical Review Letters*, 51(20):1888–1891, November 1983.

[191] Richard M. Martin, Lucia Reining, and David M. Ceperley. *Interacting Electrons: Theory and Computational Approaches*. Cambridge University Press, Cambridge, 2016.

[192] H. Lehmann. Über Eigenschaften von Ausbreitungsfunktionen und Renormierungskonstanten quantisierter Felder. *Il Nuovo Cimento (1943-1954)*, 11(4):342–357, April 1954.

[193] Dorothea Golze, Marc Dvorak, and Patrick Rinke. The GW Compendium: A Practical Guide to Theoretical Photoemission Spectroscopy. *Frontiers in Chemistry*, 7, 2019.

[194] Lucia Reining. The GW approximation: Content, successes and limitations. *WIREs Computational Molecular Science*, 8(3):e1344, 2018.

[195] Mark S. Hybertsen and Steven G. Louie. Electron correlation in semiconductors and insulators: Band gaps and quasiparticle energies. *Physical Review B*, 34(8):5390–5413, October 1986.

[196] Fabien Bruneval, Nathalie Vast, and Lucia Reining. Effect of self-consistency on quasiparticles in solids. *Physical Review B*, 74(4):045102, July 2006.

[197] Andrea Marini and Rodolfo Del Sole. Dynamical Excitonic Effects in Metals and Semiconductors. *Physical Review Letters*, 91(17):176402, October 2003.

[198] F. Bechstedt, K. Tenelsen, B. Adolph, and R. Del Sole. Compensation of Dynamical Quasiparticle and Vertex Corrections in Optical Spectra. *Physical Review Letters*, 78(8):1528–1531, February 1997.

[199] Gordon Baym and Leo P. Kadanoff. Conservation Laws and Correlation Functions. *Physical Review*, 124(2):287–299, October 1961.

[200] Giovanni Onida, Lucia Reining, and Angel Rubio. Electronic excitations: Density-functional versus many-body Green's-function approaches. *Reviews of Modern Physics*, 74(2):601–659, June 2002.

[201] Michael Rohlfing and Steven G. Louie. Electron-hole excitations and optical spectra from first principles. *Physical Review B*, 62(8):4927–4944, August 2000.

[202] J. Bardeen. Tunnelling from a Many-Particle Point of View. *Physical Review Letters*, 6(2):57–59, January 1961.

[203] Sai Duan, Guangjun Tian, and Xin Xu. A General Framework of Scanning Tunneling Microscopy Based on Bardeen's Approximation for Isolated Molecules. *JACS Au*, 3(1):86–92, January 2023.

[204] M. Büttiker, Y. Imry, R. Landauer, and S. Pinhas. Generalized many-channel conductance formula with application to small rings. *Physical Review B*, 31(10):6207–6215, May 1985.

[205] L. V. Keldysh. *Diagram Technique for Nonequilibrium Processes*, pages 47–55. WORLD SCIENTIFIC, November 2023.

[206] C. Caroli, R. Combescot, P. Nozieres, and D. Saint-James. A direct calculation of the tunnelling current: IV. Electron-phonon interaction effects. *Journal of Physics C: Solid State Physics*, 5(1):21, January 1972.

[207] Jose Manuel Blanco, Cesar González, Pavel Jelínek, José Ortega, Fernando Flores, and Rubén Pérez. First-principles simulations of STM images: From tunneling to the contact regime. *Physical Review B*, 70(8):085405, August 2004.

[208] Haiping Lin, Janosch M. C. Rauba, Kristian S. Thygesen, Karsten W. Jacobsen, Michelle Y. Simmons, and Werner A. Hofer. First-principles modelling of scanning tunneling microscopy using non-equilibrium Green's functions. *Frontiers of Physics in China*, 5(4):369–379, December 2010.

[209] N. Mingo, L. Jurczyszyn, F. J. Garcia-Vidal, R. Saiz-Pardo, P. L. de Andres, F. Flores, S. Y. Wu, and W. More. Theory of the scanning tunneling microscope: Xe on Ni and Al. *Physical Review B*, 54(3):2225–2235, July 1996.

[210] A. Martín-Rodero, F. Flores, and N. H. March. Tight-binding theory of tunneling current with chemisorbed species. *Physical Review B*, 38(14):10047–10050, November 1988.

[211] L. Jurczyszyn, N. Mingo, and F. Flores. The influence of the geometry of the tip on the STM images. *Czechoslovak Journal of Physics*, 47(4):407–413, April 1997.

[212] J. Ferrer, A. Martín-Rodero, and F. Flores. Contact resistance in the scanning tunneling microscope at very small distances. *Physical Review B*, 38(14):10113–10115, November 1988.

[213] C González, E Abad, Y J Dappe, and J C Cuevas. Theoretical study of carbon-based tips for scanning tunnelling microscopy. *Nanotechnology*, 27(10):105201, March 2016.

[214] F.J. García-Vidal, F. Flores, and S.G. Davison. Propagator theory of quantum-wire transmission. *Progress in Surface Science*, 74(1-8):177–184, December 2003.

[215] César González Pascual. *Métodos DFT y STM de primeros principios para el estudio de superficies semiconductoras con adsorbatos: pasivación, nanohilos y transiciones de fase*. doctoralThesis, February 2006.

[216] F. Guinea, C. Tejedor, F. Flores, and E. Louis. Effective two-dimensional Hamiltonian at surfaces. *Physical Review B*, 28(8):4397–4402, October 1983.

[217] Paolo Giannozzi, Stefano Baroni, Nicola Bonini, Matteo Calandra, Roberto Car, Carlo Cavazzoni, Davide Ceresoli, Guido L. Chiarotti, Matteo Cococcioni, Ismaila Dabo, Andrea Dal Corso, Stefano de Gironcoli, Stefano Fabris, Guido Fratesi, Ralph Gebauer, Uwe Gerstmann, Christos Gougoussis, Anton Kokalj, Michele Lazzeri, Layla Martin-Samos, Nicola Marzari, Francesco Mauri, Riccardo Mazzarello, Stefano Paolini, Alfredo Pasquarello, Lorenzo Paulatto, Carlo Sbraccia, Sandro Scandolo, Gabriele Sclauzero, Ari P. Seitsonen, Alexander Smogunov, Paolo Umari, and Renata M. Wentzcovitch. QUANTUM ESPRESSO: A modular and open-source software project for quantum simulations of materials. *Journal of Physics. Condensed Matter: An Institute of Physics Journal*, 21(39):395502, September 2009.

[218] P. Giannozzi, O. Andreussi, T. Brumme, O. Bunau, M. Buongiorno Nardelli, M. Calandra, R. Car, C. Cavazzoni, D. Ceresoli, M. Cococcioni, N. Colonna, I. Carnimeo, A. Dal Corso, S. de Gironcoli, P. Delugas, R. A. DiStasio, A. Ferretti, A. Floris, G. Fratesi, G. Fugallo, R. Gebauer, U. Gerstmann, F. Giustino, T. Gorni, J. Jia, M. Kawamura, H.-Y. Ko, A. Kokalj, E. Küçükbenli, M. Lazzeri, M. Marsili, N. Marzari, F. Mauri, N. L. Nguyen, H.-V. Nguyen, A. Otero-de-la-Roza, L. Paulatto, S. Poncé, D. Rocca, R. Sabatini, B. Santra, M. Schlipf, A. P. Seitsonen, A. Smogunov, I. Timrov, T. Thonhauser, P. Umari, N. Vast, X. Wu, and S. Baroni. Advanced capabilities for materials modelling with Quantum ESPRESSO. *Journal of Physics: Condensed Matter*, 29(46):465901, October 2017.

[219] Denis Gratias and Marianne Quiquandon. Crystallography of homophase twisted bilayers: Coincidence, union lattices and space groups. *Acta Crystallographica Section A Foundations and Advances*, 79(4):301–317, July 2023.

[220] Joe Finney, Aaron L. Sharpe, Eli J. Fox, Connie L. Hsueh, Daniel E. Parker, Matthew Yankowitz, Shaowen Chen, Kenji Watanabe, Takashi Taniguchi, Cory R. Dean, Ashvin Vishwanath, M. A. Kastner, and David Goldhaber-Gordon. Unusual magnetotransport in twisted bilayer graphene. *Proceedings of the National Academy of Sciences*, 119(16):e2118482119, April 2022.

[221] Bing Liu, Lede Xian, Haimen Mu, Gan Zhao, Zhao Liu, Angel Rubio, and Z. F. Wang. Higher-Order Band Topology in Twisted Moiré Superlattice. *Physical Review Letters*, 126(6):066401, February 2021.

[222] Lede Xian, Dante M. Kennes, Nicolas Tancogne-Dejean, Massimo Altarelli, and Angel Rubio. Multiflat Bands and Strong Correlations in Twisted Bilayer Boron Nitride: Doping-Induced Correlated Insulator and Superconductor. *Nano Letters*, 19(8):4934–4940, August 2019.

[223] Dong Seob Kim, Roy C. Dominguez, Rigo Mayorga-Luna, Dingyi Ye, Jacob Embley, Tixuan Tan, Yue Ni, Zhida Liu, Mitchell Ford, Frank Y. Gao, Saba Arash, Kenji Watanabe, Takashi Taniguchi, Suenne Kim, Chih-Kang Shih, Keji Lai, Wang Yao, Li Yang, Xiaoqin Li, and Yoichi Miyahara. Electrostatic moiré potential from twisted hexagonal boron nitride layers. *Nature Materials*, pages 1–6, August 2023.

[224] Giovanni Scuri, Trond I. Andersen, You Zhou, Dominik S. Wild, Jiho Sung, Ryan J. Gelly, Damien Bérubé, Hoseok Heo, Linbo Shao, Andrew Y. Joe, Andrés M. Mier Valdivia, Takashi Taniguchi, Kenji Watanabe, Marko Lončar, Philip Kim, Mikhail D. Lukin, and Hongkun Park. Electrically Tunable Valley Dynamics in Twisted WSe 2 / WSe 2 Bilayers. *Physical Review Letters*, 124(21):217403, May 2020.

[225] Leon Balents, Cory R. Dean, Dmitri K. Efetov, and Andrea F. Young. Superconductivity and strong correlations in moiré flat bands. *Nature Physics*, 16(7):725–733, July 2020.

[226] Dante M. Kennes, Martin Claassen, Lede Xian, Antoine Georges, Andrew J. Millis, James Hone, Cory R. Dean, D. N. Basov, Abhay N. Pasupathy, and Angel Rubio. Moiré heterostructures as a condensed-matter quantum simulator. *Nature Physics*, 17(2):155–163, February 2021.

[227] E. Suárez Morell, J. D. Correa, P. Vargas, M. Pacheco, and Z. Barticevic. Flat bands in slightly twisted bilayer graphene: Tight-binding calculations. *Physical Review B*, 82(12):121407, September 2010.

[228] Rafi Bistritzer and Allan H. MacDonald. Moiré bands in twisted double-layer graphene. *Proceedings of the National Academy of Sciences*, 108(30):12233–12237, July 2011.

[229] A. O. Sboychakov, A. L. Rakhmanov, A. V. Rozhkov, and Franco Nori. Electronic spectrum of twisted bilayer graphene. *Physical Review B*, 92(7):075402, August 2015.

[230] Hridis K. Pal, Stephen Spitz, and Markus Kindermann. Emergent Geometric Frustration and Flat Band in Moiré Bilayer Graphene. *Physical Review Letters*, 123(18):186402, October 2019.

[231] Chiranjit Mondal, Rasoul Ghadimi, and Bohm-Jung Yang. Quantum valley and subvalley Hall effect in large-angle twisted bilayer graphene. *Physical Review B*, 108(12):L121405, September 2023.

[232] Sung Joon Ahn, Pilkyung Moon, Tae-Hoon Kim, Hyun-Woo Kim, Ha-Chul Shin, Eun Hye Kim, Hyun Woo Cha, Se-Jong Kahng, Philip Kim, Mikito Koshino, Young-Woo Son, Cheol-Woong Yang, and Joung Real Ahn. Dirac electrons in a dodecagonal graphene quasicrystal. *Science*, 361(6404):782–786, August 2018.

[233] Wei Yao, Eryin Wang, Changhua Bao, Yiou Zhang, Kenan Zhang, Kejie Bao, Chun Kai Chan, Chaoyu Chen, Jose Avila, Maria C Asensio, Junyi Zhu, and Shuyun Zhou. Quasicrystalline 30° twisted bilayer graphene as an incommensurate superlattice with strong interlayer coupling. *Proceedings of the National Academy of Sciences of the United States of America*, 115(27):6928–6933, July 2018.

[234] G. Trambly de Laissardière, D. Mayou, and L. Magaud. Localization of Dirac Electrons in Rotated Graphene Bilayers. *Nano Letters*, 10(3):804–808, March 2010.

[235] Bing Deng, Binbin Wang, Ning Li, Rongtan Li, Yani Wang, Jilin Tang, Qiang Fu, Zhen Tian, Peng Gao, Jiamin Xue, and Hailin Peng. Interlayer Decoupling in 30° Twisted Bilayer Graphene Quasicrystal. *ACS Nano*, 14(2):1656–1664, February 2020.

[236] Leonid A. Chernozatonskii and Aleksey I. Kochaev. BN Diamane-like Quasicrystal Based on 30° Twisted H-BN Bilayers and Its Approximants: Features of the Atomic Structure and Electronic Properties. *Crystals*, 13(3):421, March 2023.

[237] G. Trambly de Laissardière, D. Mayou, and L. Magaud. Numerical studies of confined states in rotated bilayers of graphene. 86(12):125413.

[238] Sylvain Latil, Hakim Amara, and Lorenzo Sponza. Structural classification of boron nitride twisted bilayers and ab initio investigation of their stacking-dependent electronic structure. *SciPost Physics*, 14(3):053, March 2023.

[239] Lorenzo Sponza, Van Binh Vu, Elisa Serrano Richaud, Hakim Amara, and Sylvain Latil. Emergence of flat bands in the quasicrystal limit of boron nitride twisted bilayers. *Physical Review B*, 109(16):L161403, April 2024.

[240] Hendrik J. Monkhorst and James D. Pack. Special points for Brillouin-zone integrations. *Physical Review B*, 13(12):5188–5192, June 1976.

[241] Xing-Ju Zhao, Yang Yang, Dong-Bo Zhang, and Su-Huai Wei. Formation of Bloch Flat Bands in Polar Twisted Bilayers without Magic Angles. *Physical Review Letters*, 124(8):086401, February 2020.

[242] Lorenzo Sponza. Direct and indirect excitons in boron nitride polymorphs: A story of atomic configuration and electronic correlation. *Physical Review B*, 98(12), 2018.

[243] Fulvio Paleari, Thomas Galvani, Hakim Amara, François Ducastelle, Alejandro Molina-Sánchez, and Ludger Wirtz. Excitons in few-layer hexagonal boron nitride: Davydov splitting and surface localization. *2D Materials*, 5(4):045017, August 2018.

[244] Guodong Yu, Yunhua Wang, Mikhail I. Katsnelson, and Shengjun Yuan. Origin of the magic angle in twisted bilayer graphene from hybridization of valence and conduction bands. *Physical Review B*, 108(4):045138, July 2023.

[245] Shiang Fang, Rodrick Kuate Defo, Sharmila N. Shirodkar, Simon Lieu, Georgios A. Tritsaris, and Efthimios Kaxiras. Ab initio tight-binding Hamiltonian for transition metal dichalcogenides. *Physical Review B*, 92(20):205108, November 2015.

[246] Daniel Medina-Lopez, Thomas Liu, Silvio Osella, Hugo Levy-Falk, Nicolas Rolland, Christine Elias, Gaspard Huber, Pranav Ticku, Loïc Rondin, Bruno Jousselme, David Beljonne, Jean-Sébastien Lauret, and Stephane Campidelli. Interplay of structure and photophysics of individualized rod-shaped graphene quantum dots with up to 132 sp^2 carbon atoms. *Nature Communications*, 14, August 2023.

[247] Gaël Rouillé, Mathias Steglich, Friedrich Huisken, Thomas Henning, and Klaus Müllen. UV/visible spectroscopy of matrix-isolated hexa-peri-hexabenzocoronene: Interacting electronic states and astrophysical context. *The Journal of Chemical Physics*, 131(20):204311, November 2009.

[248] Yunhai Li, Huabing Shu, Shudong Wang, and Jinlan Wang. Electronic and Optical Properties of Graphene Quantum Dots: The Role of Many-Body Effects. *The Journal of Physical Chemistry C*, 119(9):4983–4989, March 2015.

[249] Caterina Cocchi, Deborah Prezzi, Alice Ruini, Marilia J. Caldas, and Elisa Molinari. Anisotropy and Size Effects on the Optical Spectra of Polycyclic Aromatic Hydrocarbons. *The Journal of Physical Chemistry A*, 118(33):6507–6513, August 2014.

[250] InterfaceBuilder — | QuantumATK V-2023.12 Documentation. https://docs.quantumatk.com/manual/Types/InterfaceBuilder/InterfaceBuilder.html#interface-builder.

[251] Atomistic Simulation Software | QuantumATK - Synopsys. https://www.synopsys.com/manufacturing/quantumatk.html.

[252] Line Jelver, Peter Mahler Larsen, Daniele Stradi, Kurt Stokbro, and Karsten Wedel Jacobsen. Determination of low-strain interfaces via geometric matching. *Physical Review B*, 96(8):085306, August 2017.

[253] Jianmin Huang, Hongxing Jia, Tao Wang, Lin Feng, Pingwu Du, and Junfa Zhu. Kinetic Control over Morphology of Nanoporous Graphene on Surface. *ChemPhysChem*, 20(18):2327–2332, 2019.

[254] Daniel Medina Lopez. *Synthesis and Optical Properties of Graphene Nanostructures*. These de doctorat, université Paris-Saclay, October 2023.

[255] Jinming Cai, Carlo A. Pignedoli, Leopold Talirz, Pascal Ruffieux, Hajo Söde, Liangbo Liang, Vincent Meunier, Reinhard Berger, Rongjin Li, Xinliang Feng, Klaus Müllen, and Roman Fasel. Graphene nanoribbon heterojunctions. *Nature Nanotechnology*, 9(11):896–900, November 2014.

[256] Mohammad Mehdi Pour, Andrey Lashkov, Adrian Radocea, Ximeng Liu, Tao Sun, Alexey Lipatov, Rafal A. Korlacki, Mikhail Shekhirev, Narayana R. Aluru, Joseph W. Lyding, Victor Sysoev, and Alexander Sinitskii. Laterally extended atomically precise graphene nanoribbons with improved electrical conductivity for efficient gas sensing. *Nature Communications*, 8(1):820, October 2017.

[257] Ting Cao, Fangzhou Zhao, and Steven G. Louie. Topological Phases in Graphene Nanoribbons: Junction States, Spin Centers, and Quantum Spin Chains. *Physical Review Letters*, 119(7):076401, August 2017.

[258] Amina Kimouche, Mikko M. Ervasti, Robert Drost, Simo Halonen, Ari Harju, Pekka M. Joensuu, Jani Sainio, and Peter Liljeroth. Ultra-narrow metallic armchair graphene nanoribbons. *Nature Communications*, 6(1):10177, December 2015.

[259] Marco Di Giovannantonio, Okan Deniz, José I. Urgel, Roland Widmer, Thomas Dienel, Samuel Stolz, Carlos Sánchez-Sánchez, Matthias Muntwiler, Tim Dumslaff, Reinhard Berger, Akimitsu Narita, Xinliang Feng, Klaus Müllen, Pascal Ruffieux, and Roman Fasel. On-Surface Growth Dynamics of Graphene Nanoribbons: The Role of Halogen Functionalization. *ACS Nano*, 12(1):74–81, January 2018.

[260] Matthias Georg Schwab, Akimitsu Narita, Yenny Hernandez, Tatyana Balandina, Kunal S. Mali, Steven De Feyter, Xinliang Feng, and Klaus Müllen. Structurally Defined Graphene Nanoribbons

with High Lateral Extension. *Journal of the American Chemical Society*, 134(44):18169–18172, November 2012.

[261] Julien Lavie. *Synthesis and Properties of Graphene Quantum Dots and Nanomeshes*. PhD thesis, Université Paris Saclay (COmUE), October 2018.

[262] Xin-Jing Zhao, Hao Hou, Xue-Ting Fan, Yu Wang, Yu-Min Liu, Chun Tang, Shun-He Liu, Peng-Peng Ding, Jun Cheng, Dong-Hai Lin, Cheng Wang, Ye Yang, and Yuan-Zhi Tan. Molecular bilayer graphene. *Nature Communications*, 10(1):3057, July 2019.

[263] András Pálinkás, György Kálvin, Péter Vancsó, Konrád Kandrai, Márton Szendrő, Gergely Németh, Miklós Németh, Áron Pekker, József S. Pap, Péter Petrik, Katalin Kamarás, Levente Tapasztó, and Péter Nemes-Incze. The composition and structure of the ubiquitous hydrocarbon contamination on van der Waals materials. *Nature Communications*, 13(1):6770, November 2022.

[264] L. E. Dinca, F. De Marchi, J. M. MacLeod, J. Lipton-Duffin, R. Gatti, D. Ma, D. F. Perepichka, and F. Rosei. Pentacene on Ni(111): Room-temperature molecular packing and temperature-activated conversion to graphene. *Nanoscale*, 7(7):3263–3269, 2015.

[265] Julien Lavie, Van Binh Vu, Daniel Medina-Lopez, Yannick Dappe, Thomas Liu, Loïc Rondin, Jean-Sébastien Lauret, Sylvain Latil, and Stéphane Campidelli. Bottom-Up Synthesis, Dispersion and Properties of Rectangular-Shaped Graphene Quantum Dots. *Helvetica Chimica Acta*, 106(6):e202300034, 2023.

[266] Kamal Choudhary, Kevin F. Garrity, Charles Camp, Sergei V. Kalinin, Rama Vasudevan, Maxim Ziatdinov, and Francesca Tavazza. Computational scanning tunneling microscope image database. *Scientific Data*, 8(1):57, February 2021.

[267] Ce Wang, Haiwei Li, Zhenqi Hao, Xintong Li, Changwei Zou, Peng Cai, Yayu Wang, Yi-Zhuang You, and Hui Zhai. Machine learning identification of impurities in the STM images*. *Chinese Physics B*, 29(11):116805, November 2020.

[268] Frédéric Joucken, John L. Davenport, Zhehao Ge, Eberth A. Quezada-Lopez, Takashi Taniguchi, Kenji Watanabe, Jairo Velasco Jr., Jérôme Lagoute, and Robert A. Kaindl. Denoising Scanning Tunneling Microscopy Images of Graphene with Supervised Machine Learning, November 2022.

[269] Zhiwen Zhu, Jiayi Lu, Shaoxuan Yuan, Yu He, Fengru Zheng, Hao Jiang, Yuyi Yan, and Qiang Sun. Automated Generation and Analysis of Molecular Images Using Generative Artificial Intelligence Models. *The Journal of Physical Chemistry Letters*, 15(7):1985–1992, February 2024.

[270] S. Lebègue, B. Arnaud, M. Alouani, and P. E. Bloechl. Implementation of an all-electron GW approximation based on the PAW method without plasmon pole approximation: Application to Si, SiC, AlAs, InAs, NaH and KH. *Physical Review B*, 67(15):155208, April 2003.

[271] Alberto Guandalini, Pino D'Amico, Andrea Ferretti, and Daniele Varsano. Efficient GW calculations in two dimensional materials through a stochastic integration of the screened potential, June 2022.

[272] Daniele Stradi, Line Jelver, Søren Smidstrup, and Kurt Stokbro. Method for determining optimal supercell representation of interfaces. *Journal of Physics: Condensed Matter*, 29(18):185901, March 2017.